

**Alma Mater Studiorum – Università di Bologna**

---

---

DOTTORATO DI RICERCA IN ASTRONOMIA

Ciclo XXII

Settore scientifico-disciplinare di afferenza: FIS/05

**An X-ray absorption line spectroscopy study of ultra-fast  
outflows from the innermost regions of AGNs**

PhD Thesis of:

**Francesco Tombesi**

Supervisor:

**Prof. Giorgio G. C. Palumbo**

PhD Coordinator:

**Prof. Lauro Moscardini**

Co-Supervisor:

**Dr. Massimo Cappi**

Esame finale 2010

---

---

Scuola di Dottorato in Scienze Matematiche, Fisiche e Astronomiche

Dottorato di Ricerca in Astronomia – XXII Ciclo

PhD Thesis in Astronomy

*Bologna, Marzo 2010*



*This PhD Thesis has been carried out  
at the INAF-IASF of Bologna as part  
of the institute's research activities*



# Contents

|  |           |
|--|-----------|
| <b>Introduction</b>  | <b>1</b>  |
| <b>1 Basic X-ray properties of Active Galactic Nuclei</b>                                    | <b>5</b>  |
| 1.1 Active Galactic Nuclei and Super-massive Black Holes . . . . .                           | 5         |
| 1.1.1 The AGN taxonomy and the “unified model” . . . . .                                     | 6         |
| 1.2 The complex X-ray spectrum of Active Galactic Nuclei . . . . .                           | 10        |
| 1.2.1 The Continuum . . . . .  | 10        |
| 1.2.2 The other spectral components . . . . .  | 13        |
| 1.2.3 Highly ionized Fe K-shell transitions . . . . .  | 14        |
| 1.3 X-ray observations of AGN outflows . . . . .   | 16        |
| 1.3.1 Warm absorbers . . . . .   | 16        |
| 1.3.2 Ultra-fast Outflows . . . . .  | 19        |
| 1.4 Open questions on UFOs and goals of this Thesis . . . . .                                | 22        |
| 1.4.1 The importance of winds/outflows on the overall AGN structure . .                      | 22        |
| 1.4.2 The physics of AGN winds/outflows . . . . .  | 25        |
| 1.4.3 Impact of AGN winds/outflows on the host galaxy and cosmological<br>feedback . . . . . | 30        |
| 1.4.4 Significance of blue-shifted Fe K absorption lines in AGN . . . . .                    | 32        |
| <b>2 Data analysis and statistical methods</b>   | <b>36</b> |
| 2.1 Line search method . . . . .   | 36        |
| 2.2 Line significance from Monte Carlo simulations . . . . .                                 | 38        |
| <b>3 The radio-quiet AGN sample</b>  | <b>43</b> |
| 3.1 Sample selection . . . . .   | 43        |
| 3.2 XMM-Newton observations and data reduction . . . . .                                     | 43        |

|          |   |           |
|----------|---|-----------|
| 3.3      | Data analysis . . . . .   | 45        |
| 3.3.1    | Continuum and emission lines modelling . . . . .                      | 46        |
| 3.3.2    | Absorption lines search . . . . .                                     | 48        |
| 3.3.3    | EPIC pn background and calibration checks . . . . .                   | 51        |
| 3.3.4    | Absorption lines detection significance . . . . .                     | 52        |
| 3.3.5    | Consistency check with the EPIC MOS cameras . . . . .                 | 54        |
| 3.4      | Results . . . . .   | 55        |
| 3.4.1    | Absorption lines identification . . . . .                             | 55        |
| 3.4.2    | Global incidence of blue-shifted Fe K absorption lines . . . . .      | 60        |
| 3.4.3    | Mean parameters of the Fe K absorption lines . . . . .                | 63        |
| <b>4</b> | <b>The radio-loud AGN sample</b>                                      | <b>66</b> |
| 4.1      | Sample selection . . . . .  | 66        |
| 4.2      | Suzaku observations and data reduction . . . . .                      | 67        |
| 4.3      | Data analysis . . . . .   | 68        |
| 4.3.1    | Continuum and emission lines modelling . . . . .                      | 69        |
| 4.3.2    | 3C 111 . . . . .  | 70        |
| 4.3.3    | 3C 390.3 . . . . .  | 73        |
| 4.3.4    | 3C 120 . . . . .  | 74        |
| 4.3.5    | 3C 382 . . . . .  | 76        |
| 4.3.6    | 3C 445 . . . . .  | 77        |
| 4.3.7    | XIS-FI background and consistency checks . . . . .                    | 78        |
| <b>5</b> | <b>Photo-ionization modelling</b>                                     | <b>81</b> |
| 5.1      | The Spectral Energy Distribution . . . . .                            | 81        |
| 5.2      | Detailed photo-ionization modelling . . . . .                         | 85        |
| 5.2.1    | The Xstar code . . . . .  | 85        |
| 5.2.2    | Curve of growth analysis of the Fe K-shell absorption lines . . . . . | 86        |
| 5.2.3    | The Xstar tables . . . . .  | 95        |
| 5.3      | Spectral fits of the radio-quiet AGN sample . . . . .                 | 97        |
| 5.4      | Spectral fits of the radio-loud AGN sample . . . . .                  | 99        |

|  |            |
|--|------------|
| <b>6 Discussion</b>  | <b>103</b> |
| 6.1 Evidence for Ultra-fast Outflows in the radio-quiet AGN sample . . . . . | 103        |
| 6.2 Evidence for Ultra-fast Outflows in the radio-loud AGN sample . . . . .  | 110        |
| 6.3 Physical properties of Ultra-fast Outflows . . . . .                     | 113        |
| 6.4 Comparison with accretion disk winds/outflows models . . . . .           | 123        |
| <b>7 Future perspectives</b>   | <b>131</b> |
| 7.1 Astro-H . . . . .  | 131        |
| 7.1.1 Simulations of the X-ray Calorimeter Spectrometer . . . . .            | 132        |
| 7.2 IXO . . . . .  | 134        |
| 7.2.1 Simulations of the X-ray Microcalorimeter Spectrometer . . . . .       | 135        |
| <b>Conclusions</b>   | <b>139</b> |
| <b>Acknowledgements</b>  | <b>143</b> |
| <b>Appendices</b>  | <b>144</b> |
| <b>A The radio-quiet sample data</b>   | <b>145</b> |
| <b>B Ratios and contour plots of the radio-quiet sample</b>                  | <b>156</b> |
| <b>C Notes on single sources of the radio-quiet sample</b>                   | <b>169</b> |
| <b>D The XMM-Newton and Suzaku X-ray observatories</b>                       | <b>179</b> |
| D.1 XMM-Newton . . . . .   | 179        |
| D.1.1 General characteristics . . . . .                                      | 179        |
| D.1.2 The EPIC cameras . . . . .   | 181        |
| D.2 Suzaku . . . . .   | 185        |
| D.2.1 General characteristics . . . . .                                      | 185        |
| D.2.2 XIS . . . . .  | 186        |
| D.2.3 HXD . . . . .  | 187        |
| <b>Bibliography</b>  | <b>190</b> |

# Introduction

Thanks to the high throughput of recent X-ray observatories, there has been increasing evidence for the presence of narrow blue-shifted absorption lines at rest-frame energies greater than 6.4 keV in the spectra of a number of radio-quiet AGN and quasars (see review by Cappi 2006). These features are commonly identified with Fe XXV and/or Fe XXVI K-shell resonant absorption from a highly ionized ( $\log\xi\simeq 3-6$  erg s<sup>-1</sup> cm) zone of circumnuclear gas, with column densities as large as  $N_H\simeq 10^{22}-10^{24}$  cm<sup>-2</sup>. The lines blue-shifts are also often quite large, reaching (mildly) relativistic velocities (up to 0.2–0.4c). In some cases short term variability has been reported (e.g. Pounds et al. 2003a; Reeves et al. 2004; Dadina et al. 2005; Markowitz et al. 2006; Braitto et al. 2007; Cappi et al. 2009). These findings suggest the presence of previously unknown Ultra-fast Outflows (UFOs) from the central regions of AGN, possibly connected with accretion disk winds/ejecta.

Fast outflows are commonly observed in several classes of AGN in different wavebands, from the relativistic jets in radio-loud quasars to the broad-absorption lines (BAL) in the UV spectra of distant quasars (see review by Crenshaw et al. 2003). Moreover, theoretical models and numerical simulations of black hole accretion systems naturally require the formation of UFOs (with velocities up to relativistic values), possibly in the form of accretion disk winds/outflows (e.g. Proga et al. 2000; King & Pounds 2003; Proga & Kallman 2004; Ohsuga et al. 2009; King 2009). These extreme outflows from the central regions of AGN have the possibility to bring outward a significant amount of mass and energy, which can have an important influence on the surrounding environment (see review by Cappi 2006, Elvis 2006 and Fabian 2009). In fact, feedback from AGN is expected to have a significant role in the evolution of the host galaxy, such as the enrichment of the ISM or the reduction of star formation, and could also explain some fundamental relations (e.g. Ferrarese & Merritt 2000; King 2009). The ejection of a huge amount of mass from the central regions of AGN can also inhibit the growth of the super-massive black

holes (SMBHs), potentially affecting their evolution. The study of such outflows gives also important insights on the working of AGN and on the black hole accretion/ejection physics in general.

The main observational evidence for UFOs is the detection of narrow blue-shifted Fe K-shell absorption lines above 6 keV, where instrumental resolution and signal-to-noise are usually much lower than in the soft X-rays (e.g. Schurch et al. 2009). Moreover, this highly ionized gas is hard to observe in soft X-ray spectra because all the elements lighter than Fe are almost completely ionized and this may be the reason why it has not been reported previously. In fact, extensive studies of local Seyfert galaxies (which constitute the majority of the local radio-quiet AGN population) in the soft X-rays (0.1–2 keV) demonstrated the presence of layers of ionized absorbing gas in about 50% of the sources, the so-called warm absorbers (WAs) (e.g. Blustin et al. 2005; McKernan et al. 2007). This gas has values of the ionization parameter ( $\log \xi \sim 0\text{--}2 \text{ erg s}^{-1} \text{ cm}$ ), column density ( $N_H \sim 10^{20\text{--}22} \text{ cm}^{-2}$ ) and outflow velocity ( $\sim 100\text{--}1000 \text{ km/s}$ ) that are far less extreme than those of UFOs. This would suggest that the classical warm absorbing gas has a different origin, probably connected with the optical-UV BLR or torus winds (Blustin et al. 2005; McKernan et al. 2007), further away from the SMBH (at distances of the order of 1–100 pc). There could therefore be significant columns of gas associated with the UFOs which have previously been unobserved due to an observational effect. These findings have opened a large discovery space to increase our understanding of the inner structure of AGN.

However, even if in recent years there have been several papers in the literature reporting the detection of blue-shifted Fe K absorption lines in radio-quiet AGN and quasars (e.g. Pounds et al. 2003a; Reeves et al. 2004; Dadina et al. 2005; Markowitz et al. 2006; Braitto et al. 2007; Cappi et al. 2009) there is still some debate on their real statistical significance. In fact, the detections of these blue-shifted absorption features in the spectra of different sources have been published by several authors using distinct instruments, analysis and statistical techniques. Moreover, the fact that the detection significance of each single line can be weak and the lack of a global analysis on a complete sample of sources led Vaughan & Uttley (2008) to claim the presence of a publication bias. Thus, there is the need to put a solid observational basis on the global veracity of such blue-shifted Fe K absorption lines.

The aim of the present work is to address this point. Therefore, we will statistically quantify the incidence and characteristics of the blue-shifted Fe K absorption lines (at  $E > 6.4$  keV) with a comprehensive and uniform analysis on a large sample of radio-quiet and radio-loud AGN. We will also perform a detailed modeling of the data using the Xstar (Kallman & Bautista 2001) photo-ionization code and a curve of growth analysis to derive the physical parameters of the absorbing material. The results of this study are reported in several papers. This Thesis is structured as follows:

- In Chapter 1 we describe the basic X-ray properties of Active Galactic Nuclei, such as their classification, the “unification model” and the main components of their X-ray spectrum. We describe also the characteristics of X-ray absorbers in AGN, i.e. the warm absorbers and the ultra-fast outflows, and we report a list of open questions regarding the UFOs and the goals of this Thesis.
- In Chapter 2 we describe the line search technique that has been developed for the detection of blue-shifted Fe K absorption lines and the Monte Carlo method used to assess their statistical significance.
- In Chapter 3 we present the analysis of the radio-quiet AGN sample. In particular, we describe a uniform and systematic analysis of the XMM-Newton spectra of the sources and a search for blue-shifted Fe K absorption lines. We report the incidence of the lines on the population and the blue-shifted velocity distribution. The results on the single source Mrk 509 have already been presented by us in Cappi et al. (2009), instead the results on the whole sample will be reported in Tombesi et al. (2010, A&A submitted).
- In Chapter 4, instead, we present the analysis of the radio-loud AGN sample. In particular, we describe the detailed analysis of the Suzaku observations of the sources and the search for blue-shifted Fe K absorption lines. The results of this study will be reported in Tombesi et al. (2010, ApJ submitted).
- In Chapter 5 we describe the detailed photo-ionization modeling of the Fe K absorbers. In particular, we derive the mean SED for the radio-quiet AGN sample, we report a curve of growth analysis of the Fe K-shell absorption lines and we present a direct fit to the spectral data using the Xstar photo-ionization code. The results of this study will be reported in Tombesi et al. (2010, in prep.).

- In Chapter 6 we discuss the evidence for UFOs in both radio-quiet and radio-loud AGN. We also report their physical properties and present a comparison with accretion disk winds/outflows models.
- In Chapter 7 we discuss the improvements in the field that will be brought by the micro-calorimeter spectrometers on board the future X-ray satellites Astro-H and IXO (the results of this study have been reported in Tombesi et al. 2009), and finally we draw our conclusions.
- In Appendix A, B and C we report the tables, the ratios and contour plots and the notes on the sources of the radio-quiet AGN sample, respectively. In Appendix D we present a description of the XMM-Newton and Suzaku X-ray observatories.

# Chapter 1

## Basic X-ray properties of Active Galactic Nuclei

### 1.1 Active Galactic Nuclei and Super-massive Black Holes

In general, the term Active Galactic Nuclei (AGN) refers to the existence of extremely energetic phenomena in the central regions of a significant fraction ( $\sim 10\text{--}20\%$ ) of all galaxies. AGN are associated with the emission of a huge amount of radiation over the whole electromagnetic spectrum. For instance, their optical-UV luminosity can reach or even exceed that of the integrated stellar population of the host galaxy ( $L > 10^{10}\text{--}10^{11} L_{\odot}$ ).

In particular, the bolometric luminosity of AGN is typically in the range  $\sim 10^{42}\text{--}10^{46} \text{ erg s}^{-1}$ , which makes them the most luminous persistent sources of electromagnetic radiation in the universe. Moreover, from variability studies, their emission region can be constrained on *sub pc* scales (e.g. Peterson 1997). These evidences, corroborated by the intense emission extending up to the X-ray and  $\gamma$ -ray bands, suggest a non stellar origin for these sources and possibly a relation with compact objects.

In fact, the only viable physical process that is capable to explain such huge production of energy in a so compact region is the emission of radiation from material in accretion onto a Super-massive Black Hole (SMBH) (e.g. Salpeter 1964). This is the most effective process to generate energy by converting the gravitational potential into radiation and it is even ten times more efficient than the thermonuclear reactions in the interior of stars<sup>1</sup>. In the limit of a stationary accretion flow, the efficiency of the process depends on the compactness of the system:  $\eta \propto M/R$ , where  $M$  is the mass of the object and  $R$  its

---

<sup>1</sup>The most efficient of which is the fusion of Hydrogen nuclei into Helium, that can reach a value of  $\eta \simeq E/mc^2 \simeq 0.007$ .

typical dimension. The more massive or the more compact is the structure, the higher is the efficiency. In the case of SMBHs in the center of AGN this depends on the spin of the black hole, ranging from  $\eta \sim 0.1$  for a non-rotating Schwarzschild BH up to  $\eta \sim 0.4$  for a maximally spinning Kerr BH (e.g. Frank, King & Raine 1992). This is due to the fact that the Innermost Stable Circular Orbit (ISCO) of the accretion disk in the two cases is different:  $\sim 3 r_s$  (Schwarzschild radii,  $r_s = 2GM_{BH}/c^2$ ) for a Schwarzschild BH and goes down to  $\sim 0.5r_s$  for a Kerr BH. Moreover, the gravitational potential induced by SMBH provides a huge reservoir of energy and may explain the observed long-lasting emission from AGN.

The masses of SMBHs have been estimated from the orbital speed or through the reverberation mapping of gas in the central regions of AGN and they are enormous, in the range  $\sim 10^6$ – $10^9 M_\odot$  (e.g. Peterson et al. 2004). The processes that led the mass of the SMBH to growth to such large values are still under debate. It should be noted that two other classes of black holes exist in astrophysics, which are classified depending on their mass. At the lower extreme there are the stellar mass black holes, with masses of the order of  $\sim 2$ – $50 M_\odot$ . They are the direct remnants of the collapse of the core of massive stars at the end of their lifetime. The luminosity generated by their accretion processes is relatively low ( $L \sim 10^{38}$  erg s $^{-1}$ ) and therefore their observation have been limited only to the Milky Way and nearby galaxies (e.g. black hole binaries). Then, there is evidence, albeit still debated, for the existence of Intermediate-mass Black Holes (IMBHs), with masses of the order of  $\sim 10^2$ – $10^4 M_\odot$ . They are associated with Ultra-luminous X-ray sources (ULXs), which can reach high luminosities ( $L \sim 10^{39}$ – $10^{41}$  erg s $^{-1}$ ) and are not always localized in the central regions of galaxies. However, it is important to note that all the processes associated with accretion onto black holes result in the production of significant X-ray emission.

### 1.1.1 The AGN taxonomy and the “unified model”

The structure of the AGN is rather complex and this is reflected in their spectra/images, with many different emission/absorption processes acting at the same time. Therefore, from an observational point of view, their classification can be rather complex and confusing, because it can differ depending on the waveband in which they are observed and the values of the parameters used for the differentiation have been arbitrarily chosen.

In the following we report a simple and not exhaustive taxonomy of the main types of AGN (e.g. Peterson 1997):

- **Seyfert galaxies:** are composed by AGN of moderate bolometric luminosity ( $L_{bol} \sim 10^{41} - 10^{44}$  erg s<sup>-1</sup>). They are preferentially found in nearby ( $z < 0.1$ ) spiral galaxies. From a spectroscopic point of view they show an intense continuum emission ranging from the IR up to the X-rays. In particular, in the optical-UV these objects show several highly ionized emission lines from different atomic species (e.g. C, O, Ne). These lines can be narrow, FWHM  $\sim 1000 - 2000$  km/s, and broad, FWHM  $> 2000$  km/s. If both lines are present the Seyfert is said type 1, otherwise if only the narrow lines are observable it is classified as type 2. They usually have low radio emission and weak or absent radio jets and for this reason they are generally classified as *radio-quiet* (RQ) AGN.
- **Quasars:** (or QSOs) are the most luminous of all AGN ( $L_{bol} \sim 10^{44} - 10^{47}$  erg s<sup>-1</sup>). Their spectra are similar to those of Seyferts. However, they are usually found at higher red-shifts ( $z > 0.1$ ) and the host galaxy is hardly, if not at all, resolved. They can have a significant radio emission, in which case this radiation can be connected with relativistic jets or extended emission lobes.
- **Radio Galaxies:** are moderate or bright AGN ( $L_{bol} \sim 10^{42} - 10^{46}$  erg s<sup>-1</sup>) and their peculiarity is their powerful emission in the radio-mm band. The radio emission can be identified with radio jets or lobes and can significantly extend outside the host galaxy. They are preferentially found in giant elliptical galaxies located in the central regions of rich cluster of galaxies. They can be classified as Broad Line radio Galaxies (BLRGs) or Narrow Line radio Galaxies (NLRGs) depending on the presence of broad or narrow emission lines in their optical-UV spectra. In particular, their spectrum can be rather similar to that of the Seyferts for energies greater than the IR. The main difference is the much higher emission in the radio-mm. Therefore, they can be regarded as the *radio-loud* (RL) counterpart of Seyfert galaxies.
- **OVV & BL Lac objects:** the Optically Violent Variables (OVV) show the highest variability of the emission among all AGN, from the radio up to the X-ray band. Their optical emission is also strongly polarized. BL Lac objects are different from

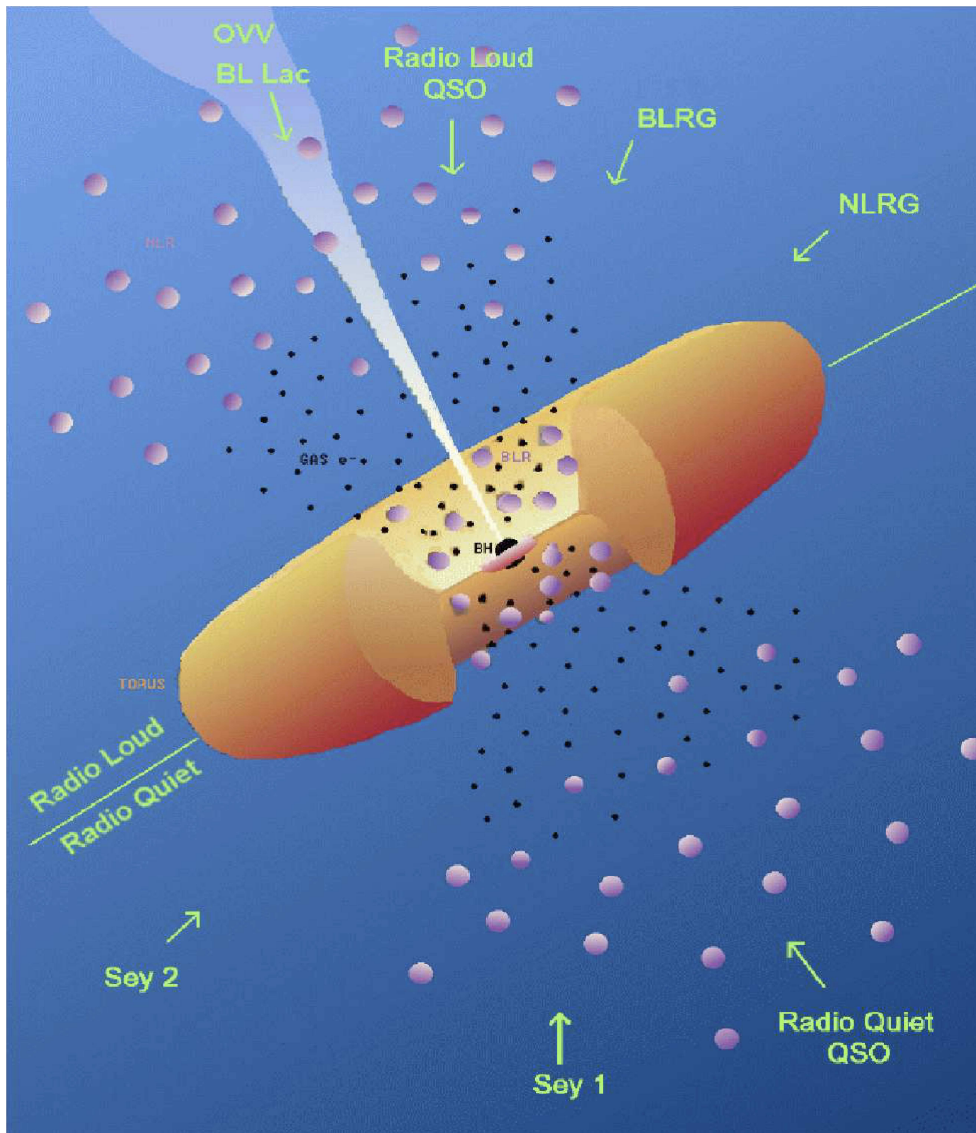


Figure 1.1: General structure of AGN according to the “unified model”. This scheme accounts for the different classification of radio-quiet and radio-loud AGN depending on the line of sight inclination with respect to the obscuring torus and radio jet (M. Polletta 1996, Laurea Thesis; adapted from Urry & Padovani 1995).

the OVV because they do not show strong emission/absorption lines. They are also radio sources.

Besides this observational diversity, it is now widely accepted that all classes of AGN share the same intrinsic structure and the observed characteristics are mainly due to the

different inclination angle through which the sources are observed. In fact, according to the so called “unified model” (e.g. Antonucci 1993; Urry & Padovani 1995) all AGN are powered by the accretion of matter onto a central SMBH. The general structure of AGN according to the “unified model” is illustrated in Fig 1.1. The material approaching the black hole forms an accretion disk and the conversion of part of the gravitational potential into radiation through viscous drag is the base of their emission. The temperature of the disk increases approaching the innermost regions and the resultant spectrum is a combination of thermal black bodies, with the peak of emission in the far UV (the so called “big blue bump”). The interaction of this soft radiation with a corona of hot electrons on top of the disk through inverse Compton is then supposed to produce the observed X-rays.

In the regions surrounding the nucleus there are clouds of gas in (possibly Keplerian) motion with respect to the SMBH. These produce the broad and narrow emission lines observed in the optical-UV. In particular, the former are generated in a high density region ( $n \sim 10^8 - 10^{10} \text{ cm}^{-3}$ ) called the Broad Line Region (BLR), located at a distance of less than  $\sim 1$  pc from the central source, where the typical velocity of the gas is  $\sim 10^4$  km/s. The latter, instead, are produced in a region further away from the nucleus called Narrow Line Region (NLR), at a distance of the order of  $\sim 1 - 100$  pc, and have slower typical velocities (less than  $\sim 10^3$  km/s). Furthermore, the fact that some of the narrow lines are forbidden suggests that they are produced in a low density material ( $n \sim 10^3 - 10^6 \text{ cm}^{-3}$ ).

The inner parts of the AGN, up to the BLR, are then supposed to be embedded by a Compton thick ( $N_H > 10^{24} \text{ cm}^{-2}$ ) torus-like structure, essentially composed by molecular clouds and dust. Depending on the inclination with respect to the line of sight, the torus causes a different obscuration of the central regions. Finally, perpendicular to the accretion disk plane, there can be highly collimated jets of particles with relativistic velocities. These are associated with an intense synchrotron radio emission and are preferentially observed in radio-loud objects. The general structure of AGN according to the “unified model” is illustrated in Fig 1.1.

Therefore, according to this paradigm, the emission from AGN is rather anisotropic and the presence of the obscuring torus and relativistic jets specify a privileged axis of symmetry. Consequently, the observational classification of the AGN listed previously is not due to intrinsic differences but it is essentially due to a distinct inclination angle of

the system with respect to the line of sight (e.g. Antonucci 1993; Urry & Padovani 1995). This is again illustrated in Fig. 1.1.

The presence or absence of a powerful relativistic jet differentiates between *radio-loud* and *radio-quiet* AGN. Instead, the level of obscuration by the torus causes the main differences relative to the line of sight. If the inclination with respect to the polar axis is very low (less than  $\sim 10^\circ$ ), the emission is saturated by the intense luminosity of the central source and the sources are classified as OVV, BL Lac objects. For intermediate angles ( $\sim 30^\circ$ ), the central regions are directly visible and both BLR and NLR are observable. In this case the sources are classified as type 1 Seyferts or BLRGs, depending on the intensity of their radio emission. For high inclination angles ( $> 60^\circ$ ), the inner parts of the AGN are obscured by the torus. Only some scattered continuum emission is visible in the optical-UV and we can still directly see the NLR but the BLR only through polarized light (e.g. Antonucci & Miller 1985). Therefore, the sources are classified as type 2 Seyferts or NLRGs, depending on the intensity of the radio emission. Finally, QSOs are the high luminosity counterparts of Seyferts and radio galaxies ( $L_{bol} > 10^{44}$  erg/s).

## 1.2 The complex X-ray spectrum of Active Galactic Nuclei

The X-ray emission from AGN shows the highest variability amplitudes on the shortest time scales (less than  $\sim 1$  day) with respect to the other wavebands. From a simple causality argument, we can estimate an upper limit on the emission region of  $r \sim c\Delta t \sim 10^{-3}$  pc (e.g. Mushotzky et al. 1993). Therefore, the study of the X-ray emission from AGN is a fundamental tool have to directly probe their innermost regions.

### 1.2.1 The Continuum

The typical X-ray continuum of AGN can be roughly represented by a power-law with photon index<sup>2</sup>  $\Gamma \sim 2$ , with an exponential cut-off at energies  $\sim 100$ - $300$  keV (e.g. Dadina 2008). The typical X-ray spectrum of a type 1 Seyfert galaxy and a schematic view of the AGN zones which contribute to each emission component is shown in Fig. 1.2.

The production of the X-ray continuum radiation from AGN is well explained by a “two-phases model” (e.g. Haardt & Maraschi 1991). This postulates that the emitting

---

<sup>2</sup>The photon index  $\Gamma$  is defined as  $F(E) \propto E^{-\Gamma}$  in units of  $\text{ph cm}^{-2} \text{s}^{-1} \text{keV}^{-1}$  and the relation with the spectral index is  $\alpha = 1 - \Gamma$ .

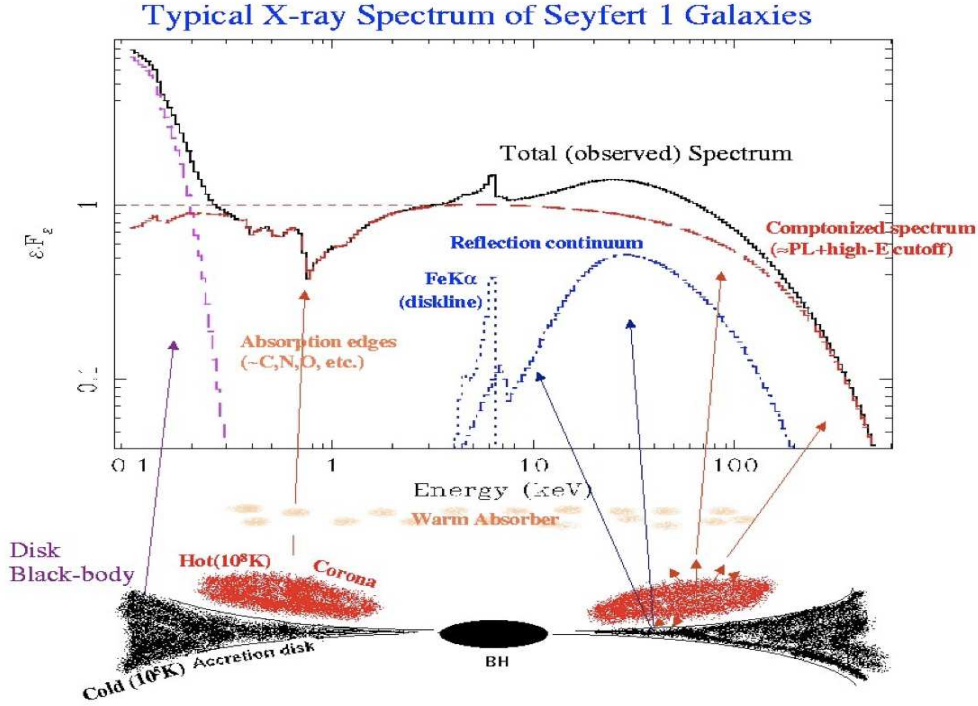


Figure 1.2: Typical spectrum of Seyfert 1 galaxies in the X-rays ( $E \sim 0.1\text{--}300$  keV) with superimposed a schematic view of the AGN zones which contributes to each emission component (courtesy of M. Cappi).

region is composed by two different structures: a Compton thick ( $\tau > 1$ ) and relatively cold ( $T \sim 10^5\text{--}10^6$  K) accretion disk underneath a Compton thin ( $\tau < 1$ ) and hot corona of plasma. It is assumed that a significant amount of gravitational energy of the disk is then released in the corona, possibly through magnetic reconnection processes (Burm 1986). This can heat up the corona to temperatures of the order of  $T \sim 10^9$  K ( $kT \sim 100$  keV) and, consequently, the electron population of the corona is expected to be semi-relativistic. From the equipartition of the thermal energy among the electrons,  $\frac{m_e v^2}{2} = \frac{3kT}{2}$ , we have  $\beta = v/c = \sqrt{\frac{3kt}{m_e c^2}} \sim 0.7$ , which corresponds to a Lorentz factor of  $\gamma = 1/\sqrt{1 - \beta^2} \sim 1.4$ . The mutual interaction of these two phases (the “cold” accretion disk and the “hot” corona) gives rise to a rather complex emission process which, however, can be exemplified in three main components:

- The innermost regions of the accretion disk produce a black body emission in the

UV and soft X-rays (see Fig. 1.2).

- Part of this soft seed radiation interacts by inverse Compton with the hot electrons of the corona ( $E_{ph} \ll kT$ ) and is shifted to higher energies. For each photon-electron encounter there is a transfer of energy from the electron to the photon of the order of  $\Delta E_{ph} \simeq \gamma^2 E_{ph} \simeq 2E_{ph}$ . This represents the most effective cooling process of the corona. The resultant spectrum is a power-law with  $\Gamma \sim 2$  which extends also in the X-ray band, well beyond  $\sim 10$  keV. This is completely in agreement with the observations (e.g. Dadina 2008). Moreover, given that the scattered photons cannot reach energies higher than the thermal energy of the corona, this model predicts an exponential cut-off of the power-law at  $E > 100\text{--}200$  keV, as observed (e.g. Dadina 2008).
- As a first approximation, the X-ray emission from the corona is isotropic. Therefore approximately half of the radiation leaves the system and the other half is directed back onto the accretion disk and its surrounding regions. The illumination of this relatively cold and Compton thick material with high energy photons gives rise to photo-absorption and reflection processes. This effect is usually referred as *Compton reflection*. In particular, the interaction of X-ray photons with energies  $E \simeq 1\text{--}100$  keV with the disk produces the so called *reflection component* (Lightman & White 1988; Guilbert & Rees 1991; George & Fabian 1991). The corona is then transparent to this high energy continuum and this additional components is radiated directly towards the observer (see Fig. 1.2)

Several emission features can be imprinted on the reflection component by the reflecting material. In fact, the absorption of photons with energies  $E < 10$  keV and their re-emission can give rise to several fluorescence emission lines from the most abundant heavy elements. In particular, one can note the presence of several neutral/ionized Fe K emission lines in the range of energies  $E \sim 6\text{--}7$  keV (see Fig. 1.2). If the reflection region is very close to the central SMBH, the line profile will be broadened and deformed by relativistic effects (e.g. Tanaka et al. 1995; Fabian et al. 2000).

Another interesting feature of the reflection component is the enhanced emission in the  $E \sim 30\text{--}50$  keV energy range (the so called *reflection hump*). This is due

to the combination of several effects, such as: the absorption and re-emission in lines at lower energies of the photons with  $E < 10$  keV; the sudden decrease of the absorption cross-section at energies  $> 20$  keV ( $\sigma_{abs} \propto E^{-3}$ ) and the consequent increase of the number of photons which leave the disk surface; the loss of energy of high energy photons through Compton down-scattering with the cold electrons of the disk ( $\sigma_{abs} \ll \sigma_e$  for  $E > 10$ – $100$  keV).

### 1.2.2 The other spectral components

Besides the primary continuum and the reflection component, several other features can be present in the typical X-ray spectrum of AGN. In the following we report a non-exhaustive list of the possible spectral components (see Fig. 1.2):

- **Soft excess:** it is a broad excess of emission in the soft X-rays, at energies below  $\sim 1$  keV. It is usually characterized by a steepening of the power-law continuum slope. However, the origin of this component is still unknown. One possibility is that this is related with the thermal emission from the innermost regions of the accretion disk. In fact, in these regions the temperature can rise to values of  $T \sim 10^5$ – $10^6$  K and the high energy tail of the disk black body emission may well extend up into the soft X-ray band.
- **Neutral absorption:** this component is due to photo-electric absorption from neutral material located along the line of sight. This can be due to absorption from our Galaxy, with  $N_H \sim 10^{20}$ – $10^{21}$   $\text{cm}^{-2}$ , or intrinsic to the AGN, with column densities ranging from  $N_H \sim 10^{20}$   $\text{cm}^{-2}$  up to  $N_H \sim 10^{23}$ – $10^{24}$   $\text{cm}^{-2}$  for type 2 sources.
- **Ionized absorption:** it is due to resonance lines or absorption edges from intervening material in different ionization states. Usually the absorbers in the central regions of AGN are photo-ionized, rather than collisionally ionized, because of the intense radiation field which spans from the IR to hard X-rays. In particular, the *warm absorbers* (WA) are detected as ionized absorption in the soft X-rays ( $E < 2$ – $3$  keV) from several elements, but especially C, O, Ne. The ionization state<sup>3</sup> of the material is  $\log \xi \sim 0$ – $2$   $\text{erg s}^{-1} \text{cm}$  and its column density is  $N_H \sim 10^{20}$ – $10^{22}$   $\text{cm}^{-2}$

---

<sup>3</sup>We used the definition of the ionization parameter  $\xi = L_{ion}/nr^2$  from Tarter, Tucker & Salpeter (1969), where  $L_{ion}$  is the ionizing luminosity between 1 Ryd and 1000 Ryd (1 Ryd = 13.6 eV),  $n$  the number density of the material and  $r$  the distance from the central source.

(e.g. Blustin et al. 2005; McKernan et al. 2007). Recently there have been also the detection of much more extreme absorbers through Fe XXV and Fe XXVI K-shell absorption lines at  $E > 6-7$  keV, with higher ionization parameters  $\log \xi \sim 3-6$  erg s<sup>-1</sup> cm and column densities  $N_H \sim 10^{22}-10^{24}$  cm<sup>-2</sup> (see e.g. review Cappi 2006). Most, if not all, ionized absorbers are found to be systematically in outflows. Their velocities span values from  $\sim 100-1000$  km/s for the WA and up to  $\sim 10^4-10^5$  km/s ( $\sim 0.03-0.3c$ ) for the latter types.

- **Emission lines:** several emission lines can be present in the spectrum from neutral or ionized species. In particular, the most intense in the soft X-rays are due to Oxygen, Neon and Fe L-shell. At higher energies, in the range  $\sim 6-7$  keV, there are instead Fe K-shell fluorescence emission lines. These lines can be produced by transmission or reflection in a Compton thick medium. The ubiquitous narrow neutral Fe K $\alpha$  is at  $E \simeq 6.4$  keV and sometimes there can be further ionized lines in the range  $E \sim 6.5-7$  keV. Moreover, sometimes the Fe K lines show the typical broad profile, distorted by relativistic effects due to the reflection from the innermost regions of the accretion disk (see §1.2.1).

### 1.2.3 Highly ionized Fe K-shell transitions

In this thesis we focus on the analysis of Fe K-shell absorption lines in the spectra of a large sample of radio-quiet and radio-loud AGN. Their study can provide us fundamental insights on the study of recently discovered highly ionized absorbers in the Fe K band of several AGN. In particular, in this section we report a description of the main Fe XXV and Fe XXVI K-shell absorption lines and we refer to the work by Kallman et al. (2004) for a more detailed study of the photo-ionization modeling and treatment of the Fe K-shell transitions. All line parameters reported in this Thesis have been taken from the NIST<sup>4</sup> atomic database, if not otherwise stated. In Table 1.1 we report the main parameters of the Fe XXV and Fe XXVI K-shell transitions.

In particular, the Fe XXV lines are composed by four He-like ( $1s^2-1snp$ ) series transitions, each of which further subdivide in a resonance (r) and one inter-combination (i) line. For each line we reported also the mean energy of the transition, weighted for the oscillator strengths of its components. Their energies are in the range from  $\sim 6.7$  keV

---

<sup>4</sup><http://physics.nist.gov/PhysRefData/ASD/index.html>.

Table 1.1: Main Fe XXV and Fe XXVI K-shell transitions. (1) Iron ion. (2) Line identification. (3) Atomic transition. (4) Mean line energy, weighted for the oscillator strengths of its components. (5) Line components. (6) Energy of the specific transition. (7) Oscillator strength. (8) Einstein coefficient.

| Ion     | ID          | Transition            | $\langle E \rangle$<br>(eV) | Line              | E<br>(eV) | $f_{lu}$              | $A_{ul}$              |
|---------|-------------|-----------------------|-----------------------------|-------------------|-----------|-----------------------|-----------------------|
| (1)     | (2)         | (3)                   | (4)                         | (5)               | (6)       | (7)                   | (8)                   |
| Fe XXV  | He $\alpha$ | 1s <sup>2</sup> -1s2p | 6697                        | (r)               | 6700      | $7.04 \times 10^{-1}$ | $4.57 \times 10^{14}$ |
|         |             |                       |                             | (i)               | 6668      | $6.87 \times 10^{-2}$ | $4.42 \times 10^{13}$ |
|         | He $\beta$  | 1s <sup>2</sup> -1s3p | 7880                        | (r)               | 7881      | $1.38 \times 10^{-1}$ | $1.24 \times 10^{14}$ |
|         |             |                       |                             | (i)               | 7872      | $1.70 \times 10^{-2}$ | $1.00 \times 10^{13}$ |
|         | He $\gamma$ | 1s <sup>2</sup> -1s4p | 8295                        | (r)               | 8295      | $5.07 \times 10^{-2}$ | $5.05 \times 10^{13}$ |
|         |             |                       |                             | (i)               | 8292      | $6.00 \times 10^{-3}$ | $2.00 \times 10^{12}$ |
|         | He $\delta$ | 1s <sup>2</sup> -1s5p | 8487                        | (r)               | 8487      | $2.44 \times 10^{-2}$ | $2.54 \times 10^{13}$ |
|         |             |                       |                             | (i)               | 8485      | $2.90 \times 10^{-3}$ | $1.00 \times 10^{12}$ |
| Fe XXVI | Ly $\alpha$ | 1s-2p                 | 6966                        | (r <sub>1</sub> ) | 6973      | $2.80 \times 10^{-1}$ | $2.96 \times 10^{14}$ |
|         |             |                       |                             | (r <sub>2</sub> ) | 6952      | $1.40 \times 10^{-1}$ | $2.93 \times 10^{14}$ |
|         | Ly $\beta$  | 1s-3p                 | 8250                        | (r <sub>1</sub> ) | 8253      | $5.32 \times 10^{-2}$ | $7.86 \times 10^{13}$ |
|         |             |                       |                             | (r <sub>2</sub> ) | 8246      | $2.65 \times 10^{-2}$ | $7.83 \times 10^{13}$ |
|         | Ly $\gamma$ | 1s-4p                 | 8701                        | (r)               | 8701      | $1.95 \times 10^{-2}$ | $3.20 \times 10^{13}$ |
|         | Ly $\delta$ | 1s-5p                 | 8909                        | (r)               | 8909      | $9.35 \times 10^{-3}$ | $1.61 \times 10^{13}$ |

up to  $\sim 8.5$  keV. However, the most intense (see ratios of their oscillator strengths  $f_{lu}$  in Table 1.1) are the He $\alpha$  at E=6.700 keV and the He $\beta$  at E=7.881 keV.

Instead, the Fe XXVI lines are composed by the four Lyman series (1s- $np$ ) lines. These lines are subdivided in resonance doublets and, when available, we reported also the mean energy of the transition, weighted for the oscillator strengths of its components. We can see from Table 1.1 that their energies spans from E $\sim 7$  keV up to E $\sim 9$  keV, but the most intense are the Ly $\alpha$  at E=6.966 keV and Ly $\beta$  at E=8.250 keV.

These line parameters will be used throughout this Thesis, in particular for the identification of the blue-shifted absorption lines detected in the Fe K band of several AGN in §3.4.1 and §4.3. Their curve of growth analysis will be presented in §5.2.2.

## 1.3 X-ray observations of AGN outflows

Blue-shifted absorption lines in the UV and X-ray spectra of AGN reveal the presence of massive outflows of ionized gas from their central regions. The intrinsic UV and X-ray absorbers show large global covering factors of the central continuum source and the inferred mass loss rates may even be comparable to the mass accretion rates (e.g. Pounds et al. 2003a; Cappi et al. 2009 and references therein).

In particular, studies of intrinsic ionized absorption concentrate on type 1 sources for the practical reason that it is much easier to detect the absorption against strong nuclear continua. In fact, the obscuring material along the line of sight of type 2 source (see §1.1.1) can greatly attenuate the emission from their AGN, from the optical up to medium ( $\sim$  few keV) X-rays. In the next subsections we describe with more detail the evidence for outflows that can be found in the X-ray spectra of AGN.

### 1.3.1 Warm absorbers

Absorption from layers of photo-ionized gas in the circumnuclear regions of AGN is commonly observed in more than half of radio-quiet objects, the so-called warm absorbers. X-ray photons are sufficiently energetic to excite or ionize inner-shell electrons of all cosmically abundant elements from C to Ni (primarily K-shell electrons) and transitions from higher shells (mainly L-shell) in the case of the high-Z elements such as Fe.

In particular, the detection of resonance lines and absorption edges in the soft X-ray ( $E \simeq 0.1\text{--}2$  keV) spectra of Seyfert galaxies employing the high energy resolution Chandra and XMM-Newton gratings have confirmed these results (e.g. Blustin et al. 2005; McKernan et al. 2007). In Fig. 1.3 we report an example of the complex spectral features imprinted by the warm absorber in the soft X-ray spectrum of the bright Seyfert 1 galaxy NGC 3783.

The typical characteristics of this material are an ionization parameter of  $\log \xi \sim 0\text{--}2$  erg s $^{-1}$  cm, a column density of  $N_H \sim 10^{20}\text{--}10^{22}$  cm $^{-2}$  and an outflow velocity of  $\sim 100\text{--}1000$  km/s. Their distance from the central SMBH has been estimated to be of the order of  $\sim 1\text{--}100$  pc, consistent with the location of the Broad Line Region or Narrow Line Region. In fact, it has been suggested that the origin of this gas might be connected with the optical-UV BLR or NLR or possibly with winds generated by evaporation from the inner edge of the putative obscuring torus (e.g. Krolik & Kriss 2001; Blustin et al. 2005;

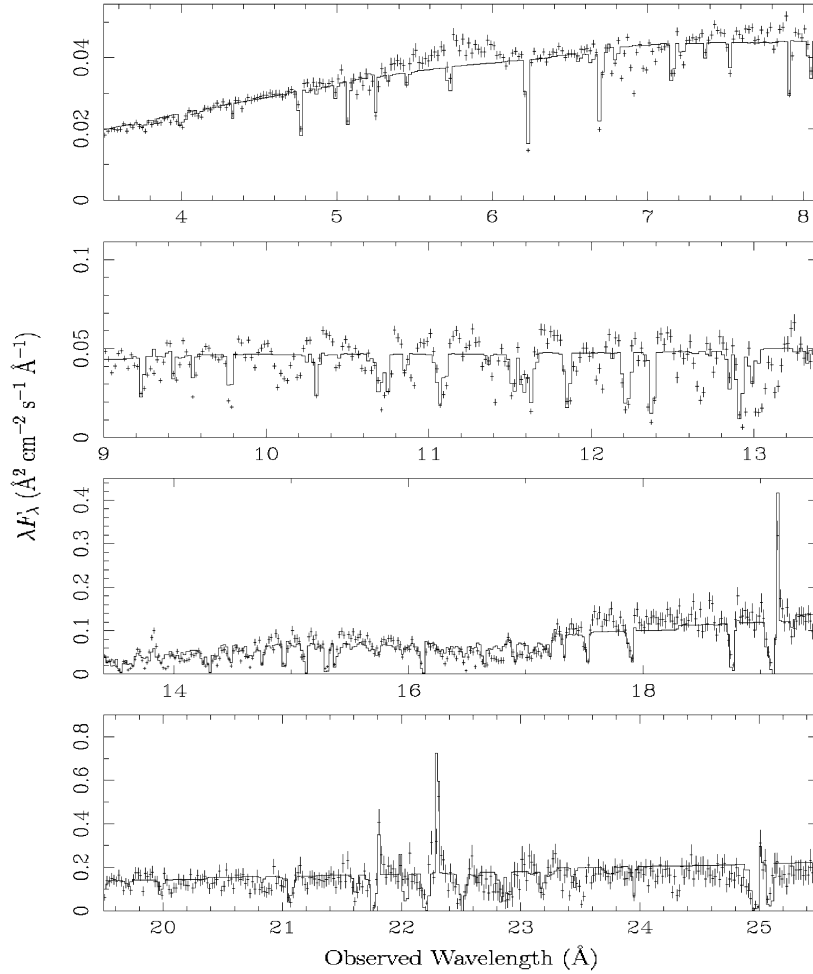


Figure 1.3: Chandra gratings spectrum in the  $E=0.5\text{--}3$  keV band with superimposed the best fit photo-ionization model for the warm absorber of NGC 3783 (figure from McKernan et al. 2007).

McKernan et al. 2007).

The WAs can span a large range in ionization parameter and temperature, even in the same galaxy. Moreover, components of the same WA may undergo dramatic changes in response to changes in the ionizing flux. Hence, some of the absorbing gas may be unstable to thermal perturbations and it is possible that fluctuations can produce a two-component gas in which a Compton-heated medium can give rise to low ionization knots (Crenshaw et al. 2003).

In particular, as discussed by Krolik et al. (1981), photo-ionized gases can exist in

two regimes of thermal equilibrium: one when the ionization state of the gas is low enough that there is a balance between heating by ionization and cooling by collisionally excited emission lines and the other at very high ionization, when thermal equilibrium is established between Compton and inverse Compton processes. At intermediate values of the ionization state and temperature, the gas might undergo large temperature fluctuations in response to changes in the ionizing flux and may be unstable to such perturbations.

This would generate a two-phase absorber, composed by cold and dense filaments or clouds occupying a small fraction of the available volume, confined by a hot inter-cloud medium. In this picture, the clouds are associated to the optical-UV BLRs or NLRs and the confining medium is provided by what is seen as the warm absorber (Krolik & Kriss 1995, 2001).

However, Reynolds & Fabian (1995) stated that this simple two-phase model is incomplete because it neglects dynamical effects and it does not explain the formation of broad-line clouds. Moreover, it suffers from inherent difficulties such as an optically thick intercloud medium and rapid fragmentation of the broad-line clouds into optically thin filaments. A full description of the WAs clearly has to be dynamic in nature. Material in the environment of the central engine is prone to thermal instabilities if its temperature lies between  $\sim 10^4$  K and the Compton temperature of  $10^7$ – $10^8$  K. The WAs appear to be in an intermediately ionized state at  $T \sim 10^5$  K and can exist only in a small region of stability in a multi-phase regime, for different values of temperature and ionization state. Since radiation pressure on the material can be comparable with the gravitational attraction of the central compact body, Reynolds & Fabian (1995) suggested the possibility for the WAs to be in the form of radiatively driven outflows.

When the nucleus is heavily obscured, such as in type 2 objects (see §1.1.1), warm absorbing gas may be seen in the soft X-ray band by a combination of bremsstrahlung, intrinsic line emission and Thomson scattering of the nuclear continuum. Instead, when the line of sight towards the nucleus is not obscured, as in type 1 AGN, the dominant effect is absorption, and ionization edges of highly ionized species and resonance lines can be observed in the soft X-rays. In the UV, this gas is almost transparent, except for a small number of resonance lines that are essentially due to the more weakly ionized gas clouds that are embedded in the main body of the warm, scattering gas (Krolik & Kriss 1995, 2001).

However, the notion that the UV and soft X-ray absorbers originate in the same gas, characterized by a single ionization parameter, is clearly inadequate. The individual kinematic components in the UV show a wide range in ionization but most produce negligible O VII or O VIII absorption in the soft X-ray region. Furthermore, the soft X-ray absorber itself is often complex and composed of at least two zones with different ionization parameters. However, although most UV and soft X-ray absorbers do not arise from the same gas, there is a statistical connection that indicates a physical and/or geometric relationship between the two. In fact, it has been found that there is a one-to-one correspondence between Seyfert 1 galaxies that show intrinsic UV absorption and those that show intrinsic soft X-ray absorption and their global incidence of  $\sim 50\text{--}60\%$  is in agreement (see review by Crenshaw et al. 2003). This high incidence allows to estimate that the covering factor of the material is quite large, of the order of  $\sim 2\pi$  (e.g. Blustin et al. 2005; McKernan et al. 2007).

Finally, it should be noted that thanks to the superior sensitivity and energy resolution of current X-ray satellites (such as Chandra and XMM-Newton), we are starting now to find evidence for warm outflowing gas in radio-loud AGN as well. In fact, the recent detection of a warm absorber in the Broad-Line Radio galaxy 3C 382 (Torresi et al. 2009; Reeves et al. 2009) has been the starting point for a possible change to the classical picture of the radio-quiet vs. radio-loud dichotomy, at least in the X-ray domain. This gas has an ionization parameter of  $\log\xi \simeq 2\text{--}3$  erg s<sup>-1</sup> cm, column density of  $N_H \simeq 10^{21}\text{--}10^{22}$  cm<sup>-2</sup> and is outflowing with a velocity of  $\sim 800\text{--}1000$  km/s. These parameters are somewhat similar to those of the typical warm absorbers of Seyfert 1 galaxies, which are the radio-quiet counterparts of BLRGs. This indicates the presence of ionized outflowing gas in a radio-loud AGN at a distance of  $\sim 100$  pc from the central engine, suggesting its association with the optical-UV Narrow Line Region (Torresi et al. 2009; Reeves et al. 2009). This is an important result because it suggests that a plasma ejected at velocities near the speed of light (the relativistic radio jet) and a photo-ionized gas with much slower outflow velocities (the warm absorber) can indeed coexist in the same source beyond the broad-line region.

### 1.3.2 Ultra-fast Outflows

Thanks to the high throughput of recent X-ray observatories, there is increasing evidence for the presence of narrow blue-shifted absorption lines at rest-frame energies greater than

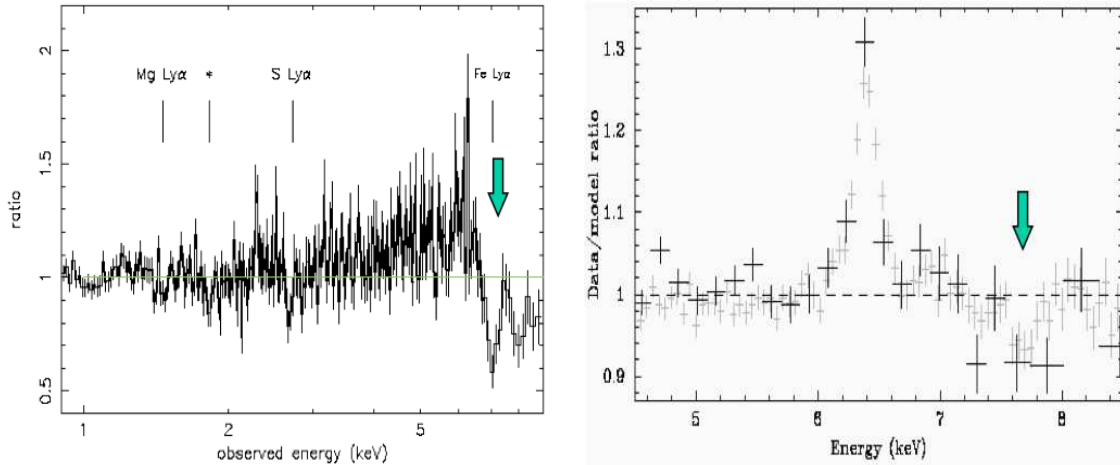


Figure 1.4: Examples of blue-shifted Fe K absorption lines detected at  $E > 7$  keV from the literature. *Left panel:* Ratios of the XMM-Newton pn spectrum of PG1211+143, adapted from Pounds & Page (2006). *Right panel:* Ratios of the XMM-Newton pn spectrum of IC4329A, adapted from Markowitz et al. (2006).

6.4 keV in the spectra of a number of radio-quiet AGN (e.g. Pounds et al. 2003a; Reeves et al. 2004; Dadina et al. 2005; Markowitz et al. 2006; Braitto et al. 2007; Cappi et al. 2009). Some examples of blue-shifted Fe K absorption lines detected in the XMM-Newton spectra of radio-quiet AGN are shown in Fig. 1.4 and Fig. 1.5.

These features are commonly identified with Fe XXV and/or Fe XXVI K-shell resonant absorption from a highly ionized ( $\log \xi \simeq 3-6$  erg s $^{-1}$  cm) zone of circumnuclear gas, with column densities as large as  $N_H \simeq 10^{22}-10^{24}$  cm $^{-2}$ . The lines blue-shifts are also often quite large, reaching (mildly) relativistic velocities (up to 0.2–0.4c). In some cases variability on time scales as short as  $\sim 1$  day have been reported. Moreover, the typical location has been estimated to be within  $\sim 0.01-0.1$  pc ( $< 10^3 r_s$ ) from the central SMBH.

The characteristics of these absorbers are far more extreme than those of the WAs reported in the previous section. In fact, these findings suggest the presence of previously unknown ultra-fast outflows (UFOs) from the central regions of radio-quiet AGN, possibly connected with accretion disk winds/ejecta (see review by Cappi 2006).

In particular, here we define UFOs those highly ionized absorbers detected, essentially, through Fe XXV and Fe XXVI K-shell absorption lines and with outflow velocities  $v_{out} \geq 10^4$  km/s ( $\simeq 0.033c$ ), i.e. much greater than the maximum value for typical X-ray warm absorbers in AGN (e.g. Blustin et al. 2005; McKernan et al. 2007).

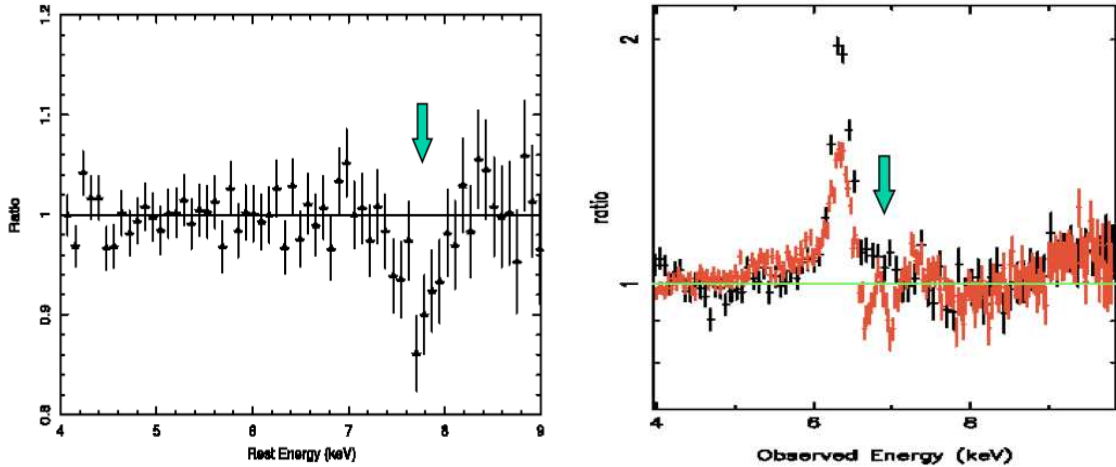


Figure 1.5: Examples of blue-shifted Fe K absorption lines detected at  $E > 7$  keV from the literature. *Left panel:* Ratios of the XMM-Newton spectrum pn of MCG-5-23-16, adapted from Braitto et al. (2007). *Right panel:* Ratios of the XMM-Newton pn spectrum of NGC 3516, adapted from Turner et al. (2008).

The main observational evidence for UFOs is the detection of narrow blue-shifted Fe absorption lines above 6 keV, where instrumental resolution and signal-to-noise are usually much lower than in the soft X-rays (Schurch et al. 2009). Moreover, this highly ionized gas is hard to observe in soft X-ray spectra because all the elements lighter than Fe are almost completely ionized and this may be the reason why it has not been reported previously.

However, we stress that fast outflows are commonly observed in several classes of AGN in different wavebands, from the relativistic jets in radio-loud quasars to the broad-absorption lines (BAL) in the UV spectra of distant quasars (with velocities up to  $\sim 0.1c$ ) (see review by Crenshaw et al. 2003). Moreover, theoretical models and simulations of black hole accretion systems naturally require the formation of UFOs (with velocities up to relativistic values) from the accretion disk (e.g. Proga et al. 2000; King & Pounds 2003; Proga & Kallman 2004; Ohsuga et al. 2009; King 2009).

These extreme outflows from the central regions of AGN have the possibility to bring outward a significant amount of mass and energy, which can have an important influence on the surrounding environment (see review by Cappi 2006). In fact, feedback from the AGN is expected to have a significant role in the evolution of the host galaxy, such as the enrichment of the ISM or the reduction of star formation, and could also explain some fundamental relations (e.g. Ferrarese & Merritt 2000). The ejection of a huge amount of

mass from the central regions of AGN can also inhibit the growth of the super-massive black holes (SMBHs), potentially affecting their evolution. The study of such outflows gives also important insights on the working of AGN and on the black hole accretion physics in general (Cappi 2006).

The main topic of this Thesis is the study of UFOs in a large sample of radio-quiet and radio-loud AGN. Therefore, in the next section we discuss more about the several open questions still remaining about the UFOs in AGN and the goals that we intend to reach with this Thesis.

## **1.4 Open questions on UFOs and goals of this Thesis**

Given their recent discovery, there are several open questions still to be addressed concerning the Ultra-fast Outflows in Active Galactic Nuclei. Perhaps, the most important question is, what is their origin? In other words, how the UFOs are created and accelerated outward from the nucleus with mildly relativistic velocities? What is their connection to the other components of AGN and what does this tell us about the overall geometric and dynamical structure of AGN? Then, a related question is, how does the mass outflow affect its environment, including the nuclear regions and host galaxy? There is no clear answer to these questions yet, but in this Thesis we try to address some of them and, at least, to give further insights into the physics of UFOs from the innermost regions of AGN.

### **1.4.1 The importance of winds/outflows on the overall AGN structure**

As already discussed in previous sections, outflows/winds and jets are routinely observed in several classes of AGN at different wavebands and can play an important role in their overall structure and classification. Here we are interested in those originating from the innermost regions of AGN, such as accretion disk winds, and that can be observed in X-rays, such as the WAs in the soft band and the UFOs in the Fe K band.

In particular, it is important to discuss here the ambitious model proposed by Elvis (2000) (see Fig. 1.6). The author empirically derived a simple, though very effective, unifying structure for the inner regions of AGN. This picture is able to consistently explain the different components observed in several classes of AGN, such as the optical-UV Broad Line Regions, the Narrow Line Regions, the X-ray warm absorbers, the fast outflowing winds detected in BAL QSOs and several of the different reflection/scattering features

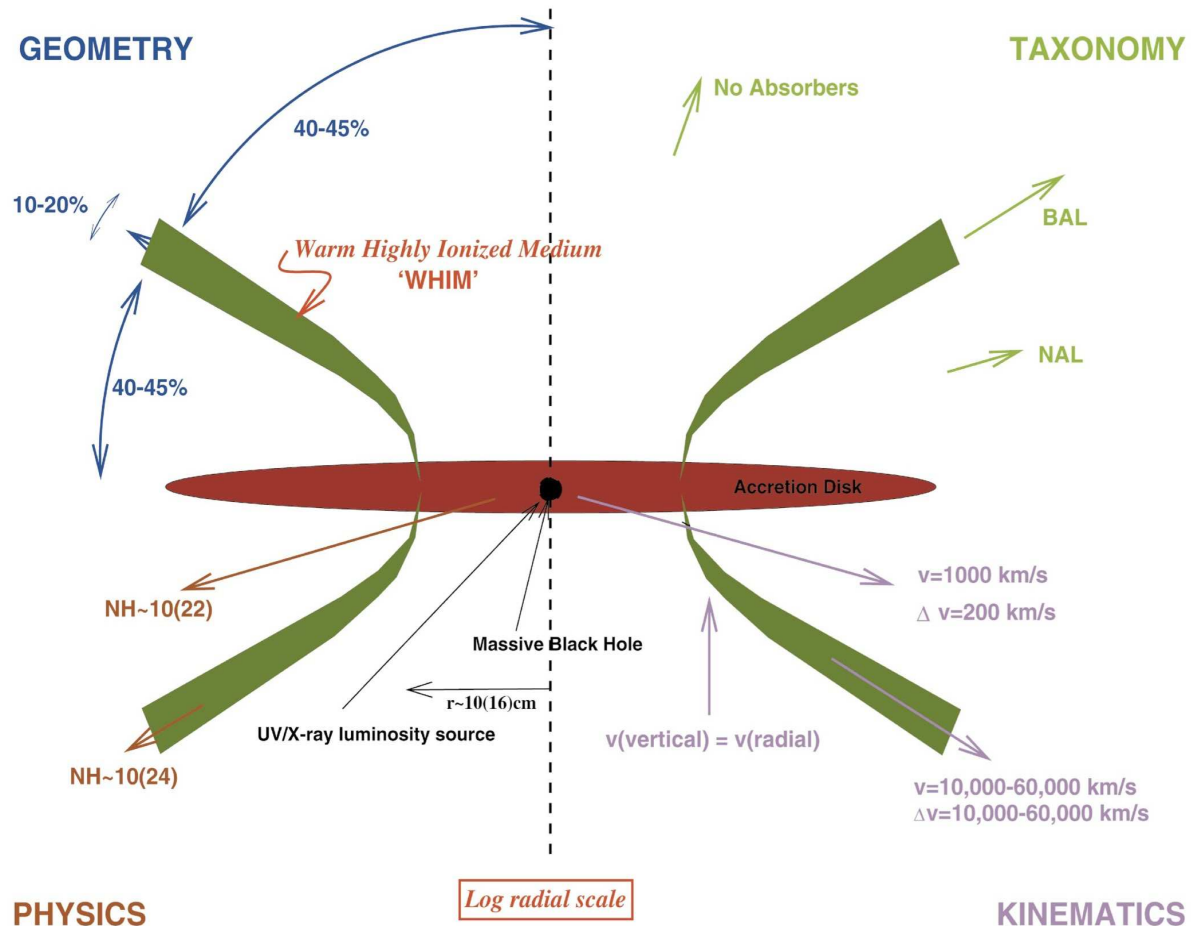


Figure 1.6: A proposed structure of accretion disk winds in AGN from Elvis (2000). Clockwise from top left: the opening angles, the spectroscopic appearance to a distant observer at various angles, the outflow velocities along different lines of sight and some representative radii and typical column densities.

(see §1.1.1).

The model proposes that a funnel-shaped thin shell outflow creates all these features. The wind arises vertically from a narrow range of radii on a disk. Then, it is accelerated vertically by radiation force and it bends outward to a cone angle of  $\sim 60^\circ$ , with a divergence angle of  $\sim 6^\circ$  (this gives a covering factor of  $\sim 10\%$ ). When the central continuum is viewed from the side, through this wind, narrow high-ionization ultraviolet absorption lines and the X-ray ionized absorbers are seen, with velocities  $\sim 1000$  km/s.

When viewed end-on, the full range of velocities is seen in absorption (up to  $\sim 0.1c$ ) with a large total column density, giving rise to broad absorption line systems, such as those seen in BAL QSOs.

The wind is both warm ( $T \sim 10^6$  K), highly ionized and it has a high density ( $n \sim 10^9 \text{ cm}^{-3}$ ). This warm wind is also significantly Thomson thick ( $\tau \sim 1$ ) along the radial flow direction and partially ionized, possibly producing the reflection features typical of AGN, such as the broad fluorescent 6.4 keV Fe  $K\alpha$  emission line and the Compton hump at  $E > 10$  keV. Moreover, in this picture the Broad Line Region clouds might well represent a cool phase embedded in this overall outflow and the fact that the two phases are in pressure equilibrium would avoid the cloud destruction through shear (see also §1.3.1). Finally, the structure presented by Elvis (2000) is not directly inimical to the obscuring torus model (see §1.1.1), but it is less strongly required and, actually, the wind itself could be considered as a form of obscuring torus.

The fact that massive winds/outflows could actually play an important, if not fundamental, role in the innermost regions of AGN has also been suggested by several absorption dominated models that have been proposed to, at least partially, explain the X-ray emission in AGN.

For instance, Miller et al. (2009) proposed a model dominated by clumpy, partial covering absorption that is able to simultaneously explain the broad relativistic Fe K line, the high energy excess at  $E > 20$  keV and the variability of the well studied galaxy MCG-6-30-15. A key ingredient of this model is that at least one of the absorbing zones should be partial-covering, implying that the absorber is clumpy, near and of similar size to the X-ray source. Some of these zones are outflowing and the authors suggested that the absorption could be part of an accretion disk wind. An important point in this case is that, as the absorbing gas is expected to be photo-ionized, we should be able to see recombination and fluorescent emission from it and, in principle, we can use the line luminosities to constrain the global covering factor and the overall absorber geometry.

As stated by Miller et al. (2009), the observed broad Fe  $K\alpha$  line emission in MCG-6-30-15 may be fluorescent emission from the absorbing material, in which case the global covering factor of the material is  $\sim 0.5$ . These absorption dominated models are in direct competition with reflection dominated models, which instead assume that the main spectral features in the X-ray spectra of AGN are due to relativistic blurred reflection

from the innermost regions of the accretion disk (e.g. Miniutti & Fabian 2004). If the absorption dominated models are correct, they imply that a large fraction of the observed X-ray variability may be caused by variation in absorber covering fraction and that a large fraction of the source 2–10 keV luminosity may be partially obscured even in type 1 AGN. Instead, if the reflection dominated models are correct, time-lags due to reverberation of Fe K-shell and Fe L-shell emission lines are expected (as already seen, e.g. Fabian et al. 2009) as well as strong relativistic distortion of the lines shapes. However, we note that a most realistic and general scenario might require a combination of both absorption and reflection effects.

#### 1.4.2 The physics of AGN winds/outflows

There are three main mechanisms that are invoked for the generation of winds/outflows from the accretion disk in AGN: magnetic, radiation and thermal driving mechanisms. In this section we briefly describe these processes. However, it is important to note that it is difficult to distinguish, both from observational and theoretical point of view, which of these wind driving mechanisms dominate and probably the more realistic explanation would require a combination of them (see reviews by Crenshaw et al. 2003; Elvis 2006; Proga 2007).

An accretion disk can lose its mass if the upper atmosphere is heated. In the context of an AGN disk, significant heating can result from irradiation of the outer/cooler parts of the disk by the radiation from the inner/hotter disk. Theoretical models predict that heating, especially X-ray heating, can have significant effects on the gas dynamics in disks. In fact, X-rays tend to heat low density gas, through Compton heating, to a high temperature of  $T \sim 10^7$  K (the so-called Compton temperature). With such a high temperature, an upper disk atmosphere is expected to either puff up and form a static corona, or to produce a thermal wind, depending on whether the thermal velocity exceeds the local escape velocity. Because the escape velocity is a function of radius, for a given temperature of the heated gas, the effects of thermal driving depend on the considered radius too. Generally, thermal driving is effective at large radii where the escape velocity is small. This mechanism acts isotropically and can impart a maximum wind velocity of  $\sim 100$  km/s for a gas at  $T \sim 10^7$  K. However, this scenario alone has problems in interpreting current data because the outflow velocities are very low and isotropic acceleration produces a 100% covering factor wind, in

contrast with what has been found for UV and X-ray winds of  $\sim 50\text{--}60\%$ . Thermal driving is likely less important for temperatures below  $T \sim 10^7$  K because the other two forces can dominate. In particular, radiation forces can be significant for a gas with temperature lower than  $T \sim 10^5$  K.

Radiation pressure is a more attractive means for accelerating gas from an AGN, if only for the reason that the central engine is a tremendous source of continuum radiation. It acts radially and can effectively reach velocities up to a few  $\sim 10^4$  km/s. The exact nature of this mechanism depends on the source of opacity to the radiation, such as Thomson scattering, bound-bound (line-driven) or bound-free (photo-electric) transitions. Efficient line-driving requires the presence of bound electrons, therefore the ability of the gas to be accelerated in this way reduces increasing the ionization state. In fact, line force can be significant if the gas is moderately ionized and can interact with the UV continuum through very many UV line transitions. For gas photo-ionized by the UV radiation in the optically thin case, the total line opacity compared to the electron scattering can be as high as  $\sim 2000\text{--}4000$ . Instead, for highly ionized gas, line force is inefficient because of a lower concentration of ions capable of providing line opacity. Therefore, line-driving winds need an effective X-ray shielding mechanism and can better explain the outflows observed in UV, such as the BAL QSOs, which are preferentially launched from the outer parts of the putative accretion disk. In the vicinity of the black hole, the higher X-ray luminosity can over-ionize the gas. In particular, absorbers with column densities  $N_H > 10^{21}$  cm $^{-2}$  and  $\log \xi \sim 1$  erg s $^{-1}$  cm, typical of X-ray warm absorbers (see §1.3.1), can likely be accelerated essentially by bound-free transitions. In case of a fully ionized gas, radiation pressure is only due to electron scattering. Therefore, the system luminosity needs to be higher, possibly of the order of the Eddington luminosity.

Magnetic effects must also be important in AGN. In fact, they appear to be essential for the existence of all accretion disks. The magneto-rotational instability (MRI) has been shown to be a very robust and universal mechanism to produce turbulence and transport angular momentum in disks at all radii. It is therefore likely that magnetic fields control mass accretion inside the disk and play a key role in producing a mass outflow from the disk. In fact, the wind might consist of ionized material in the disk that is frozen onto (locally) open, rotating magnetic field lines. As the field lines rotate, material is centrifugally accelerated above and away from the disk plane. The field lines are anchored

to the disk, so mass ejected in the wind removes angular momentum from the disk and allows disk material to fuel the AGN engine. There are two possible types of magnetically driven winds: magneto-centrifugal winds, where the dominant contribution to the Lorentz force is the magnetic tension and magnetic-pressure driven winds, where the dominant contribution to the Lorentz force is the magnetic pressure. Generally, magneto-centrifugal disk winds require the presence of a sufficiently strong, large-scale, ordered magnetic field threading the disk. They are able to predict the geometry and kinematics of the winds but they do not predict the mass-loss rate, which needs to be assumed. Magnetic winds do not require radiation pressure and thus can be important in low luminosity systems and in those where gas can be over-ionized by very strong radiation, such as in the innermost regions of AGN. In particular, in the context of AGN outflows, models usually rely on the effects of magnetic fields as well as on radiation driving. One of the differences between magneto-centrifugal and radiation driven disk winds is that the former co-rotate with the disk, at least close to the disk, whereas the latter do not necessarily co-rotate. The magneto-centrifugal winds can reach higher terminal velocities, formally up to the speed of light, due to the strong centrifugal force. In fact, it has been suggested that this could be the main mechanism responsible for the formation of relativistic jets (e.g Blandford & Payne 1982).

The main conclusion from the theoretical studies of AGN winds is that they cannot be explained by just one driving mechanism. If it is the disk itself which loses its mass, as assumed, then one should not expect just one mechanism, even if there is a favorite one, to dominate and all terms (thermal, radiation and magnetic) should be considered at the same time. However, radiation and magneto-centrifugal are the two most promising mechanisms to explain the formation of winds/outflows in AGN. Depending on the strength of the magnetic field relative to the system luminosity, the disk wind can be mainly radiation- or MHD-driven.

In this direction, Proga (2000) and Proga & Kallman (2004) studied the two-dimensional, time-dependent hydrodynamics of radiation-driven winds from luminous accretion disks threaded by a strong, large-scale, ordered magnetic field. The geometry of the wind is mainly controlled by the magnetic field lines. Instead, the wind is mainly accelerated by magneto-centrifugal and radiation forces, the latter mediated by spectral lines. The opacity is mainly due to many UV spectral lines and requires the gas to be

lowly ionized. Thus, this model better applies to winds that are far away from the central source or that are shielded from the intense X-ray radiation from the source.

Ohsuga et al. (2009) proposed a unified model of inflow/outflow from accretion disks in AGN based on global, two-dimensional radiation-magnetohydrodynamic (R-MHD) simulations. They studied the formation of winds/outflows very close to the SMBH (at a distance of less than  $\sim 100 r_s$ ) and included general relativistic effects. The opacity was considered mainly from Thomson scattering, free-free absorption and bound-free absorption. Therefore, this treatment can be applied to the highly ionized absorbers in the central regions of AGN. Notably, disk outflows with helical magnetic fields, which are driven either by radiation-pressure force or magnetic-pressure, are ubiquitous in any accretion modes. By controlling a density normalization, they could reproduce three distinct modes of accretion flow and outflow with one numerical code (see Fig. 1.7). When the density is large, (model A) a geometrically thick, very luminous disk forms ( $L \simeq L_{Edd}$ ). In this case, the strong radiation-pressure force is responsible for driving quasi-steady outflows, with velocities that can reach up to  $\sim 0.25c$ . When the density is moderate (model B), the accreting gas can effectively be cooled by emitting radiation, thus generating a thin disk (possibly associated with standard disks). In this case relatively slow ( $v \sim 0.01c$ ) and large opening angle disk winds are generated by magnetic pressure. When the density is too low for radiative cooling to be important (model C), the disk becomes hot, thick and faint (possibly associated with radiatively inefficient accretion flow, RIAF, disks). As we can see from Fig. 1.7, in model A and C magnetic-field lines stretch out vertically in the vicinity of the rotation axis, powering well collimated jets of material. However, this configuration is more accentuate in model A.

Moreover, King & Pounds (2003) and King (2009) showed that black holes accreting at or above the Eddington rate probably produce winds that are Compton-thick in the continuum and the momentum outflow rate ( $\dot{M}_{out}v$ ) can be of the order of the radiation momentum rate ( $L_{Edd}/c$ ). They considered only radiation pressure, in the form of Thomson scattering. Therefore, the enhanced opacity due to spectral lines and magnetic effects have not been treated. The mass conservation strongly suggests that any outflow with  $\dot{M}_{out} \simeq \dot{M}_{Edd}$  is likely to be optically thick to electron scattering, with a photospheric radius of the order of few  $\sim 10 r_s$ . Since the wind is Compton-thick, most of the photons have scattered and thus on average given up their original momentum to the outflow.

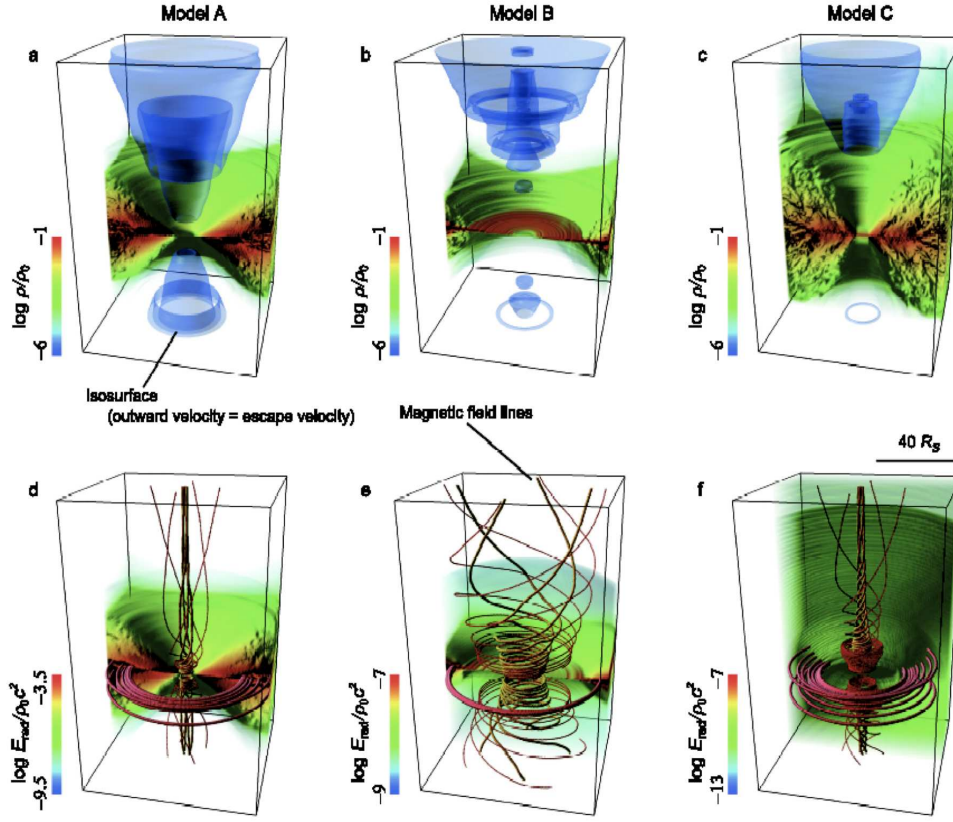


Figure 1.7: Perspective view of inflow and outflow patterns for three different accretion modes resulting from extensive Radiation-MHD simulations by Ohsuga et al. (2009).

Outside the photospheric radius, the photons decouple from the matter and there is no more acceleration. The derived outflow velocities can be as high as  $\sim 0.1c$  and the ionization of the material is expected also to be high, with  $\log \xi \sim 4 \text{ erg s}^{-1} \text{ cm}$ .

As discussed in this section, currently there are already several physical models capable to explain the formation of very fast winds/outflows from accretion disks in AGN (e.g. Proga & Kallman 2004; Ohsuga et al. 2009; King 2009 and references therein). They essentially rely on radiation and/or magnetic pressure as driving mechanisms. Therefore, from this Thesis we intend also to provide some more insights into the physics and mechanisms behind the formation of Ultra-fast Outflows, possibly in the form of winds/outflows from the putative accretion disk in AGN.

### 1.4.3 Impact of AGN winds/outflows on the host galaxy and cosmological feedback

Outflows from AGN have been recently recognized as potentially significant sources of feedback on both small scales, such as host galaxy bulge and Inter Stellar Medium (ISM), and large scales, such as the Inter Galactic Medium (IGM) (e.g. Lapi, Cavaliere & Menci 2005). However, order of magnitudes, or more, uncertainties in the structure of their innermost regions and especially on the characteristics of their outflows/winds still make now predictions highly uncertain (see review by Elvis 2006 and Fabian 2009). Nevertheless, there are several areas and processes where AGN can contribute to the cosmological feedback, such as:

- **Co-evolution of SMBHs and their host galaxies:** some form of feedback is required by the  $M_{BH}-\sigma$  relation (Ferrarese & Merritt 2000), which demonstrates the existence of a tight connection between the black hole and the bulge of the host galaxy. Moreover, this tells us that there are mechanisms which prevent the SMBH to grow at a rate independent of the surrounding environment and dark matter halo.
- **Prevention of star formation in mergers:** observations did not find the predicted number of blue branch young stars among massive galaxies, implying that star formation is prevented during mergers that form these galaxies (so called “dry mergers”). The AGN can potentially be effective in removing the cold ISM gas from these galaxies.
- **Limiting the upper mass of galaxies:**  $\Lambda$ CDM models produce too many high mass galaxies, contrary to observations. The reduced cooling and feedback from supernovae are insufficient to prevent galaxy growth and heating by AGN can be a promising alternative.
- **Inhibition of cooling flows:** it has been demonstrated using XMM-Newton and Chandra X-ray observations that the hot intracluster medium in the dense cores of rich clusters of galaxies is not cooling and so not inflowing onto the central galaxy, contrary to hydrostatic equilibrium model predictions. This means that there must be something providing an extra heat source, possibly the relativistic jets from AGN.

- **Enrichment of the intergalactic medium:** both the cool Lyman- $\alpha$  forest and the hotter Warm-Hot Intergalactic Medium (WHIM) that produces the “X-ray forest” are far from having primordial composition, but are instead enriched with heavy elements. Supernovae driven “super-winds” from star-burst galaxies and AGN winds can both potentially escape their galaxies and provide the IGM enrichment
- **Dust at high redshift:** the presence of dust has been detected in  $z\sim 6$  quasars. Dust is important to catalyze efficient star formation by shielding gas from UV heating and by enhancing cooling. But dust at so high redshifts is hard to make and cannot be created in AGB-star winds (the process that dominates in our Galaxy), as these stars take  $\sim 1$  Gyr to evolve. Supernovae may create dust, but the rate is unknown, so the origin of high redshift dust is open. Cool clumps in AGN winds may be an effective alternative site.

AGN are powerful sources in almost all the electromagnetic spectrum and can provide feedback through radiation. In particular, this can enrich the IGM by heating, ionizing and accelerating the ISM from the AGN host galaxy, which consequently inhibits star formation in the host. Moreover, it is usually observed that tightly collimated jets with relativistic velocities emanate from the central galaxy in rich cluster of galaxies. In X-rays, the hot intra-cluster medium show holes or cavities into which the radio structures fit almost perfectly. Hence, there is clearly a close interaction between the relativistic plasma and the X-ray emitting hot plasma in these clusters. Even a tightly collimated jet can spread heat throughout the intra-cluster medium and so prevent cooling flows and setting an upper bound to galaxy and black hole masses. However, only the most powerful jets are able to escape their clusters to enrich the IGM and the total fraction of radio-loud AGN with jets is relatively low, only  $\sim 10\%$ . Therefore, the total amount of energy and momentum available from radio jets is not sufficient and they may have difficulty in solving other feedback problems, especially in less massive systems.

Alternatively, winds with moderate outflow velocity ( $\sim 1000\text{--}2000$  km/s), such as the warm absorbers (see §1.3.1) observed in soft X-rays, might provide an additional input for feedback. They are detected in about  $\sim 50\%$  of AGN and form weakly collimated, wide angle winds. Being almost universal in AGN, these winds could create co-evolution between the SMBH and the host galaxy, and enrichment of the ISM, but they can reach the outskirts of galaxies only with difficulty due to their slow velocities.

Due to their recent discovery, the impact of Ultra-fast Outflows on the cosmological feedback from the AGN is still unknown. However, there are several reasons that suggest this to be a promising mechanism. In fact, it has been reported that the mass outflow rate associated with the UFOs can be comparable to the accretion rate and also their kinetic energy can be of the order of the bolometric luminosity of the source (e.g. Pounds et al. 2003a; Cappi et al. 2009 and references therein).

Moreover, there are theoretical works, such as King (2009), which claim that Eddington accretion episodes in AGN can effectively generate momentum-driven winds with parameters very similar to those typical of UFOs, such as outflow velocity of  $v_{out} \sim 0.1c$ , high ionization ( $\log \xi \sim 4 \text{ erg s}^{-1} \text{ cm}$ ). The interaction of these massive winds with ISM and bulge of the host galaxy is then able to explain important relations such as the  $M_{BH}-\sigma$  (e.g. Ferrarese & Merritt 2000) and black hole-bulge mass relation (e.g. Häring & Rix 2004). Therefore, the UFOs can have indeed an important impact on the environment surrounding the AGN and on the host galaxy evolution and need to be studied and quantified with more details.

#### 1.4.4 Significance of blue-shifted Fe K absorption lines in AGN

Due to the extremely high ionization levels, the Ultra-fast Outflows from AGN can be essentially observed only through narrow blue-shifted Fe K-shell absorption lines from Fe XXV and Fe XXVI at energies greater than  $\sim 7 \text{ keV}$ . Unfortunately, there are currently several issues and biases that can complicate their analysis (see review by Cappi 2006).

There is an intrinsic difficulty to unambiguously identify and model absorption lines in the Fe K-shell energy band. In fact, photo-ionization modeling of Fe K absorption spectra depend sensitively on details of energy levels, transitions probabilities and photo-ionization cross-sections. Moreover, there is an observational bias against the detection of blue-shifted lines in that orbiting X-ray observatories are of limited spectral and sensitivity capabilities at energies greater than  $\sim 7 \text{ keV}$ . Then, the apparent sporadic nature of the features, inherent to these types of extreme phenomena, can induce another detection bias. Finally, the detailed diagnostic of the gas will ever only be possible through Fe K-shell absorption lines (the lower- $Z$  elements being almost completely ionized), which implies a further, somewhat physical, bias against their detectability.

The calculation of the statistical significance of these absorption lines is often a matter

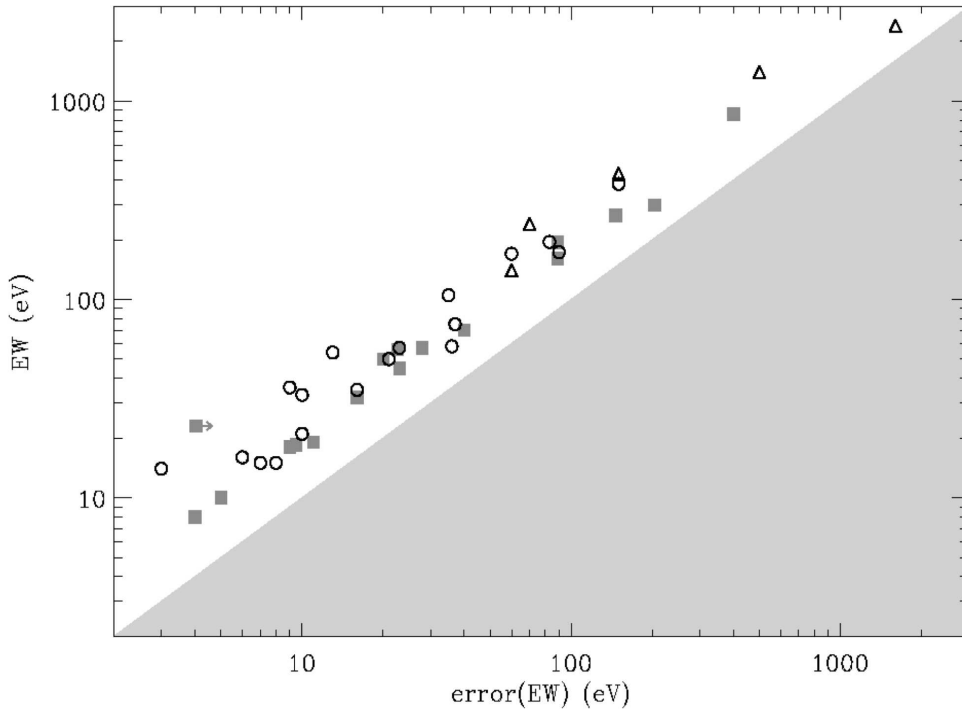


Figure 1.8: EW with respect to its 90% error for the blue/red-shifted emission (filled squares) and absorption (open circles) lines with  $v \geq 0.05c$  selected from the literature by Vaughan & Uttley (2008).

of debate. The reported features are all modest detections, in the sense that the statistical significance is typically in the range  $\sim 3-5\sigma$ . Moreover, the blue-shifted absorption lines appear to be transient and are detected at energies which are shifted with respect to expected atomic values. Thus, the analysis often requires a “blind” search in the time and energy parameters space. Therefore, the statistical significance (and  $\chi^2$  results) must either correct for the number of trials performed or account on proper Monte Carlo simulations (e.g. Protassov et al. 2002; Cappi et al. (2009) and references therein).

In particular, Vaughan & Uttley (2008) claimed that the results on the blue-shifted Fe K absorption lines are affected by a publication bias. They performed a literature search for papers reporting the detection of narrow, strongly red/blue-shifted ( $v \geq 0.05c$ ) emission/absorption lines in the X-ray spectra of Seyfert galaxies and quasars. They found 36 reported lines (17 emission and 19 absorption) from 23 sources.

Fig. 1.8 from Vaughan & Uttley (2008) reports a scatter diagram for these two

quantities, where the EW is an indication of the “signal” and the 90% error of the “noise”. This diagram shows whether the strength of the measured effect (EW) depends on the quality of the data (as indicated by the EW error). If most of the lines are real, some observations should populate the upper left portion of the diagram. The zone of avoidance in the lower right arises from the fact that any line with a 90% confidence interval on its EW that includes (or extends very close to) zero, would probably not be reported as a detection. Despite the three decades of range in the line strengths, there is a clear trend for all the data points to lie close to the edge of the zone of avoidance, that is just above the detection limit, irrespective of the line strength. If the lines do indeed span this range in strengths, the strongest lines should be easily detectable in the best observations, but only weak features are claimed in all these cases. It would appear that the strength of any narrow shifted lines depends on the quality of the data they were detected in.

The tendency for stronger lines to be accompanied by proportionately larger uncertainties (see Fig. 1.8) or equivalently the relatively constant  $\text{EW}/\text{error}\langle\text{EW}\rangle$  ratio over the large range in EWs, requires explanation. The lines with larger EW should be easy to detect in more sensitive observations (and should give smaller uncertainties) and so should populate the upper-left region of Fig. 1.8, but this is not the case. The authors claimed that a simple explanation could be that many of the line detections are actually the most significant false detections from a large population of data.

The wide bandpass and good spectral resolution of modern detectors, combined with the number of data sets that have been processed mean that data archives for recent spectroscopy missions may contain many modest signal-to-noise features simply from random sampling fluctuations in the photon-counting signal from otherwise featureless continua. The many hundreds of observations that have been examined and not provided detections would populate the shaded region in the lower right part of Fig. 1.8 if only they were published. In fact, the publication bias represents the tendency for positive results to be published and negative results to go unreported.

Therefore, the reported detections may be the strongest or most significant of a population of random fluctuations, with the rest of the population unseen due to publication bias. If the lines are genuine, the challenge is to explain why all the detections are close to the detection limit despite the huge range in the quality of the data, or equivalently, why the largest EW lines appear only in the poorest data with the largest

error bars. Of course, it is possible that Fig. 1.8 actually shows a mixture of false and true detections. Moreover, estimating the statistical significance of possible line features is indeed rather difficult and the use of inappropriate tests (e.g. the F-test) may increase the number of false detections. Perhaps the detection probabilities, especially if derived from the F-test, were systematically overestimated, leading to an over-abundance of false detection. However, this effect would not change the trend but only shift the distribution and can be corrected performing extensive Monte Carlo simulations (e.g. Cappi et al. 2009). The result of the publication bias is that the vastly greater number of null results will go largely unpublished, making it difficult to estimate the global significance of any individual detection on the whole population.

As stated by the authors, the only way to solve the publication bias for the blue-shifted Fe K absorption lines would be to perform a uniform and systematic search for these lines in the X-ray spectra of a large sample of AGN and directly report the fraction of detections over non-detections. Moreover, the significance of the lines should be directly compared to random fluctuations using extensive Monte Carlo simulations. This was actually what we (independently) used as an obvious strategy for the present Thesis.

## Chapter 2

# Data analysis and statistical methods

In this chapter we describe the line search method that we applied to find blue-shifted Fe K absorption lines in the X-ray spectra of our samples of radio-quiet and radio-loud AGN and the method used to establish their detection significance, which is based on extensive Monte Carlo simulations.

### 2.1 Line search method

In this section we focus on describing the line search method that will be systematically applied to the 4–10 keV spectra of the radio-quiet and radio-loud AGN to find blue-shifted Fe K absorption features (see §3.3 and §4.3, respectively). It essentially consists of screening the spectral data with a test Gaussian line and look for positive/negative line-like deviations in the  $\Delta\chi^2$  distribution with respect to a baseline model. This technique for the search and visualization of features in the data is similar to the widely used contour plot method for the determination of the error contours of spectral features in the energy-intensity plane (e.g. Miniutti & Fabian 2006; Miniutti et al. 2007; Cappi et al. 2009).

The procedure can be outlined as follows : 1) we fitted the 3.5–10.5 keV data with the baseline model (without any absorption line) and stored the resulting  $\chi^2$  value; 2) we then added a further narrow (unresolved,  $\sigma = 10$  eV) Gaussian line to the model and searched for the presence of both emission and absorption features by making a series of fits stepping the line energy in the 4–10 keV band (at intervals of 100 eV) and its normalization in positive or negative values, each time storing the new  $\chi^2$ ; 3) in this way we derived a grid of  $\chi^2$  values and then made a plot of the contours with the same  $\Delta\chi^2$

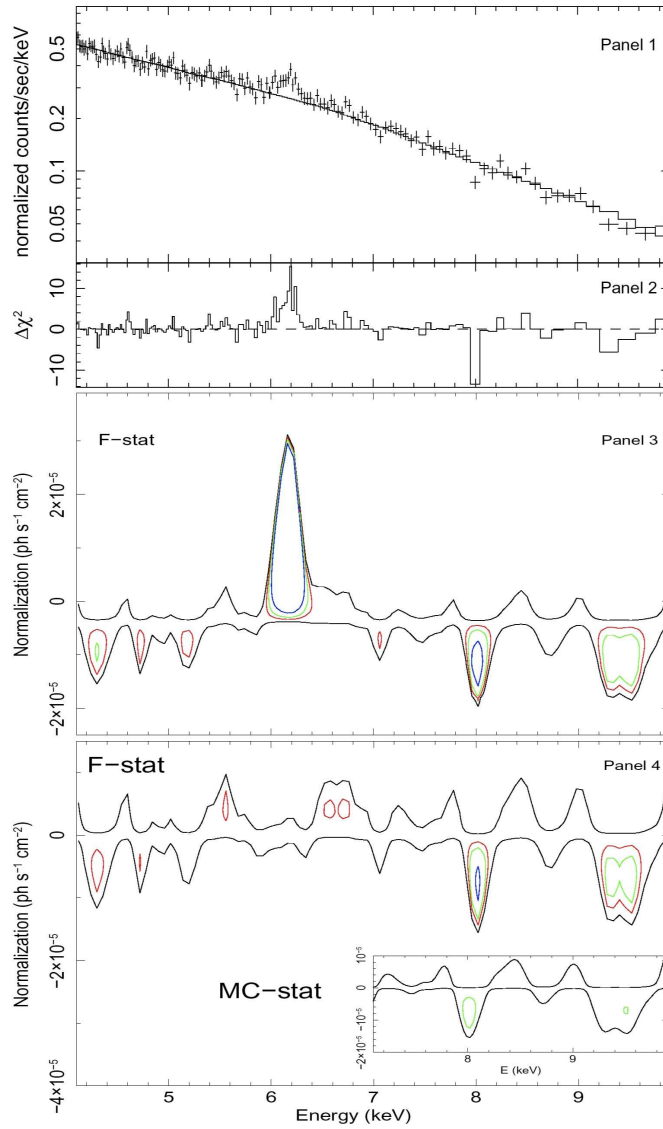


Figure 2.1: Example of the application of the line search technique to one XMM-Newton observation of Mrk 509 reported by us in Cappi et al. (2009) (see their Fig. 1). *Panel 1*: EPIC pn spectrum of one observation of Mrk 509 fitted in the 3.5–10.5 keV band with a single power-law continuum. (*Panel 2*:)  $\Delta\chi^2$  residuals. *Panel 3*: F-statistics confidence contours (68% (red), 90% (green) and 99% (blue) levels) with respect to a power-law continuum. *Panel 4*: F-statistics confidence contours after the addition of a Gaussian emission line to model the neutral Fe  $K\alpha$  line. *Panel 4, inset*: confidence contours in the 7–10 keV band calculated using Monte Carlo simulations. Contours (in black) calculated with  $\Delta\chi^2=0.5$  are reported to indicate the continuum level.

level relative to the baseline model fit. These levels are  $\Delta\chi^2 = -2.3, -4.61$  and  $-9.21$ , which can be translated using the F-test in statistical confidence levels for the addition of two more parameters of 68%, 90% and 99%, respectively. Even if we were mainly interested in the 7–10 keV band, we performed this check on the whole 4–10 keV interval in order to have a general view of the Fe K band.

In Fig. 2.1 we show the application of this line search technique to one XMM-Newton observation of the bright Seyfert 1 galaxy Mrk 509, reported by us in Cappi et al. (2009). This example clearly illustrates the procedure used systematically for the search of blue-shifted absorption lines, going from the actual spectral data modelling to the contour plots.

It should be noted that the negative  $\Delta\chi^2$  values with respect to the baseline model indicate that a better fit would be reached with the inclusion of a line, reducing the  $\chi^2$  value. In fact, the relative confidence levels do not depend on the  $\Delta\chi^2$  sign but only on its absolute value. This method is similar to the one obtained with the *steppar* command in XSPEC, but in this way the contours are inverted, *which means that inner contours indicate higher significance than the outer ones*. This is indeed a powerful technique to visualize the presence of spectral structures in the data and simultaneously have an idea of their energy, intensity and confidence levels. However, it gives only a semi-quantitative indication. Therefore, the absorption line parameters have then been determined by a direct spectral fitting to the data.

Finally, we note that the confidence levels shown in the contour plots (see panels three and four of Fig. 2.1) are derived from the F-test and thus they do not take into account the number of energy bins over which the blind line search have been performed. Therefore, extensive Monte Carlo simulations are required as an additional test on the significance of some of the observed lines, as explained in the next section.

## 2.2 Line significance from Monte Carlo simulations

Protassov et al. (2002) pointed out that the standard likelihood ratio tests such as the  $\chi^2$ , Cash and related F-test can provide misleading results when applied to highly structured models, such as those used in the fitting of X-ray spectral data. Sometimes, in fact, the basic regularity conditions required by these standard tests are not met and the statistics do not follow the assumed null distributions. In particular, the F-test method

can overestimate the actual detection significance for a blind search of emission/absorption lines as it does not take into account the possible range of energies where a line might be expected to occur, nor does it take into account the number of bins (resolution elements) present over that energy range. The F-test can yield the probability of finding a feature at a given energy if the line energy is known in advance from theory or laboratory results. Therefore, this problem requires an additional test on the blue-shifted lines significance and can be solved by determining the unknown underlying statistical distribution by performing extensive Monte Carlo (MC) simulations (e.g. Porquet et al. 2004; Yaqoob & Serlemitsos 2005; Miniutti & Fabian 2006; Markowitz et al. 2006; Cappi et al. 2009).

In particular, in this work we are interested in finding possible narrow absorption lines in the energy range between 7 keV and 10 keV. Given that there is no a priori preference in finding the line at a particular energy in this interval, we have to estimate the probability distribution of random generated lines in the whole energy range and compare this with that of the observed line to properly assess its detection significance.

We will focus our continuum spectral modelling to the Fe K band, in particular to energies between 3.5 keV and 10.5 keV. Once we have determined a phenomenological baseline model which adequately represents the spectrum in this band, we will apply the line search technique outlined in the last section (§2.1) to find possible hints for blue-shifted absorption features at energies greater than 7 keV (with F-test confidence contours greater than 99%). We will then perform a direct spectral fitting of the absorption lines with inverted Gaussian and determine their  $\Delta\chi^2$  and associated F-test probability. Our Monte Carlo method will serve as an additional check on the line significance, by essentially testing the null hypothesis that the spectra are adequately fitted by a model that does not include the narrow absorption lines.

The procedure can be outlined as follows: 1) we simulated a spectrum (with the *fakeit* command in XSPEC) using a baseline model without any absorption line and considered the same exposure as the real data. We subtracted the appropriate background and grouped the data; 2) we fitted again this spectrum with the baseline model in the 3.5–10.5 keV band, stored the new parameters values, and generated another simulated spectrum as before but using this refined model. This is a redundant security test in order to account for the uncertainty in the null hypothesis model itself and is particularly relevant when the original data set is relatively noisy (Markowitz et al. 2006); 3) this new

simulated spectrum was fitted again with the baseline model in the 3.5–10.5 keV and the resultant  $\chi^2$  was stored; 4) then, a new Gaussian line (unresolved,  $\sigma = 10$  eV) was added to the model, with its normalization initially set to zero and let free to vary between positive and negative values. In order to account for the possible range of energies in which the line could be detected in a blind search, we then stepped its centroid energy between 7 and 10 keV at intervals of 100 eV (to adequately sample the EPIC pn spectral resolution at these energies), each time making a fit and stored only the maximum of the resultant  $\Delta\chi^2$  values; 5) this procedure was repeated  $S = 1000$  times and consequently a distribution of simulated  $\Delta\chi^2$  values was generated. This would indicate the fraction of random generated narrow emission/absorption features in the 7–10 keV band that are expected to have a  $\Delta\chi^2$  greater than a threshold value. In particular, if  $N$  of these simulated  $\Delta\chi^2$  values are greater or equal to the real value, then the estimated detection confidence level from Monte Carlo simulations is simply  $1 - N/S$ .

In Fig. 2.2 we show an example of the  $\Delta\chi^2$  distribution for 1000 random generated lines in the 7–10 keV band with the Monte Carlo simulations. The distribution tends to cluster around a mean value of  $\Delta\chi^2 \sim 5$  (which corresponds to a probability of  $\sim 50\%$ ). Moreover, for this specific simulated distribution, only 10 points have values greater than the threshold  $\Delta\chi^2 \simeq 14$ , which means that the probability to find random generated lines with  $\Delta\chi^2 \geq 14$  in the 7–10 keV interval is only 1%. Fig. 2.3 represents the cumulative probability from the same simulated  $\Delta\chi^2$  distribution. In particular, we can clearly see again that only 1% of the random generated lines have  $\Delta\chi^2 \simeq 14$ . Therefore, if an observed narrow absorption line in the 7–10 keV band has this  $\Delta\chi^2$  value, we can associate a detection confidence level of 99% from MC simulations.

Finally, in Fig. 2.4, we show a comparison between a cumulative probability from the F-test and another from  $10^3$  Monte Carlo simulations. The two curves are almost parallel, with the normalization of the MC a bit higher. This means that for the same  $\Delta\chi^2$  level, the estimated significance (confidence) level for the blind search of lines is slightly higher (lower) for the F-test compared to the MC method. In other words, the number of random generated lines in the 7–10 keV from MC simulations is slightly higher than that predicted by the F-test. In fact, we can note that in this case the confidence level for a line with  $\Delta\chi^2 \simeq 14$  from the F-test is 99.9%. Instead, from the MC simulations it is slightly lower, 99.6%. This clearly demonstrates that the F-test can slightly overestimate the confidence

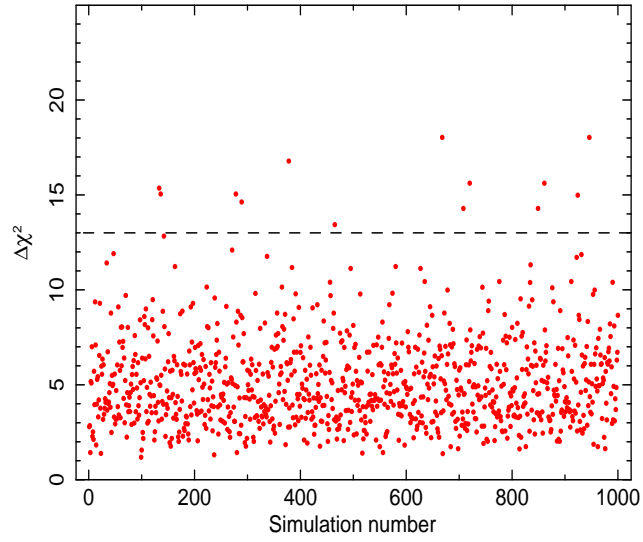


Figure 2.2: Example of a  $\Delta\chi^2$  distribution of 1000 random lines generated with the Monte Carlo simulations. The horizontal line indicates the  $\Delta\chi^2 \simeq 14$ , which in this case refer to a probability of  $\simeq 99\%$ .

level for a blind search of narrow emission/absorption lines in a wide energy interval and this can be corrected using our Monte Carlo method.

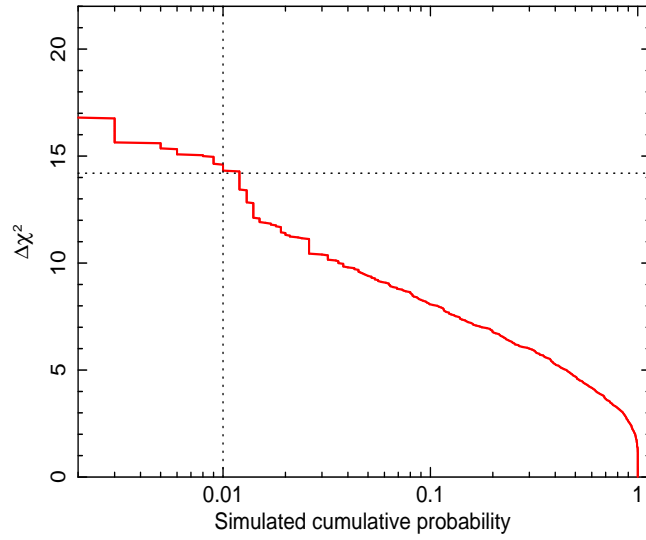


Figure 2.3: Example of cumulative frequency distribution from the 1000 Monte Carlo simulations. The lines indicate that in this case the confidence level of  $\simeq 99\%$  is reached for a  $\Delta\chi^2 \simeq 14$ .

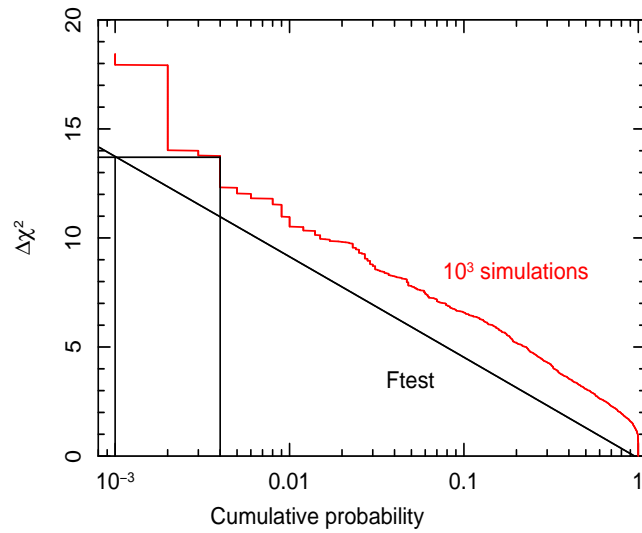


Figure 2.4: Comparison between the cumulative probability from the F-test and from 1000 Monte Carlo simulations. In this case, the probability for random generated lines to have a  $\Delta\chi^2$  equal or greater than  $\simeq 14$  is  $\simeq 10^{-3}$  from the F-test and slightly higher,  $\simeq 4 \times 10^{-3}$ , from the MC simulations.

## Chapter 3

# The radio-quiet AGN sample

### 3.1 Sample selection

The sample of radio-quiet AGN has been drawn from the RXTE All-Sky Slew Survey Catalog (XSS; Revnivtsev et al. 2004), which provides a list of 294 sources serendipitously detected in the hard X-rays. The survey is 90% complete to a  $4\sigma$  limiting flux of  $\simeq 10^{-11}$  erg s $^{-1}$  cm $^{-2}$  in the 4–10 keV band. From this catalog we extracted all the sources thereby classified as NLSy1, Sy1 and Sy2. In order to keep the selection criterion as general as possible we did not place further constraints on other source characteristics. The detailed classification and redshifts of the sources were then cross-checked with the accurate database of NED<sup>1</sup> (NASA/IPAC Extragalactic Database). Thus, the preliminary sample contains a total of 57 sources. These were divided into 41 type 1 (including NLSy1, Sy1, Sy1.2 and Sy1.5) and 16 type 2 (including Sy1.8, Sy1.9 and Sy2). However, it is worth noting that the X-ray spectra of the sources that are classified as type 2 are affected by absorption from neutral matter that is always less than  $N_H \sim 10^{24}$  cm $^{-2}$ . This allows the direct observation of the nuclear continuum at the Fe K band (E=4–10 keV) for both type 1 and type 2 objects.

### 3.2 XMM-Newton observations and data reduction

The high effective area between 4–10 keV, coupled with the moderate spectral resolution (FWHM $\simeq$ 150 eV at 6.4 keV) of the EPIC pn detector aboard XMM-Newton make this one of the best available instrument to perform a detailed spectral study in the Fe K band. Moreover, after about a decade of operation, the XMM catalogue contains a large

---

<sup>1</sup><http://nedwww.ipac.caltech.edu>

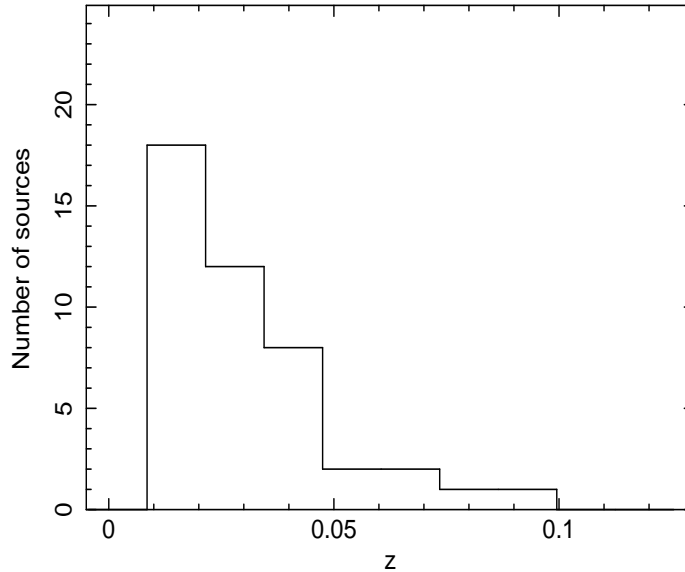


Figure 3.1: Distribution of the cosmological red-shifts of the radio-quiet sample.

number of pointed AGN observations suitable for a statistical study. See Appendix D for a detailed description of the XMM-Newton X-ray observatory. Therefore, we cross-correlated the RXTE selected sample with the XMM-Newton Accepted Targets Catalog and downloaded all the pointed observations publicly available at the date of October 2008. This resulted in a total of 102 observations for the type 1 and 22 observations for the type 2, respectively.

We limited our analysis to the mean spectra of the XMM-Newton EPIC pn observations. The data reduction was performed following the standard procedure with the XMM-SAS v 8.0.1 package. We used the calibration files updated to October 2008. We checked the observations for high background contamination, looking for flares in the light curves at energies greater than 10 keV. We excluded these bad intervals from the successive analysis. We then selected only those observations with resultant net exposure time greater than 10 ks. Considering that the minimum 4–10 keV flux of the observations in the sample is  $\sim 10^{-12}$  erg s $^{-1}$  cm $^{-2}$ , this assures to have a minimal spectral sampling in this energy band (that is, to have at least 25 counts per  $\sim 100$  eV energy resolution element). After these filtering processes, the total number of objects with at least one good XMM-Newton EPIC pn observation decreased to 44. This constitutes about 80% of the original 57 radio-quiet AGN directly selected from the XSS catalog. The total number of observations is instead 104. In particular, the number of type 1 sources decreased to

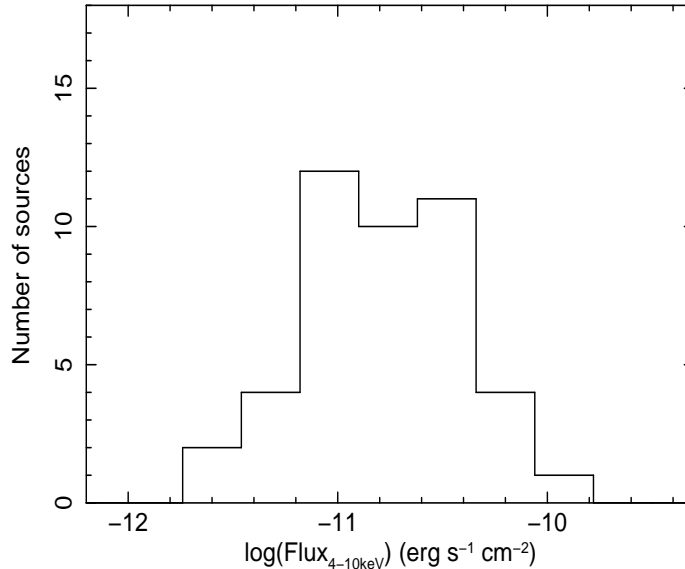


Figure 3.2: Distribution of the 4–10 keV flux among the radio-quiet sample. The values refer to the mean flux among the XMM-Newton observations for each source.

34 with 86 observations and that of type 2 to 10 sources with 18 observations. These sources and the parameters of their XMM-Newton EPIC pn observations are reported in Table A.1 of Appendix A. It can be seen from the histograms in Fig. 3.1 and Fig. 3.2 that the sources in the final sample are local (with cosmological redshifts  $z \leq 0.1$ ) and relatively X-ray bright (with 4–10 keV fluxes in the range of  $\simeq 10^{-12}$ – $10^{-10}$  erg s<sup>-1</sup> cm<sup>-2</sup> and a mean value of  $\simeq 2 \times 10^{-11}$  erg s<sup>-1</sup> cm<sup>-2</sup>).

### 3.3 Data analysis

We then proceeded with the uniform EPIC pn spectral analysis of the sample observations. We extracted the source photons from a circular region of 40 arcsec radius, while the background ones were collected from an adjacent source free circular region of the same size. Only single and double events were selected. Using the SAS task *epatplot* we checked that the Pile-up fraction was always negligible ( $< 1\%$ ). Then, we extracted the source spectrum for all the observations, subtracted the corresponding background and grouped the data to a minimum of 25 counts per energy bin (to enable the use of the  $\chi^2$  statistics when performing spectral fitting). The analysis of the EPIC pn observations was carried out using the *heasoft* v. 6.5.1 package and XSPEC v. 11.3.2.

### 3.3.1 Continuum and emission lines modelling

We limited our study to the Fe K band, between 3.5 keV and 10.5 keV. In order to perform a straightforward uniform analysis on the whole sample, we decided to use a phenomenological model composed by the same fundamental spectral components for all the sources, that is: a power-law continuum absorbed by neutral material (*zwabs* in XSPEC) and narrow Gaussian emission lines. Given the narrow energy band considered ( $E \simeq 4\text{--}10$  keV), this modelling provides an excellent characterization of the data with the lowest number of free parameters. However, the derived absorber column densities should not be considered for any further physical interpretation. We did not find necessary to include neutral absorption from our own Galaxy because the relatively low column densities involved ( $N_H \leq 10^{21}$  cm $^{-2}$ ) have no effects at all in this energy band.

The spectral fitting process was carried out in a uniform way for all the observations, starting from a simple power-law continuum and adding new components whenever they were required at more than the 99% confidence level (from the F-test). We first checked for the presence of power-law continuum curvature due to absorption intrinsic to the sources and then added Gaussians to model the expected Fe fluorescence emission lines. We followed the method of adding consecutive spectral components to the model with decreasing  $\chi^2$  improvement. We confirm the ubiquitous presence of a neutral or mildly ionized Fe K $\alpha$  emission line at rest frame energy of  $E \simeq 6.4\text{--}6.5$  keV. In several cases we also detected emission lines at higher energies, ascribable to Fe XXV He $\alpha$  (1s $^2$ –1s2p) at  $E \simeq 6.7$  keV and a possible blend of neutral Fe K $\beta$  at  $E \simeq 7.06$  keV and Fe XXVI Ly $\alpha$  (1s–2p) at  $E \simeq 6.97$  keV. These emission lines turned out to be always marginally or not resolved at the energy resolution of the EPIC pn and we fixed their widths to 100 eV (or 10 eV, depending on the higher  $\chi^2$  improvement). The ratios of the spectral data with respect to a power-law (with neutral absorption if required) for all the XMM-Newton observations are showed in Appendix B, from Fig. B.1 to Fig. B.13 (upper panels). Instead, the best-fit parameters of the baseline models for all the observations of the sample are reported in Appendix A (Table A.2).

It should be noted that, besides our simple absorbed power-law and emission lines model, additional components might well be present in the X-ray spectra of local Seyfert galaxies, such as: a reflection continuum, a broad relativistic Fe line and ionized absorption. However, we found these components to be relatively weak in the limited

energy band of  $E=4\text{--}10$  keV. Our modelling choice provides an excellent first order characterization of the spectral data and is adequate to determine a good estimate of the continuum level. We stress that our choice of using a simple phenomenological model composed by a power-law continuum absorbed by neutral material and narrow Gaussian emission lines is indeed adequate to derive a good estimate of the continuum.

To further support this statement, we simulated several spectra assuming a 4–10 keV flux of  $10^{-11}$  erg s $^{-1}$  cm $^{-2}$  and a power-law continuum with  $\Gamma=2$ , typical of our sample, and added further components: a reflection continuum (modelled with *pe xrav* in XSPEC), with the typical value of reflection fraction  $R\simeq 1$  and high energy cut-off  $E_c\simeq 250$  keV (e.g. Dadina 2008); a broad relativistic Fe line (modelled with a *diskline* in XSPEC) with energy  $E\simeq 6.4$  keV,  $EW\simeq 80$  eV, emissivity  $\beta\simeq -3$  and inclination  $i\simeq 30^\circ$  (e.g. Nandra et al. 2007); and a neutral/ionized absorption (modelled with *absori* in XSPEC) with column density in the range  $N_H\simeq 10^{21}\text{--}10^{23}$  cm $^{-2}$  and ionization parameter  $\log\xi\simeq 0\text{--}3$  erg s $^{-1}$  cm (e.g. Blustin et al. 2005; McKernan et al. 2007). We then fitted the simulated spectra with our phenomenological model and found that the continuum parameters were always consistent within the 90% errors (the difference is  $<5\%$ ).

Therefore, we conclude that our baseline models are adequate to determine the 4–10 keV continuum with an excellent level of accuracy, which is important for the successive analysis of the narrow absorption lines at energies greater than 6.4 keV. We adopted an approach which directly examines the requirement imposed by the data, without excessive modelling or using some complex (sometimes over-complex, given the data quality) physical scenarios.

Finally, we note that in some observations we found evidence for sporadic weak line-like emission features in the 5–6 keV energy band (e.g. IC4329A, NGC 4151, NGC 3783, MCG-6-30-15), that could be associated with relativistically shifted lines. However, we did not find necessary to include also these features because, given their weak intensity, our phenomenological model is adequate to provide a good continuum characterization. We did not further investigate the interpretation of these emission features because at this stage we are only interested in deriving suitable best-fit phenomenological baseline models for the subsequent search for blue-shifted Fe K absorption lines and we refer the reader to the recent work by De Marco et al. (2009), who performed a comprehensive study of these features in the X-ray spectra of a sample of Seyfert 1 galaxies.

### 3.3.2 Absorption lines search

We performed a systematic search for blue-shifted Fe K absorption lines at energies greater than 6.4 keV in all the XMM-Newton observations of the radio-quiet sample. We applied the line search technique which has been widely discussed in §2.1. This enabled us to directly check for line-like deviations in the data with respect to the baseline models reported in Table A.2 (see Appendix A). In particular, the visualization of the  $\Delta\chi^2$  distribution in contour plots allowed us to have a preliminary estimate of the energy and intensity of the possible lines and to evaluate their detection confidence levels. Even if we were mainly interested in the 7–10 keV band, we performed this check on the whole 4–10 keV interval in order to have a general view of the Fe K band.

In Fig. 3.3 we report the case of the first observation of PG1211+143 (0112610101). This example illustrates the procedure used systematically for the search of blue-shifted absorption lines, going from the actual spectral data modelling to the visualization in contour plots. The plots with respect to the baseline models for all the XMM-Newton observations of the radio-quiet sample are showed in Appendix B, from Fig.B.1 to Fig.B.13 (lower panels).

However, it should be noted that, even if this is indeed a powerful technique to visualize the presence of spectral structures in the data and simultaneously have an idea of their energy, intensity and confidence levels, it gives only a semi-quantitative indication. Therefore, the absorption line parameters have been then determined by a direct spectral fitting to the data. We added narrow Gaussian absorption lines to the baseline models, where indications for narrow line-like absorption features at energies greater than 6.4 keV with confidence contours greater than 99% were present. We considered only the lines with a  $\Delta\chi^2$  value greater than a fixed detection threshold level of 9.21, which corresponds to a confidence level greater than 99% (for two more parameters, with the F-test).

We also performed a check to assure that the presence of these absorption lines in the contour plots is not affected by our choice of the baseline models. Therefore, we fitted again the spectra which showed the presence of absorption lines in the contour plots, this time modelling all the residuals with phenomenological Gaussian emission lines. We found that all the absorption lines with confidence levels greater than 99% are still present in the contour plots and their parameters were consistent within the 90% errors. We obtained the same results applying the sometimes more complex models reported in the literature for

each source (see Appendix C). This assures that our absorption line search is not globally biased and that the model dependence of our results is only marginal.

We note that in the contour plots of some sources (see Appendix B) there is evidence for the presence of sporadic narrow absorption lines at energies lower than 6.4 keV (e.g. NGC 4151, NGC 3783, NGC 3516, MCG-6-30-15, Mrk 335, ESO 198-G024 and NGC 7582), with confidence levels  $\simeq 99\%$ . Moreover, broad absorption features at energies greater than 7 keV can be observed in some cases (e.g. IC4329A and Mrk 766). The possible interpretation of these spectral structures is briefly discussed in §3.4.1 and in Appendix C for each source. However, they are not analyzed in more detail in this Thesis as the topic of the present work is to assess the global incidence and significance of narrow blue-shifted Fe K absorption lines in the X-ray spectra of AGN.

Finally, we note that the confidence levels shown in the contour plots (see Appendix B) were derived from the F-test and thus they do not take into account the number of energy bins over which the blind line search have been performed. Therefore, extensive Monte Carlo simulations are required as an additional test on the significance of some of the observed lines (see §3.3.4).

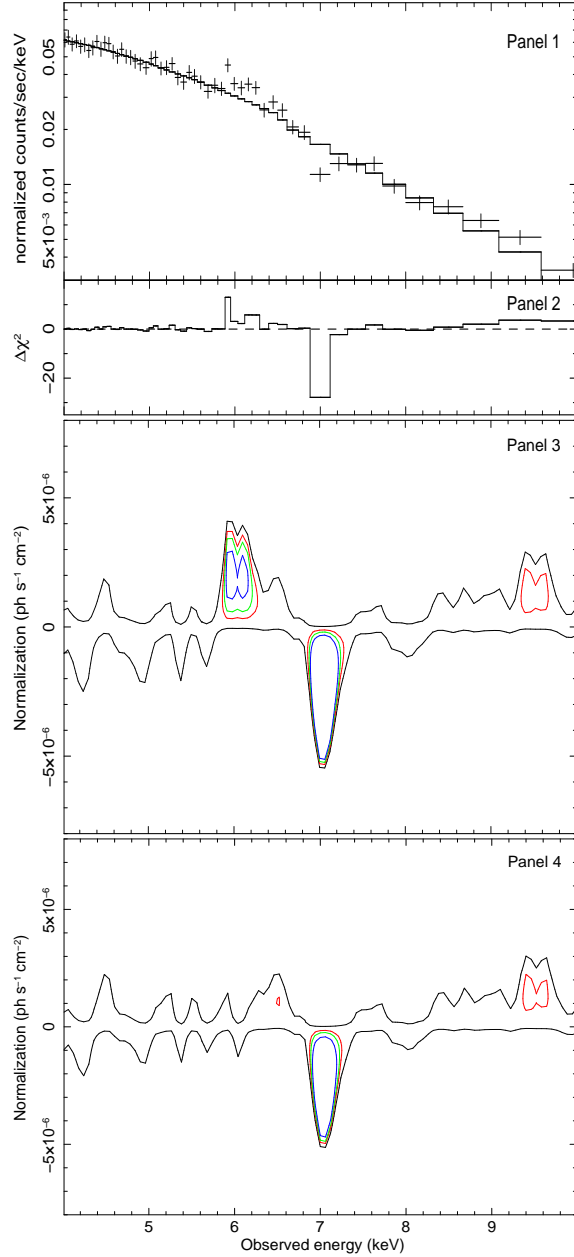


Figure 3.3: *Panel 1*: EPIC pn spectrum of PG1211+143 (observation 0112610101) fitted with a simple absorbed power-law model in the 4–10 keV band; *Panel 2*:  $\Delta\chi^2$  residuals; *Panel 3*: confidence contour plot with respect to the simple absorbed power-law model (68% (red), 90% (green), 99% (blue) levels); *Panel 4*: contour plot after the inclusion of the Gaussian emission line in the model. The blue-shifted absorption line at the observed energy of  $\sim 7$  keV is clearly visible with high significance. The contours in black (calculated with  $\Delta\chi^2 = 0.5$ ) indicate the baseline model reference level.

### 3.3.3 EPIC pn background and calibration checks

The EPIC pn background is known to have intense instrumental emission lines from Ni  $K\alpha$  and Cu  $K\alpha$  at the energies of 7.48 keV and 8.05 keV, respectively (Katayama et al. 2004). These lines originate from the interaction of the cosmic rays with the sensor housing and electronics and this causes also their intensity to be slightly dependent on the location on the detector, increasing with off-axis angles. Therefore, the selection of the background on a region of the CCD where the intensity of the lines is slightly higher/lower than that of those actually on the source extraction region can possibly induce spurious absorption/emission lines in the background subtracted spectrum. This effect is more relevant for low flux or extended sources. We performed some tests to exclude such eventuality.

Since the most intense instrumental background emission lines are present at specific energies (e.g. Ni  $K\alpha$  at  $E=7.48$  keV and Cu  $K\alpha$  at  $E=8.05$  keV, Katayama et al. 2004), we checked that the observed energies of the absorption lines are indeed not consistent with those values. We also inspected that the values of the energy and equivalent width of the absorption lines at  $E>7$  keV in the source spectra (see Table A.2 in Appendix A) are consistent with or without background subtraction. These tests assure that our results on the absorption lines detected in the 7–10 keV band are indeed not affected by any contamination from the EPIC pn instrumental background.

Moreover, the detected features cannot be attributed to some sort of EPIC pn calibration artifact because they have been detected most often at different energies and are narrow. Instead, if due to instrumental calibration problems, they would be expected to be observed always at some specific energies or, if due to effective area calibration problems, to induce broad continuum distortions.

However, it should be noted that a correction of the calibration files describing the EPIC pn effective area that could potentially affect the spectral analysis of the data in the  $\sim 6$ –10 keV band was introduced in April 2007. As explained in the calibration file release note XMM-CCF-REL-205<sup>2</sup>, the EPIC pn mirror effective area was corrected in order to take into account broad emission residuals above 6 keV systematically observed in the spectra of bright AGN. The change was not very large and consisted in a flattening of the effective area at high energies, with a smooth decrease between  $\sim 6$ –10 keV and

---

<sup>2</sup>[http:xmm2.esac.esa.intexternalxmm\\_sw\\_calcalibindex.shtml](http:xmm2.esac.esa.intexternalxmm_sw_calcalibindex.shtml)

an increase above 10 keV, both of the order of  $\sim 5\%$ . The main effect of such calibration correction has been to slightly change the continuum curvature. We checked that such calibration correction has not significantly affected the results on the narrow absorption features we detected (because it mainly introduced a weak broad effect) and that there is still an overall good agreement between our spectral analysis and those published before this calibration correction.

### 3.3.4 Absorption lines detection significance

As already discussed in §2.2, the F-test method can overestimate the actual detection significance for a blind search of emission/absorption lines in a wide energy interval as it does not take into account the possible range of energies where a line might be expected to occur, nor does it take into account the number of bins (resolution elements) present over that energy range. The F-test can yield the probability of finding a feature at a given energy if the line energy is known in advance from theory or laboratory results. Therefore, following the method widely discussed in §2.2, we performed extensive Monte Carlo simulations as an additional test on the significance of the blue-shifted absorption lines.

The most intense absorption lines expected in the 4–10 keV interval are the inner K-shell transitions of iron and, in particular, the  $K\alpha$  (1s–2p). The energy of this line depends on the ionization state of iron:  $E \simeq 6.4$ – $6.5$  keV for Fe I–XVIII,  $E \simeq 6.5$ – $6.6$  keV for Fe XIX–XXIV,  $E \simeq 6.7$  keV for Fe XXV and  $E \simeq 6.97$  keV for Fe XXVI (e.g. Kallman et al. 2004). Therefore, it is expected to find the presence of lines in this energy range. Moreover, it is well established that at least half of the X-ray spectra of Seyfert galaxies are affected by intrinsic absorption from nuclear photo-ionized gas, the so-called warm absorbers (see §1.3.1). This material is usually outflowing with velocities lower than  $\sim 1000$  km/s (e.g. Blustin et al. 2005; Risaliti et al. 2005; McKernan et al. 2007). If we allow for this possible low blue-shift, we would preferentially expect the lines to be present in the energy interval  $E \simeq 6.4$ – $7.1$  keV. Therefore, we can take a conservative approach assuming that the lines in this energy interval are rest-frame or low blue-shift Fe  $K\alpha$  transitions and the standard F-test alone is adequate to estimate their confidence level. The 14 absorption lines which satisfy this condition and which have F-test confidence levels greater than 99% (see contour plots in Appendix B) are reported in Table A.2 (in Appendix A). As we can see, their

energies are indeed consistent with those of Fe XXV or Fe XXVI 1s–2p transitions within 1–2% (that corresponds to velocity shifts of about  $\pm 5000$  km/s), which are known to dominate the Fe ions distribution for highly ionized absorbers (e.g. Kallman et al. 2004).

Instead, there is no a priori expectation to observe single narrow resonant Fe K absorption lines in the energy range 7.1–10 keV (if not consistent with higher order K-shell series lines). Given that there is no a priori preference in finding the line at a particular energy in this interval, we have to estimate the probability distribution of random generated lines in the whole energy range and compare this with that of the observed line to properly assess its detection significance. Therefore, even if their F-test derived confidence levels are greater than 99%, we performed extensive Monte Carlo simulations (see §2.2) to clearly assess the significance of the narrow absorption lines detected in the 7.1–10 keV band.

We decided to select only those features with Monte Carlo derived confidence levels  $\geq 95\%$ . Therefore, the number of narrow absorption lines at  $E \geq 7.1$  keV that are beyond this detection threshold is 22. We reported these lines and their parameters in Table A.2 (in Appendix A). As expected, the Monte Carlo detection confidence levels are slightly lower than those derived from the F-test, because they take into account the blind search for lines in the whole 7.1–10 keV energy interval.

We performed a sanity check on the possible dependence of the Monte Carlo probabilities on the assumed baseline models. In particular, for those sources showing more complex spectra in the 4–10 keV band (e.g. IC4329A, NGC 3783, MCG-6-30-15, NGC 4051), we fitted the data including also the possible continuum reflection, relativistic lines and warm absorption (i.e. making use of the more detailed models already reported in the literature, see Appendix C). Then, we performed the extensive Monte Carlo simulations (see §2.2) using these complex models and derived the  $\Delta\chi^2$  distributions fitting again the data with the same complex models or with the phenomenological baseline models listed in Table A.2. We derived that the difference in the derived confidence levels can be at maximum of the order of  $\pm 0.5\%$ . Therefore, we are confident enough that the global Monte Carlo results are not affected by any significant model dependent systematics.

It is important to note here that from these results we can also estimate the global probability to find such narrow absorption features at  $E \geq 7.1$  keV in the whole sample using the Binomial distribution. In fact, this distribution gives us the probability of the

happening of a certain event  $k$  times on  $n$  trials, if the probability of the event is  $p$  ( $q = 1-p$  for the contrary). Its expression is:

$$P(k; n, p) = \frac{n!}{k! (n - k)!} p^k (1 - p)^{n-k} \quad (3.1)$$

where  $k = 0, 1, 2, \dots, n$ . We have 21 observations with at least one absorption line detected at  $E \geq 7.1$  keV with Monte Carlo confidence level  $\geq 95\%$ . We can apply a conservative approach saying that the random probability of finding such features in the 7–10 keV band for each observation is then  $p < 0.05$ . Therefore, we can estimate the probability that the line detections in  $k=21$  out of a total of  $n=104$  observations are merely due to random fluctuations. This turned out to be  $P < 3 \times 10^{-8}$ . Therefore, even if some of the individual line detections can be weak, the global probability for these features to be generated by random fluctuations is extremely low.

### 3.3.5 Consistency check with the EPIC MOS cameras

We have performed a consistency check of the EPIC pn spectral results using the data from the MOS1 and MOS2 cameras. These instruments have a lower effective area, and hence the spectra have a lower S/N, compared to the EPIC pn. However, they provide simultaneous observations of the same pointed source in the 0.5–10 keV band and therefore they help to independently confirm the veracity of the narrow absorption lines detected in the EPIC pn spectra.

We reduced the MOS1 and MOS2 data of the XMM-Newton observations for which blue-shifted Fe K absorption lines were detected in their EPIC pn spectrum. We followed the standard reduction procedure and used the XMM-SAS v.8.0.1 package. Initially, we checked for the presence of high background flares looking at the light curves at energies greater than 10 keV and excluded the relative bad time intervals from the analysis. Then, we extracted the source photons from a circular region of 40 arcsec radius centered on the source and the background ones from an adjacent source free circular region of the same size. The pile-up fraction for observations performed with the MOS cameras can be high, especially for the brightest sources in our sample (even greater than 10%). However, we expect such effect to have negligible influence on the narrow absorption lines we are interested in. In fact, the main result of the pile-up is to induce an overall distortion of the observed continuum, as it basically consists in counting two or more low-energy photons

as a single high-energy photon.

Therefore, we extracted the MOS1 and MOS2 source and background spectra and grouped them to a minimum of 25 counts per energy bin (in order to allow the use of the  $\chi^2$  statistics in spectral fitting). We considered the 3.5–10.5 keV energy band. Then, we fitted the MOS data with the same baseline models derived from the EPIC pn (see Table A.2 in Appendix A) and looked for a confirmation of the presence of the narrow absorption lines detected in the Fe K band. When possible the MOS1 and MOS2 data have been combined in order to increase the statistics.

The parameters of the absorption lines derived from the MOS1 and MOS2 cameras are reported in Table A.3 (in Appendix A). We can clearly confirm the detection of 25 out of 36 features from the MOS data. The relative  $\Delta\chi^2$  levels are in the range from a minimum of 3 up to 26, for the addition of two more model parameters. Instead, for the remaining 11 features, we have been able only to put the 90% upper limits on the equivalent widths (EWs) by fixing the line energy to the best-fit EPIC pn value. However, all the measured EWs are consistent with the values obtained from the EPIC pn data.

The fact that we have been able to independently confirm the detection of several of the absorption lines also with the MOS cameras and that the results are consistent with what was measured using the EPIC pn is a very strong point in favour of the veracity of these spectral features.

## 3.4 Results

### 3.4.1 Absorption lines identification

The total number of narrow absorption lines detected at energies greater than 6.4 keV in all the observations is 36 (see Table A.2 in Appendix A). We identified these features with highly ionized Fe absorption lines, specifically associated with Fe XXV and Fe XXVI K-shell absorption (see §1.2.3 and Table 1.1 for more details on the lines parameters).

In particular, the most prominent Fe XXV lines are due to the He $\alpha$  ( $1s^2-1s2p$ ) and He $\beta$  ( $1s^2-1s3p$ ) transitions, which further subdivide into inter-combination and resonance lines. At the moderate energy resolution of the EPIC pn instrument, these fine structure line components are not distinguishable and we can measure only a blend. Therefore, we averaged their energies, weighted for the respective oscillator strengths. The consequent line energies are 6.697 keV for the Fe XXV He $\alpha$  and 7.880 keV for the Fe XXV He $\beta$ ,

respectively. The most intense lines from Fe XXVI are instead due to Ly $\alpha$  (1s–2p) and Ly $\beta$  (1s–3p) transitions, each of which further subdivide into two resonance doublets. The average energies of these lines, weighted for their oscillator strengths, are 6.966 keV for the Fe XXVI Ly $\alpha$  and 8.250 keV for the Fe XXVI Ly $\beta$ , respectively. From a simple comparison of the lines oscillator strengths, the equivalent widths of the 1s–3p transitions are expected to be  $\sim 20\%$  of the 1s–2p. However, this is only a lower limit because their ratio can increase up to  $\sim 1$  if saturation effects are significant (which can be enhanced for higher column densities or lower line velocity broadening) (see §5.2.2).

If the measured line energy was not consistent with these expected values, we calculated the relative velocity shift using the Relativistic Doppler formula:

$$v/c = \frac{\left(\frac{E_o}{E_e}\right)^2 - 1}{\left(\frac{E_o}{E_e}\right)^2 + 1}. \quad (3.2)$$

where  $E_o$  is the rest-frame energy of the line and  $E_e$  is the expected energy. We adopted the convention to use the positive and negative signs for blue-shifted and red-shifted line velocities, respectively.

The absorption lines and their best-fit parameters are reported in Table A.2 (in Appendix A) for all the radio-quiet sources. In the table we reported only the lines that have been detected in the 6.4–7.1 keV band with F-test confidence levels  $\geq 99\%$  and those detected at energies greater than 7.1 keV, with additional Monte Carlo probability  $\geq 95\%$ .

It should be noted that, in principle, less intense higher order Fe XXVI Lyman series lines could be observed as well, such as: the Ly $\gamma$  (1s–4p) at  $E=8.700$  keV and the Ly $\delta$  (1s–5p) at  $E=8.909$  keV (equivalent width  $\sim 5\%$  of the Fe XXVI Ly $\alpha$ , but can be comparable if saturation effects are significant) (see §1.2.3 and Table 1.1 for more details). However, their detection is hampered by the fact that they are at energies where the instrumental effective area and energy resolution are worse and the S/N is lower. Nevertheless, we found that in one observation of IC4329A the broad absorption trough observable at energy greater than  $\simeq 9$  keV (see contour plot in Fig. B.2 in Appendix B) can be well described by a blend of unresolved higher order Fe XXVI Lyman series lines with a blue-shift consistent with that of the narrow Fe XXVI Ly $\alpha$  line reported in Table A.2 (see notes on this source reported in Appendix C for more details).

Moreover, even if the cosmic abundance of nickel is negligible with respect to that

of iron ( $\sim 5\%$ , from Grevesse et al. 1996), the K-shell transitions of this element are distributed at energies greater than 7 keV and could, in principle, complicate our line identification. However, the contamination by neutral or mildly ionized Ni K $\alpha$  lines is very unlucky, because it would require extremely high column densities ( $N_H \geq 10^{24} - 10^{25} \text{ cm}^{-2}$ ) for these lines to be intense enough to be observable, which would consequently generate strong absorption lines and edges from all the other lighter elements as well. For instance, none of the absorption lines in Table A.2 have a rest-frame energy consistent with Ni I K $\alpha$  at  $E \simeq 7.47 \text{ keV}$ .

The only possible contamination could be due to He/H-like Ni, whose 1s–2p transitions are at rest-frame energies of  $E \simeq 7.8 \text{ keV}$  and  $E \simeq 8.1 \text{ keV}$ , respectively. Also in this case the column densities required to have lines with measurable intensities would be extremely high ( $N_H \geq 10^{24} - 10^{25} \text{ cm}^{-2}$ ). However, the very high ionization level required to have significant columns of these ions are so extreme ( $\log \xi \geq 5 \text{ erg s}^{-1} \text{ cm}$ ) that all the lighter elements would be completely ionized (possibly with the only exception of iron) and therefore they will not contribute with other absorption features. We found that only 4 over 22 absorption lines detected at  $E \geq 7.1 \text{ keV}$  have energies consistent (at the 90% level) with these values. Therefore, we conclude that even if the unlucky interpretation of these lines as rest-frame resonant absorption from highly ionized Ni turned out not to be a mere coincidence, this would have a negligible effect on the global results anyway.

Furthermore, even if H/He-like Fe K resonance absorption lines are the most intense lines expected from an extremely ionized absorber, in some cases there can be also a contamination by lower ionization species of iron. The relative lines are at slightly lower energies and therefore, in case of line blending, the estimated centroid energy would falsely appear red-shifted. The only case in which the absorption lines are not consistent with the rest-frame values (at the 90% level) and red-shifted is for NGC 3783. In fact, as Reeves et al. (2004) already discussed, there is evidence for a blending of the Fe XXV K $\alpha$  line with lower ionization components from Fe XXIII (6.630 keV) and Fe XXIV (6.659 keV). This would explain why its centroid energy is measured between  $E \simeq 6.61 - 6.67 \text{ keV}$ , resulting in an apparent red-shifted velocity. However, the contribution of these lower ionization lines is negligible on the whole sample and will be taken into account in the detailed modelling of the absorbers using the photo-ionization code Xstar (see §5.3).

The search for narrow absorption lines in the 7–10 keV energy band could be

complicated also by the presence of ionized Fe K edges at energies in the range from  $E \simeq 7.1$  keV to  $E \simeq 9.3$  keV, depending on the ionization state of iron (from neutral to H-like). Hence, one could object that some of the spectral structures we identified as blue-shifted absorption lines could actually be interpreted equally well as ionized Fe K edges. As a sanity check, we tested that the alternative modelling of the Gaussian absorption lines with simple sharp absorption edges (*zedge* in XSPEC) did not significantly improve the spectral fits, as expected from the narrowness of the observed spectral features. Moreover, it is important to note that the commonly held view of sharp Fe K edges is an oversimplification of the real process and could lead to misleading results. In fact, it has been demonstrated that if the adequate treatment of the decay pathways of resonances converging to the K threshold is properly taken into account, the resulting edges are not sharp but smeared and broadened (e.g. Palmeri et al. 2002; Kallman et al. 2004). This effect can be negligible for neutral or extremely ionized iron (He/H-like) but is quite relevant for intermediate states (with energies in the range  $E \simeq 7.2$ – $9$  keV). Furthermore, intense Fe K resonance absorption lines from different ionization states would be expected to accompany the edges. A proper modelling of the Fe K edges can be performed only using the more sophisticated photo-ionization code Xstar, as in §5.3. The only case in which a significant broad absorption trough is observed at the energies of  $\sim 8$ – $9$  keV is in one observation of Mrk 766 (0109141301, see contour plot in Fig. B.7 in Appendix B). As already reported by Pounds et al. (2003c), this feature can be well modeled by a rest-frame ionized Fe K edge (see Appendix C for more detailed information on this source) and therefore it has not been included in Table A.2.

It is worth noting that in the contour plots in Appendix B there are 10 spectra (over a total of 104) which show narrow absorption lines at energies lower than 6.4 keV with confidence levels  $\simeq 99\%$ . The spectra are relative to these sources: NGC 4151, NGC 3783, NGC 3516, MCG-6-30-15, Mrk 335, ESO 198-G024 and NGC 7582. We did not include these lines in Table A.2 and we did not further investigate their detection significance with extensive Monte Carlo simulations because in this work we focused in the study of absorption lines at energies greater than 6.4 keV. However, it is important to discuss here at least some possible explanations for their presence.

A possibility could be that they are Doppler or gravitationally red-shifted Fe XXV He $\alpha$  or Fe XXVI Ly $\alpha$  lines. There have been several papers in the literature reporting

the detection of such red-shifted lines in the X-ray spectra of Seyfert galaxies or quasars (e.g. Nandra et al. 1999; Dadina et al. 2005; Reeves et al. 2005; Yaqoob & Serlemitsos 2005; Longinotti et al. 2007a), with velocities in the range  $\sim 0.1\text{--}0.4c$ . Our observed lines are in the energy range  $E \simeq 4\text{--}5$  keV, which would imply substantial red-shift velocities of  $\sim 0.4\text{--}0.7c$ . Instead, some of these lines could be identified with rest-frame or blue-shifted K-shell absorption lines from neutral or ionized elements lighter than iron, such as: Si, Ar, Ca (Sc, Ti).

Therefore, another intriguing possibility is to check whether these features are consistent with absorption lines from elements lighter than iron with the same blue-shift inferred from the Fe K lines. In fact, if the ionization state of the material is not extremely high ( $\log \xi \simeq 2\text{--}4$  erg  $s^{-1}$  cm) there is the possibility to find also K-shell absorption lines from H/He-like ions of Si, S, Ar or Ca, which can be blue-shifted in the  $E \simeq 4\text{--}5$  keV band.

This finding has already been reported by Pounds & Page (2006) in one XMM-Newton observation of PG 1211+143 (obs. 0112610101). Combining the EPIC pn based results with the analysis of the lower energy ( $E \leq 3$  keV, below our low energy boundary) MOS and RGS data, the authors have been able to detect several K-shell absorption lines from highly ionized Ne, Mg, Si, S, Ar and Fe, all consistently blue-shifted with the same mildly-relativistic velocity of  $\simeq 0.13c$ .

There are three observations in the contour plots of Appendix B which show a narrow absorption line at an energy greater than 7.1 keV and another between 4 keV and 5 keV. In particular, two observations of NGC 4151 (obs. 0112830201 and 0402660201) and one of NGC 7582 (obs. 0112310201). For the former, we found that the absorption lines at energies lower than 5 keV are consistent with being Ca XIX He $\alpha$  ( $1s^2\text{--}1s2p$ ;  $E \simeq 3.9$  keV) and Ca XX Ly $\alpha$  ( $1s\text{--}2p$ ;  $E \simeq 4.11$  keV), blue-shifted by the same velocity ( $\simeq 0.1c$ ) of the Fe XXVI Ly $\alpha$ . However, we did not report in Table A.2 the detection of an absorption line at  $E \sim 7.8$  keV in the first observation of NGC 4151 because the resultant Monte Carlo confidence level was lower than the threshold level of 95%.

The latter case, NGC 7582, is even more interesting. From a further detailed analysis we found the presence of three narrow absorption lines between 4 keV and 5.3 keV (one with an F-test confidence level  $\geq 99\%$  and the other two  $\simeq 95\%$ ). If the absorption line at  $E \simeq 9$  keV is identified with the Fe XXV He $\alpha$  transition, these lines are consistent with being absorption from Ar XVII He $\alpha$  ( $E \simeq 3.14$  keV), Ar XVIII Ly $\alpha$  ( $E \simeq 3.3$  keV) and Ca XIX

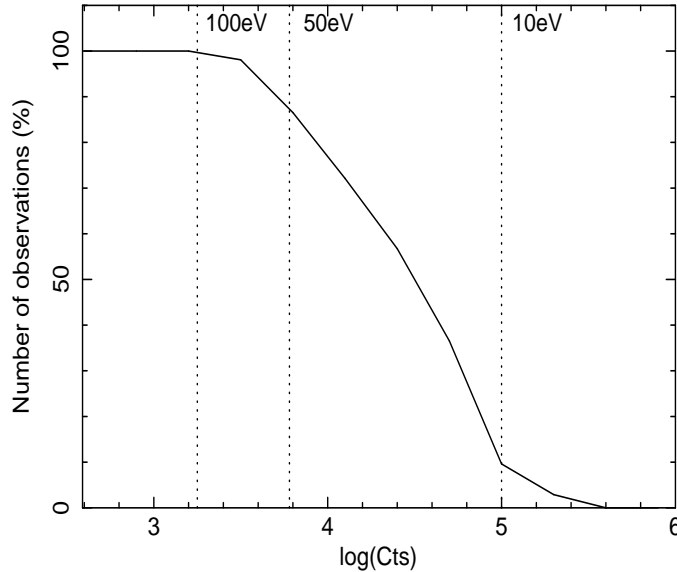


Figure 3.4: Percentage of XMM-Newton EPIC pn observations of the whole sample with total 4–10 keV counts greater than a fixed value. The vertical lines indicate the counts level over which it would be possible to detect a narrow emission/absorption line at 7 keV at the  $3\sigma$  level for EWs of 100 eV, 50 eV and 10 eV, respectively. It should be noted that the statistics would allow to detect the presence of such lines in 100%, 80-90% and only in 10% of the observations, respectively.

He $\alpha$  ( $E \simeq 3.9$  keV) blue-shifted by the same common velocity of  $\simeq 0.255c$ . The probability for random fluctuations to give rise to this series of lines with the exact energy spacing and common blue-shift is very low,  $\simeq 2 \times 10^{-6}$ . This is an astonishing result, which contributes to strengthen our conclusions on the veracity of the blue-shifted Fe K lines. We refer the reader to Appendix C for more detailed information regarding each source. The energies of the K-shell transitions of the elements lighter than iron have been taken from Verner et al. (1996).

### 3.4.2 Global incidence of blue-shifted Fe K absorption lines

We can divide the detected absorption lines into two groups: at rest, if their blue-shifted velocity is consistent with or slightly less than zero at the 90% level and blue-shifted, if their velocity is greater than zero at the 90% level. The first group is composed of only 8 features, the second instead of 28. Therefore, the majority of the detected features are consistent with the presence of outflows. The total number of objects with at least one absorption line detected in the Fe K band is 19 over 44, that translates into a frequency

of  $\sim 43\%$ . If we further consider the fraction of objects having at least one feature with blue-shifted velocity, the fraction is instead  $17/44$ , which corresponds to about  $40\%$  of the cases.

It is important to note that in the spectrum of three sources (namely IC4329A, NGC 3783 and ESO 323-G77) we detected two Fe XXV/XXVI K-shell absorption lines with the same common blue-shift. Instead, in NGC 3516 we detected two Fe XXV/XXVI K-shell lines in three different spectra and even four Fe XXV/XXVI K-shell lines with the same common blue-shift in another observation. Furthermore, in other two sources we have been able to detect blue-shifted K-shell absorption lines from highly ionized species of elements lighter than iron in the range of energies  $E \sim 4\text{--}5$  keV. In particular, in one observation of NGC 4151 we detected a Ca XX Ly $\alpha$  absorption line with the same blue-shift as the Fe XXVI Ly $\alpha$  and in one spectrum of NGC 7582 we detected even three K-shell lines from helium- and hydrogen-like Ar and Ca with blue-shift consistent with that of the Fe XXV He $\alpha$ . The detection of these lines and their parameters are discussed in §3.4.1 and reported in Table A.2 (in Appendix A), respectively.

In §1.3.2 we have defined UFOs those highly ionized absorbers detected through Fe XXV and Fe XXVI K-shell absorption lines with outflow velocities  $v_{out} \geq 10^4$  km/s ( $\simeq 0.033c$ ), i.e. much greater than the maximum value for typical X-ray warm absorbers in AGN (e.g. Blustin et al. 2005; McKernan et al. 2007). The ratio of sources with at least one detection of a narrow absorption feature with blue-shifted velocity  $v_{out} \geq 0.033c$  is  $15/44$  ( $\simeq 35\%$ ) (see Table A.2). This fraction is very high. If we consider it with respect to the number of sources with blue-shifted lines it is  $15/17$  ( $\simeq 90\%$ ). Therefore, the majority of the sources with detected lines show the presence of UFOs. If we consider the lines with relativistic outflow velocities  $v_{out} \geq 0.1c$ , these fractions are instead  $11/44$  ( $\simeq 25\%$ ) and  $11/17$  ( $\simeq 65\%$ ).

However, we stress that the observed blue-shift velocities depend on the unknown inclination angle of the outflow with respect to the line of sight (e.g. Elvis 2000). Therefore, the obtained fractions are only conservative estimates and the number of objects showing UFOs can be even higher, potentially extending to all the sources with detected Fe K absorption lines (i.e.  $19/44$ ).

Moreover, it is important to note that these fractions are actually only lower limits, because they do not take into account the number of observations that have low counts

levels and therefore do not have enough statistics for the detection of lines even if they were present.

The total 4–10 keV counts level of each observation can be regarded as an indication of their statistics. The percentage of observations of the whole sample with a total 4–10 keV counts level greater than a fixed value is shown in Fig. 3.4. To estimate the effect of the different statistics in the XMM-Newton observations on the detectability of the absorption lines we calculated the counts levels needed for a  $3\sigma$  detection of a narrow emission/absorption feature at the energy of 7 keV (we assumed a power-law continuum with  $\Gamma = 2$ ) for different EWs. As it can be seen from Fig. 3.4, 100% of the observations have a 4–10 keV counts level greater than  $\simeq 10^3$ , that would allow the detection of a line of EW=100 eV if present. For lower EWs, however, the counts levels needed for the detection consequently increase. For instance, for a line of EW= 50 eV the limit is at  $\simeq 6 \times 10^3$  counts which implies that it could be detected only in the  $\sim 80$ – $90\%$  of the observations. Finally, only  $\sim 10\%$  of the sources have a total 4–10 keV counts level greater than  $\sim 10^5$ , that would allow the detection of a line with EW= 10 eV at 7 keV. If instead we consider lines at energies greater than 7 keV, the counts needed increase further because the intrinsic power-law spectrum has less photons at those energies and also the instrument effective area drops. For instance, the number of 4–10 keV counts needed for a  $3\sigma$  detection of a narrow absorption line of EW= 100 eV (10 eV) are  $\sim 2 \times 10^3$  ( $\sim 10^5$ ) at 7 keV and  $\sim 5 \times 10^3$  ( $\sim 4 \times 10^5$ ) at 9 keV. This means that from a statistical point of view we would be able to detect the presence of narrow absorption features with EW=100 eV (10 eV) in  $\sim 100\%$  ( $\sim 10\%$ ) of the observations at 7 keV and in  $\sim 90\%$  ( $\leq 1\%$ ) of the sample observations at 9 keV.

This clearly states that there is a bias against the detection of narrow absorption lines at higher energies/velocities with respect to those at lower energies/velocities. However, we can derive a rough estimate of the global effect of the statistics available in the spectra of the whole sample considering that for a mean EW of  $\sim 50$  eV and a mean line energy of  $\sim 8$  keV (that would correspond to a blue-shift velocity of about  $0.1c$  for Fe XXVI Ly $\alpha$ ), the 4–10 keV counts level for a  $3\sigma$  detection is  $\sim 10^4$  counts. From Fig. 3.4 we can note that only about 80% of the available XMM-Newton observations have enough counts and instead for about 20% of them there is not enough statistics for a proper detection of a narrow absorption line if present. Hence, we can estimate that the total fraction of sources

with blue-shifted absorption features (40%) could actually be larger, up to a maximum of 60%.

Finally, if we consider only the sources classified as type 1, the ratio of objects with detected absorption lines is 16/34 ( $\simeq 47\%$ ). The ratio of sources having blue-shifted lines is 14/34 ( $\simeq 40\%$ ). If we consider those with velocities  $v_{out} \geq 0.033c$ , the number is 12. Therefore, the fraction of type 1 sources with detected UFOs is 12/34 ( $\simeq 35\%$ ). If we limit to those with relativistic velocities ( $\geq 0.1c$ ) the fraction reduces to 8/34 ( $\sim 23\%$ ). The remaining fraction of objects with line velocities consistent with zero (when negative they were probably indicating a blending with lower ionization Fe species) is 2/34 ( $\sim 6\%$ ). Instead, only absorption lines with blue-shifted velocities greater than 0.033c (actually, higher than 0.1c) have been detected in type 2 sources. Therefore, the fraction of UFOs in this class of objects is of 3/10 (30%), consistent with the type 1s.

### 3.4.3 Mean parameters of the Fe K absorption lines

We estimated the average properties of the narrow absorption lines detected in the Fe K band for the whole sample. We did not consider the line detections for each XMM-Newton observation separately because we would have introduced a bias. In fact, there are different numbers of observations for each source and consequently there are sources with more line detections (e.g. NGC 3783 and NGC 3516). In this way, the sources with more observations would have had a higher weight. Thus, for each source we calculated the mean EW and blue-shifted velocity of the lines among all the relative XMM-Newton observations.

The list of sources with their mean Fe absorption line parameters (EW and blue-shift velocity) are reported in Table A.4 (in Appendix A). This has been divided according to the line identification as Fe XXV ( $\text{He}\alpha$  and  $\text{He}\beta$ ) and Fe XXVI ( $\text{Ly}\alpha$  and  $\text{Ly}\beta$ ), respectively. The distribution of mean EWs of these lines with respect to the number of sources in which they have been detected is shown in the histograms of Fig. 3.5. It can be seen that Fe XXVI  $\text{Ly}\alpha$  lines have been detected in the majority of sources (16), with a spread in EW ranging from  $\sim 10$  eV to  $\sim 100$  eV and a peak around  $\sim 40$ – $50$  eV.

Instead, the distribution of mean velocities is showed in the histogram of Fig. 3.6. As it can be seen, the distribution spans from about zero up to  $\sim 0.3c$ , with a strong tendency toward high velocities. In fact, there is a clear peak at  $v_{out} \simeq 0.1c$ , which also

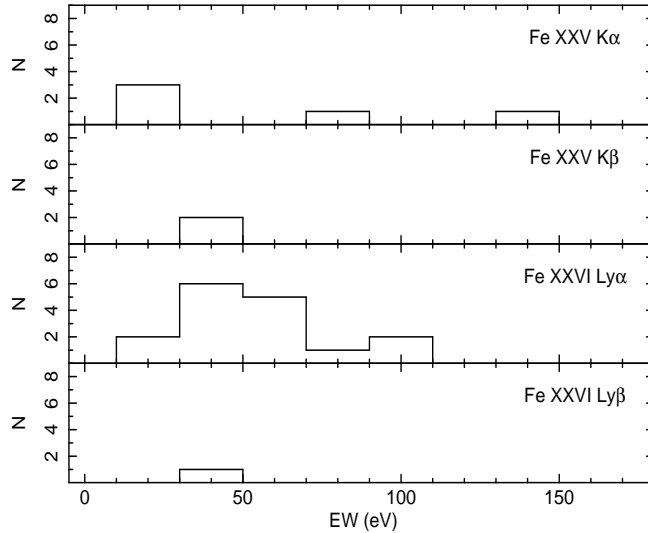


Figure 3.5: Histograms representing the mean EW distribution of each Fe absorption line type with respect to the number of sources in which such lines have been detected. The plot has been divided in four panels according to the line classification in Fe XXV ( $\text{He}\alpha$  and  $\text{He}\beta$ ) and Fe XXVI ( $\text{Ly}\alpha$  and  $\text{Ly}\beta$ ), respectively. The values have been taken from Table A.4.

coincides with the mean value of the velocity distribution (in this calculation we did not consider those with negative values). The majority of the outflow velocities are higher than  $v_{out} \simeq 0.033c$ , which means that the absorbers can be associated with UFOs. However, it should be noted that these velocities are conservative estimates, because they depend on the unknown inclination angle of the outflows with respect to the line of sight (e.g. Elvis 2000). Therefore, their intrinsic values could be even higher and potentially all the absorbers could be identified with UFOs.

The percentage of sources with outflow velocities greater than a fixed value with respect to the total number of sample sources is shown in Fig. 3.7. We can note that about 40% of the sample sources show absorption lines with blue-shift velocities greater than zero. Moreover, about 35% of the sources have outflow velocities greater than  $v_{out} = 10^4$  km/s and can be associated with UFOs. In particular, 25% have mildly relativistic velocities greater than  $0.1c$ . However, it is worth noting that these fractions are only lower limits because some of the sources have XMM-Newton observations with not enough statistics to clearly detect the presence of narrow absorption lines in the Fe band (see §3.4.2).

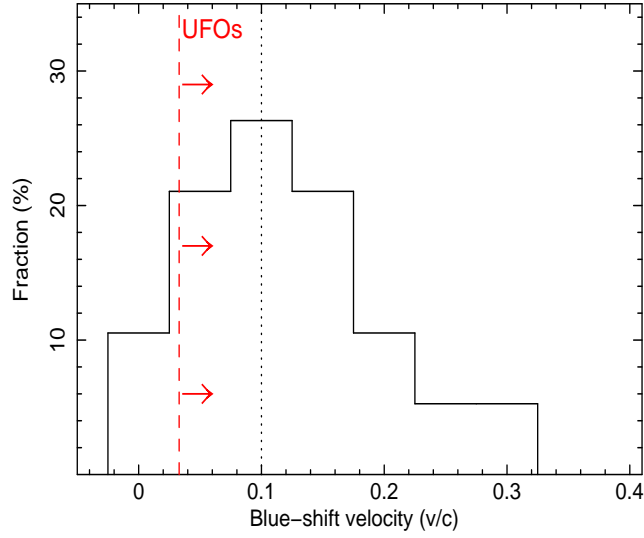


Figure 3.6: Histogram representing the distribution of the mean blue-shifted velocity for each source with detected Fe K absorption lines with respect to the total number of radio-quiet sources. The mean velocities have been taken from Table A.4 (column 10). The vertical dashed line (in red) indicates the threshold velocity value of  $v_{out}=10^4$  km/s ( $\simeq 0.033c$ ) over which the absorbers can be associated with UFOs. The vertical dotted line indicates the peak and mean value of the velocity distribution at  $v_{out}\simeq 0.1c$ .

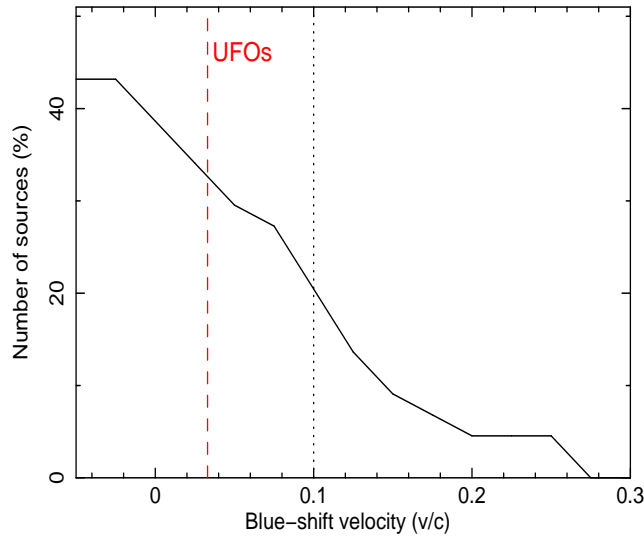


Figure 3.7: Fraction of sources with mean blue-shifted velocity of the Fe K absorption lines greater than a fixed value with respect to the total number of radio-quiet sources. The mean velocities have been taken from Table A.4 (column 10). The vertical dashed line (in red) indicates the threshold velocity value of  $v_{out}=10^4$  km/s ( $\simeq 0.033c$ ) over which the absorbers can be associated with UFOs. The dotted line refers the mean value of the velocity distribution at  $v_{out}\simeq 0.1c$ .

## Chapter 4

# The radio-loud AGN sample

The Broad Line Radio Galaxies (BLRGs) are the radio-loud counterpart of the Seyfert 1 galaxies and therefore they are a logical extension of our search for UFOs in the central regions of AGN. The main differences with respect to the Seyfert galaxies are essentially: lower X-ray brightness, a lower number density and the presence of observable radio jets. The detection of UFOs in BLRGs would provide further clues on the relation between the accretion disk and formation of winds/jets, and the feedback between the AGN and the host galaxy.

### 4.1 Sample selection

The number of BLRGs with a good S/N in the Fe K band ( $E=4-10$  keV) available in the X-ray archives is very limited, especially if compared to that of Seyferts. This is probably due to their intrinsic lower number density and lower X-ray fluxes. In fact, we checked the XMM-Newton archive and found only the observations of five sources available, namely: 3C 111, 3C 390.3, 3C 120, 3C 382, and 3C 445. These five BLRGs represent the “classical” X-ray brightest radio-loud AGN.

We have downloaded and analyzed the XMM-Newton observations of these five BLRGs and did not detect any significant blue-shifted absorption lines at energies greater than 6.4 keV. The XIS cameras of the Suzaku X-ray satellite (Mitsuda et al. 2007) have a combined effective area comparable to the XMM-Newton EPIC pn (see Appendix D for a detailed description of the Suzaku satellite). Therefore, we decided to check the Suzaku archive and found that observations of these sources with significantly better statistics were available.

The exposures of the XMM-Newton observations are shorter than those of Suzaku, the only exception being 3C 390.3, for which the XMM observation is  $\sim 40\%$  longer than the Suzaku one. Therefore, even if the effective area of the pn is slightly higher than the XIS-FI, the S/N of the pn spectra in the 7–10 keV band with respect to the XIS-FI is lower for 3C 111 ( $\simeq 89\%$ ), 3C 120 ( $\simeq 68\%$ ), 3C 382 ( $\simeq 20\%$ ) and 3C 445 ( $\simeq 9\%$ ) and is slightly higher ( $\simeq 50\%$  more) for 3C 390.3.

In the next sections we describe the analysis of the Suzaku XIS data and the discovery of blue-shifted Fe K absorption lines in the spectra of three of these sources, namely 3C 111, 3C 390.3 and 3C 120. In §4.3.7 we report a consistency check between the Suzaku and XMM-Newton results.

## 4.2 Suzaku observations and data reduction

The observational details for the five BLRGs observed with Suzaku are summarized in Table 4.1. The data were taken from the X-ray Imaging Spectrometer (XIS, Koyama et al. 2007) and processed using v2 of the Suzaku pipeline. The observations were taken with the XIS nominal (on-axis) pointing position, with the exception of the 3C 111 observation, which was taken with the HXD nominal pointing. The Suzaku observation of 3C 120 is composed by four different exposures of  $\sim 40$  ks each, taken over a period of about one month (see Table 4.1). We looked at the individual spectra and we found that while observation 2, 3 and 4 did not change significantly overall, observation 1 instead showed a much strong emission, especially in the soft X-ray part of the spectrum. Therefore, we decided to add only observations 2, 3 and 4 (we will call this observation 3C 120b) and to analyze the spectrum of observation 1 separately (we will call this observation 3C 120a).

Data were excluded within 436 seconds of passage through the South Atlantic Anomaly (SAA) and within Earth elevation angles or Bright Earth angles of  $< 5^\circ$  and  $< 20^\circ$ , respectively. XIS data were selected in  $3 \times 3$  and  $5 \times 5$  edit-modes using grades 0, 2, 3, 4, 6, while hot and flickering pixels were removed using the SISCLEAN script. Spectra were extracted from within circular regions of between 2.5 arcmin and 3.0 arcmin radius, while background spectra were extracted from circles offset from the source and avoiding the chip corners containing the calibration sources. The response matrix (RMF) and ancillary response (ARF) files were created using the tasks XISRMFGEN and XISSIMARFGEN, respectively, the former accounting for the CCD charge injection and the latter for the

Table 4.1: List of the sources and Suzaku XIS-FI observations. Column 1: source name. Column 2: cosmological red-shift. Column 3: observation ID. Column 4: starting date of the observation (in year-month-day). Column 5: net exposure for each XIS. Column 6: flux in the 4–10 keV band, in units of  $\text{erg s}^{-1} \text{cm}^{-2}$ . Column 7: total source/background counts in the 7–10 keV band.

| Source               | $z$    | OBSID                  | Date       | Net Expo<br>(ks) | Flux<br>( $10^{-11}$ ) | Source/Bkgd<br>( $10^3$ cts) |
|----------------------|--------|------------------------|------------|------------------|------------------------|------------------------------|
| 3C 111               | 0.0485 | 703034010 <sup>a</sup> | 2008-08-22 | 109              | 1.3                    | 9.2/0.6                      |
| 3C 390.3             | 0.0561 | 702125010 <sup>a</sup> | 2007-04-27 | 43               | 2.0                    | 13.3/0.5                     |
| 3C 120a              | 0.0330 | 700001010 <sup>b</sup> | 2006-02-09 | 42               | 2.9                    | 13.8/0.3                     |
| 3C 120b <sup>c</sup> | 0.0330 | 700001020 <sup>b</sup> | 2006-02-16 | 42               | 2.6                    | 12.5/0.3                     |
| 3C 120b <sup>c</sup> | 0.0330 | 700001030 <sup>b</sup> | 2006-02-23 | 41               | 2.6                    | 12.2/0.3                     |
| 3C 120b <sup>c</sup> | 0.0330 | 702125010 <sup>b</sup> | 2006-03-02 | 41               | 2.5                    | 11.7/0.3                     |
| 3C 382               | 0.0579 | 701060010 <sup>a</sup> | 2006-12-14 | 58               | 2.5                    | 21.2/0.5                     |
| 3C 445               | 0.0562 | 702056010 <sup>a</sup> | 2007-05-25 | 108              | 0.7                    | 13.8/0.3                     |

(a) For the XIS 0 and XIS 3 cameras combined.

(b) For the XIS 0, XIS 2 and XIS 3 cameras combined.

(c) These observations have been added together in 3C 120b.

hydrocarbon contamination on the optical blocking filter.

Spectra from the front illuminated XIS 0, XIS 2 (where available) and XIS 3 chips were combined to create a single source spectrum (hereafter XIS-FI). Given its superior sensitivity in the region of interest, 4–10 keV, we restricted our analysis to the XIS-FI data. The data from the back illuminated XIS 1 (hereafter XIS-BI) chip were analysed separately and checked for consistency with the XIS-FI results. In all cases, the power-law continuum and Fe  $K\alpha$  emission line parameters were completely consistent, although the lower S/N of the XIS-BI in the 4–10 keV band ( $\sim 40\%$  of the XIS-FI) allowed us to place only lower limits to the equivalent widths of the blue-shifted absorption lines (see Table 4.4).

### 4.3 Data analysis

We performed a uniform spectral analysis of the small sample of five BLRGs in the Fe K band ( $\sim 4$ –10 keV). We used the *heasoft* v. 6.5.1 package and XSPEC v. 11.3.2. We extracted the source spectra for all the observations, subtracted the corresponding background and grouped the data to a minimum of 25 counts per energy bin to enable the

Table 4.2: Best fit baseline model in the 4–10 keV band. Column 1: source name. Column 2: power-law photon index. Column 3: equivalent Hydrogen column density due to neutral absorption intrinsic to the source, if present. Column 4: rest-frame energy of the Gaussian emission line. Column 5: line width. Column 6: equivalent width. Column 7: ratio between best fit  $\chi^2$  and degrees of freedom. Errors are at the  $1\sigma$  level.

| Source   | $\Gamma$               | $N_H$<br>( $10^{22} \text{ cm}^{-2}$ ) | E<br>(keV)      | $\sigma$<br>(eV)  | EW<br>(eV)        | $\chi^2/\nu$ |
|----------|------------------------|--|-----------------|-------------------|-------------------|--------------|
| 3C 111   | $1.47^{+0.02}_{-0.04}$ | ...                                    | $6.40 \pm 0.01$ | $110^{+25}_{-19}$ | $86 \pm 16$       | 412/427      |
| 3C 390.3 | $1.58 \pm 0.01$        | ...                                    | $6.42 \pm 0.01$ | $120^{+25}_{-20}$ | $68 \pm 14$       | 466/450      |
| 3C 120a  | $1.75 \pm 0.01$        | ...                                    | $6.40 \pm 0.02$ | $90^{+25}_{-31}$  | $68 \pm 13$       | 1386/1393    |
| 3C 120b  | $1.67 \pm 0.01$        | ...                                    | $6.38 \pm 0.01$ | $130^{+13}_{-16}$ | $90 \pm 10$       | 1729/1707    |
|          |                        |  | $6.94 \pm 0.03$ | $83^{+32}_{-28}$  | $24 \pm 8$        |              |
| 3C 382   | $1.75 \pm 0.01$        | ...                                    | $6.40 \pm 0.02$ | $120 \pm 20$      | $60 \pm 11$       | 1490/1516    |
|          |                        |  | $6.91 \pm 0.02$ | $10^a$            | $16 \pm 8$        |              |
| 3C 445   | $1.64 \pm 0.04$        | $19 \pm 4$                             | $6.38 \pm 0.01$ | $50 \pm 20$       | $133^{+22}_{-20}$ | 416/391      |

(a) Parameter held fix during the fit.

use of the  $\chi^2$  when performing spectral fitting. We limited the analysis to the 3.5–10.5 keV energy band.

### 4.3.1 Continuum and emission lines modelling

The X-ray spectra of BLRGs in the  $\sim 2$ –10 keV band are known to be remarkably similar to those of their radio-quiet counterparts, the Seyfert 1 galaxies. Indeed, previous ASCA observations of BLRGs (Sambruna et al. 1999 and references therein), showed that their 2–10 keV spectra are well fitted by a single power-law with photon index  $\Gamma \sim 1.7$  and a neutral Fe K $\alpha$  emission line at the rest-frame energy of 6.4 keV. Since our analysis is restricted to the energy range 4–10 keV, a plausible phenomenological representation of the spectrum will be provided by a power-law continuum plus a neutral Fe K $\alpha$  emission line at  $E \simeq 6.4$  keV and possible further highly ionized Fe K emission lines between  $E \simeq 6.4$  keV and  $E \simeq 7$  keV (from Fe II up to Fe XXVI). We adopted this baseline model for all the five sources and included only those emission lines with detection confidence levels greater than 99%.

The only exception is 3C 445, where the continuum is intrinsically absorbed by a column of neutral/mildly-ionized gas as high as  $\sim 10^{23} \text{ cm}^{-2}$  (Sambruna, Reeves, & Braitto

2007); for this source we included a neutral intrinsic absorption component with a column density of  $\sim 2 \times 10^{23} \text{ cm}^{-2}$  (see Table 4.2).

Given the narrow energy band considered ( $E \simeq 4\text{--}10 \text{ keV}$ ), this model provides an excellent phenomenological characterization of the data with the lowest number of free parameters. We did not find necessary to include neutral absorption from our own Galaxy because the relatively low column densities involved ( $N_H \leq 10^{21} \text{ cm}^{-2}$ ) have no effects in the considered energy band.

The ratios of the spectral data against a simple power-law continuum (or absorbed power-law for 3C 445) for the five BLRGs are shown in the upper panels of Fig. 4.1, Fig. 4.2 and Fig. 4.3. Some additional spectral complexity can be clearly seen, such as: the ubiquitous presence of an intense neutral Fe  $K\alpha$  emission line at the rest frame energy of 6.4 keV, some absorption structures at energies greater than 7 keV (i.e. 3C 111, 3C 120 and 3C 390.3) and some narrow emission features red/blue-ward to the neutral Fe  $K\alpha$  line (i.e. 3C 120, 3C 382 and 3C 445). However, we did not further investigate the interpretation of the weak narrow emission lines because in this work we focused in the search for Fe K absorption features. We refer the reader to other papers for a detailed treatment of the Fe K emission lines on the same Suzaku data set (e.g. Kataoka et al. 2007 for 3C 120; Sambruna et al. 2009 for 3C 390.3; Ballo et al. 2010 in prep. for 3C 111 and 3C 382; Braitto et al. 2010 in prep for 3C 445). We checked that neglecting to include the weak red-shifted emission lines in the baseline models does not affect our results on the blue-shifted absorption lines.

The baseline model was fitted systematically to the XIS-FI spectra of all five BLRGs and the results are reported in Table 4.2. These best-fit phenomenological models will be used in the successive search for blue-shifted Fe K absorption lines. Given the limited number of sources (five) in the radio-loud sample, in the next sections we discuss the detailed spectral analysis for each of them.

### 4.3.2 3C 111

The 4–10 keV XIS-FI spectrum of this source is well described by a simple power-law continuum (with  $\Gamma \simeq 1.5$ ) and a narrow neutral Fe  $K\alpha$  emission line at the rest-frame energy of 6.4 keV (see Table 4.2). A detailed broad-band spectral analysis of the Suzaku spectrum of this source will be reported in Ballo et al. (2010, in prep.). However, as it can

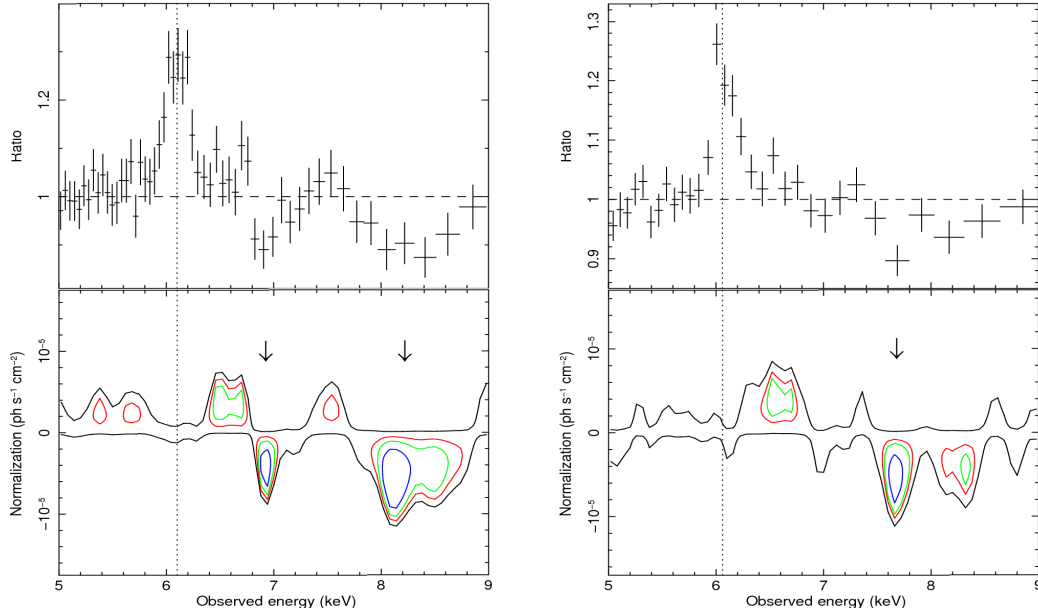


Figure 4.1: Suzaku XIS-FI spectra of 3C 111 (*left*) and 3C 390.3 (*right*) zoomed in the 5–9 keV band to emphasize the Fe K complex. *Upper panel*: ratio against a power-law continuum. *Lower panel*: energy-intensity contours with respect to the baseline model described in Table 4.2, the arrows indicate the location of the blue-shifted absorption features (see Table 4.3 for more details).

be seen from the ratio of the spectral data against a simple power-law continuum reported in the upper panel of Fig. 4.1 (left), further complexities are present in the spectrum. In fact, besides the narrow emission line, two absorption features can be clearly seen at the observed energies of  $\sim 7$  keV and  $\sim 8$ –9 keV.

These absorption features are still present in the energy-intensity contour plot (described in §2.2) calculated with respect to the baseline model reported in Table 4.2 (see lower panel of Fig. 4.1, left), which suggests that their detection confidence levels should be higher than 99%.

Therefore, we performed a direct spectral fitting to the data, adding two further absorption lines to the baseline model. The detailed line parameters are reported in Table 4.3. The first absorption line is not resolved and is detected at a rest-frame energy of  $E = 7.26 \pm 0.03$  keV, with an equivalent width of  $EW = -31 \pm 15$  eV. Its detection confidence level is high: 99.9% from the standard F-test and 99% from extensive Monte Carlo simulations (see §2.3). The most intense spectral features expected at energies  $\geq 7$  keV are the inner K-shell resonances from Fe XXVI (see §1.2.3 for more details).

These lines are those of the Lyman series, that is: the Ly $\alpha$  (1s–2p) at E= 6.966 keV, the Ly $\beta$  (1s–3p) at E=8.250 keV, the Ly $\gamma$  (1s–4p) at E= 8.700 keV and the Ly $\delta$  (1s–5p) at E= 8.909 keV (see Table 1.1). However, the observed line energy is not consistent with any of these known atomic transition. If identified with Fe XXVI Ly $\alpha$  resonant absorption, the centroid of the line indicates a substantial blue-shift velocity of  $+0.041 \pm 0.003c$ .

The second absorption line is at a measured rest-frame energy of  $E=8.69^{+0.13}_{-0.08}$  keV. It is broader than the first one, with a resolved width of  $\sigma=390^{+270}_{-70}$  eV and an equivalent width of  $EW=-154 \pm 80$  eV. The detection confidence level of the line is higher than 99.9% with both the F-test and Monte Carlo simulations (see §2.3). Also in this case the energy of the line is not consistent with any known atomic transition. If identified with Fe XXVI Ly $\beta$ , the centroid of the line indicates a blue-shift velocity of  $\sim 0.05c$ . This value is comparable with that of the former line. However, if this is the case, the ratio of the EWs of the Fe XXVI Ly $\alpha$  and Ly $\beta$  would be  $\sim 0.2$ . This is at odd with what expected from theory. In fact, the ratio between these lines must be instead equal to  $\simeq 5$  (which is the ratio of their oscillator strengths: 0.42 and 0.08, respectively) and it could decrease to a minimum of  $\simeq 1$  when the lines are substantially saturated (see right panel of Fig. 5.10). This would suggest that the second broad absorption line could actually be a blend of different blue-shifted resonance lines, such as the Ly $\beta$ , Ly $\gamma$  and Ly $\delta$ . This scenario is supported by the fact that the energy resolution of the XIS instruments degrades with increasing energy (at  $E\sim 8-9$  keV it is of the order of  $FWHM\geq 200$  eV) and therefore these lines could not be separated properly.

To test whether a line blend is consistent with the data, we performed a fit adding to the baseline model four additional narrow absorption lines with energies fixed to the expected values for the Fe XXVI Lyman series and leaving their common energy shift as a free parameter. These lines provide a very good modelling of both absorption features at  $E>7$  keV, with a global  $\Delta\chi^2 = 42$  for five additional parameters. The probability of having these four absorption lines at these exact energies simply from random fluctuations is very low, about  $10^{-8}$ . Interestingly enough, their common blue-shift velocity is  $+0.041\pm 0.004c$ , consistent with the one calculated above for the first absorption line. The resultant EWs of the four Fe XXVI lines are:  $EW= -25 \pm 8$  eV for the Ly $\alpha$ ,  $EW= -35 \pm 14$  eV for the Ly $\beta$ ,  $EW= -27 \pm -16$  for the Ly $\gamma$  and  $EW> -60$  eV for the Ly $\delta$ . Their ratios are now consistent with the theoretical expectations and the fact that are close to unity suggests

possible saturation effects.

A more physically consistent modeling of these spectral features is discussed in §5.4, where we performed a fit using the Xstar photo-ionization code. The XIS-FI background analysis and the consistency check of the line parameters among the different XIS cameras are discussed in §4.3.7 and listed in Table 4.4. In §4.3.7 we also briefly report on a search for blue-shifted Fe K absorption lines on an XMM-Newton EPIC pn observation of the source.

### 4.3.3 3C 390.3

A power-law continuum (with  $\Gamma \simeq 1.6$ ) plus a narrow neutral Fe  $K\alpha$  emission line at 6.4 keV provide a good modeling of the 4–10 keV XIS-FI spectrum of this source (see Table 4.2). The broad-band spectral analysis of this Suzaku data set has been reported by Sambruna et al. (2009). From the spectral ratios and the energy-intensity contour plots (see description in §2.1) of Fig. 4.1 (right) there is indication of a possible narrow absorption feature at the observed energy of  $\sim 7.7$  keV, with a detection confidence level greater than 99%.

Therefore, we performed a direct spectral fitting to the data adding a further narrow (unresolved) absorption line to the baseline model. The rest-frame energy of the line is  $E=8.11 \pm 0.07$  keV and its equivalent width is  $EW=-32 \pm 16$  eV (see Table 4.3). The detection confidence level of the line is high: 99.9% from the standard F-test and 99.5% from extensive Monte Carlo simulations (see § 2.2). Also in this case the energy of the line is not consistent with any known atomic transition. However, the expected most intense lines from a highly ionized absorber at  $E \geq 7$  keV are the Fe XXVI Lyman series (see §1.2.3). If identified with Fe XXVI Ly $\alpha$  resonant absorption, the centroid of the line indicates a substantial blue-shift velocity of  $+0.150 \pm 0.005c$ .

A more physically consistent modeling of these spectral features is discussed in §5.4, where we performed a fit using the Xstar photo-ionization code. The XIS-FI background analysis and the consistency check of the line parameters among the different XIS cameras are discussed in §4.3.7 and listed in Table 4.4. In §4.3.7 we also briefly report on a search for blue-shifted Fe K absorption lines on an XMM-Newton EPIC pn observation of the source.

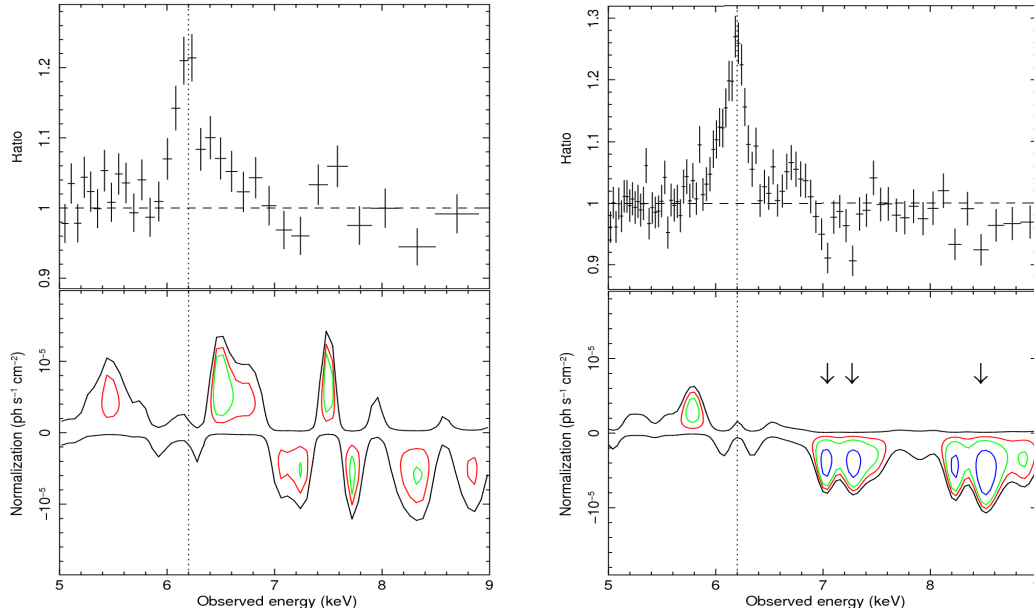


Figure 4.2: Suzaku XIS-FI spectra of 3C 120 (observations 3C 120a and 3C 120b on the *left* and *right*, respectively) zoomed in the 5–9 keV band to emphasize the Fe K complex. *Upper panel*: ratio against a power-law continuum. *Lower panel*: energy-intensity contours with respect to the baseline model described in Table 4.2, the arrows indicate the location of the blue-shifted absorption features (see Table 4.3 for more details).

#### 4.3.4 3C 120

The 4–10 keV XIS-FI spectrum of observation 3C 120a (see §4.2) is well modeled by a power-law continuum ( $\Gamma \simeq 1.75$ ) and a narrow neutral Fe  $K\alpha$  emission line at the rest-frame energy of 6.4 keV (see Table 4.2). As it can be seen from the ratio of the spectrum against a power-law continuum and the contour plots (see description in §2.1) with respect to the baseline model in the left part of Fig. 4.2 (upper and lower panels, respectively) there are no significant emission/absorption features in the Fe K band apart from the narrow Fe  $K\alpha$  emission line.

The 4–10 keV XIS-FI spectrum of observation 3C 120b (see §4.2) is well described by a power-law continuum (with  $\Gamma \simeq 1.6$ ) plus a narrow neutral Fe  $K\alpha$  emission line at  $E \simeq 6.4$  keV and a further narrow emission line at  $E \simeq 6.9$  keV (see Table 4.2). These overall results are in agreement with the spectral analysis of this data set previously reported by Kataoka et al. (2007). However, the spectral ratio and the energy-intensity contour plots (see description in §2.1) in the right part of Fig. 4.2 (upper and lower panels, respectively), suggest that further complexities might be present in the Fe K band. In particular, there

is evidence for absorption structures at the observed energies of  $\sim 7$ – $7.4$  keV and  $\sim 8$ – $9$  keV. The contours in the right part of Fig. 4.2 (lower panel) suggest that their detection confidence levels are higher than 99%.

A direct spectral fitting to the data revealed that the absorption structures at  $\sim 7$ – $7.4$  keV are actually composed of two narrow (unresolved,  $\sigma = 10$  eV) absorption lines. They are detected at rest-frame energies of  $E = 7.25 \pm 0.03$  keV and  $E = 7.54 \pm 0.04$  keV, respectively. Their equivalent widths are  $EW = -10 \pm 5$  eV and  $EW = -12 \pm 6$  eV, respectively. Their detection confidence level is  $\simeq 99\%$  from the F-test, which slightly reduces to 91% and 92% from Monte Carlo simulations, respectively (see §2.2 for a description of the method). The detailed line parameters are listed in Table 4.3. Their energies are not consistent with any known atomic transition. However, their location in the spectrum and their energy spacing suggest a possible identification with blue-shifted resonance absorption lines from Fe XXV  $K\alpha$  ( $1s^2-1s2p$ ) at  $E = 6.697$  keV and Fe XXVI  $Ly\alpha$  ( $1s-2p$ ) at  $E = 6.966$  keV (see Table 1.1). Their corresponding blue-shift velocities are substantial and consistent one with each other, i.e.  $+0.076 \pm 0.003c$  and  $+0.076 \pm 0.004c$ , respectively.

The second absorption structure that is observed at the energy of  $E \sim 8$ – $9$  keV is broad. If modeled with a simple inverted Gaussian, the resultant rest-frame energy is  $E = 8.76 \pm 0.12$  keV, with a broadening of  $\sigma = 360_{-120}^{+160}$  eV and equivalent width of  $EW = -50 \pm 13$  eV. Its detection confidence level is 99.9% from the F-test and slightly reduces to 99.8% with Monte Carlo simulations (see Table 4.3). Also in this case the energy of the line is not consistent with any known atomic transition. However, from the identification of two previous absorption lines, we can infer the possible presence of other resonance features from the same ionic species. In fact, the lower energy resolution of the instrument at those energies ( $FWHM \geq 200$  eV) and the spacing with respect to the first two lines suggest this broad absorption structure could actually be a blend of at least two further narrow resonance lines, namely Fe XXV  $K\beta$  ( $1s^2-1s3p$ ) at  $E = 7.88$  keV and Fe XXVI  $Ly\beta$  ( $1s-3p$ ) at  $E = 8.25$  keV (see Table 1.1).

To test the consistency of this global line identification, we performed a fit adding to the baseline model four narrow absorption lines with energies fixed to the expected values for these Fe XXV and Fe XXVI resonances and leaving their common energy shift as a free parameter. This provided a very good modeling of all the absorption structures

at  $E \geq 7$  keV, with a  $\chi^2$  improvement of 25 (for five additional parameters). The global probability to have these four absorption lines at these exact energies simply from random fluctuations is low, about  $4 \times 10^{-4}$ . Interestingly enough, their common blue-shift velocity is  $+0.076 \pm 0.003$ , completely consistent with what derived fitting each line separately. The resultant EWs of these lines are:  $EW = -10 \pm 5$  eV for the Fe XXV  $K\alpha$ ,  $EW = -11 \pm 8$  eV for the Fe XXV  $K\beta$ ,  $EW = -11 \pm 7$  eV for the Fe XXVI  $Ly\alpha$  and  $EW = -13 \pm 9$  eV for the Fe XXVI  $Ly\beta$ . Their relative ratios are of the order of unity, which would suggest possible saturation effects.

We checked for variability of the blue-shifted Fe K absorption lines between observations 3C 120a and 3C 120b. We added two narrow absorption lines to the base line model of observation 3C 120a, with energies fixed to those of observation 3C 120b, and calculated the 90% lower limits on the equivalent widths. The values are reported in Table 4.3. Unfortunately, the statistics of the data in the observation 3C 120a alone is not good enough to state if the lack of absorption lines was due to temporal variability.

A more physically consistent modeling of these spectral features is discussed in §5.4, where we performed a fit using the Xstar photo-ionization code. The XIS-FI background analysis and the consistency check of the line parameters among the different XIS cameras are discussed in §4.3.7 and listed in Table 4.4. In §4.3.7 we also briefly report on a search for blue-shifted Fe K absorption lines on an XMM-Newton EPIC pn observation of the source.

### 4.3.5 3C 382

The 4–10 keV XIS-FI spectrum of this source is well represented by a power-law continuum (with  $\Gamma \simeq 1.75$ ) plus a narrow neutral Fe  $K\alpha$  emission line at  $E=6.4$  keV and a further weak narrow emission line at  $E \simeq 6.9$  keV (see Table 4.2). A broad-band spectral analysis of this Suzaku data set will be reported in Ballo et al. (2010, in prep.). From the spectral ratio and the energy-intensity contour (see description §2.1) plots of Fig. 4.3 (left panel) it can be seen that an additional narrow weak emission line at the rest-frame energy of  $\sim 7$  keV is observable (we refer the reader to Ballo et al. 2010, in prep.). However, there are no significant absorption structures at energies  $\geq 7$  keV. We estimated the lower limit for the presence of a narrow blue-shifted absorption line at the indicative energy of 8 keV to be  $EW > -20$  eV (see Table 4.3).

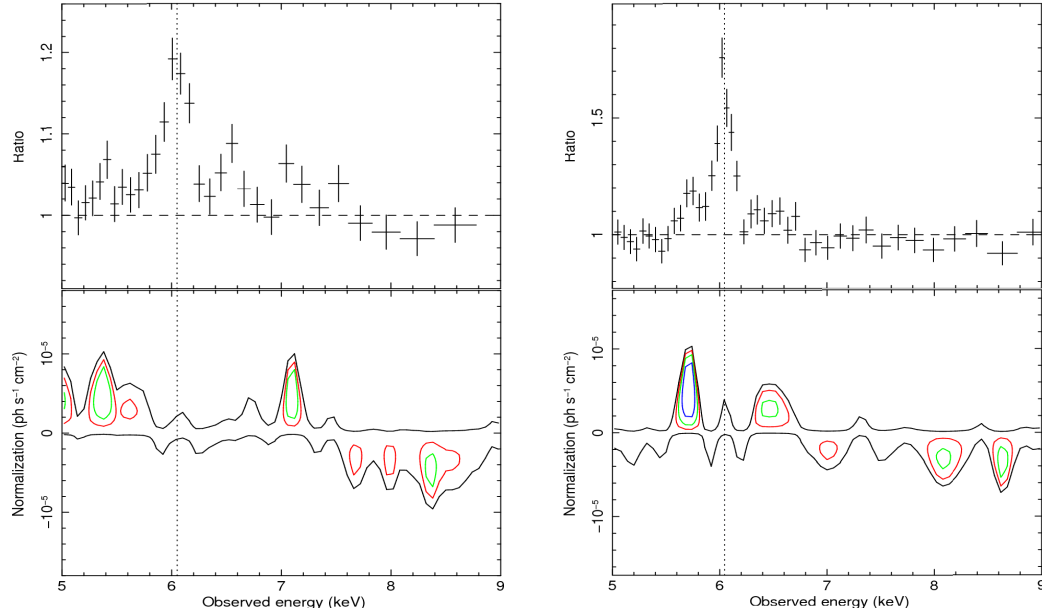


Figure 4.3: Suzaku XIS-FI spectra of 3C 382 (*left*) and 3C 445 (*right*) zoomed in the 5–9 keV band to emphasize the Fe K complex. *Upper panel*: ratio against a power-law continuum (with a neutral absorption component for 3C 445). *Lower panel*: energy-intensity contours with respect to the baseline model described in Table 4.2.

#### 4.3.6 3C 445

The 4–10 keV XIS-FI spectrum of this source is affected by substantial absorption by neutral/mildly-ionized material intrinsic to the galaxy. The baseline model is composed by a power-law continuum (with  $\Gamma \simeq 1.6$ ) absorbed by neutral material ( $N_H \simeq 2 \times 10^{23} \text{ cm}^{-2}$ ) and a narrow neutral Fe K $\alpha$  emission line at 6.4 keV (see Table 4.2). The broad-band spectral analysis of this Suzaku data set will be reported in Braitto et al. (2010, in prep.). From the spectral ratios and the energy-intensity contour plots of Fig. 4.3 (right panel) there is indication for a possible narrow weak emission feature red-ward to the Fe K $\alpha$  line (we refer the reader to Braitto et al. 2010, in prep.) but there is no evidence for significant absorption features at  $E \geq 7$  keV. We estimated the lower limit for the presence of a narrow blue-shifted absorption line at the indicative energy of 8 keV to be  $\text{EW} > -45$  eV (see Table 4.3).

Table 4.3: Absorption line parameters. Column 1: source name. Column 2: absorption line identification,  $K\alpha/K\beta$  refer to K-shell transitions from Fe XXV,  $Ly\alpha/Ly\beta/Ly\gamma/Ly\delta$  refer to the Fe XXVI Lyman series and the “-” indicates a possible line blending (see text for more details). Column 3: absorption line rest-frame (observer frame) energy. Column 4: line width. Column 5: line equivalent width. Column 6:  $\chi^2$  improvement adding the absorption line to the baseline model reported in Table 2 and relative number of new parameters. Column 7: detection confidence level from the F-test. Column 8: detection confidence level from extensive Monte Carlo simulations. Errors are at the  $1\sigma$  level.

| Source   | ID                          | E<br>(keV)                   | $\sigma$<br>(eV)    | EW<br>(eV)    | $\Delta\chi^2/\Delta\nu$ | F-test        | MC            |
|----------|-----------------------------|------------------------------|---------------------|---------------|--------------------------|---------------|---------------|
| 3C 111   | $Ly\alpha$                  | $7.26(6.92)^{+0.03}_{-0.03}$ | $10^a$              | $-31 \pm 15$  | 13/2                     | 99.9%         | 99%           |
|          | $Ly\beta-Ly\gamma-Ly\delta$ | $8.69(8.29)^{+0.13}_{-0.08}$ | $390^{+270}_{-70}$  | $-154 \pm 80$ | 40/3                     | $\geq 99.9\%$ | $\geq 99.9\%$ |
| 3C 390.3 | $Ly\alpha$                  | $8.11(7.68)^{+0.04}_{-0.04}$ | $10^a$              | $-32 \pm 16$  | 14.6/2                   | 99.9%         | 99.5%         |
| 3C 120a  | ...                         | $\equiv 7.25^a$              | $10^a$              | $> -29^b$     | ...                      | ...           | ...           |
|          | ...                         | $\equiv 7.54^a$              | $10^a$              | $> -32^b$     | ...                      | ...           | ...           |
|          | ...                         | $\equiv 8.76^a$              | $500^a$             | $> -160^b$    | ...                      | ...           | ...           |
| 3C 120b  | $K\alpha$                   | $7.25(7.02)^{+0.03}_{-0.03}$ | $10^a$              | $-10 \pm 5$   | 9.4/2                    | 99%           | 91%           |
|          | $Ly\alpha$                  | $7.54(7.30)^{+0.04}_{-0.04}$ | $10^a$              | $-12 \pm 6$   | 10/2                     | 99.3%         | 92%           |
|          | $K\beta-Ly\beta$            | $8.76(8.48)^{+0.12}_{-0.12}$ | $360^{+160}_{-120}$ | $-50 \pm 13$  | 18/3                     | 99.9%         | 99.8%         |
| 3C 382   | ...                         | $\equiv 8^a$                 | $10^a$              | $> -20^b$     | ...                      | ...           | ...           |
| 3C 445   | ...                         | $\equiv 8^a$                 | $10^a$              | $> -45^b$     | ...                      | ...           | ...           |

(a) Parameter held fix during the fit.

(b) Equivalent width lower limit at the 90% level.

#### 4.3.7 XIS-FI background and consistency checks

The background level for these bright sources in the 7–10 keV band is negligible, always less than 10% of the source counts (see Table 4.1). However, it is important to note that the XIS cameras have a few instrumental background emission lines at energies greater than 7 keV, the most intense of which is the Ni  $K\alpha$  at  $E=7.47$  keV (Yamaguchi et al. 2006). These lines originate from the interaction of the cosmic rays with the sensor housing and electronics and this causes also their intensity to be slightly dependent on the location on the detector. Therefore, the selection of the background on a region of the CCD where the intensity of the lines is slightly higher/lower than that of those actually on the source extraction region can possibly induce spurious absorption/emission lines in the background subtracted spectrum. We performed some tests to exclude such eventuality.

First, since the XIS background emission lines are present at specific energies (see Table 1 of Yamaguchi et al. 2006), we checked that the observed energies of the absorption

lines are indeed not consistent with those values (see Table 4.3). If the background is not subtracted from the source spectrum, these lines would show up as weak emission lines. Therefore, second, we checked that the intensity of the emission lines in the background and in the source spectrum without background subtraction are indeed consistent. Finally, third, we inspected that the values of the energy and equivalent width of the absorption lines at  $E > 7$  keV in the source spectrum (see Table 4.3) are consistent (within the errors) with or without background subtraction. These tests assure that our results on the absorption lines detected in the 7–10 keV band are indeed not affected by any contamination from the XIS instrumental background.

In Table 4.4 we report a consistency check of the absorption lines detected in 3C 111, 3C 390.3 and 3C 120b among the different XIS instruments. The values have been derived by independently fitting the XIS 0, XIS 2 (when available), XIS 3 and XIS-BI spectra. The lower S/N of the separate XIS spectra does not allow to clearly detect the absorption lines in each spectrum. However, the parameters are always consistent with those reported in Table 4.3. This demonstrates that the line parameters derived from the different instruments are indeed consistent one with each other and assures the absence of any systematics induced by the combination of the XIS-FI spectra.

Finally, we have analyzed the XMM-Newton EPIC pn observations of the BLRGs in which we have detected the blue-shifted Fe K absorption lines for a consistency check. However, we did not detect any significant blue-shifted absorption line at  $E > 6.4$  keV. We could only place lower limits in the EWs of the lines, fixing their energies to the Suzaku best-fit values (see Table 4.3). In particular, for 3C 111 we have found  $EW > -30$  eV for the first absorption line at  $E \simeq 7.26$  keV and  $EW > -130$  eV for the second line at  $E \simeq 8.69$  keV. For 3C 390.3 we found  $EW > -25$  eV for the line at  $E \simeq 8.11$  keV. Finally, for 3C 120, we derived  $EW > -12$  eV,  $EW > -15$  eV and  $EW > -60$  eV for the absorption lines at  $E \simeq 7.25$  keV,  $E \simeq 7.54$  eV and  $E \simeq 8.76$  keV, respectively. Comparing these values with the EWs in Table 4.3 we can see that they are consistent and the S/N of the EPIC pn data are just at the limit for the possible detection of the lines. However, the non-detection could be partially due to the lower S/N of the pn observations or to intrinsic line variability (in particular for 3C 390.3), given that the XMM-Newton and Suzaku observations were not simultaneous.

Table 4.4: Consistency checks for the absorption lines. Column 1: source name. Column 2: Suzaku instrument; broad stands for broad band fit, using both XIS-FI and PI. Column 3: Absorption line rest-frame energy. Column 4: line width. Column 5: line equivalent width. Errors are at the  $1\sigma$  level.

| Source          | Inst            | E<br>(keV)             | $\sigma$<br>(eV)    | EW<br>(eV)         |
|-----------------|-----------------|------------------------|---------------------|--------------------|
| 3C 111          | XIS 0           | $7.27 \pm 0.04$        | 10                  | $-36 \pm 22$       |
|                 |                 | $8.80 \pm 0.14$        | $380^{+540}_{-130}$ | $-140 \pm 40$      |
|                 | XIS 3           | $7.24 \pm 0.02$        | 10                  | $-34 \pm 19$       |
|                 |                 | $8.61 \pm 0.09$        | $390^{+180}_{-110}$ | $-170^{+30}_{-40}$ |
|                 | XIS-BI          | $\equiv 7.26^a$        | 10                  | $> -60^b$          |
|                 | $\equiv 8.69^a$ | $\equiv 390^a$         | $> -190^b$          |                    |
| 3C 390.3        | XIS 0           | $8.06 \pm 0.07$        | 10                  | $> -50^b$          |
|                 | XIS 3           | $8.11 \pm 0.03$        | 10                  | $-32 \pm 19$       |
|                 | XIS-BI          | $\equiv 8.11^a$        | 10                  | $> -50^b$          |
| 3C 120b         | XIS 0           | $7.24^{+0.10}_{-0.16}$ | 10                  | $> -40^b$          |
|                 |                 | $7.58 \pm 0.08$        | 10                  | $> -50^b$          |
|                 |                 | $8.83 \pm 0.18$        | $285^{+220}_{-130}$ | $-70 \pm 40$       |
|                 | XIS 2           | $7.25 \pm 0.05$        | 10                  | $> -46^b$          |
|                 |                 | $7.51 \pm 0.07$        | 10                  | $> -42^b$          |
|                 |                 | $8.79^{+0.25}_{-0.29}$ | $312^{+339}_{-264}$ | $-55 \pm 33$       |
|                 | XIS 3           | $7.24 \pm 0.05$        | 10                  | $> -43^b$          |
|                 |                 | $7.65 \pm 0.10$        | 10                  | $> -48^b$          |
|                 |                 | $\equiv 8.76^a$        | $\equiv 360^a$      | $> -70^b$          |
|                 | XIS-BI          | $\equiv 7.25^a$        | 10                  | $> -40^b$          |
| $\equiv 7.54^a$ |                 | 10                     | $> -48^b$           |                    |
| $\equiv 8.76^a$ |                 | $\equiv 360^a$         | $> -71^b$           |                    |

(a) Parameter held fix during the fit.

(b)Equivalent width lower limit at the 90% level.

## Chapter 5

# Photo-ionization modelling

### 5.1 The Spectral Energy Distribution

The Spectral Energy Distribution (SED) describes the power or flux emitted by the object at each specific energy across all the electromagnetic spectrum. The integral over all energies (or frequencies) gives the total bolometric luminosity ( $L_{bol}$ , in erg/s) emitted by the object. The shape of the SED in different energy bands depends on the emission processes which dominate the production of that radiation. In the case of AGN, one can have: the power-law synchrotron from the relativistic jet in the radio band, the thermal black body from the accretion disk in the optical-UV, the inverse Compton in X-ray band, and so on.

In particular, the X-ray emission of radio-quiet AGN is supposed to come from inverse Compton of optical-UV seed photons in a hot corona surrounding the accretion disk. This component is represented by a power-law continuum with a typical photon index  $\Gamma \simeq 2$  (Haardt & Maraschi 1991), where  $F_E \simeq E^{-\Gamma}$  ph s<sup>-1</sup> cm<sup>-2</sup> keV<sup>-1</sup> (see §1.2.1). In fact, as already stated by Elvis et al. (1994), a single, nearly horizontal power-law is a good representation of the typical SED of AGN from the IR to the X-rays. However, from a phenomenological point of view, some further weak deviations can be observed, such as (see Fig. 5.1):

- The *millimeter break*, which is a drop in the power output in the sub-millimeter band. The sources in which the drop is only  $\sim 2$  orders of magnitude are called “radio-loud”, instead those with a larger drop of  $\sim 5$ – $6$  decades are called “radio-quiet”. The latter are far more common, about 10 times more than the former.

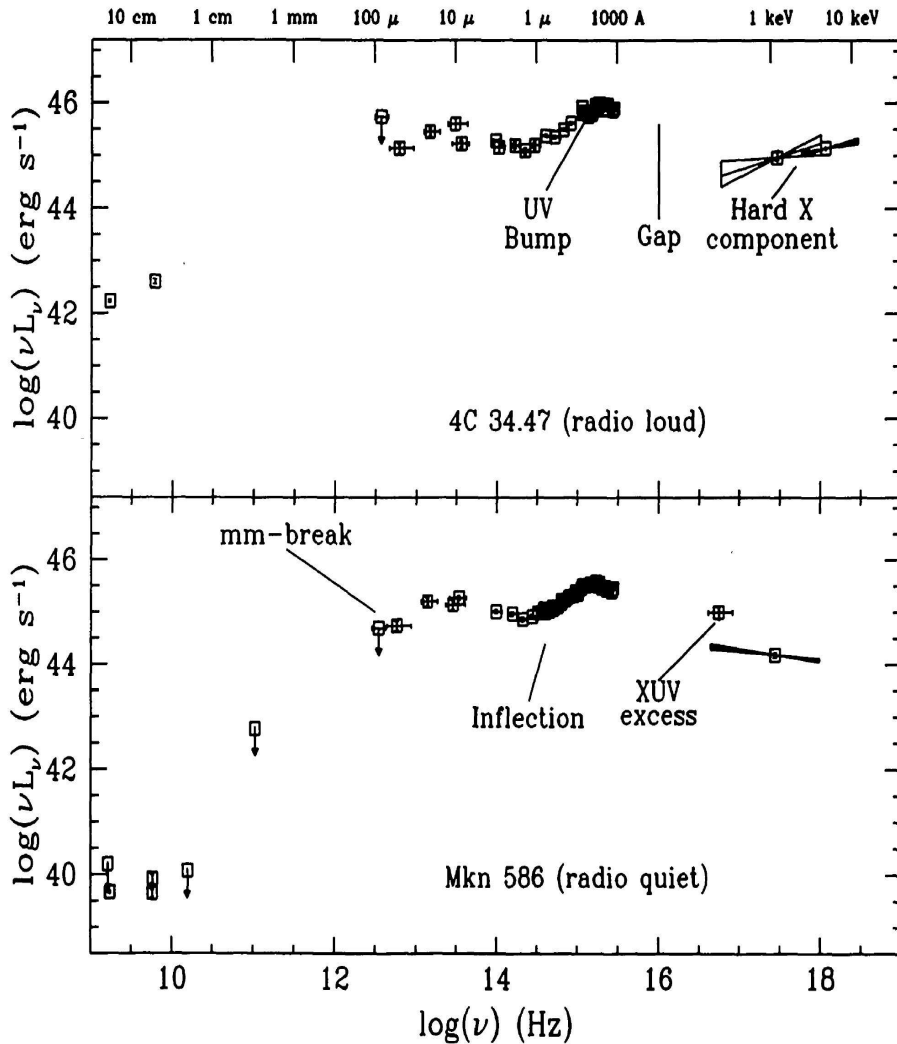


Figure 5.1: Examples of a radio-loud (4C 34.47, *top*) and a radio-quiet (Mrk 586, *bottom*) observed SEDs, illustrating the typical continuum features (from Elvis et al. 1994).

- The *UV bump* (or big blue bump), which is a rise of the optical-UV continuum above the IR. It is often interpreted in terms of thermal emission from the putative accretion disk. In particular, the beginning of the bump is marked by an inflection between 1 and 1.5  $\mu$ m, which is called the *near-IR inflection point*. This is the only continuum feature whose wavelength is well defined and it will be important for the successive calculation of the mean SED.

In the following, we will focus on the radio-quiet type 1 sources of our sample, because they constitute the majority of the objects studied in this work. The intrinsic SED of

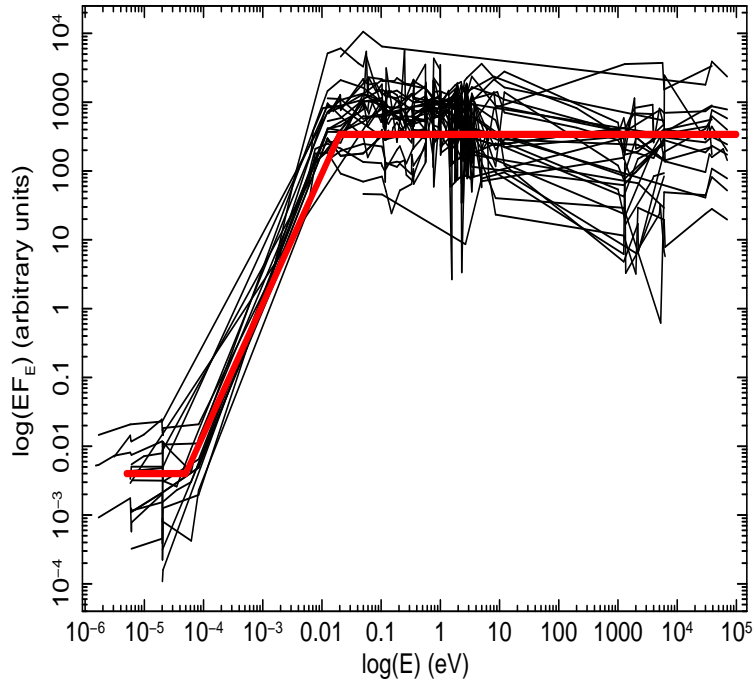


Figure 5.2: SEDs of the radio-quiet type 1 AGN normalized at the near-IR inflection point (black lines) and the resultant mean SED (red line).

the radio-quiet type 2 sources is not known very well because their spectra can be heavily affected by obscuration and stellar contamination. Therefore, we will make the reasonable assumption that their central engine is analogous to that in type 1s and that the overall shape of their intrinsic SED is the same.

A good knowledge of the SED of each source is important for the successive photoionization modelling of the Fe K absorbers with the Xstar code. However, given the large number of sources (44 for the radio-quiet sample), it would be too much time consuming to calculate an Xstar grid for each case ( $\sim 6 \times 10^5$  s each). Moreover, the observed SEDs have been taken by different instruments at different times and therefore the sources could have been caught in different emission states and also there are cases with very few flux measures available. Thus, we need to find a reasonable approximation of the typical SED to generate the Xstar grid which will be used to fit the blue-shifted Fe K absorption lines.

Therefore, we derived a mean SED of the radio-quiet type 1 sources as follows: we downloaded the observed SEDs of all the 34 type 1 objects (listed in Appendix A, Table A.1) from the NED database<sup>1</sup>. These are composed by a collection of flux values

<sup>1</sup><http://nedwww.ipac.caltech.edu>

Table 5.1: Mean SED for type 1 radio-quiet AGN of our sample.

| Interval | E (eV)                                | $\Gamma$ | $\alpha$ |
|----------|---------------------------------------|----------|----------|
| 1        | $5 \times 10^{-6} - 5 \times 10^{-5}$ | 2        | -1       |
| 2        | $5 \times 10^{-5} - 2 \times 10^{-2}$ | 0.1      | 0.9      |
| 3        | $2 \times 10^{-2} - 1 \times 10^{+5}$ | 2        | -1       |

measured at energies from radio to  $\gamma$ -rays. The flux values at each energy were taken at different epochs by different instruments with also some scattering due to the source variability and instrument cross-calibration uncertainties. Therefore, we first calculated the mean flux for each energy point and derived a mean SED for each object. Then, we followed the approach of Elvis et al. (1994) and normalized all SEDs to the same arbitrary flux value at the near-IR inflection point at  $\simeq 1.25 \mu\text{m}$  ( $E \simeq 1 \text{ eV}$ ), see Fig. 5.2. Interestingly enough, the overall shape of the SEDs is similar for all the sources (apart from some level of scattering). Finally, we averaged again the flux values in each energy point for all the SEDs and derived a single mean SED. This was further smoothed to only four interesting points and then interpolated with power-laws (see Fig. 5.2). This well represents the typical phenomenological SED of type 1 AGN. As reported in Table 5.1, this could be divided in three main intervals: from radio to millimetric ( $\Gamma \simeq 2$ ), from millimetric to IR ( $\Gamma \simeq 0.1$ ) and from IR to X-rays ( $\Gamma \simeq 2$ ). We remind that the relation between the photon index ( $\Gamma$ ) and spectral index ( $\alpha$ ) is  $\alpha = -\Gamma + 1$ .

In Fig. 5.3 we compare our mean SED with that proposed by Mathews & Ferland (1987) and a simple power-law with  $\Gamma = 2$ . Mathews & Ferland (1987) estimated the SED of “classical” quasars by combining direct observations and inferences based on the emission-line spectra. They did not consider the radio properties, as they were mainly interested in constraining the higher energy part, from the IR to the  $\gamma$ -ray bands. Mathews & Ferland (1987) tried to model all the major continuum component of the SED. In fact, there is a bump in the optical-UV band, a steep soft X-ray excess, a typical X-ray continuum (assumed with  $\Gamma = 1.7$ ) and a high energy break in the hard X-rays (see Fig. 5.3).

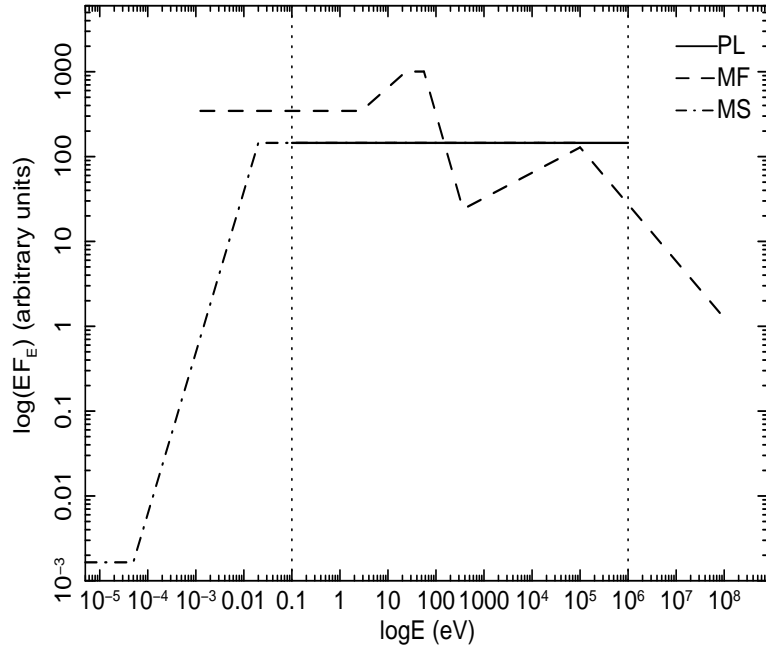


Figure 5.3: Comparison of some proposed SEDs for radio-quiet type 1 AGN: a simple power-law with  $\Gamma = 2$  (solid line, PL), the SED from Mathews & Ferland (1987) (dashed line, MF) and our mean SED reported in Table 5.1 (dash-dot line, MS). The vertical dotted lines delimit the input energy band for Xstar (from 0.1 eV to  $10^6$  eV). It is important to note that the MS SED stops at  $10^5$  eV and is assumed to be null for higher energies.

## 5.2 Detailed photo-ionization modelling

Due to the intense luminosity from the central source, the absorbers observed in the inner regions of AGN are mainly photo-ionized by this radiation instead of being locally ionized by thermal collisions (e.g. Kinkhabwala et al. 2002; Crenshaw et al. 2003). In this way, they can reach very high levels of ionization maintaining a relatively low temperatures of  $T \sim 10^5 - 10^6$  K (e.g. Nicastro et al. 1999; Bianchi et al. 2005a).

Therefore, in order to properly parametrize the blue-shifted Fe K absorption lines that we have detected in the X-ray spectra of several AGN (see Table A.2 in Appendix A and Table 4.3), we need to study the strength of these lines for different physical conditions and to derive realistic models to directly fit the data.

### 5.2.1 The Xstar code

We used the Xstar code (version 2.1kn8), which allows to calculate the physical conditions and the spectra of photo-ionized gases, specifically developed for X-ray astronomy

(Kallman & Bautista 2001). The code assumes that a spherical gas shell surrounds the source of ionizing radiation and it calculates the transfer of the incident radiation into the gas and the ionization balance. It can be used also to derive detailed photo-ionization grids (containing all the main resonance lines and photoelectric edges) to directly model the X-ray data. The input parameters are: the shape and intensity of the incident continuum (between 0.1 eV and  $10^6$  eV), the elemental abundances in the gas, its density, pressure, temperature and turbulent velocity. The Xstar code takes into account the main X-ray transitions from all the relevant atoms, such as: H, He, Ca, N, O, Mg, Si, S, Ar, Ca, Fe, Ni.

The main parameters used to describe the physical state of the gas are the equivalent hydrogen column density  $N_H$  (in units of H atoms  $\text{cm}^{-2}$ ) and the ionization parameter. We use the standard definition of the ionization parameter  $\xi = L_{ion}/nr^2$  (in units of  $\text{erg s}^{-1} \text{cm}$ ) (e.g. Tarter, Tucker & Salpeter 1969), where  $L_{ion}$  is the ionizing luminosity between 1 Ryd and 1000 Ryd (1 Ryd is the energy needed to ionize the Hydrogen atom from the ground level, i.e.  $E=13.6$  eV),  $n$  is the number density of the material and  $r$  is the distance from the central source. This expression directly derives from the ionization balance equations and essentially represents the ratio between the density of the ionizing photons and the density of the absorbing material.

### 5.2.2 Curve of growth analysis of the Fe K-shell absorption lines

We performed a curve of growth analysis of the most intense Fe XXV and Fe XXVI K-shell absorption lines. We used the line parameters discussed in §1.2.3 and reported in Table 1.1. This study allows us to have a quantitative estimate on the dependence of the EW of the lines on the different values of the main physical parameters describing the absorbing material, such as the ionization parameter ( $\xi$ ), the column density ( $N_H$ ) and the velocity broadening parameter ( $b$ ).

We carried out extensive Xstar simulations to derive the expected iron ionic abundances. We assumed a power-law ionizing continuum with  $\Gamma = 2$ , which is the typical value for type 1 AGN (see §5.1) in the X-rays and is essentially equivalent to our mean phenomenological SED in the input energy band for Xstar (the only difference being that the mean SED is assumed null for  $E > 10^5$  keV, see Fig. 5.3). We assumed standard solar abundances and in particular an iron abundance of  $A_{\text{Fe}} = 3.16 \times 10^{-5}$

relative to Hydrogen (Grevesse et al. 1996). We assumed a constant density of the gas, with the typical value used for the Broad Line Region of  $n = 10^{10} \text{ cm}^{-3}$  (e.g. Crenshaw et al. 2003). We did not fix the gas temperature but left the code to calculate the thermal equilibrium. However, the resultant temperatures were always consistent with the typical value of  $T \sim 10^6 \text{ K}$  (e.g. Nicastro et al. 1999; Bianchi et al. 2005a). Finally, we limited the treatment to a Compton thin absorber ( $N_H \leq 10^{24} \text{ cm}^{-2}$ ), distributed on a geometrically thin shell ( $\Delta r/r = N_H \xi^{1/2} (Ln)^{-1/2} < 1$ ).

To calculate the equivalent width of the lines we followed the approach of Nicastro et al. (1999) and Bianchi et al. (2005a). The EW of a resonant absorption line is defined as:

$$\text{EW} = \int_0^{+\infty} (1 - e^{-\tau_\nu}) d\nu, \quad (5.1)$$

where  $\tau_\nu$  is the dimensionless frequency specific optical depth of the considered transition:

$$\tau_\nu = \int_0^L \alpha_\nu ds = n_l L \frac{\pi e^2}{m_e c} f_{lu} \Phi(\nu). \quad (5.2)$$

In the above equation  $\alpha_\nu$  is the absorption coefficient at the frequency  $\nu$ ,  $n_l$  is the number density of ions of the given element that populates the lower level of the transition considered,  $L$  is the linear extension of the material along the line of sight,  $f_{lu}$  is the oscillator strength of the electron transition from the lower to the upper level and  $\Phi(\nu)$  is the normalized Voigt profile. We then directly integrated the Voigt profile of the line, which can be written as (e.g Rybicki & Lightman 1979):

$$\Phi(\nu) = \frac{1}{\Delta\nu_D \sqrt{\pi}} H(a, u), \quad (5.3)$$

where  $H(a, u)$  is the Voigt function:

$$H(a, u) = \frac{a}{\pi} \int_{-\infty}^{+\infty} \frac{e^{-y^2}}{a^2 + (u - y)^2} dy. \quad (5.4)$$

where  $a = \gamma/(4\pi\Delta\nu_D)$  and  $u = (\nu - \nu_0)/\Delta\nu_D$ . This is essentially a convolution of the Gaussian and Lorentzian line profiles. The Gaussian profile, which represents the

core of the line, depends on the Doppler broadening  $\Delta\nu_D = \nu_0 b/c$ , where  $\nu_0$  is the rest-frame specific frequency of the transition and  $b$  is the velocity broadening parameter. The latter is the square root of the quadratic sum of the thermal velocity of the ions,  $v_{\text{th}}^2 = 2kT/m$ , where  $T$  is the gas temperature and  $m$  the ion mass, and their turbulent velocity (dispersion) along the line of sight,  $v_{\text{tu}}$ :

$$b = (v_{\text{th}}^2 + v_{\text{tu}}^2)^{1/2}. \quad (5.5)$$

For a highly ionized gas in photo-ionization equilibrium the temperature is of the order of  $T \sim 10^6$  K and the opacity is dominated by Fe ions. We can estimate that the thermal velocity of the gas is  $< 20$  km/s and its contribution is therefore always negligible (less than 20%) for values of the turbulent velocity of  $\sim 100$ – $1000$  km/s (e.g. Nicastro et al. 1999; Bianchi et al. 2005a). Therefore, the dominant term in the velocity broadening is given by the turbulence and this is also strengthened from the dependence  $b \propto v_{\text{tu}}$ , instead of  $b \propto T^{1/2}$ . The Lorentzian profile, instead, contributes to the broadening of the line wings and is a function of the natural broadening parameter  $\gamma$ , which in turn depends on the Einstein coefficient for spontaneous emission for the transition considered,  $A_{ul}$  (e.g. Rybicki & Lightman 1979) (see values in Table 1.1).

The curve of growth of the Fe XXV He $\alpha$  and Fe XXVI Ly $\alpha$  lines for a fixed ionization parameter  $\log\xi = 3.5$  erg s $^{-1}$  cm are reported in Fig. 5.4. All calculations were performed separately for each line component listed in Table 1.1 and only their final EWs were summed. For relatively low column densities, between  $\sim 10^{20}$  cm $^{-2}$  and  $\sim 10^{22}$  cm $^{-2}$ , the curves follow a linear relation and the increase in EW is proportional to  $N_H$  ( $\text{EW} \propto \tau \propto N_H f_{lu}$ ). For larger columns, instead, saturation effects become more intense and the increase in EW is lower. However, here we can clearly see the effects of increasing the velocity broadening. The line core broadens and the column densities needed to saturate the line are larger. Therefore, the linear branch of the curve of growth spans over a larger range of  $N_H$  before saturating and the lines can reach higher EWs. In other words, for a fixed value of  $N_H$ , the resultant line EW is greater if the velocity parameter is higher. We can see that for column densities of  $N_H \sim 10^{23}$ – $10^{24}$  cm $^{-2}$ , the EW of both lines can reach values up to  $\sim 100$  eV for velocities of  $\sim 1000$  km/s. Given that the temperature of the photo-ionized gas remains almost constant at the value of  $T \sim 10^6$  K, which corresponds to a thermal velocity of less than  $\sim 20$  km/s, the broadening

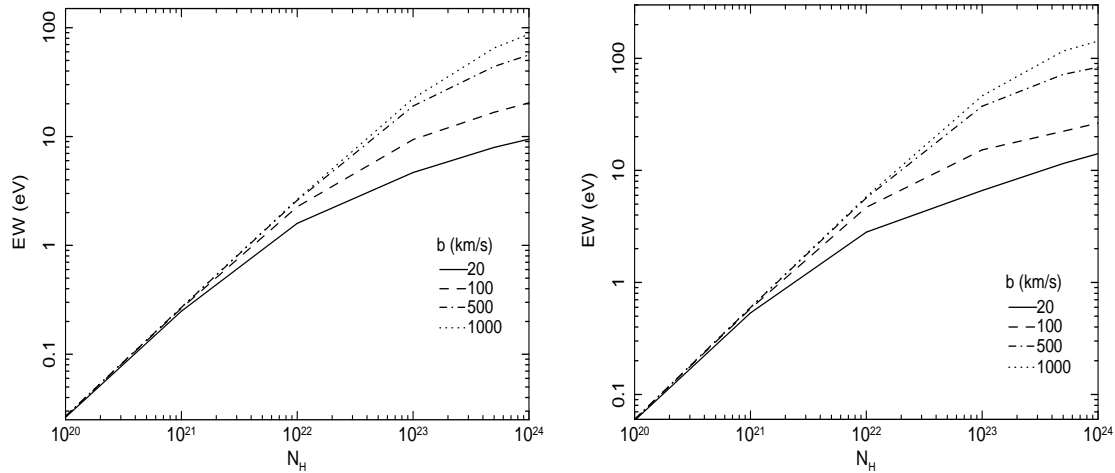


Figure 5.4: Curve of growth for the Fe XXV He $\alpha$  (r + i) (*left panel*) and Fe XXVI Ly $\alpha$  (r<sub>1</sub> + r<sub>2</sub>) (*right panel*) lines, for different values of the velocity broadening parameter  $b$ . The ionization parameter is fixed to  $\log\xi=3.5$  erg s<sup>-1</sup> cm.

is essentially dominated by an increase in turbulent velocity. We stress here that turbulent velocities as high as  $\sim 100$ – $1000$  km/s are not unrealistic, since many Broad-line AGN show absorption lines broadened by similar values (e.g. Crenshaw et al. 2003) and are easily reached in gas moving close to the SMBH (e.g. Nicastro et al. 1999; Bianchi et al. 2005a).

The EWs of the lines with respect to the ionization parameter and for different column densities are shown in Fig. 5.5 to Fig. 5.8 for Fe XXV, He $\alpha$  and He $\beta$ , and Fe XXVI, Ly $\alpha$  Ly $\beta$ , respectively (see the different line parameters in Table 1.1). The peak of the distributions depend on the iron ions abundance for different ionization states. In fact, the maximum in EWs for Fe XXV lines is around  $\log\xi \simeq 3$  erg s<sup>-1</sup> cm and that for the Fe XXVI lines is shifted to slightly higher values, at about  $\log\xi \simeq 3.5$  erg s<sup>-1</sup> cm. Moreover, the distribution of the Fe XXV is narrow, with a sharp rise and decline, and drops almost to zero for  $\log\xi > 4$  erg s<sup>-1</sup> cm. That of Fe XXVI, instead, is broad, with a tail extending towards higher ionization levels, up to  $\log\xi \sim 5$ – $6$  erg s<sup>-1</sup> cm. It is also important to note the rise of the EWs for higher velocity parameters, which is equivalent to say, for higher turbulent velocities. In fact, for an increase of a factor of 10 in  $b$ , from 100 km/s to 1000 km/s (see left and right panels of Fig. 5.5 to Fig. 5.8), the resultant EWs at the peak is a factor of  $\sim 5$  higher. This, again, demonstrates that the increase in turbulent velocity is a very efficient mechanism to broaden the line profile, effectively reducing the columns needed for the line to reach higher EWs before saturating.

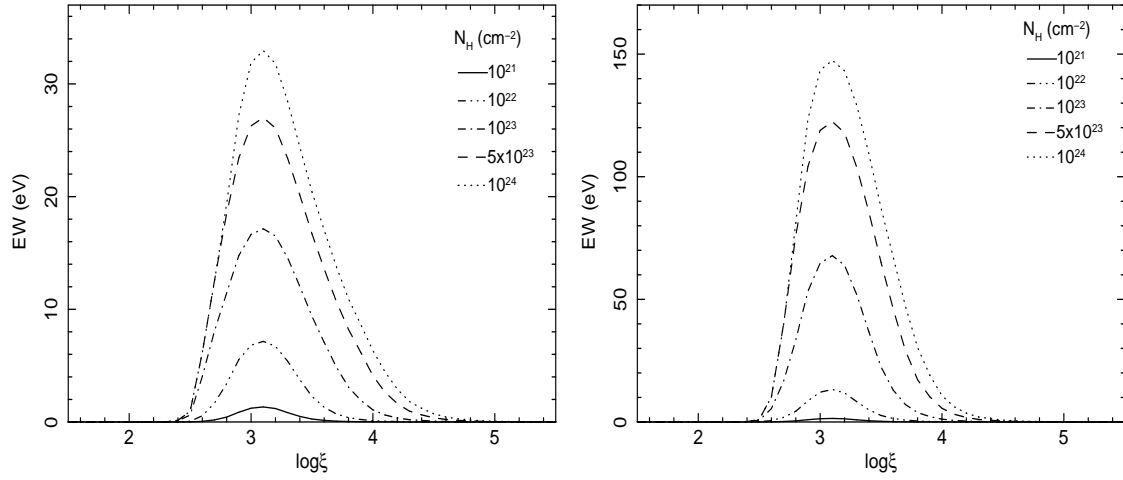


Figure 5.5: Estimated EW of the Fe XXV He $\alpha$  (r + i) transition as a function of  $\log\xi$ , for different column densities. The velocity broadening is  $b = 100$  km/s (*left panel*) and  $b = 1000$  km/s (*right panel*).

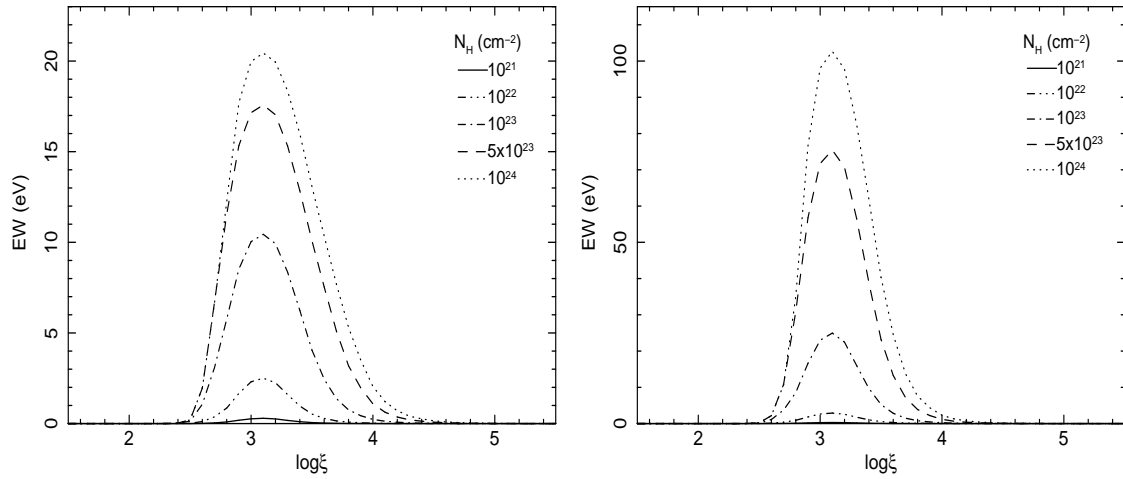


Figure 5.6: Estimated EW of the Fe XXV He $\beta$  (r + i) transition as a function of  $\log\xi$ , for different column densities. The velocity broadening is  $b = 100$  km/s (*left panel*) and  $b = 1000$  km/s (*right panel*).

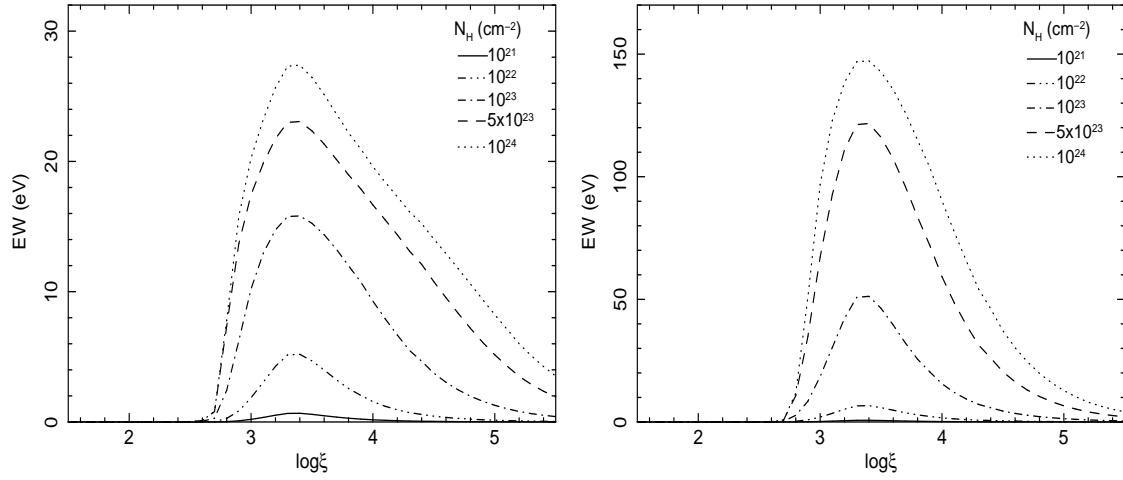


Figure 5.7: Estimated EW of the Fe XXVI Ly $\alpha$  ( $r_1 + r_2$ ) transition as a function of  $\log\xi$ , for different column densities. The velocity broadening is  $b = 100$  km/s (*left panel*) and  $b = 1000$  km/s (*right panel*).

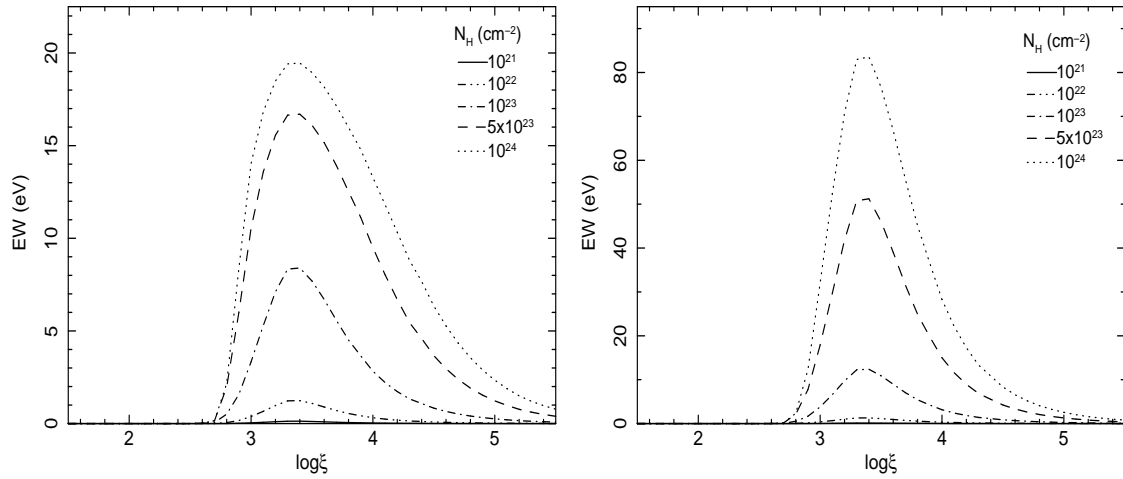


Figure 5.8: Estimated EW of the Fe XXVI Ly $\beta$  ( $r_1 + r_2$ ) transition as a function of  $\log\xi$ , for different column densities. The velocity broadening is  $b = 100$  km/s (*left panel*) and  $b = 1000$  km/s (*right panel*).

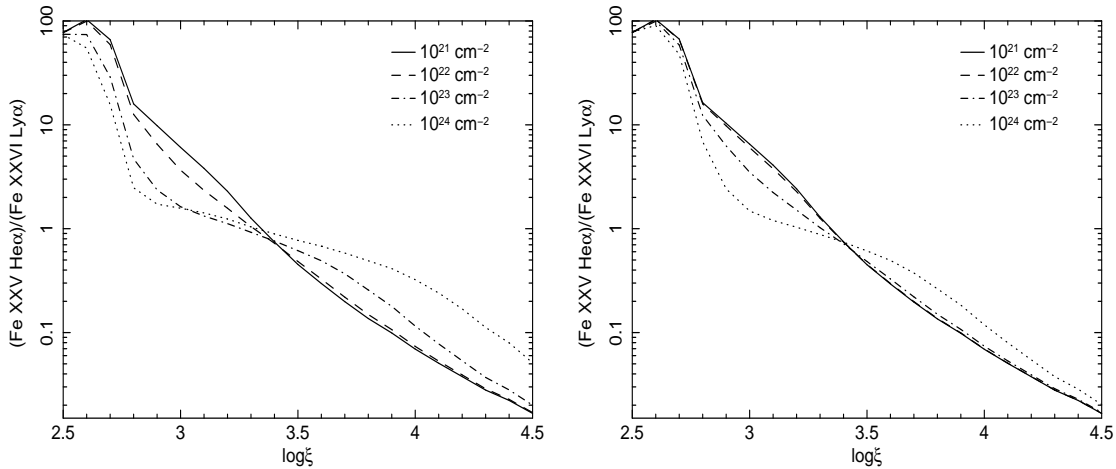


Figure 5.9: Ratio of the EWs of the Fe XXV He $\alpha$  ( $r + i$ ) and Fe XXVI Ly $\alpha$  ( $r_1 + r_2$ ) lines as a function of  $\log\xi$ , for different column densities. The velocity broadening is  $b = 100$  km/s (*left panel*) and  $b = 1000$  km/s (*right panel*).

In Fig. 5.9 we report the ratios of the EWs of the Fe XXV He $\alpha$  and Fe XXVI Ly $\alpha$  lines as a function of the ionization parameter and for different column densities. We can note that for a ionization level of  $\log\xi \sim 3.5$  erg s $^{-1}$  cm the ratio is  $\sim 1$  and we expect to observe both lines in the spectrum with similar EWs. Instead, for lower or higher values of the ionization parameter, the Fe XXV line or the Fe XXVI line respectively dominate. In this case, we expect to observe only one of these two strong lines in the spectrum. We can also see that the ratio is more sensitive on the column density rather than on the velocity parameter (see left and right panels of Fig. 5.9). In fact, for high column densities, the ratio tends to approach unity for a wider range of ionization levels. In the limit of  $N_H \sim 10^{24}$  cm $^{-2}$ , the ratio is  $\sim 1$  for  $\log\xi \sim 3-4$  erg s $^{-1}$  cm. Therefore, we would expect to observe both lines in the spectrum with similar EWs. Also this effect is due to saturation of the lines and it slightly decreases for higher velocity parameters.

In Fig. 5.10 we report the ratios of the EWs of Fe XXV He $\alpha$ /He $\beta$  and Fe XXVI Ly $\alpha$ /Ly $\beta$  for different column densities and velocity parameters and for a fixed ionization level of  $\log\xi = 3.5$  erg s $^{-1}$  cm. We note that for column densities smaller than  $\sim 10^{21}-10^{22}$  cm $^{-2}$  the ratios are basically dictated by the different oscillator strengths of the transitions (see values in Table 1.1). However, for increasing columns, there is a tendency to approach unity. This is due again to line saturation. In fact, the transitions with higher oscillator strengths (He $\alpha$  and Ly $\alpha$ ) can quickly reach high EWs, but they also reach the

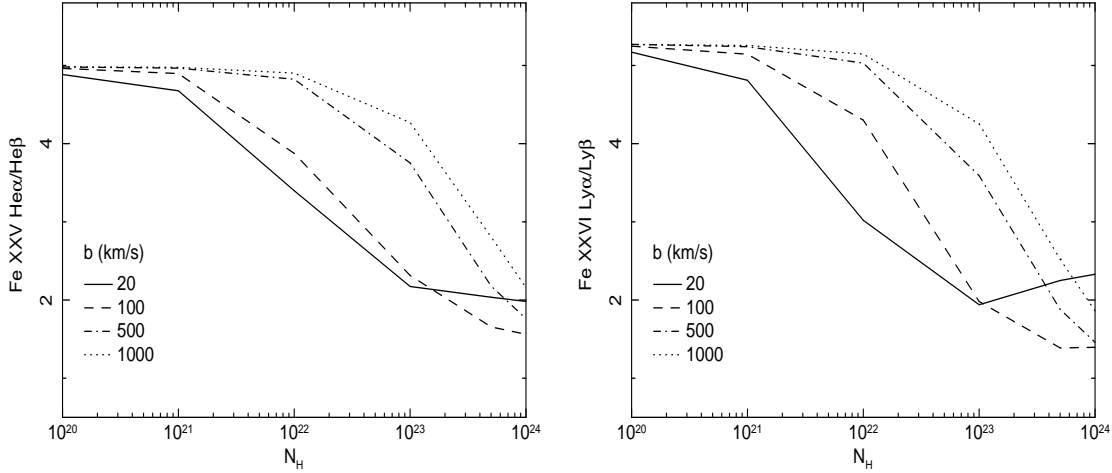


Figure 5.10: Ratio of the EWs of Fe XXV He $\alpha$ /He $\beta$  ( $r + i$ ) (*left panel*) and Fe XXVI Ly $\alpha$ /Ly $\beta$  ( $r_1 + r_2$ ) (*right panel*) lines as a function of the column density, for different values of the velocity parameter  $b$ . The ionization parameter is fixed to  $\log\xi=3.5$  erg s $^{-1}$  cm.

saturation earlier than the weaker lines and cannot raise anymore. This effect can be mitigated by an increase in the velocity broadening. As clearly shown in Fig. 5.10, higher values of  $b$  cause the decrease trend to shift toward higher columns and the EW ratios are maintained for a wider range of  $N_H$ . These line ratios are overall consistent with those published by Risaliti et al. (2005).

Given that the ionization of the gas in the central regions of AGN is dominated by photo-ionization from the nuclear radiation, it is important to check if the actual shape of the input SED in the Xstar simulations can induce important differences in the estimated parameters. We checked that for changes of the power-law photon index in the range  $\Gamma=1.5-2.5$  the parameters ( $N_H$  and  $\xi$ ) required to obtain the same line EWs are consistent within 10%. The main difference is on the value of the ionization parameter. For instance, in Fig. 5.11 we report the estimated EW of the Fe XXV He $\alpha$  and Fe XXV Ly $\alpha$  as a function of  $\log\xi$  for three different SEDs: a power-law with  $\Gamma=2$  (PL), the mean SED from our radio-quiet type 1 AGN sample (MS) (see §5.1) and the “classical” AGN SED from Mathews & Ferland (1987) (MF) (see the comparison of these different SEDs in Fig. 5.3). We can clearly note that the only difference is a slight shift toward higher ionization parameters to obtain the same EW at the peak, going from the PL, to the MS and MF. Looking at the SEDs shape in Fig. 5.3, we can deduce that this effect is mainly due to a difference in the high energy part. The input energy band for Xstar is between 0.1 eV

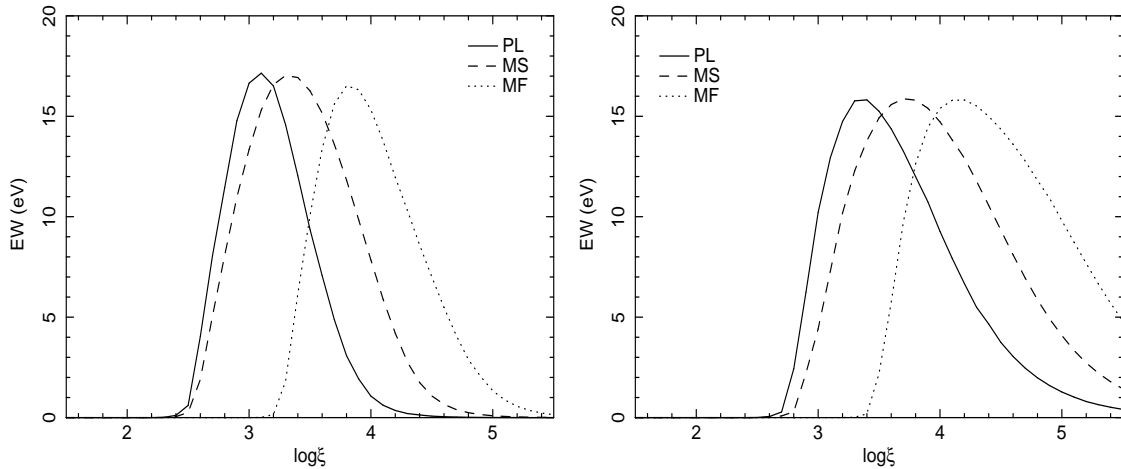


Figure 5.11: Comparison of the EWs the Fe XXV He $\alpha$  (r + i) (*left panel*) and Fe XXVI Ly $\alpha$  (r<sub>1</sub> + r<sub>2</sub>) (*right panel*) lines as a function of  $\log\xi$ , for a fixed column density  $N_H=10^{23}$  cm<sup>-2</sup> and velocity broadening  $b=100$  km/s. We used different input SEDs: a power-law with  $\Gamma=2$  (PL, solid line), our mean SED from the radio-quiet type 1 AGN (MS, dashed line) and the SED from Mathews & Ferland (1987) (MF, dotted line).

and 10<sup>6</sup> eV. The PL and MS are the same in this band, however the MS stops at 10<sup>5</sup> eV and then goes to zero. The MF has a much more complex shape with respect to the other two, but also in this case we can note that it is less intense than the PL and MS for energies greater than  $\sim 100$  eV. This means that for the same bolometric luminosity, the MF and MS have less high energy photons that can effectively ionize iron, with respect to the PL. Therefore, to obtain the same iron ionic abundances, the MF and MS need to increase the global ionization level of the material. The presence of a UV-bump between  $\sim 1-100$  eV in the MF SED with respect to the other two gives only a marginal contribution to this difference. In fact, as already stated by McKernan et al. (2003a), the presence or absence of the bump in the SED does not change significantly the parameters of the photo-ionized gas in the Fe K band because the main driver is the ionizing continuum in the hard X-rays. As already noted by several other authors (e.g. Yaqoob et al. 2003; Bianchi et al. 2005a), we checked that the gas density does not play an important role in the overall modelling and the results are basically the same for a wide range of values ( $n\sim 10^2-10^{12}$  cm<sup>-3</sup>). This is due to the fact that changing the density is equivalent to change the distance or luminosity, while leaving the same ionization parameter.

Finally, we have compared our curve of growth analysis of the main Fe K-shell absorption lines with that reported by Bianchi et al. (2005a). The authors were interested

in low-velocity photo-ionized outflows in AGN, instead of the ultra-fast outflows discussed in this Thesis. However, the physical processes are the same and their results can be directly compared with ours. Bianchi et al. (2005a) used the photo-ionization code CLOUDY to derive the iron ion abundances and assumed a power-law SED with  $\Gamma=2$ , a gas density of  $n=10^6 \text{ cm}^{-3}$  and a constant temperature of  $T=10^6 \text{ K}$ . They also used a different definition of the ionization parameter ( $U_x$ ), but the relation with ours is simply  $\log\xi \simeq 4 + \log U_x$  (for a power-law continuum with  $\Gamma=2$ ). The results showed in our Fig. 5.4 to Fig. 5.9 are overall quantitatively consistent with those showed in their Fig. 1 to Fig. 6. The consistency between these two independent studies means that the results do not drastically depend on the different assumptions and photo-ionization codes employed and this puts our conclusions on a solid theoretical ground.

### 5.2.3 The Xstar tables

The Xstar code allows to generate photo-ionization grids to directly model the spectral data. We sampled the ionization parameter between  $\log\xi=0 \text{ erg s}^{-1} \text{ cm}$  and  $\log\xi=6 \text{ erg s}^{-1} \text{ cm}$  in 20 steps and the column density between  $N_H=10^{20} \text{ cm}^{-2}$  and  $N_H=10^{24} \text{ cm}^{-2}$  in 20 steps, for a total of 400 Xstar simulations.

For the radio-quiet AGN sample we used the mean SED derived in §5.1. For the BLRGs, instead, there are less data available to estimate a proper mean SED and we assumed a reasonable ionizing continuum in the X-ray band. The X-ray continuum of BLRGs in the  $\sim 2\text{--}10 \text{ keV}$  band can be well approximated by a single power-law with photon index  $\Gamma \sim 1.7$  (e.g. Sambruna et al. 1999 and references therein). Therefore, we modeled the nuclear X-ray ionizing continuum of BLRGs with a power-law of photon index  $\Gamma = 2$ , which is usually assumed also for Seyfert galaxies and takes into account also of the possible steeper soft excess component (e.g. Bianchi et al. 2005a). We already discussed in the previous section (§5.2.2) that a different choice of the power-law slope ( $\pm 30\%$ ) has negligible effects ( $< 10\%$ ) on the parameter estimates in the considered Fe K band ( $E=4\text{--}10 \text{ keV}$ ), well within the measurement errors.

The typical velocity broadening ( $b$ ) of UV emission lines in the Broad Line Region of type 1 active galaxies is of the order of  $b \sim 500\text{--}1000 \text{ km/s}$ , the narrow lines from the Narrow Line Region instead have  $b < 300 \text{ km/s}$  (e.g. Crenshaw et al. 2003). Moreover, the turbulent velocities for the highly ionized absorbers in the central regions of Seyfert

galaxies are usually assumed to be in the range  $\sim 100\text{--}1000$  km/s (e.g. Risaliti et al. 2005; Cappi et al. 2009 and references therein). The velocity broadening of the lines is expected to be dominated by the turbulent component for values greater than  $\sim 100$  km/s (e.g. Nicastro et al. 1999; Bianchi et al. 2005a).

The energy resolution of the EPIC pn camera of XMM-Newton and of the XIS instruments of Suzaku in the Fe K band is  $\text{FWHM} \sim 100\text{--}200$  eV, which means that lines with velocity broadening lower than  $\sim 2000\text{--}4000$  km/s cannot be resolved. The absorption lines discussed in the sections on the data analysis (§3.3 and §4.3) are all unresolved and sometimes there are indications for saturation effects (the ratios of their EWs can be of the order of unity). Therefore, given that we cannot estimate the velocity broadening of the lines directly from the spectral data, we decided to assume the most likely value for the turbulent velocity of the gas of 500 km/s (equivalent to the mean between the two extreme values discussed in §5.2.2). We checked that for higher choices of this parameter ( $\geq 1000$  km/s) the resultant estimate of the ionization parameter would not be affected but the derived absorber column density would be slightly lower (because the core of the lines tend to saturate at higher  $N_H$  when increasing the velocity broadening). However, the resultant differences of  $\sim 5\text{--}10\%$  in the derived values are completely negligible and are well constrained within the errors of measure. Therefore, in the following sections we apply these photo-ionization grids to directly model the different absorption lines detected in the Fe K band in both the radio-quiet and radio-loud AGN samples and derive estimates of the column density  $N_H$ , ionization state  $\xi$  and velocity shift of the absorbing material.

It should be noted that the turbulent velocity considered in the Xstar grids is different from the velocity broadening parameter  $b$  considered in the previous curve of growth analysis (§5.2.2), which is the square root of the quadratic sum of the turbulent and thermal velocities. Xstar already incorporates the thermal broadening of the lines. However, as already stated in the previous section (see 5.2.2), the thermal velocity term is usually negligible and the velocity broadening is dominated by the turbulent term, for values greater than  $\sim 100$  km/s.

Finally, we stress that the velocities and column densities derived by fitting the spectral data with the Xstar code depends on the unknown inclination angle of the outflow with respect to the line of sight. In other words, they depend whether we are actually looking directly down to the outflowing stream or if we intercept only part of it (e.g. Elvis 2000).

Therefore, the obtained values are only conservative estimates and they can be intrinsically much higher.

### 5.3 Spectral fits of the radio-quiet AGN sample

In order to have a more physically consistent modelling of the blue-shifted Fe K absorption lines detected in the XMM-Newton observations of the radio-quiet AGN sample (see Table A.2 in Appendix A), we carried out a fit of the spectra using the Xstar photoionization grid discussed in § 5.2.3. We performed a fit of the EPIC pn data between 3.5–10.5 keV, adding the Xstar grid to the baseline models listed in Appendix A, Table A.2 (which do not include any Gaussian absorption lines). The best-fit parameters for all the observations with detected absorption Fe K lines are listed in Table 5.2. The estimated column densities are significant, always greater than  $N_H \sim 10^{22} \text{ cm}^{-2}$ , and the ionization parameters are high, in the range  $\log \xi \sim 3\text{--}5.5 \text{ erg s}^{-1} \text{ cm}$ .

There is evidence for a systematic blue-shift of the spectral lines with respect to the rest-frame energies and the derived outflow velocities are consistent with those estimated from the previous phenomenological fit of the data (see Table A.2 in Appendix A). The only cases in which the absorbers are consistent with zero velocity are Mrk 279 and NGC 3783. In particular, the modeling of the 4–10 keV spectrum of NGC 3783 is complicated by the presence of a narrow weak absorption line at  $E \sim 6.7 \text{ keV}$  just between two intense emission lines. Therefore, we have been forced to fix the outflow velocity of the absorber to zero to derive a good fit of the spectrum of the first two observations (see Table 5.2).

Given the derived high ionization levels for the Fe K absorbers, no other intense absorption signatures are expected at lower energies as all the elements lighter than iron are almost completely ionized. However, as already discussed in §3.4.1, there are two important exceptions in which we have been able also to detect blue-shifted absorption lines from helium- and/or hydrogen-like ions of elements lighter than iron (e.g. Ar, Ca) with blue-shifted velocities consistent with the Fe K lines, namely NGC 4151 and NGC 7582. These features are indeed all well self-consistently reproduced by the Xstar grid for intermediate/high ionization parameters of  $\log \xi \simeq 3.7\text{--}3.8 \text{ erg s}^{-1} \text{ cm}$  (see Table 5.2), with a possible requirement for abundances slightly higher than solar. Moreover, similar results have been reported by Pounds & Page (2006) for one observation of PG 1211+143 (0112610101).

Table 5.2: Best-fit parameters of the Fe K absorption lines detected in the radio-quiet sample and modelled with the Xstar photo-ionization code. We used a grid with turbulent velocity fixed to 500 km/s. The errors are at the  $1\sigma$  level. The lower limits on  $N_H$  and upper limits on  $v_{out}$  are at the 90% confidence level. (1) Source name. (2) XMM-Newton observation ID. (3) Ionized absorber column density. (4) Logarithm of the ionization parameter. (5)  $\chi^2$  improvement with respect to the baseline model and the addition of three more parameters. (6) Outflow velocity.

| Source         | OBSID      | $N_H$<br>( $10^{22}$ cm $^{-2}$ ) | $\log\xi$<br>(erg s $^{-1}$ cm) | $\Delta\chi^2$  | $v_{out}$<br>(c)   |
|----------------|------------|-----------------------------------|---------------------------------|-----------------|--------------------|
| (1)            | (2)        | (3)                               | (4)                             | (5)             | (6)                |
| Type 1 objects |            |                                   |                                 |                 |                    |
| NGC 4151       | 0402660201 | $1.5^{+1.0}_{-0.5}$               | $3.8 \pm 0.2$                   | 17              | $+0.118 \pm 0.005$ |
| IC4329A        | 0147440101 | >1                                | $4.6^{+1.4}_{-0.5}$             | 14              | $+0.096 \pm 0.002$ |
| NGC 3783       | 0112210101 | $1.3 \pm 0.2$                     | $2.6 \pm 0.1$                   | 18 <sup>a</sup> | $\equiv 0^b$       |
|                | 0112210201 | $1.2 \pm 0.1$                     | $2.6^{+0.4}_{-0.5}$             | 28 <sup>a</sup> | $\equiv 0^b$       |
|                | 0112210501 | $1.3 \pm 0.1$                     | $2.7 \pm 0.4$                   | 76              | < 0.009            |
| NGC 3516       | 0401210401 | $3.2^{+2.0}_{-0.8}$               | $3.7 \pm 0.1$                   | 50              | $+0.005 \pm 0.002$ |
|                | 0401210501 | $4.3^{+2.9}_{-1.3}$               | $3.9 \pm 0.1$                   | 40              | $+0.007 \pm 0.002$ |
|                | 0401210601 | $10.0^{+2.7}_{-1.3}$              | $3.9 \pm 0.1$                   | 61              | $+0.011 \pm 0.002$ |
|                | 0401211001 | $2.7^{+2.4}_{-0.9}$               | $3.8^{+0.2}_{-0.1}$             | 23              | $+0.012 \pm 0.004$ |
| Mrk 509        | 0130720101 | >6                                | $5.1^{+0.3}_{-0.6}$             | 12              | $+0.170 \pm 0.003$ |
|                | 0306090201 | >3                                | $5.6^{+0.2}_{-1.2}$             | 14              | $+0.138 \pm 0.002$ |
|                | 0306090401 | >2                                | $5.3^{+0.6}_{-1.0}$             | 12              | $+0.195 \pm 0.003$ |
| Ark 120        | 0147190101 | >2                                | $5.5^{+0.2}_{-1.2}$             | 12              | $+0.269 \pm 0.003$ |
| Mrk 279        | 0302480501 | $0.6 \pm 0.2$                     | $3.2 \pm 0.1$                   | 10              | < 0.007            |
| Mrk 79         | 0400070201 | $23^{+40}_{-14}$                  | $4.1^{+0.3}_{-0.2}$             | 19              | $+0.090 \pm 0.002$ |
| NGC 4051       | 0109141401 | >3                                | $5.6^{+0.2}_{-1.1}$             | 11              | $+0.017 \pm 0.005$ |
|                | 0157560101 | $7.5^{+14.4}_{-3.6}$              | $3.8^{+0.3}_{-0.2}$             | 13              | $+0.154 \pm 0.003$ |
| Mrk 766        | 0304030301 | >7                                | $5.2^{+0.2}_{-0.5}$             | 13              | $+0.041 \pm 0.004$ |
|                | 0304030501 | $7.5^{+19.5}_{-3.7}$              | $4.0^{+0.3}_{-0.2}$             | 20              | $+0.090 \pm 0.002$ |
| Mrk 841        | 0205340401 | >10                               | $4.7^{+0.3}_{-0.4}$             | 12              | $+0.034 \pm 0.004$ |
| ESO 323-G77    | 0300240501 | $17.6^{+8.4}_{-6.2}$              | $3.6 \pm 0.1$                   | 71              | $+0.009 \pm 0.002$ |
| 1H419-577      | 0148000201 | >10                               | $4.9^{+0.3}_{-0.4}$             | 10              | $+0.034 \pm 0.007$ |
| Mrk 290        | 0400360601 | >3                                | $4.2^{+0.8}_{-0.4}$             | 11              | $+0.140 \pm 0.004$ |
| Mrk 205        | 0124110101 | >11                               | $4.9 \pm 0.3$                   | 10              | $+0.101 \pm 0.004$ |
| PG 1211+143    | 0112610101 | $4.2^{+2.6}_{-1.3}$               | $3.2 \pm 0.1$                   | 28              | $+0.130 \pm 0.003$ |
| Type 2 objects |            |                                   |                                 |                 |                    |
| MCG-5-23-16    | 0302850201 | $1.0^{+0.5}_{-0.3}$               | $3.9 \pm 0.2$                   | 23              | $+0.115 \pm 0.004$ |
| NGC 4507       | 0006220201 | >3                                | $5.3^{+0.2}_{-1.0}$             | 13              | $+0.174 \pm 0.003$ |
| NGC 7582       | 0112310201 | >8                                | $3.7 \pm 0.2$                   | 19              | $+0.255 \pm 0.002$ |

(a) Improvement with the addition of two more parameters

(b) Parameter fixed during the fit.

Table 5.3: Best fit photo-ionization models. Column 1: source name. Column 2: ionization parameter. Column 3: equivalent Hydrogen column density of the ionized absorber. Column 4: blue-shifted (outflow) velocity. Errors are at the  $1\sigma$  level.

| Source   | $\log\xi$<br>(erg s <sup>-1</sup> cm) | $N_H$<br>(10 <sup>22</sup> cm <sup>-2</sup> ) | $v_{out}$<br>(c)   |
|----------|---------------------------------------|---|--------------------|
| 3C 111   | $5.0 \pm 0.3$                         | $> 20^a$                                      | $+0.041 \pm 0.003$ |
| 3C 390.3 | $5.6^{+0.2}_{-0.8}$                   | $> 3^a$                                       | $+0.146 \pm 0.004$ |
| 3C 120a  | ...                                   | ...   | ...                |
| 3C 120b  | $3.8 \pm 0.2$                         | $1.1^{+0.5}_{-0.4}$                           | $+0.076 \pm 0.003$ |
| 3C 382   | ...                                   | ...   | ...                |
| 3C 445   | ...                                   | ...   | ...                |

(a) Lower limit at the 90% level.

## 5.4 Spectral fits of the radio-loud AGN sample

We have detected blue-shifted Fe K absorption lines in three out of five BLRGs observed with Suzaku, namely 3C 111, 3C 390.3 and 3C 120 (see §4.3). We now apply the Xstar photo-ionization grid (§5.2.3) to model these lines (see Table 4.3) and estimate the physical parameters of the UFOs. We considered the 3.5–10.5 keV spectra of the XIS-FI and added the Xstar grid to the baseline models listed in Table 4.2 (which do not include any Gaussian absorption lines). The best-fit parameters are listed in Table 5.3.

The Xstar models simultaneously take into account all the absorption features discussed in the previous analysis (see Table 4.3) and are required with confidence levels  $>99\%$ . The lines are systematically blue-shifted and the outflow velocities, in the range  $v_{out} \simeq 0.04\text{--}0.15c$ , are completely consistent with those derived using the much more simple phenomenological models discussed in §4.3. The column densities involved are large,  $N_H \geq 10^{22}$  cm<sup>-2</sup>, and the ionization levels are very high,  $\log\xi \simeq 3.8\text{--}5.6$  erg s<sup>-1</sup> cm. These values are similar to those derived in the previous section for the UFOs in the radio-quiet AGN sample (see Table 5.2).

The conclusion that the detected absorption features are actually due to blue-shifted Fe XXV and Fe XXVI resonant lines is well represented in Fig. 5.12 and Fig. 5.13. In

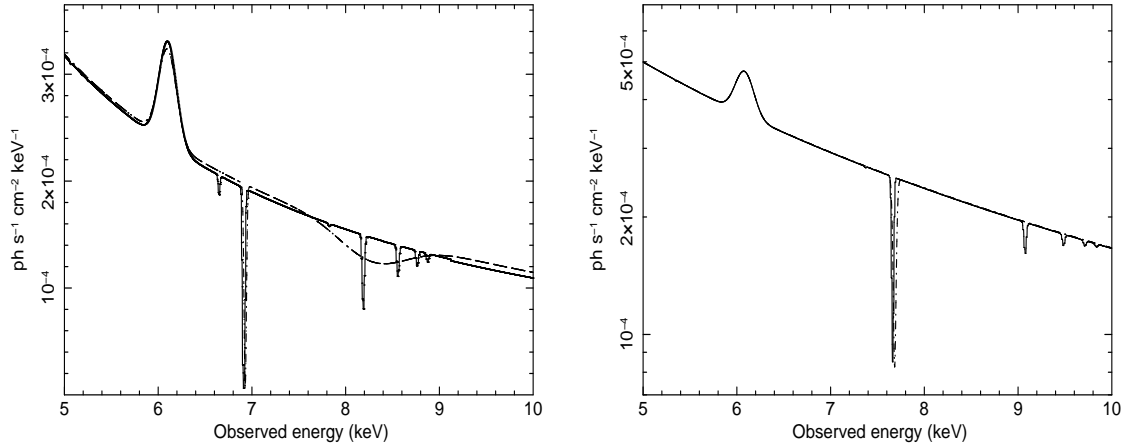


Figure 5.12: Comparison of the best fit model for 3C 111 (*left*) and 3C 390.3 (*right*) including the baseline model (see Table 4.2) plus the Gaussian absorption lines listed in Table 4.3 (dashed line) or the detailed photo-ionization modelling of the absorber reported in Table 5.3 (solid line).

these figures we show a comparison of the best-fit phenomenological baseline models with the absorption lines modelled as inverted Gaussian or with the physically consistent Xstar photo-ionization grid.

In particular, for 3C 111 (Fig. 5.12, left panel), we can see that the two models are almost completely coincident up to the first absorption line (identified as Fe XXVI Ly $\alpha$  at the observed energy of  $\sim 7$  keV, see Table 4.3) and clearly demonstrates that the apparent broadening of the second absorption feature (see Table 4.3) is actually due to a blend of the three higher order Lyman series lines (i.e. Ly $\beta$ , Ly $\gamma$  and Ly $\delta$ ).

The comparison of the best fit results for 3C 390.3 including the baseline model and superimposed the modelling of the blue-shifted absorption line (identified as Fe XXVI Ly $\alpha$ , see Table 4.3) with a simple narrow inverted Gaussian or with the Xstar photo-ionization code is shown in the right panel of Fig. 5.12. The two models coincide completely, apart from a few weak higher order Lyman series resonances which cannot be detected with sufficient significance given the limited quality of the XIS-FI spectral data.

Concerning 3C 120b, the comparison of the best fit baseline model and the superimposed modelling of the absorption structures with two narrow and one broad inverted Gaussian or with the physically self-consistent Xstar photo-ionization code is reported in Fig. 5.13. The plot clearly shows that the two models are completely coincident up to the first two narrow absorption lines (identified as blue-shifted Fe XXV K $\alpha$  and Fe

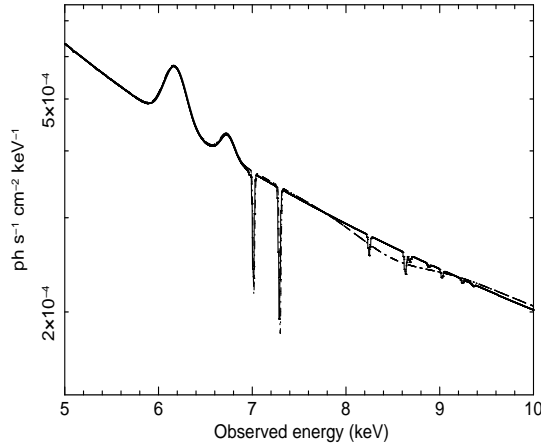


Figure 5.13: Comparison of the best fit model for 3C 120b including the baseline model (see Table 4.2) plus the Gaussian absorption lines listed in Table 4.3 (dashed line) or the detailed photo-ionization modelling of the absorber reported in Table 5.3 (solid line).

XXVI Ly $\alpha$ , see Table 4.3) and demonstrates that the broad absorption structure at higher energy (see Table 4.3) is actually composed by several narrow resonant lines from the same ionic species (i.e. mainly Fe XXV K $\beta$  and Fe XXVI Ly $\beta$ ) which appear to be blended together due to the lower instrumental resolution and signal-to-noise in this energy band (similar to the conclusion for 3C 111).

Finally, we exploited the broad-band capabilities of Suzaku to perform a consistency check of the absorber parameters reported in Table 5.3. We downloaded and reduced the PIN data of 3C 111, 3C 390.3 and 3C 120 and analyzed the combined XIS-FI and PIN spectra. The energy band covered in this way is very broad, from 0.5 keV up to 50 keV. For 3C 390.3 and 3C 120 we applied the broad-band models already published in the literature by Sambruna et al. (2009) and Kataoka et al. (2007). Instead, for 3C 111, we used the broad-band model that will be reported in Ballo et al. (2010, in prep.). This is essentially composed by a power-law continuum with Galactic absorption, plus cold reflection ( $R < 1$ ) and the Fe K $\alpha$  emission line at  $E \simeq 6.4$  keV. The resultant power-law photon index of this fit is  $\Gamma \simeq 1.6$ , which is slightly steeper than the estimate of  $\Gamma \simeq 1.5$  from the local continuum in the 4–10 keV band (see Table 4.2). Then, we modeled the blue-shifted absorption lines with the Xstar photo-ionization grid already discussed in §5.2.3.

The parameters of the absorbers derived from these broad-band fits are completely consistent with those reported in Table 5.3. In particular, for 3C 111 we obtained an ionization parameter of  $\log \xi = 4.9_{-0.4}^{+0.2}$  erg s $^{-1}$  cm, a column density of  $N_H > 1.5 \times 10^{23}$  cm $^{-2}$

and an outflow velocity of  $v_{out}=+0.039 \pm 0.003c$ . For 3C 390.3, we estimated  $\log\xi=5.6 \pm 0.5 \text{ erg s}^{-1} \text{ cm}$ ,  $N_H > 2 \times 10^{22} \text{ cm}^{-2}$  and  $v_{out}=+0.146 \pm 0.007c$ . Finally, for 3C 120b, we derived  $\log\xi=3.7 \pm 0.2 \text{ erg s}^{-1} \text{ cm}$ ,  $N_H=(1.5 \pm 0.4) \times 10^{22} \text{ cm}^{-2}$  and  $v_{out}=+0.075 \pm 0.003c$ . These best fit results are consistent within the  $1\sigma$  errors with the results reported in Table 5.3. This assures that our phenomenological modeling of the 4–10 keV energy interval alone is indeed capable to determine the local continuum with a level of accuracy suitable for a proper parametrization of the absorbers in the Fe K band.

# Chapter 6

## Discussion

In this chapter we discuss the results of our uniform and systematic search for blue-shifted Fe K absorption lines in both the radio-quiet and radio-loud AGN samples. Making use of the photo-ionization modeling results we will also derive some physical parameters for the UFOs and we will try to address some of the open questions regarding the UFOs in AGN reported in §1.4.

### 6.1 Evidence for Ultra-fast Outflows in the radio-quiet AGN sample

Despite an increasing number of studies showing evidence for the presence of narrow blue-shifted Fe K absorption lines in the X-ray spectra of radio-quiet AGN (e.g. Pounds et al. 2003a; Reeves et al. 2004; Dadina et al. 2005; Markowitz et al. 2006; Braito et al. 2007; Cappi et al. 2009), there is still much debate on their physical interpretation and even on their real statistical significance.

For instance, it has been argued by Vaughan & Uttley (2008) (see §1.4.4) that several of the published detections of narrow red/blue-shifted emission and absorption lines in the Fe K band of AGN could actually be falsified by the presence of a publication bias. In fact, only the observations with detected features have been reported in the literature and we actually do not know the fraction of detections/non-detections on the full population. Therefore, it is rather difficult to estimate the global significance of any individual case. Moreover, the fact that the significance of some of the published lines can be weak could suggest that some of them are simply the most significant from a distribution of random fluctuations.

The authors stated that the presence of this bias can be shown by simply plotting the EWs of the lines with respect their relative 90% errors (see Fig. 1.8). They restricted to the published red/blue-shifted lines with velocities  $\geq 0.05c$ . There seems to be a tendency for the data points to lay close and parallel to the border line between detection and non-detection (that is the EW and its error seem to follow a linear relation). This means that lines with higher EWs have consequently higher error bars. Moreover, the fact that none of the data display in the top left corner of the diagram (which would indicate that more intense lines have smaller error bars) would suggest that the lines with higher EWs are preferentially detected in low quality spectra.

Vaughan & Uttley (2008) claim that these properties are actually indicative of a publication bias and several (if not all) of the reported red/blue-shifted lines could actually be false detections. As also recognized by Vaughan & Uttley (2008), the only way out to overcome this bias would be to perform a uniform and systematic analysis on a complete sample of sources and directly report the ratio of line detections over non-detections. This is actually what has been done in this work, as far as blue-shifted Fe K absorption lines are concerned. To clearly define the statistical veracity of the blue-shifted lines detections one must carry out extensive Monte Carlo simulations. This should be done in a uniform and comprehensive way on a complete sample of sources, as shown here. Only in this way the line detections can be directly tested against random noise fluctuations and consequently they can be corrected for possible biases (see §2.2).

We have performed such Monte Carlo tests for the blue-shifted lines detected in the 7–10 keV energy range (see 3.3.4) and we placed a lower detection confidence level threshold of 95%. Consequently, we have been able also to estimate the global probability for these features to be generated by random fluctuations. It is very low, less than  $3 \times 10^{-8}$  (see §3.3.4). Therefore, even if some single line detection can be statistically poor, the global probability (note that this is a conservative estimate) for these blue-shifted features to be generated by random fluctuations is very low. Last but not least, we have been able to independently confirm the detection of several features with the MOS cameras (see §3.3.5). The consistency between the pn and MOS results places an additional very strong point in favour of the veracity of the lines, without relying on any statistical method.

For a comprehensive comparison with the Vaughan & Uttley (2008) work, we reproduced their EW–error<EW> plot with the lines detected in our sample. This is

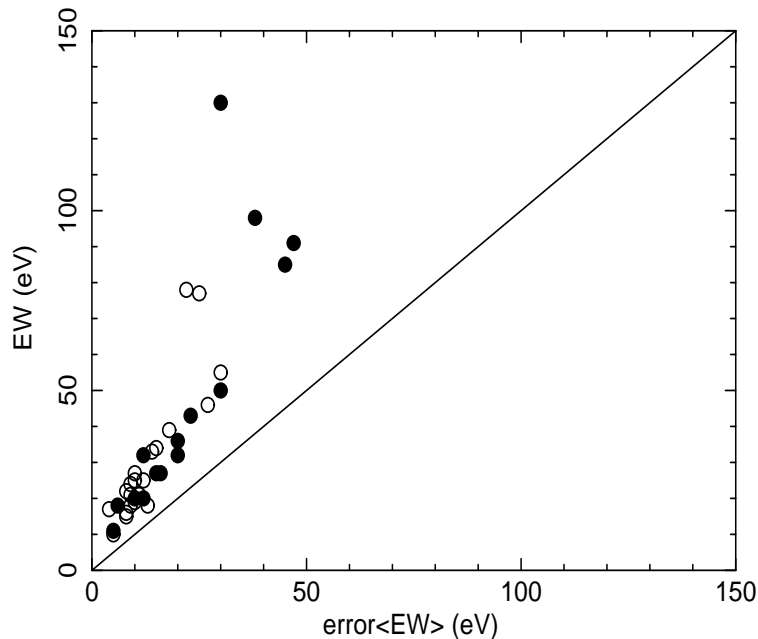


Figure 6.1: Plot of the EW of the blue-shifted absorption lines detected in the radio-quiet sample with respect to their 90% errors. The open circles refer to those with blue-shifted velocities  $v < 0.05c$  and the filled circles instead to those with  $v \geq 0.05c$ . The diagonal line indicates the border region in which  $EW = \text{error}\langle EW \rangle$ . The plot axes are in linear scale.

shown in Fig. 6.1. As it can be seen, some of the lines with more intense EWs indeed populate the upper left part of the graph and the global trend seems to diverge from the detection/non-detection border line. Moreover, the lines with measured blue-shift velocities, both less or greater than  $0.05c$ , do follow the same distribution. It should be noted that the diagram in Fig. 6.1 has been plotted with the axes in linear scale. Using logarithmic axes and a wider scale (as in Vaughan & Uttley 2008) would tend to visually compress more the data points with the line.

We also performed a further sanity check by plotting together the EWs of the blue-shifted absorption lines together with the EWs of the neutral Fe  $K\alpha$  emission lines at  $\sim 6.4$  keV detected in the sample (for which there is no doubt on the veracity). This is shown in Fig. 6.2. Interestingly enough, both the narrow absorption lines and the Fe  $K\alpha$  emission lines do follow the same trend. They actually seem to be drawn from the same distribution, with the narrow absorption lines having only systematically lower EWs. This difference is of course due to a distinct physical origin. Therefore, the data trend does seem to be rather general. The effect of closeness of the data points to the “detection line”

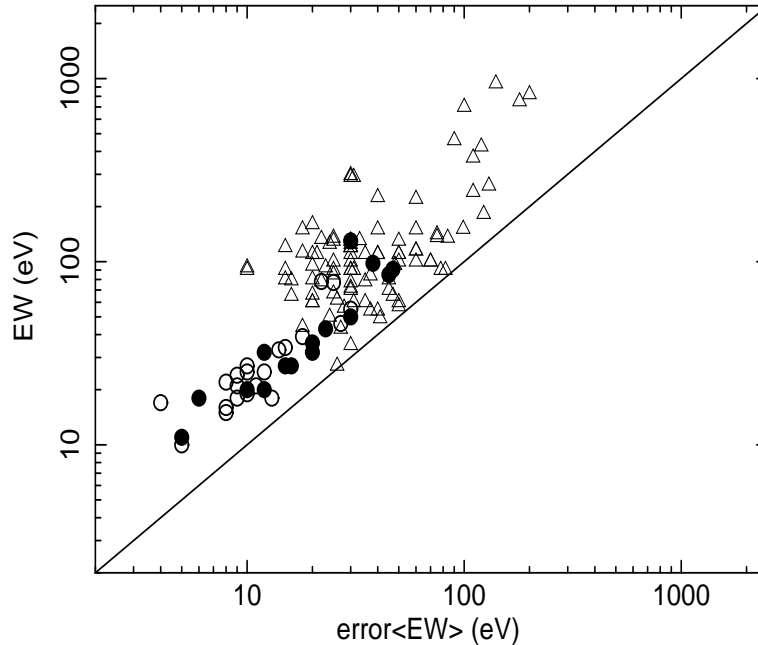


Figure 6.2: EWs with respect to the 90% errors for the narrow blue-shifted absorption features (open circles  $v < 0.05c$  and filled circles  $v \geq 0.05c$ , respectively) and the neutral Fe  $K\alpha$  emission lines (open triangles) detected in the radio-quiet sample. The plot axes are in logarithmic scale.

is again visually magnified by plotting the data in a logarithmic scale.

We therefore argue that the fact that none of the lines populate the upper left corner of the diagram does not directly tell us that the lines are fake, but that the capabilities of the X-ray instruments to detect spectral lines are intrinsically limited. In fact, to populate the upper left corner of the graph it would require, as an example, for a line of  $EW \simeq 1$  keV to have an error of less than 10 eV (at 90%), therefore indicating a detection confidence level at about  $200\sigma$ ! A measure with such accuracy has never been possible regardless of the X-ray instrument flown.

The EWs of the blue-shifted lines (with 90% errors) with respect to the 4–10 keV counts levels of the associated XMM-Newton EPIC pn observations of our sample have been plotted in Fig. 6.3. As it can be seen, there is a slight trend for the lines EWs and their respective error bars to increase for lower counts. However, this trend does not seem to be dependent on the intrinsic line detection significance, as demonstrated by the fact that it is followed by the lines detected at both 95–99% and  $\geq 99\%$  confidence levels (see Fig. 6.2).

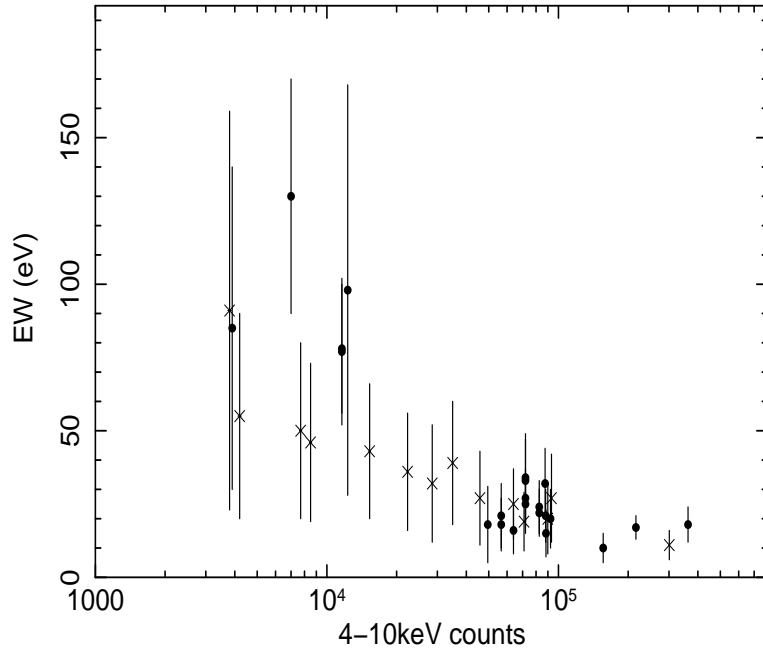


Figure 6.3: EWs of the Fe K absorption lines detected in the radio-quiet sample with respect to the 4–10 keV counts of the relative EPIC pn observation. The crosses refer to those with detection probabilities in the 95–99% range and the filled circles instead to those with  $\geq 99\%$ . The errors are at the 90% level.

However, we performed a simple test making use of a few spectral simulations. We assumed to have a narrow ( $\sigma = 10$  eV) absorption feature at 8 keV with fixed intensity of  $-5 \times 10^{-6}$  ph s $^{-1}$  cm $^{-2}$  and a simple power-law continuum with  $\Gamma = 2$  and 4–10 keV flux of  $10^{-11}$  erg s $^{-1}$  cm $^{-2}$ . The resultant EW of the line is  $\simeq 32$  eV. Then, we simulated different EPIC pn spectra, each time changing only the exposure time in order to have different total 4–10 keV counts. The resulting spectra have been fitted with the same model and the relative EWs and errors have been determined. The simulated EWs (with 90% errors) with respect to the different 4–10 keV count levels are plotted in Fig. 6.4. We note that the trend of the EW values to increase with decreasing total counts is reproduced by the simulations. However, it is followed by an increase in the error bars as well. Therefore, the EW estimates are still consistent with the assumed constant value of 32 eV (the small scattering is due to the randomization process in spectra simulation).

The increase in the estimated EW values followed by corresponding bigger error bars seems to be due to the fact that for decreasing counts levels there is an expansion of the error contours and therefore the location of the true minimum of the  $\chi^2$  distribution

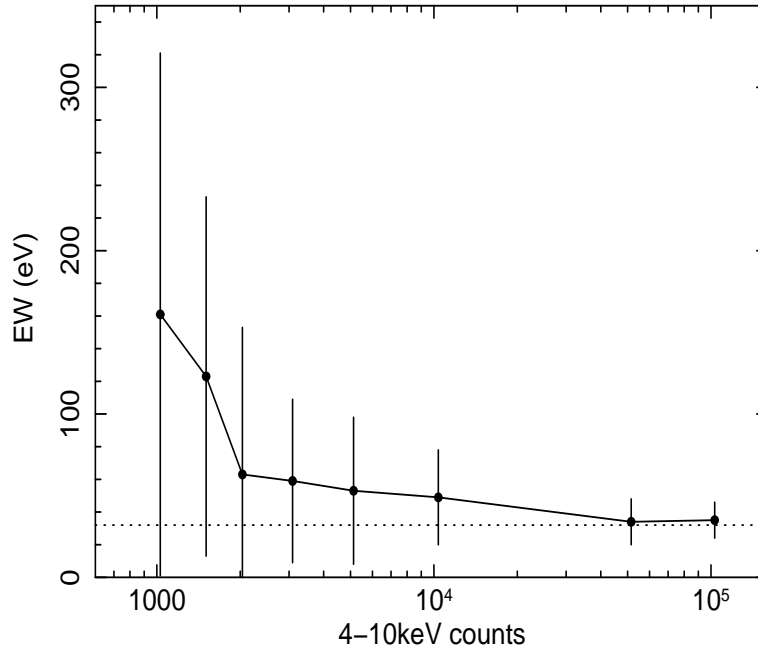


Figure 6.4: Simulated trend of the line EWs with respect to different 4–10 keV counts levels. The horizontal line refer to the simulated line with constant EW of 32 eV (see text for details). The error bars are at the 90% level.

is less constrained. For instance, if the EW best fit value is chosen as the average between the error bar limits, it is then expected to increase following the expansion of the available parameter space when the statistics is lower. This has nothing to do with random fluctuations. This can explain the trend followed by the data points in Fig. 6.1 and Fig. 6.2, that is, higher EWs have systematically higher associated error bars. Therefore, the trend does not state that the lines are fake (as we demonstrated including the line in the spectral simulations) but that we are approaching the detection limit of the instrument. It only indicates that the accuracy with which we are able to measure a certain parameter is worse when the available statistics is lower.

We have derived the blue-shift velocities associated with the narrow absorption lines (see Table A.2 in Appendix A) assuming that they were due to H/He-like Fe K-shell absorption intrinsic to the sources (see §3.4.1). However, it has been debated that some (or all) of these features could instead be indicative of local absorption at  $z = 0$  or at intermediate red-shifts, due to the fact that some of them have blue-shift velocities comparable to the sources cosmological red-shifts (McKernan et al. 2004; McKernan et al. 2005).

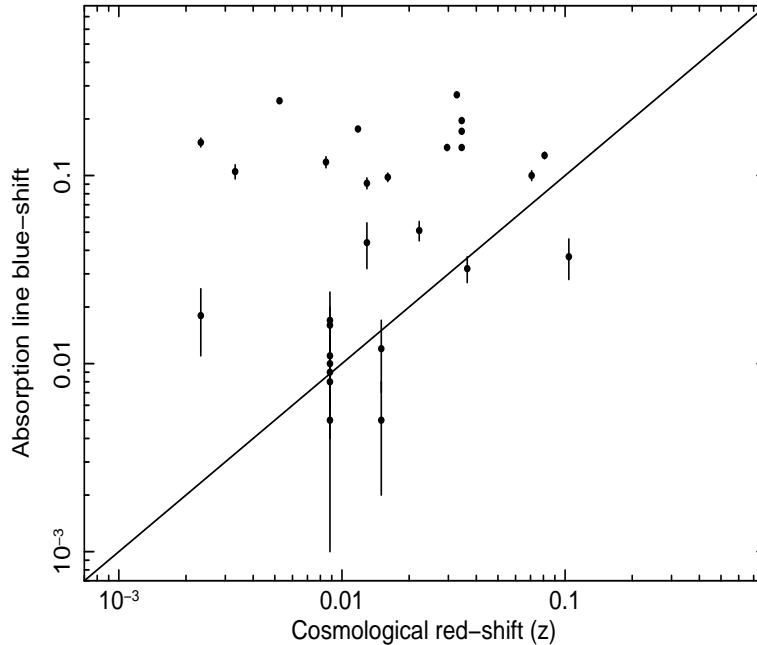


Figure 6.5: Cosmological red-shifts of the radio-quiet sample sources with respect to the blue-shift velocities (in units of  $c$ ) of the narrow Fe K absorption lines detected in their XMM-Newton observations. Errors are at the 90% level. Only positive blue-shift velocities have been reported.

To test such eventuality, we have plot the sources cosmological red-shifts ( $z$ ) with respect to the absorption lines blue-shift velocities (in units of  $c$ ) from our sample. As it can be seen from Fig. 6.5, apart from a few data points (relative to NGC 3516, Mrk 841 and ESO 323-G77), the values do not match the simple linear relation expected if the lines were due to local absorption. Furthermore, the blue-shift velocities are systematically higher compared to the sources cosmological red-shifts. This clearly demonstrates that the detected blue-shifted absorption lines in the Fe K band are indeed due to genuine absorption intrinsic to the sources.

The same conclusion using velocity information have been reached by Reeves et al. (2008), comparing some observations recently reported in the literature. Moreover, Reeves et al. (2008) also suggested further physical arguments supporting this thesis. These narrow blue-shifted absorption features have been found to be variable on time-scales ranging from  $\sim$  years to  $\sim$  100 ks (e.g. Braitto et al. 2007; Cappi et al. 2009) therefore implying a  $\leq$  pc scale absorber. This somewhat compact absorber is at odd with the expected kpc scale extension of diffuse Galactic halos or Warm-Hot Intergalactic Medium

(WHIM). Moreover, the local hot gas is expected to be collisionally ionized, instead of being photo-ionized by the AGN continuum. Therefore, the temperature required to have a substantial He/H-like iron population would be very high, greater than  $\sim 10^{7-8}$  K. Finally, the huge column densities of gas ( $N_H \geq 10^{23-10^{24}} \text{ cm}^{-2}$ ) required to reproduce the observed features are too high to be associated with any reasonable hot diffuse local gas. Otherwise, this would require a tremendously significant change to our understanding of the Galactic halo environment.

In conclusion, we are confident enough that the blue-shifted Fe K absorption lines detected in our sample are intrinsic to the sources and those with outflow velocities greater than  $\simeq 10^4$  km/s ( $\sim 0.03c$ ) can be associated to the Ultra-fast Outflows from the central regions of radio-quiet AGN (with an incidence of more than  $\sim 35\%$ ).

## 6.2 Evidence for Ultra-fast Outflows in the radio-loud AGN sample

Our discovery of absorption lines at energies greater than 7 keV ascribable to blue-shifted Fe XXV and/or Fe XXVI K-shell resonances in the Suzaku spectra of three (namely 3C 111, 3C 390.3 and 3C 120) out of five BLRGs of our small sample is consistent with our detection of UFOs in the X-ray spectra of a significant ( $\simeq 35\%$ ) fraction of radio-quiet AGN (see §3.4.2).

Moreover, the fact that we selected all the observations of BLRGs available in the Suzaku archive, which are limited to the five brightest objects, allows us to avoid any possible claim that the results are affected by a publication bias (e.g. Vaughan & Uttley 2008). In fact, we performed a uniform and systematic search for blue-shifted Fe K absorption lines in their X-ray spectra and directly reported the fraction of detections and non-detections in the sample. However, it should be noted that our small sample is not complete and the results might not be representative of the global population of BLRGs. Therefore, to obtain better constrains on the statistical incidence and parameters of UFOs in BLRGs, we should expand the sample by increasing the number of observed sources with future proposals.

It has been claimed that part of the ionized blue-shifted absorption features detected in the X-ray spectra of bright AGN could actually be due to a contamination by local ( $z \simeq 0$ ) absorption in our Galaxy or by the Warm/Hot Intergalactic Medium (WHIM) at

intermediate red-shifts (e.g. McKernan et al. 2003b; McKernan et al. 2004; McKernan et al. 2005). We performed some tests to look into this eventuality.

We can use the velocity information and compare the absorber blue-shift velocities with the cosmological red-shifts of the sources. The blue-shift velocities of the absorbers detected in 3C 120 and 3C 390.3 (see Table 5.3) are much greater than the sources cosmological red-shifts (see Table 4.1). This conclusion is strong enough to rule out any contamination due to absorption from local or intermediate red-shift material in these sources. However, the derived blue-shift velocity of  $v=+0.041 \pm 0.005c$  for the highly ionized absorber in 3C 111 is instead somewhat similar to the source cosmological red-shift of  $z = 0.0485$  and needs to be investigated in more detail. The difference between the two values is  $zc - v \simeq 0.007c$ , which could indicate absorption from highly ionized material either in our Galaxy and outflowing with that velocity ( $v \sim 2000$  km/s) along the line of sight or at rest and located at that intermediate red-shift ( $z \simeq 0.007$ ).

The galaxy 3C 111 is located at a relatively low latitude ( $b = -8.8^\circ$ ) with respect to the Galactic plane and therefore its X-ray spectrum could be, at some level, affected by local obscuration. However, the estimated column density of Galactic material along the line of sight of the source is  $N_H \sim 3 \times 10^{21} \text{ cm}^{-2}$  (Dickey & Lockman 1990; Kalberla et al. 2005), which is far too low to explain the value of  $N_H \sim 10^{23} \text{ cm}^{-2}$  of the absorber we estimated from the spectral fitting to the data (see Table 5.3). Nevertheless, the source is located near the direction of the Taurus molecular cloud, which is the nearest large star-forming region in our Galaxy.

A detailed optical and radio study of the cloud located in front (and around) of 3C 111 has been reported by Ungerer et al. (1985). From the analysis of the emission from the stars in that region and the molecular emission lines (primarily  $\text{C}^{18}\text{O } J = 1-0$ ) the authors have been able to estimate several parameters of the cloud, such as the location at a distance of  $\sim 400$  pc (with a linear extent of  $\sim 5$  pc), a kinetic temperature of  $T \simeq 10$  K, a typical velocity dispersion of  $\sim 1-3$  km/s and a low number density of  $n(\text{H}_2) \sim 300 \text{ cm}^{-3}$ . These parameters are completely inconsistent with the properties of the absorber that we have detected in the X-ray spectrum. In fact, the extreme ionization level ( $\log \xi \sim 5 \text{ erg s}^{-1} \text{ cm}$ ) needed to have sufficient Fe XXVI ions would completely destroy all the molecules and ionize all the lighter atoms. The temperature associated with such photo-ionized absorber ( $T \sim 10^6$  K) is very much higher than that estimated for the Taurus molecular cloud. Also

the outflow velocity of  $\sim 2000$  km/s, expected if associated with such Galactic clouds, would be substantially higher than the velocity dispersion estimated by Ungerer et al. (1985). The authors also stated that the mapping of the visual extinction due to the molecular cloud clearly shows that the region of the cloud in front of 3C 111 is not the densest part (see Fig. 3 of Ungerer et al. 1985).

This result is also suggested from a recent detailed X-ray study of this region that has been performed by the XMM-Newton Extended Survey of the Taurus Molecular Cloud (XEST) project (Güdel et al. 2007). This work has been focused on the study of the stars and gas located in the most populated  $\simeq 5$  square degrees region of the Taurus cloud. With a declination of  $\sim 38^\circ$ , 3C 111 is located outside the edge of this complex region, where mainly only extended cold and low density molecular clouds are distributed (see Fig. 1 of Güdel et al. 2007). Therefore, the identification of the highly ionized absorber of 3C 111 with local Galactic absorption is not feasible, as it would require a tremendously significant change to our understanding of the Galactic halo environment.

We also find very unlikely the association with absorption from diffuse WHIM at an intermediate red-shift ( $z \sim 0.007$ ). In fact, this diffuse gas is expected to be collisionally ionized, instead of being photo-ionized by the AGN continuum. Therefore, the temperature required to have a substantial He/H-like iron population would be much higher ( $T \sim 10^7 - 10^8$  K) than the expected  $T \sim 10^5 - 10^6$  K. The huge column density of gas ( $N_H \geq 10^{23}$  cm $^{-2}$ ) required to reproduce the observed features is also too high compared to those expected for the WHIM ( $N_H \leq 10^{20}$  cm $^{-2}$ ). Moreover, the detection of highly ionized absorbers in 3C 120 and 3C 390.3 with blue-shift velocities substantially larger than the relative cosmological red-shifts strongly support the association of the absorber in 3C 111 with a UFO intrinsic to the source.

It is important to note that similar conclusions have been reached also for the radio-quiet AGN in §6.1.1. Moreover, as showed in Fig. 6.5, also the evidence that in radio-quiet AGN the majority of sources with detected blue-shifted Fe K absorption lines have correspondent velocities higher than the relative cosmological red-shifts suggested that the case of 3C 111 could be a mere coincidence. We thus conclude that the evidence for UFOs in BLRGs from Suzaku data is indeed robust.

### 6.3 Physical properties of Ultra-fast Outflows

In this section we estimate the main physical parameters of the UFOs and those of the sources in the radio-quiet and radio-loud AGN samples, such as their location, their mass outflow rates and kinetic power and other quantities such as the Eddington luminosity of the sources.

The comparison of the bolometric luminosity of the sources with respect to their Eddington luminosity can give us an idea of the power of the AGN of producing outflows/winds, especially if radiation-driven. We can derive an estimate of the bolometric luminosity ( $L_{bol}$ ) of the sources from the X-ray ionizing luminosity ( $L_{ion}$ , integrated between 1 and 1000 Rydberg) following the relation  $L_{bol} \simeq 10L_{ion}$  (McKernan et al. 2007). Instead, the Eddington luminosity is defined as  $L_{Edd} \simeq 1.3 \times 10^{38} (M_{BH}/M_{\odot}) \text{ erg s}^{-1}$ , where  $M_{BH}$  is the mass of the central SMBH.

From the definition of the ionization parameter  $\xi = L_{ion}/nr^2$  (Tarter, Tucker & Salpeter 1969), where  $n$  is the average absorber number density and  $L_{ion}$  is the source ionizing luminosity integrated between 1 and 1000 Rydberg, we can estimate the maximum distance  $r$  of the absorber from the central source. The column density of the gas  $N_H$  is a function of the density of the material  $n$  and the shell thickness  $\Delta r$ :  $N_H = n\Delta r$ . Making the reasonable assumption that the thickness is less than the distance from the source  $r$  and combining with the expression for the ionization parameter, we obtain the upper limit  $r < L_{ion}/\xi N_H$ . Moreover, a rough estimate of the escape velocity along the radial distance for a Keplerian disk can be derived from the equation  $v_{esc}^2 = 2GM_{BH}/r$ , which can be re-written as  $v_{esc} = (r_s/r)^{1/2}c$ .

Moreover, assuming a constant velocity for the outflow and the conservation of the total mass, we can roughly estimate the mass loss rate  $\dot{M}_{out}$  associated to these fast outflows as  $\dot{M}_{out} = 4\pi Cr^2nm_p v$ , where  $v$  is the outflow velocity,  $n$  is the absorber number density,  $r$  is the radial distance,  $m_p$  is the proton mass and  $C \equiv (\Omega/4\pi)$  is the covering factor, which in turn depends on the solid angle  $\Omega$  subtended by the absorber. From the definition of the ionization parameter  $\xi$ , this expression can then be re-written as  $\dot{M}_{out} = 4\pi C \frac{L_{ion}}{\xi} m_p v_{out}$ . The kinetic power carried by these outflows can then be estimated as  $\dot{E}_K \equiv \frac{1}{2} \dot{M}_{out} v_{out}^2$ .

It is also important to compare the fraction of mass that goes into accretion of the system with respect to that which is lost through these outflows. Following McKernan et al. (2007), we can derive a simple relation for the ratio between the mass outflow rate and

the mass accretion rate, i.e.  $\dot{M}_{out}/\dot{M}_{acc} \simeq 6000 C(v_{0.1}/\xi_{100})\eta_{0.1}$ , where  $v_{0.1}$  is the outflow velocity in units of  $0.1c$ ,  $\xi_{100}$  is the ionization parameter in units of  $100 \text{ erg s}^{-1} \text{ cm}$  and  $\eta = \eta_{0.1} \times 0.1$  is the accretion efficiency.

In Table 6.1 we report the main physical parameters for the UFOs detected in the radio-quiet AGN sample. We used the best-fit parameters from the Xstar photo-ionization modeling reported in Table 5.2 and the source parameters listed in Table A.5 (in Appendix A).

Instead, for the UFOs in the radio-loud AGN we derived the following parameters. Using the values of  $L_{ion} \simeq 2.2 \times 10^{44} \text{ erg s}^{-1}$ ,  $L_{ion} \simeq 2.3 \times 10^{44} \text{ erg s}^{-1}$  and  $L_{ion} \simeq 5.1 \times 10^{44} \text{ erg s}^{-1}$  (calculated extrapolating the power-law X-ray continuum) and the ionization parameter and column density values listed in Table 5.3, we obtain the limits of  $r < 2 \times 10^{16} \text{ cm}$  ( $<0.007 \text{ pc}$ ),  $r < 10^{18} \text{ cm}$  ( $<0.3 \text{ pc}$ ) and  $r < 4 \times 10^{16} \text{ cm}$  ( $<0.01 \text{ pc}$ ) for 3C 111, 3C 120 and 3C 390.3, respectively. Using the black hole mass estimates of  $M_{BH} \sim 3 \times 10^9 M_{\odot}$  for 3C 111 (Marchesini et al. 2004),  $M_{BH} \sim 5 \times 10^7 M_{\odot}$  for 3C 120 (Peterson et al. 2004) and  $M_{BH} \sim 3 \times 10^8 M_{\odot}$  for 3C 390.3 (Marchesini et al. 2004; Peterson et al. 2004), the values correspond to a location for the absorber within a distance of  $\sim 20 r_s$ ,  $\sim (5-10) \times 10^4 r_s$  and  $\sim 500 r_s$  from the SMBH, respectively. The expected variability time-scale of the absorbers from the light crossing time,  $t \sim r/c$ , is  $t \sim 600-700 \text{ ks}$  ( $\sim 7 \text{ days}$ ) for 3C 111,  $t \sim 1 \text{ yr}$  for 3C 120 and  $t \sim 15-20 \text{ days}$  for 3C 390.3, respectively.

We can use the velocity estimates to infer some characteristics of the ejection region of the UFOs. Therefore, for 3C 111 the escape velocity at the location of  $\sim 20 r_s$  is  $v_{esc} \sim 0.2c$ , which is larger than the measured outflow velocity of  $v_{out} \sim 0.041c$ . This implies that most likely the absorber is actually in the form of a blob of material which would eventually fall back down, possibly onto the accretion disk. For 3C 120, the measured outflow velocity  $v_{out} \sim 0.076c$  is equal to the escape velocity at a distance of  $\sim 200 r_s$  from the black hole. Therefore, if the launching region is further away than this distance, the ejected blob is likely to escape the system. Instead, concerning 3C 390.3, the measured velocity of  $v_{out} \sim 0.146c$  is larger than the escape velocity at  $\sim 500 r_s$  and equals that at a distance of  $\sim 50-60 r_s$ . Therefore, if the blob of material has been ejected from a location between, say,  $\sim 100 r_s$  and  $\sim 500 r_s$ , it has likely enough energy to eventually leave the system.

Substituting the estimated black hole mass for each source, we have  $L_{Edd} \simeq 3.9 \times 10^{47} \text{ erg s}^{-1}$  for 3C 111,  $L_{Edd} \simeq 6.5 \times 10^{45} \text{ erg s}^{-1}$  for 3C 120 and  $L_{Edd} \simeq 3.9 \times 10^{46} \text{ erg s}^{-1}$

for 3C 390.3, respectively. Using the relation  $L_{bol} \simeq 10L_{ion}$  (McKernan et al. 2007), we can estimate the bolometric luminosities:  $L_{bol} \simeq 2.2 \times 10^{45}$  erg s<sup>-1</sup> for 3C 111,  $L_{bol} \simeq 2.3 \times 10^{45}$  erg s<sup>-1</sup> for 3C 120 and  $L_{bol} \simeq 5.1 \times 10^{45}$  erg s<sup>-1</sup> for 3C 390.3, respectively. The ratio  $L_{bol}/L_{Edd}$  is almost negligible for 3C 111 but it is of the order of  $\sim 0.1$ – $0.4$  for 3C 120 and 3C 390.3. These two sources are emitting closer to their Eddington limits and therefore are possibly more capable of producing powerful outflows/ejecta that would eventually leave the system. This supports the conclusions from the estimates on the location of the ejection regions and the comparison of the outflow velocities with respect to the escape velocities.

Moreover, substituting the relative values, we can estimate the mass outflow rates of  $\dot{M}_{out} \simeq 2C M_{\odot} \text{ yr}^{-1}$ ,  $\dot{M}_{out} \simeq 17C M_{\odot} \text{ yr}^{-1}$  and  $\dot{M}_{out} \simeq 2C M_{\odot} \text{ yr}^{-1}$  for 3C 111, 3C 120 and 3C 390.3, respectively. Instead, the kinetic power carried by these outflows can be estimated to be  $\dot{E}_K \simeq 4.5 \times 10^{43} C$  erg s<sup>-1</sup>,  $\dot{E}_K \simeq 3 \times 10^{45} C$  erg s<sup>-1</sup> and  $\dot{E}_K \simeq 1.2 \times 10^{45} C$  erg s<sup>-1</sup> for 3C 111, 3C 120 and 3C 390.3, respectively. Note that, depending on the estimated covering factor, the kinetic power injected in these outflows can be substantial, possibly reaching significant fractions ( $\sim 0.01$ – $0.5$ ) of the bolometric luminosity and can be comparable to the typical jet power of these sources of  $\sim 10^{44}$ – $10^{45}$  erg s<sup>-1</sup>, the latter being the power deposited in the radio lobes (Rawlings & Saunders 1991). Finally, we can estimate ratios between the mass outflow and accretion rates to be  $\dot{M}_{out}/\dot{M}_{acc} \sim 2C$  for 3C 111,  $\dot{M}_{out}/\dot{M}_{acc} \sim 40C$  for 3C 120 and  $\dot{M}_{out}/\dot{M}_{acc} \sim 2C$  for 3C 390.3, respectively.

However, it is important to stress that the exact values of the mass outflow rate ( $\dot{M}_{BH}$ ), the kinetic power ( $\dot{E}_K$ ) and the mass outflow/accretion rate ratio ( $\dot{M}_{out}/\dot{M}_{acc}$ ) depend on the unknown covering fraction of the material,  $C$ . A rough estimate of the global covering fraction of these absorbers, averaged over all lines of sight, can be derived from the fraction of sources showing blue-shifted Fe K absorption lines:  $C = \Omega/4\pi \simeq f$ , where  $\Omega$  is the solid angle (e.g. Crenshaw et al. 1999).

For the large sample of radio-quiet AGN we have a fraction of  $f \sim 0.4$ – $0.6$  (see §3.4.2), therefore  $C \sim 0.4$ – $0.6$ . Instead, from the small and incomplete sample of five radio-quiet AGN we have  $C \simeq f = 3/5 \sim 0.6$ . However, this covering fraction crude estimate has been derived from a very small sample which may be affected by many biases. Therefore, the previous estimate should be considered with caution. Nevertheless, it is interesting to note

the consistency of the covering fraction for both radio-quiet and radio-loud AGN classes,  $C \sim 0.4\text{--}0.6$ . This suggests that the geometrical distribution of the absorbing material is not very collimated but large opening angles are favored.

We note that the general characteristics of the outflows with velocities greater than  $10^4$  km/s ( $\simeq 0.03c$ ), the so called Ultra-fast Outflows, are completely consistent among the type 1 and type 2 radio-quiet AGN and radio-loud AGN (in particular for the BLRGs studied here). This strengthens the idea that we are actually observing the same physical phenomenon in both AGN classes. In particular, we can summarize the general properties of UFOs derived in this Thesis as:

- **Incidence:** the statistical incidence of UFOs in the large radio-quiet sample of  $\simeq 35\%$  has been discussed in detail in §3.4.2. In particular, it is equivalent between type 1 and type 2 sources, being  $\simeq 35\%$  and  $\simeq 30\%$ , respectively. However, if we consider also possible velocity underestimates due to the unknown inclination angle of the flow and the fraction of spectra with low S/N, this fraction could be as large as  $\simeq 40\text{--}60\%$ . For the five BLRGs we found a fraction of 3/5 (see §4.3), that corresponds to  $\sim 60\%$ . However, we stress that this small sample is not indeed complete and cannot be considered yet as completely representative of the whole radio-loud population. It is interesting to note that these fractions are consistent with the frequency of luminous quasar observed having fast outflows, such as BAL/NAL-QSOs (e.g. Ganguly & Brotherton 2008).
- **Velocity:** the velocity distribution of UFOs can be well represented by that from the large radio-quiet sample reported in Fig. 3.6. The absorbers are systematically outflowing with velocities in the range  $\simeq 10^4\text{--}10^5$  km/s ( $\simeq 0.03\text{--}0.3c$ ), with the peak and mean value at  $\simeq 0.1c$ .
- **Columns:** the column densities involved are large, in the range  $N_H \simeq 10^{22}\text{--}10^{24}$  cm $^{-2}$  (see Table 5.2 and Table 5.3). This suggests that the UFOs can possibly be Compton-thick, at least in their innermost regions.
- **Ionization:** the ionization state of the material is also extreme, in the range  $\log \xi \simeq 3\text{--}6$  erg s $^{-1}$  cm $^{-2}$  (see Table 5.2 and Table 5.3). In this case the most abundant ions are helium- and hydrogen-like iron, as all the lighter elements are almost completely

ionized. This means that UFOs can essentially be detected only through Fe XXV and Fe XXVI K-shell absorption.

- **Location:** the distance of the UFOs from the central SMBH is estimated to be  $r < 0.01\text{--}0.1$  pc ( $< 10^2\text{--}10^5 r_s$ ) (see §6.3 and Table 6.1). This favours the identification of these phenomena with accretion disk winds/outflows, as opposed to winds from the more distant BLR or molecular torus, as suggested for the WAs (see §1.3.1).
- **Covering fraction:** as already discussed previously in this section, the covering fraction of the UFOs is consistent in both radio-quiet and radio-loud sources with being  $C \sim 0.4\text{--}0.6$ . Thus, as an ensemble, these absorbers cover about one-half of the sky as seen by the central continuum source. This provides an important geometric constraint indicating that the distribution of the absorbing material cannot be very collimated and large opening angles are favored. In particular, the opening angle of the flow with respect to the polar axis correspond to  $\sim 60^\circ$ . This suggests a UFO geometry very similar to the accretion disk wind model of Proga & Kallman (2004) showed in Fig. 6.8. Overall this is also consistent with the covering fraction of  $\sim 0.5$  derived for the UV and classical X-ray warm absorbers detected in Seyfert 1 galaxies (e.g. George et al. 1998; Crenshaw et al. 1999).
- **Luminosity:** the estimated bolometric luminosities of the sources in the observations with detected UFOs can be comparable to the associated Eddington luminosities, i.e.  $L_{bol} \simeq 0.01\text{--}1 L_{Edd}$  (see §6.3 and Table 6.1). The plot of the bolometric luminosity of the sources in each observation with respect to the relative Eddington luminosity is reported in Fig. 6.6.
- **Mass outflow rates:** the mass outflow rate of the UFOs can be of the order of a few  $\sim M_\odot \text{yr}^{-1}$ . This is then comparable, or even higher, than the accretion rate, i.e.  $\dot{M}_{out} \sim \dot{M}_{acc}$  (see §6.3 and Table 6.1). This means that these outflows can potentially generate significant mass and energy losses from the system. However, it is important to stress that such large mass ejections would require intermittent outflows in order to permit the long-lasting growth of the central super-massive black hole.
- **Kinetic power:** the kinetic power of the UFOs is in the range  $\dot{E}_K \simeq 10^{43}\text{--}10^{45}$  erg s $^{-1}$ . This means that their energetic is significant, being comparable to

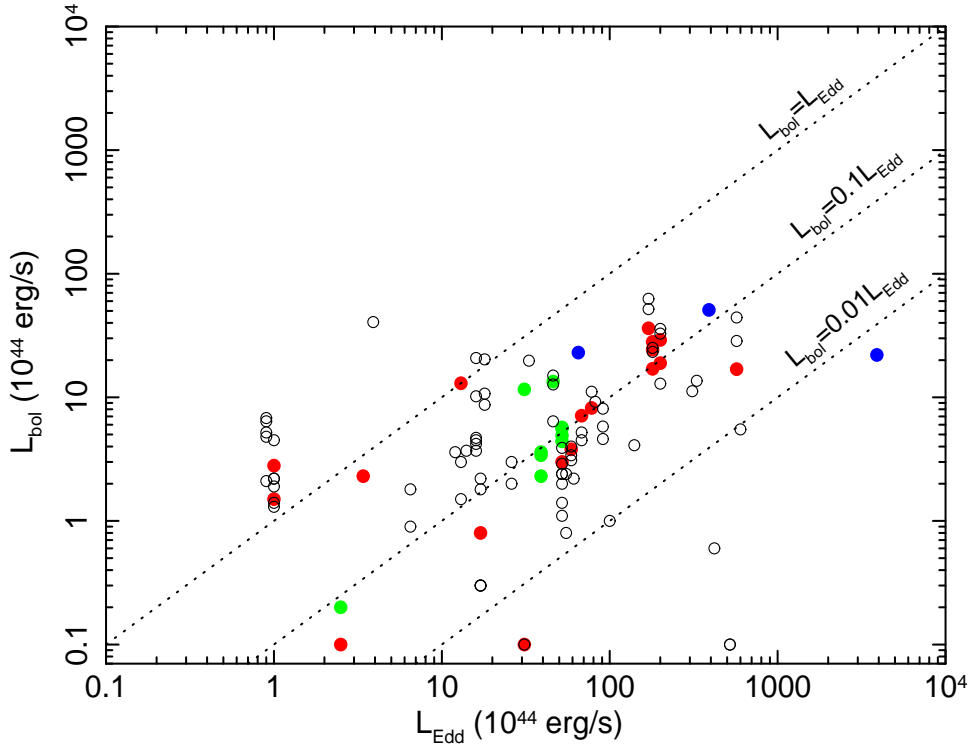


Figure 6.6: Eddington luminosity with respect to the bolometric luminosities for all the observations analyzed in this Thesis. In particular, observations of RQ AGN with detected UFOs (red filled circles), observations of RQ AGN with Fe K absorbers with  $v_{out} < 10^4$  km/s (green filled circles), observations of BLRGs with detected UFOs (blue filled circles) and observations of RQ AGN without the detection of UFOs (empty circles). The diagonal lines refer to  $L_{bol}/L_{Edd}$  ratios of 1, 0.1 and 0.01, respectively. It should be noted that the Eddington luminosity is directly proportional to the SMBH mass.

the bolometric luminosity of the sources ( $\sim 10^{43}$ – $10^{46}$  erg/s) and to the jet power ( $\sim 10^{44}$ – $10^{45}$  erg/s) for the radio-loud AGN (see §6.3 and Table 6.1).

We looked at some general trends or correlations among the different physical parameters. We considered the data from the warm absorbers in radio-quiet AGN studied by McKernan et al. (2007), the warm absorber detected in the BLRG 3C 382 by Torresi et al. (2009) and Reeves et al. (2009) and the parameters derived in this Thesis for the Fe K absorbers in both radio-quiet and radio-loud AGN.

The plot in Fig. 6.7 shows a clear correlation between the velocity and the ionization parameter of the absorbers. There seems to be a threshold at the velocity  $\sim 10^4$  km/s and ionization parameter of  $\log \xi \sim 3$ – $4$  erg s $^{-1}$  cm. The WAs are distributed only in the lower

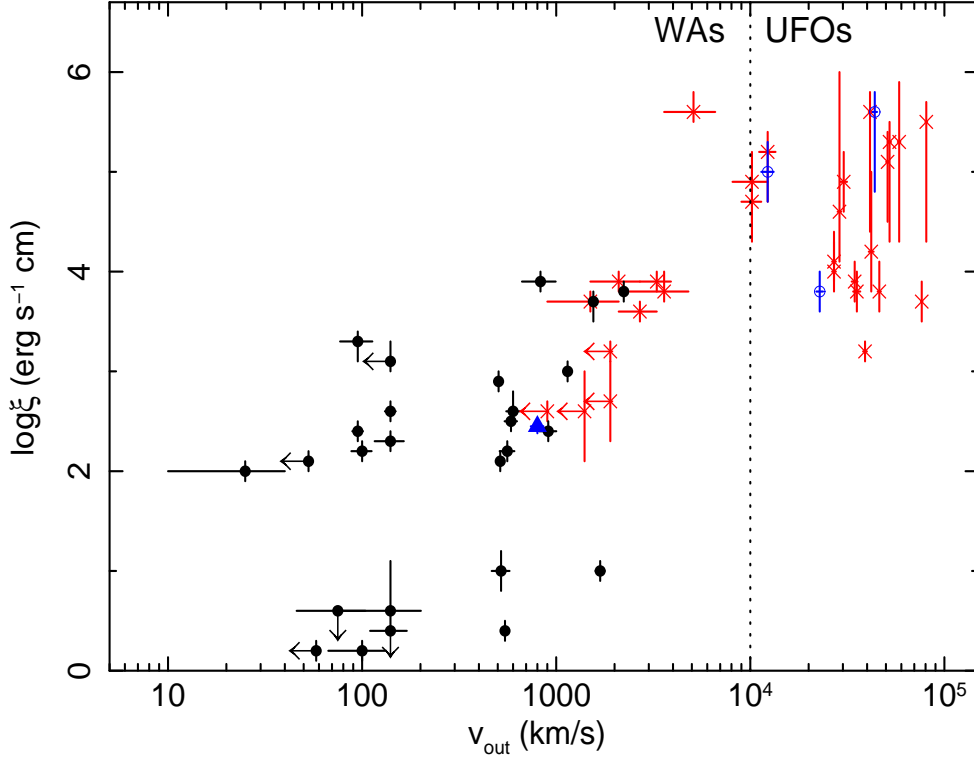


Figure 6.7: Ionization parameter with respect to the outflow velocity of the warm absorbers in radio-quiet AGN studied by McKernan et al. (2007) (black filled circles), the warm absorber detected in the BLRGs 3C 382 by Torresi et al. (2009) and Reeves et al. (2009) (blue filled triangle), the Fe K absorbers from our radio-quiet AGN sample (red crosses) and the Fe K absorbers from our radio-loud AGN sample (blue open circles). The vertical dotted line refer to the threshold velocity between WAs and UFOs at  $10^4$  km/s.

left part of the diagram and the UFOs only in the upper right portion, i.e. faster outflows are more highly ionized. In particular, there seems to be a simple linear relation between velocity and ionization, i.e.  $v_{out} \propto \xi$ .

Moreover, in Fig. 6.8 we can see a similar correlation also between the outflow velocity and the column density, i.e. faster outflows have higher total column densities. This could indicate an underlying dependence on the absorber shell thickness or density. In particular, if we assume a constant density, this mean that the fastest outflows are more compact.

Finally, in Fig. 6.9 we can note another correlation between the ionization parameter and the absorber column density. This shows that more highly ionized absorbers, that are also faster, have higher associated column densities. This is at odd with what expected

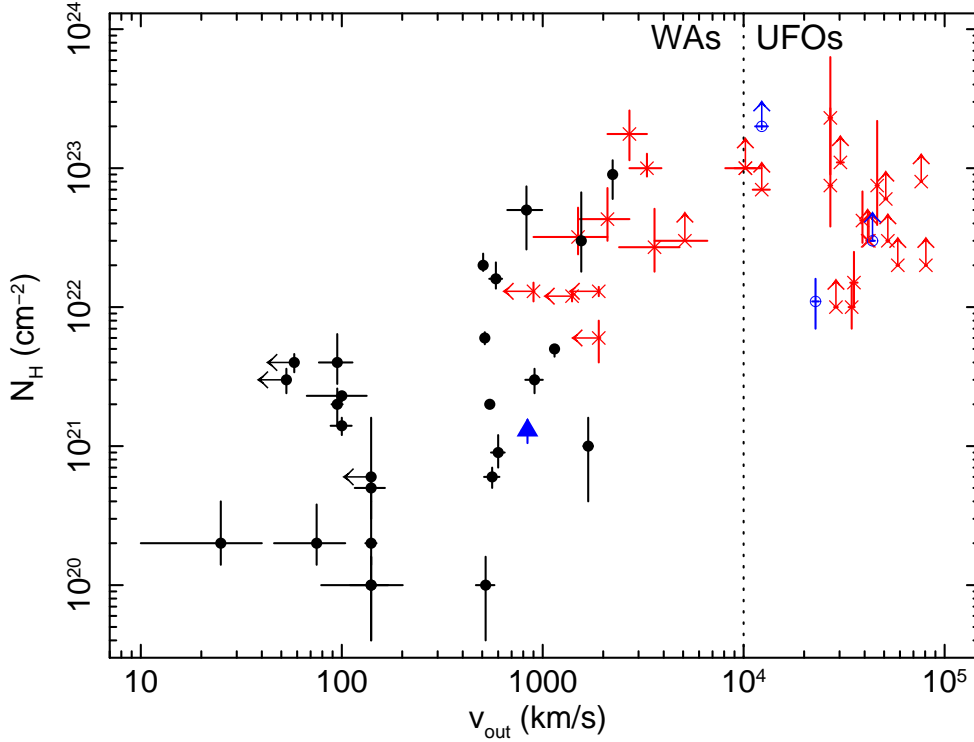


Figure 6.8: Column density with respect to the outflow velocity of the warm absorbers in radio-quiet AGN studied by McKernan et al. (2007) (black filled circles), the warm absorber detected in the BLRGs 3C 382 by Torresi et al. (2009) and Reeves et al. (2009) (blue filled triangle), the Fe K absorbers from our radio-quiet AGN sample (red crosses) and the Fe K absorbers from our radio-loud AGN sample (blue open circles). The vertical dotted line refer to the threshold velocity between WAs and UFOs at  $10^4$  km/s.

from the definition of the ionization parameter. In fact, if we assume compact absorbers ( $\Delta r \sim r$ ), we have  $N_H = n\Delta r \sim nr$  and  $\xi = L/nr^2 \sim L/N_H r$ . Therefore, the ionization parameter should decrease for increasing column densities. However, the observed relation could indicate a stronger dependence on the distance, in other words, for similar ionizing luminosities, the highest ionization absorbers are more compact and closer to the SMBH than the others.

These are indeed intriguing results and could indicate some general trends for winds/outflows in AGN. Moreover, they could possibly suggest also an underlying connection between WAs and UFOs. For instance, we cross-correlated our results with the 10 radio-quiet AGN with detected WAs in McKernan et al. (2007), which are also included in our sample, and found that in about 40% of them we detected UFOs and in

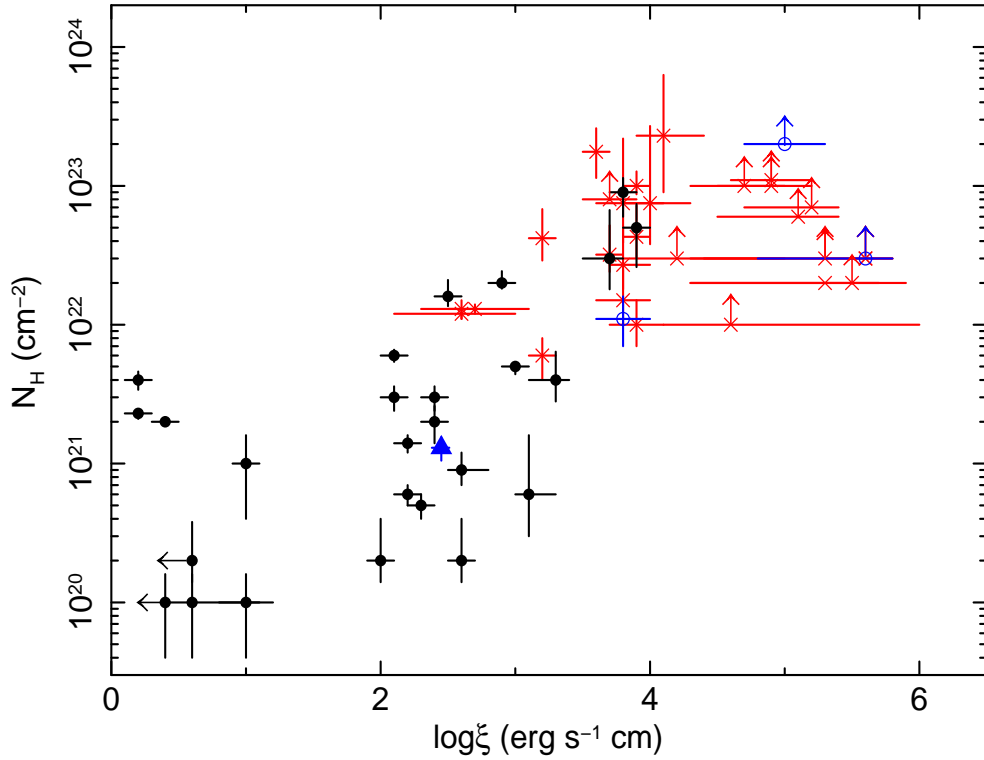


Figure 6.9: Column density with respect to the ionization parameter of the warm absorbers in radio-quiet AGN studied by McKernan et al. (2007) (black filled circles), the warm absorber detected in the BLRGs 3C 382 by Torresi et al. (2009) and Reeves et al. (2009) (blue filled triangle), the Fe K absorbers from our radio-quiet AGN sample (red crosses) and the Fe K absorbers from our radio-loud AGN sample (blue open circles).

general in about 60% of them we found Fe K absorbers. However, stress that our previous discussion is not conclusive at all and we plan to explore in more detail these important correlations in future works.

Table 6.1: Estimated parameters for the UFOs detected in the radio-quiet AGN sample. (1) Source name. (2) observation ID. (3) Upper limit on the distance from the central SMBH in units of pc and  $r_s$ . (4) Ratio between the bolometric and Eddington luminosities (5) Estimated mass outflow rate. (6) Estimated ratio of the mass outflow and accretion rates for  $\eta \equiv 0.1$ . (7) Kinetic power of the outflows. (8) Ratio between the kinetic power of the outflow and the source bolometric luminosity. It is important to note that the estimated values (5), (6), (7) and (8) depend on the covering fraction of the absorber  $C$ .

| Source         | OBSID      | $r$<br>(pc ( $r_s$ ))       | $L_{bol}/L_{Edd}$ | $\dot{M}_{out}$<br>( $M_{\odot} \text{ yr}^{-1}$ ) | $\dot{M}_{out}/\dot{M}_{acc}$ | $\dot{E}_K$<br>( $10^{42} \text{ erg s}^{-1}$ ) | $\dot{E}_K/L_{bol}$ |
|----------------|------------|-----------------------------|-------------------|--|-------------------------------|---|---------------------|
| (1)            | (2)        | (3)                         | (4)               | (5)  | (6)                           | (7)   | (8)                 |
| Type 1 objects |            |                             |                   |  |                               |   |                     |
| NGC 4151       | 0402660201 | 0.010 ( $8.2 \times 10^3$ ) | 0.05              | 1.5  | 112.2                         | 600.0   | 3.333               |
| IC4329A        | 0147440101 | 0.100 ( $1.1 \times 10^5$ ) | 1.00              | 3.1  | 14.5                          | 810.0   | 0.620               |
| NGC 3783       | 0112210101 | 2.230 ( $7.6 \times 10^4$ ) | 0.09              | $\simeq 0$   | $\simeq 0$                    | $\simeq 0$                                      | $\simeq 0$          |
|                | 0112210201 | 1.560 ( $5.3 \times 10^4$ ) | 0.06              | $\simeq 0$   | $\simeq 0$                    | $\simeq 0$                                      | $\simeq 0$          |
|                | 0112210501 | 1.680 ( $5.7 \times 10^4$ ) | 0.09              | 2.7  | 47.9                          | 1.2   | 0.004               |
| NGC 3516       | 0401210401 | 0.110 ( $2.9 \times 10^4$ ) | 0.11              | 0.6  | 6.0                           | 0.4   | 0.001               |
|                | 0401210501 | 0.040 ( $1.1 \times 10^4$ ) | 0.09              | 0.4  | 5.3                           | 0.6   | 0.001               |
|                | 0401210601 | 0.020 ( $4.6 \times 10^3$ ) | 0.08              | 0.6  | 8.3                           | 2.1   | 0.005               |
|                | 0401211001 | 0.110 ( $2.7 \times 10^4$ ) | 0.11              | 1.1  | 11.4                          | 4.5   | 0.008               |
| Mrk 509        | 0130720101 | 0.007 ( $5.2 \times 10^2$ ) | 0.10              | 2.3  | 8.1                           | 1894.4  | 1.114               |
|                | 0306090201 | 0.006 ( $4.8 \times 10^2$ ) | 0.14              | 0.8  | 2.1                           | 434.2   | 0.179               |
|                | 0306090401 | 0.022 ( $1.6 \times 10^3$ ) | 0.16              | 2.7  | 5.9                           | 2926.0  | 1.041               |
| Ark 120        | 0147190101 | 0.015 ( $1.0 \times 10^3$ ) | 0.15              | 2.5  | 5.1                           | 5155.7  | 1.772               |
| Mrk 279        | 0302480501 | 4.520 ( $1.3 \times 10^6$ ) | 0.29              | $\simeq 0$   | $\simeq 0$                    | $\simeq 0$                                      | $\simeq 0$          |
| Mrk 79         | 0400070201 | 0.008 ( $1.5 \times 10^3$ ) | 0.10              | 5.0  | 42.9                          | 1154.3  | 1.626               |
| NGC 4051       | 0109141401 | 0.001 ( $2.8 \times 10^2$ ) | 0.08              | 0.1  | 0.3                           | 0.8   | 0.040               |
|                | 0157560101 | 0.001 ( $3.5 \times 10^4$ ) | 0.04              | 0.2  | 146.4                         | 135.2   | 13.520              |
| Mrk 766        | 0304030301 | 0.001 ( $5.4 \times 10^3$ ) | 1.50              | 0.1  | 1.6                           | 4.8   | 0.032               |
|                | 0304030501 | 0.012 ( $1.5 \times 10^5$ ) | 2.80              | 2.5  | 54.0                          | 577.1   | 2.061               |
| Mrk 841        | 0205340401 | 0.005 ( $9.0 \times 10^2$ ) | 0.11              | 0.6  | 4.1                           | 19.8  | 0.024               |
| ESO 323-G77    | 0300240501 | 0.055 ( $2.3 \times 10^4$ ) | 0.37              | 2.6  | 13.6                          | 6.0   | 0.005               |
| 1H419-577      | 0148000201 | 0.014 ( $1.0 \times 10^3$ ) | 0.21              | 1.5  | 2.6                           | 49.4  | 0.014               |
| Mrk 290        | 0400360601 | 0.258 ( $5.9 \times 10^4$ ) | 0.06              | 3.4  | 53.0                          | 1899.2  | 4.998               |
| Mrk 205        | 0124110101 | 0.006 ( $1.4 \times 10^2$ ) | 0.03              | 2.1  | 7.6                           | 610.5   | 0.361               |
| PG 1211+143    | 0112610101 | 0.900 ( $6.2 \times 10^4$ ) | 0.10              | 153.5  | 492.1                         | 73933.3   | 39.118              |
| Type 2 objects |            |                             |                   |  |                               |   |                     |
| MCG-5-23-16    | 0302850201 | 0.122 ( $3.2 \times 10^4$ ) | 0.06              | 4.3  | 86.9                          | 1620.7  | 5.402               |
| NGC 4507       | 0006220201 | 0.001 ( $4.2 \times 10^3$ ) | 0.68              | 0.2  | 5.2                           | 172.6   | 0.750               |
| NGC 7582       | 0112310201 | 0.001 ( $3.5 \times 10^2$ ) | 0.01              | 0.5  | 305.3                         | 926.6   | 92.660              |

## 6.4 Comparison with accretion disk winds/outflows models

The physical characteristics of the UFOs discussed in the previous section strongly point towards an association with winds/outflows from the inner regions of putative accretion disk in AGN. In fact, simulations of accretion disks in AGN ubiquitously predict the generation of mass outflows.

For instance, the location, geometry, column densities, ionization and velocities of our detected UFOs are in good agreement with the AGN accretion disk wind model of Proga & Kallman (2004) (see Fig. 6.10). In this particular model the wind is driven only by radiation pressure from the accretion disk and the opacity is essentially provided by UV lines. They assumed the typical parameters for luminous AGN and quasars, that is: a black hole with  $M_{BH} = 10^8 M_{\odot}$ , accreting at  $\dot{M}_{acc} = 1.8 M_{\odot} \text{yr}^{-1}$ , which gives the system a dimensionless accretion rate parameter of  $0.5 \dot{M}_{Edd}$  and bolometric luminosity  $L = 0.5 L_{Edd}$ . The properties of the outflow are calculated over  $\sim 10\text{--}1000 r_s$ , making the wind very geometrically thick.

Three main components can be identified in this model, depending on the angle with respect to the polar axis (see Fig. 6.10): a hot, low density and extremely ionized (up to  $\log \xi \sim 10^8 \text{ erg s}^{-1} \text{ cm}$ ) flow in the polar region ( $\theta < 55^\circ$ ); a dense, warm and fast equatorial outflow from the disk ( $\theta > 67^\circ$ ); and a transition zone ( $55^\circ < \theta < 67^\circ$ ) in which the disk outflow is hot and struggles to escape the system. The ionization state of the wind decreases from polar to equatorial regions. Instead, the column densities increase from polar to equatorial, up to very Compton-thick values ( $N_H > 10^{24} \text{ cm}^{-2}$ ). The outflows can easily reach large velocities, even higher than  $\sim 10^4 \text{ km/s}$ .

In addition, Schurch et al. (2009) simulated the resultant X-ray spectra from the AGN accretion disk wind model of Proga & Kallman (2004) for different lines of sight through the wind flow. The properties of the resulting spectra depend on the viewing angle and clearly reflect the distinct regions apparent in the original hydrodynamic simulation (see Fig. 6.10).

Equatorial lines of sight have total column densities that are always very Compton-thick and are dominated by essentially nearly neutral absorption and Compton scattering, irrespective of the level of variability exhibited by the simulated wind, and thus show little spectral variability. Similarly, highly equatorial lines of sight usually intercept relatively small column densities of material and are too highly ionized to imprint significant features

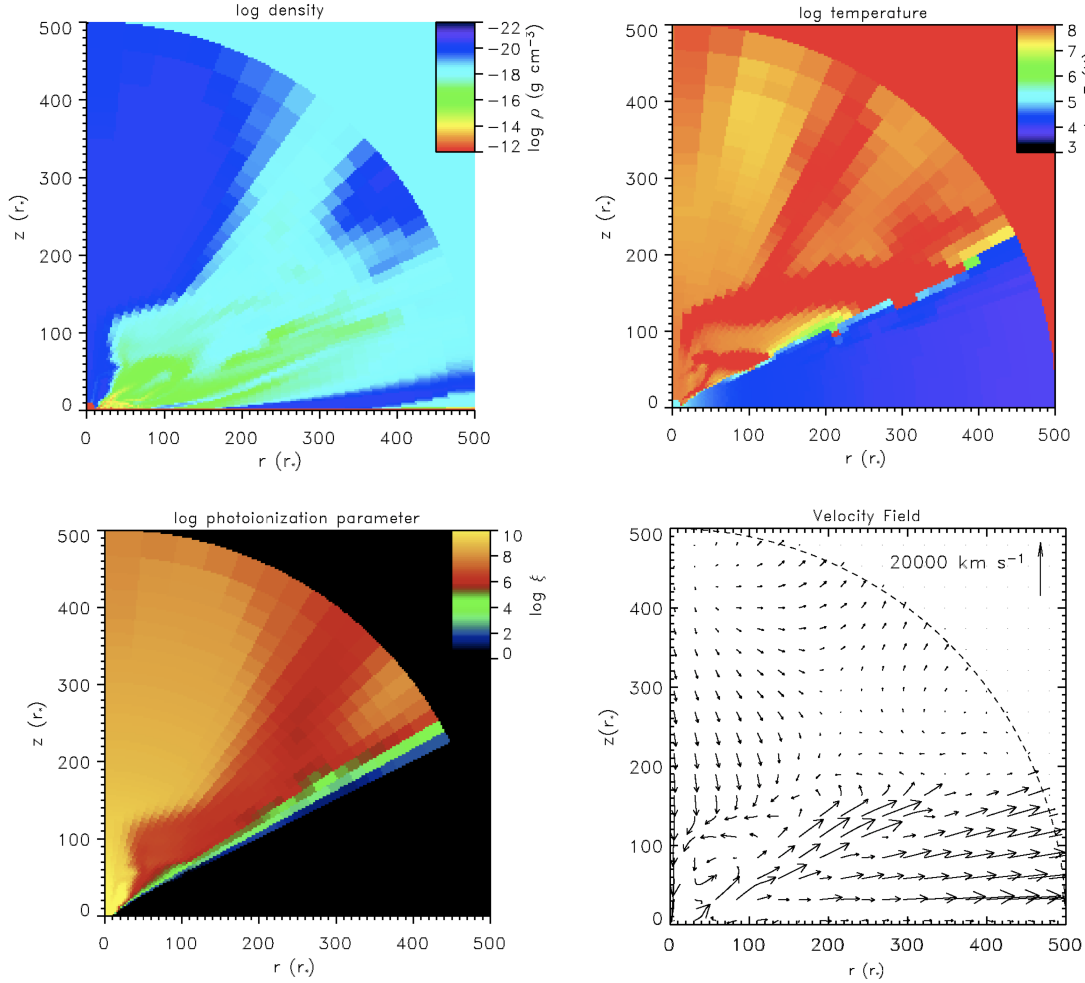


Figure 6.10: Illustrative maps of the AGN accretion disk (radiation-driven) wind model simulated by Proga & Kallman (2004). *Top left*: color density map. *Top right*: color gas temperature map. *Bottom left*: color photo-ionization parameter map. *Bottom right*: Map of the velocity field (N.B. the apparent inflow of matter in the polar region is only a simulation artifact, due to the fact that the authors did not consider the presence of a jet). In all the cases, the vertical axis refer to the disk rotation axis and the horizontal refer to the mid-plane of the disk and the distances are expressed in units of Schwarzschild radii.

in the X-ray spectrum (possibly only weak highly ionized Fe K-shell absorption lines, in agreement with the UFO detections).

Instead, lines of sight through the transition region of the simulated outflow, where the density is high ( $n \sim 10^8 - 10^{10} \text{ cm}^{-3}$ ) and the column density can reach values up to  $N_H \sim 10^{24} \text{ cm}^{-2}$ , result in spectra that have considerable absorption features from ionized species imprinted in the X-ray spectrum. The majority of this region has an

intermediate/high ionization parameter of  $\log \xi \sim 3-5$  erg s<sup>-1</sup> cm. This strongly suggests that this material could be observed in the spectrum through Fe K-shell absorption lines from Fe XXV and Fe XXVI, in complete agreement with our detection of UFOs. Moreover, if the X-ray source is considerably extended with respect to the wind material, this would support the partial covering models for the absorbers (e.g. Miller et al. 2009 and references therein).

Hydrodynamic wind simulations are highly inhomogeneous in density, column and ionization and have strong rotational velocity components (see Fig. 6.10). Therefore the outflow, especially in its innermost regions, is rather unstable. In particular, the outflow properties through the transition region show considerable variability and this is expected to be reflected by the spectral features associated with this region, i.e. by the corresponding blue-shifted Fe XXV/XXVI K-shell absorption lines. Variability is predicted on time-scales as short as  $\sim 10^5-10^7$  s (for a black hole with  $M_{BH} \sim 10^8 M_{\odot}$ ) and they are mainly due to bulk column density variations which, in turn, are due to density variations.

As stated by the authors, the dense equatorial flow ( $\theta > 67^\circ$ ), with very high column densities, results in almost complete attenuation of the spectrum by Compton scattering for lines of sight in that direction. The majority of the material in this region is essentially neutral, resulting in considerable absorption being imprinted on the X-ray spectrum. If such outflows are common in AGN, the opening angle of this flow would imply that  $\sim 20-30\%$  of AGN should be very Compton thick, even without a contribution from the putative molecular torus (as also stated by Elvis 2000, see §1.4.1).

Furthermore, this model predicts that high accretion rate AGN (with  $L_{bol}$  comparable to  $L_{Edd}$ ) are likely to be strongly affected by obscuration, in sharp contrast to the clean picture that is generally assumed, based on the observed relation between the opening angle of the obscuring torus and AGN luminosity (e.g. Polletta et al. 2008, and references therein). Therefore, these outflows should have a very strong impact on the observed X-ray spectrum of many AGN, particularly given the large covering fraction of the high-density regions of the flow.

Proga & Kallman (2004) and Schurch et al. (2009) also stated that it is possible that some parts or blobs of the flow, especially in the innermost regions, do not have enough power to allow a “true” wind to be generated. In these cases, a considerable amount of material is driven to large-scale heights above the disk but the velocity of the material

is insufficient for it to escape the system and it will eventually fall back onto the disk. Despite returning to the accretion disk at larger radii, while it is above the disk, this material can imprint features on the observed X-ray spectrum (e.g. Dadina et al. 2005 and references therein). This can indeed be the case for some of the UFOs discussed in the previous section.

This overall picture is also partially in agreement with what predicted by the “aborted jet” model by Ghisellini et al. (2004). This model was actually proposed to (at least in part) explain the high energy emission in radio-quiet quasars and Seyfert galaxies. It postulates that outflows and jets are produced by every black hole accretion system. Blobs of material can then be ejected intermittently and sometimes can travel only for a short radial distance (because their outflow velocity is lower than the escape velocity) and eventually fall back, colliding with the others approaching. Therefore, the flow can manifest itself as erratic high-velocity ejections of gas from the inner disk and it is expected that some outflows/blobs are not fast enough to escape the system and will eventually fall back onto the disk. An intriguing possibility could be that these outflows are generated by localized ejection of material from the outer regions of a bubbling corona, which emits the bulk of the X-ray radiation (Haardt & Maraschi 1991), in analogy with what observed in the solar corona during the Coronal Mass Ejection events (e.g. Low 1996). The velocity and frequency of these strong events should then be limited to some extent, in order not to cause the disruption or evaporation of the corona itself. Such extreme phenomena could then be the signatures of the turbulent environment close to the super-massive black hole.

The detection of UFOs in both radio-quiet and radio-loud galaxies suggests a similarity of their central engines and demonstrates that the presence of strong relativistic jets do not exclude the existence of winds/outflows from the putative accretion disk. Moreover, it has been demonstrated by us in Torresi et al. (2009) and independently by Reeves et al. (2009) that a warm absorber is indeed present also in BLRGs and this indicates that jets and slower winds/outflows can coexist in the same source, even beyond the broad-line region.

However, BLRGs are radio-loud galaxies and they have powerful jets. So, probably, the central engine of the radio-loud AGN is more efficient than that of radio-quiet in ejecting blobs with outflow velocities larger than the escape velocities (at certain radial distances). Moreover, the fact that for BLRGs we are observing down to the outflowing stream at

intermediate angles to the jet ( $\sim 15\text{--}30^\circ$ ; e.g. Eracleous & Halpern 1998) could suggest that the fast winds/outflows we observe are at greater inclination angles with respect to the jet axis, somewhat similar to what expected for accretion disk winds. These blobs would then not be able to undergo the processes which instead accelerate the jet particles to velocities close to the speed of light (e.g. Elvis 2000).

For instance, studies of Galactic stellar-mass black holes, or micro-quasars, showed that wind formation occurs in competition with jets, i.e. winds carry away matter halting their flow into jets (e.g. Neilsen & Lee 2009). Given the well-known analogy between micro-quasars and their super-massive analogues, one would naively expect a similar relationship for radio-loud AGN. The BLRGs 3C 111 and 3C 120 are regularly monitored in the radio and X-ray bands with the VLBA and RXTE as part of a project aimed at studying the disk-jet connection (e.g. Marscher et al 2002). In both these sources we have detected UFOs (see §4.3), and indeed in both cases the 4–10 keV fluxes measured with Suzaku corresponded to historical low(est) states if compared to the RXTE long-term light curves. For instance, correlated spectroscopic observations of 3C 111, where the shortest variability timescales are predicted ( $t \sim 7$  days), during low and high jet continuum states could provide, in a manner analogous to micro-quasars, valuable information on the synergy among disk, jet, and outflows, and go a long way towards elucidating the physics of accretion in radio-quiet and radio-loud AGN.

However, whether it is possible to produce such ultra-fast outflows with velocities up to  $\sim 0.3c$  only through line-driving is unclear. Moreover, the material needs to be shielded from the high X-ray ionizing flux in the inner regions of AGN, otherwise it would become over-ionized and the efficiency of this process would be drastically reduced. As already discussed in §1.4.2, other mechanisms as well can accelerate winds from accretion disks, in particular radiation pressure through Thomson scattering and magnetic forces.

In fact, Ohsuga et al. (2009) proposed a unified model of inflow/outflow from accretion disks in AGN based on radiation-MHD simulations. Disk outflows with helical magnetic fields, which are driven either by radiation-pressure force or magnetic-pressure are ubiquitous in their simulations. In particular, in their case A (see Fig. 1.7) a geometrically thick, very luminous disk forms with a luminosity  $L \sim L_{Edd}$ , which effectively drives a fast Compton-thick wind with velocities up to  $\sim 0.2\text{--}0.3c$ . It is important to note that the models of Ohsuga et al. (2009) include both radiation and magnetic forces which,

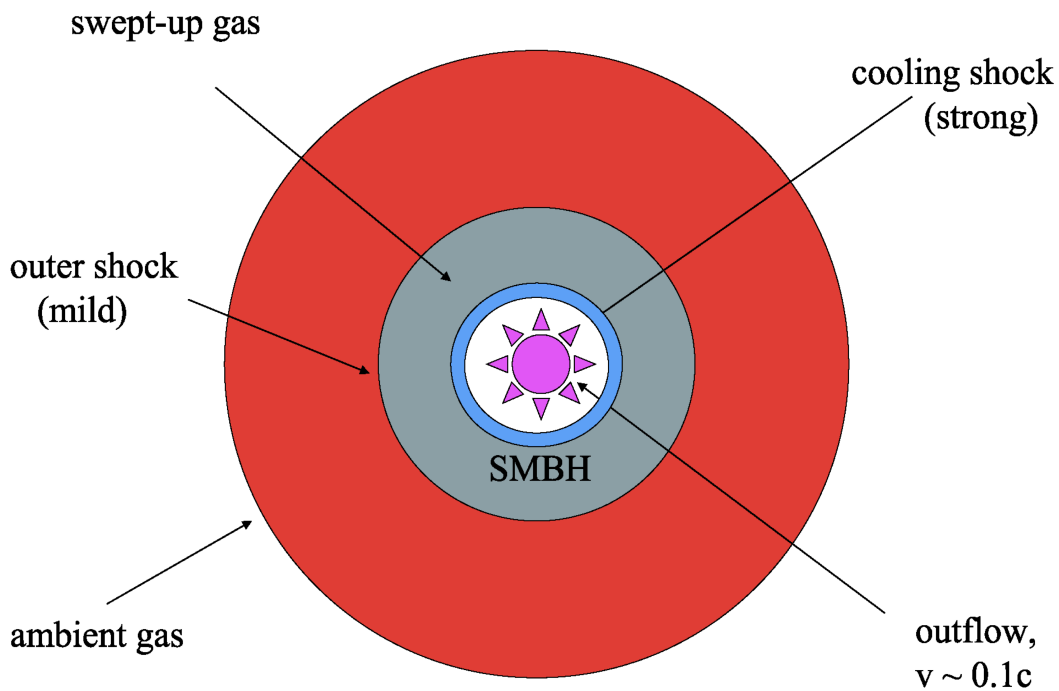


Figure 6.11: Schematic view of the shock pattern resulting from the impact of an AGN Eddington wind on the interstellar gas of the host galaxy. The model is from King (2009), see text for more details.

depending on the state of the system, can generate both relativistic jets and disk winds.

Moreover, King & Pounds (2003) and King (2009) showed that black holes accreting at or above the Eddington rate probably produce fast Compton-thick winds. They considered only radiation-pressure and therefore winds can be effectively generated by low magnetized accretion disks as well.

In particular, King (2009) examined the properties of winds/outflows from SMBH accreting with modest Eddington ratios, i.e.  $L \simeq 0.001-1L_{Edd}$ . This is a condition similar to what has been found for the UFOs in AGN (see §6.3 and Fig. 6.6). All the treatment is purely analytical and no numerical simulations has been applied. The author assumed that the outflows are quasi-spherical. Winds of this type likely have electron scattering optical depth  $\tau \sim 1$  measured from infinity. This means that on average every emitted photon scatters about once before escaping to infinity, which in turn suggests that the total wind momentum must be of the order of the photon momentum, i.e.  $\dot{M}_{out}v \simeq L_{Edd}/c$ , as is for example also found for winds in hot stars. Therefore, in this case the main wind driver is

radiation-pressure, through Compton scattering.

We can use the definition of the Eddington luminosity  $L_{Edd} = \dot{M}_{Edd} \eta c^2$ , where  $\eta$  is the accretion radiative efficiency and it is usually assumed  $\eta \sim 0.1$  for black hole accretion systems. In the case of modest Eddington outflows,  $\dot{m} = \dot{M} / \dot{M}_{Edd} \simeq 1$ , the momentum relation naturally gives an estimate of the typical velocity of the wind  $v \simeq \eta c \sim 0.1c$ . This is consistent with the UFO velocity distribution showed in Fig. 3.6 and the location of the peak and mean value exactly  $\sim 0.1c$  is likely not only a coincidence.

From the mass conservation and the definition of the ionization parameter, the author derives a simple linear relation between the outflow velocity and the ionization state of the gas,  $v_{out} \propto \xi$ . This trend is remarkably similar to correlation between the outflow velocity and ionization parameter reported in Fig. 6.7. Moreover, from the wind momentum and mass rates, the author estimated that the typical ionization parameter of the wind is quite large,  $\log \xi \sim 4 \text{ erg s}^{-1} \text{ cm}$ . Therefore, this gas should be observable in the X-ray spectrum mainly through Fe XXV and XXVI K-shell absorption lines. Then, it follows that the wind has a kinetic power of  $\dot{E}_K = \frac{1}{2} \dot{M}_{out} v^2 \simeq \frac{v}{c} L_{Edd} \simeq \frac{\eta}{2} L_{Edd} \simeq 0.05 L_{Edd}$  (similar to the UFOs, see §6.3).

In fact, King (2009) clearly stated that *"Eddington winds from AGN are likely to have velocities of  $\sim 0.1c$  and show the presence of helium- or hydrogen-like iron"*. Therefore, these characteristics strongly point toward an association with Ultra-fast Outflows from the innermost regions of AGN with Eddington winds/outflows from the putative accretion disk. The strong similarities with the model of King (2009) suggest that the main acceleration process for UFOs is radiation-pressure (and not, or not only, UV line pressure), possibly through Compton scattering. Moreover, since the wind moves with a sub-luminal speed of  $\sim 0.1c$ , it can persist long after the AGN is observed to have become sub-Eddington and this may be the reason why some AGN showing signs of super-Eddington phenomena are seen to have sub-Eddington luminosities.

From an evolutionary point of view, outflows driven by black holes in AGN offer a simple way to explain some cosmological feedback processes and to establish relations between the SMBH and its host galaxy, hence potentially explaining important relations such as the  $M_{BH} - \sigma$  (e.g. Ferrarese & Merritt 2000). Such outflows, like those here discussed, are plausible as AGN must feed at high rates to grow the observed SMBH masses. For instance, King (2009) demonstrated that the Eddington winds from AGN

accretion disks can have important impacts on the interstellar medium of the host galaxy. Fig. 6.11 shows a schematic view of the shock pattern resulting from the impact of the Eddington winds studied by King (2009) on the interstellar gas of the host galaxy.

A SMBH accreting close to the Eddington rate drives a fast wind, with velocity  $v \sim 0.1c$ , whose ionization state makes it observable in X-ray absorption lines. The outflow collides with the ambient gas in the host galaxy and is slowed, forming a strong shock. The inverse Compton effect from the AGN's radiation field rapidly cools the shocked gas, removing its thermal energy and strongly compressing and slowing it over a very short radial extent. This gas may be observable in inverse Compton continuum and lower excitation emission lines associated with lower velocities. The cooled gas exerts the pre-shock ram pressure on the galaxy's interstellar gas and sweeps it up into a thick shell, similar to a "snowplough". This shell's motion drives a milder outward shock into the ambient interstellar medium. This shock then propagates beyond the black hole's sphere of influence on a time-scale shorter than  $\sim 3 \times 10^5$  yr. Outside this radius, the shell stalls unless the black hole mass has reached a value that satisfies the  $M_{BH}-\sigma$  relation.

The interaction between the AGN wind and its host galaxy establishing the  $M_{BH}-\sigma$  relation is crucially "momentum-driven" rather than "energy-driven". In other words, the wind interacts with the host galaxy interstellar medium mainly through its ram pressure rather than its energy which, in turn, is equivalent to requiring efficient shock cooling. Finally, the author noted that galaxy-wide outflows with velocities significantly exceeding the typical stellar velocity dispersion,  $\sigma$ , probably result from minor Eddington accretion episodes with low gas fractions. These can appear as fossil outflows in galaxies where there is little current AGN activity.

# Chapter 7

## Future perspectives

We performed extensive simulations to test the capabilities offered by the future X-ray observatories, namely Astro-H and IXO, regarding the detection of narrow absorption lines in the Fe K band. In particular, the high effective area and high energy resolution of the calorimeters on board these future missions will provide important improvements in the study of Ultra-fast Outflows (UFOs) that we have detected in the X-ray spectra of radio-quiet and radio-loud AGN.

### 7.1 Astro-H

Astro-H is the next mission in the series of Japanese X-ray satellites (Takahashi et al. 2008), following Suzaku (Astro-E2). It will be developed mainly by the Japan Aerospace Exploration Agency (JAXA) and it is planned to be launched in 2013.

As long as the spacecraft is concerned, it will be similar to Suzaku (see Appendix D) in terms of orbit, pointing and tracking capabilities, although its mass will be larger. Astro-H will be inserted into a circular orbit with altitude  $\sim 500$ – $600$  km and inclination of  $\sim 30^\circ$ . Also the science operations will be similar to Suzaku, with pointed observations of each target until the integrated observing time is accumulated, and then slewing to the next target. A typical observation will require 40–100 ks of integrated observing time, which corresponds to 1–2.5 days of clock time.

However, the instruments on board Astro-H will be very different from those of Suzaku. It will offer a combination of wide band X-ray spectroscopy ( $E \simeq 3$ – $80$  keV) provided by multi-layer coating, focusing hard X-ray mirrors and hard X-ray imaging detectors, and high energy resolution soft X-ray spectroscopy ( $E \simeq 0.3$ – $10$  keV) provided by thin-foil X-ray

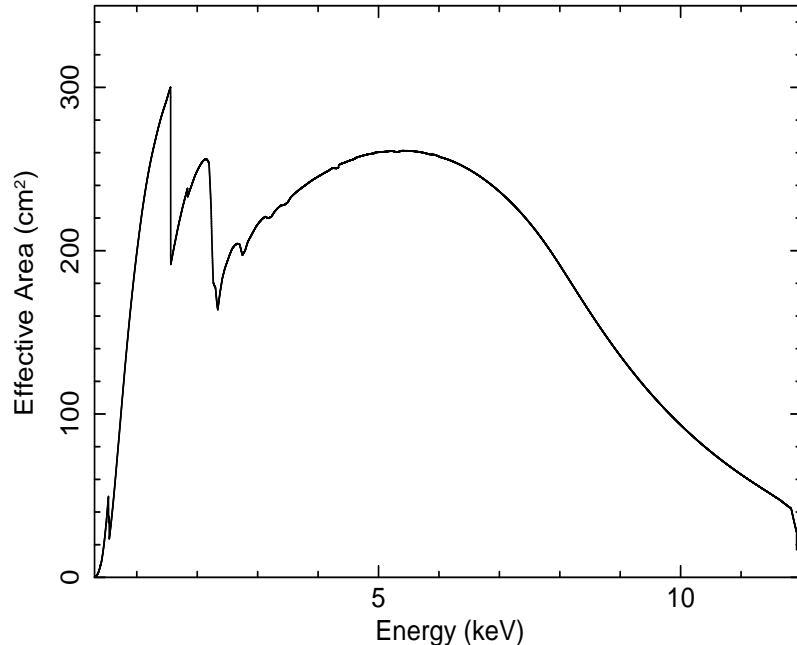


Figure 7.1: Expected effective area of the XCS on board Astro-H in the 0.3–12 keV energy band.

optics and a micro-calorimeter array. The mission will also carry an X-ray CCD camera as a focal plane detector for a soft X-ray telescope and a non-focusing soft gamma-ray detector. With these instruments, Astro-H will cover a very wide energy range from 0.3 keV up to 600 keV. All instruments operate simultaneously. To increase the focal length, the satellite will be equipped with an extensible optical bench, which will increase it up to 12 m. Therefore, the simultaneous broad bandpass, coupled with high spectral resolution ( $\Delta E \sim 7$  eV up to  $\sim 10$  keV) by the micro-calorimeter will provide important improvements in all branches of observational X-ray astronomy.

### 7.1.1 Simulations of the X-ray Calorimeter Spectrometer

We focused on the X-ray Calorimeter Spectrometer (XCS), which is developed by an international collaboration between ISAS/JAXA and the NASA/Goddard Space Flight Center. This instrument will provide an effective area of  $\sim 250$  cm<sup>2</sup> at  $\sim 6$  keV (see Fig. 7.1) and, more importantly, a high energy resolution of  $\text{FWHM} \simeq 7$  eV from  $\sim 0.1$  keV up to  $\sim 12$ –13 keV.

We derived the 2–10 keV flux limits for the  $5\sigma$  detection of a narrow absorption line in the 3–11 keV band of the XCS (the same results also apply to narrow emission lines).

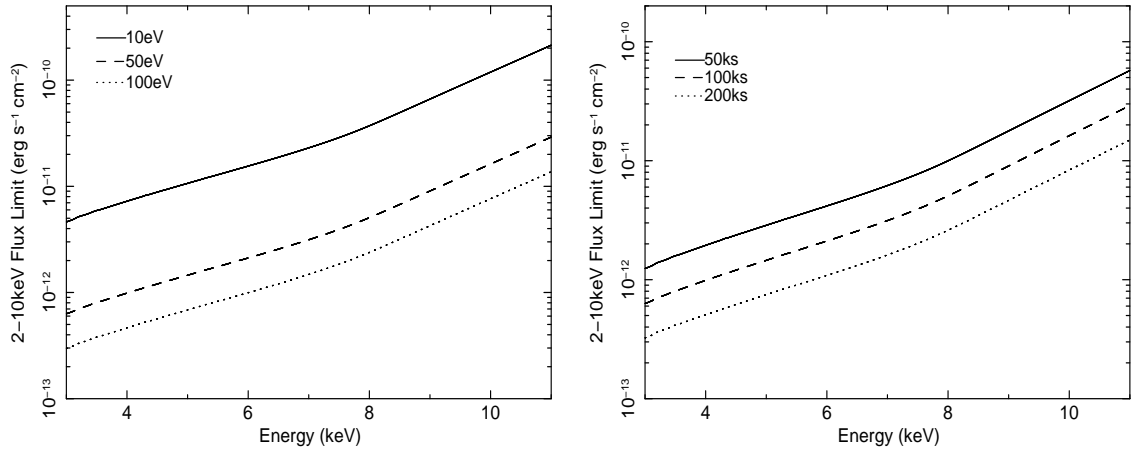


Figure 7.2: 2–10 keV flux limits for the  $5\sigma$  detection of narrow absorption lines with the XCS in the 3–11 keV band. *Left panel:* different line equivalent widths of 10 eV (solid line), 50 eV (dashed line) and 100 eV (dotted line) for a fixed exposure time of 100 ks. *Right panel:* different exposure times of 50 ks (solid line) 100 ks (dashed line) and 200 ks (dotted line) for a fixed line equivalent width of 50 eV.

We assumed a typical AGN power-law continuum with  $\Gamma = 2$ . The background has been modeled with two components: the internal non-X-ray background, parametrized with an energy-independent photon flux of  $2 \times 10^{-2}$  ph cm $^{-2}$  keV $^{-1}$  and a contribution from unresolved AGN (treated as in De Luca & Molendi 2004).

The flux limits for the detection of absorption lines of EW=10, 50 and 100 eV for an exposure of 100 ks are reported in the left panel of Fig. 7.2. We can note that the sources in our radio-quiet and radio-loud AGN samples have a mean 2–10 keV flux of  $\sim 2 - 3 \times 10^{-11}$  erg s $^{-1}$  (see §3.2 and Table 4.1, respectively), therefore we would be able to detect narrow absorption lines of EW=10 (50, 100) eV up to  $E \sim 8$  (10) keV for the majority of them ( $\sim 70$ – $80\%$ ). Instead, in the right panel of Fig. 7.2 we show the flux limits for a line of EW=50 eV (which corresponds to the mean value of the blue-shifted absorption lines, see §3.4.3) for different exposure times of 50, 100 and 200 ks.

In Fig. 7.3 and Fig 7.4 we report the realistic XCS spectra simulations of the UFOs detected in the Suzaku spectra of the three BLRGs, 3C 111, 3C 390.3 and 3C 120. We used the baseline models reported in Table 4.3 and the absorber parameters from the Xstar fit in Table 5.3. The exposure is 100 ks (comparable to that of the Suzaku observations).

We find that all the blue-shifted absorption lines will be detectable with high significance and, thanks to the high energy resolution, they will be resolved and their

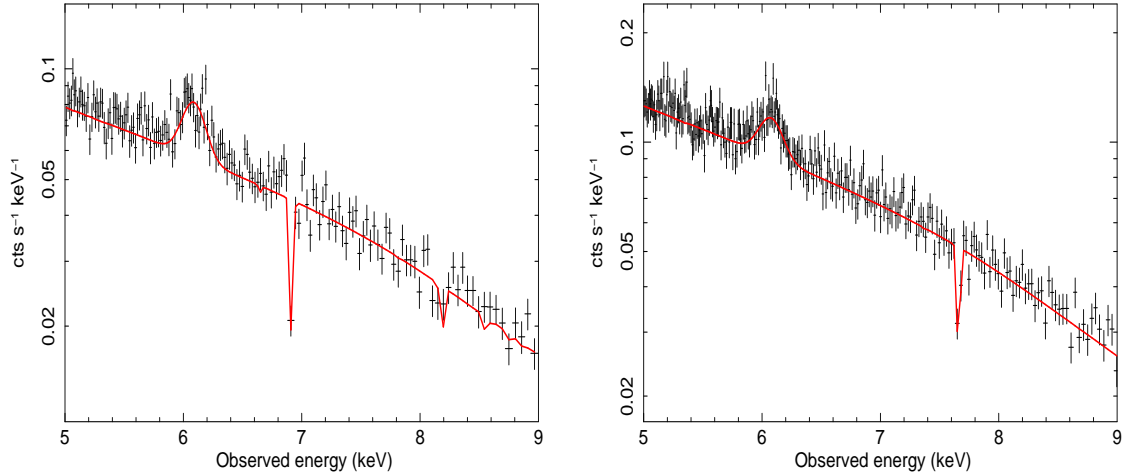


Figure 7.3: Simulated XCS spectra of the UFOs detected in the Suzaku spectra of the BLRGs 3C 111 (*left panel*) and 3C 390.3 (*right panel*). We used the baseline models reported in Table 4.2 and the best fit parameters of the absorbers reported in Table 5.3. We used an exposure of 100 ks.

velocity broadening (down to values of  $\sim 100\text{--}200$  km/s) will be measured with  $\sim 10\%$  errors. This will allow to better constrain the column density and ionization parameter of the absorbers. Moreover, also the other parameters of the lines will be measured with improved accuracy with respect to the previous Suzaku XIS-FI observations, such as a factor of  $\sim 5$  more for the EW and  $\sim 10$  for the centroid energy and blue-shift velocity. Ideally, one would be able to study in good detail also the profile of the lines and/or follow their spectral variability on time scales greater than  $\sim 50\text{--}100$  ks. This demonstrates that important improvements in the study of Ultra-fast Outflows in AGN will be provided in the next future by the calorimeter on board Astro-H.

## 7.2 IXO

The International X-ray Observatory (IXO) is a future large X-ray observatory (Parmar 2009). It is a joint project of the European Space Agency (ESA), the American National Aeronautics and Space Administration (NASA) and the Japanese Japan Aerospace Exploration Agency (JAXA). It is planned to be launched by 2021 and it will be directly inserted into an 800,000 km semi-major axis halo orbit around the Sun-Earth L2 libration point. The observatory will be equipped with a  $\simeq 3.3$  m diameter grazing-incidence mirror assembly with a 20 m focal length and several X-ray instruments, such as: the

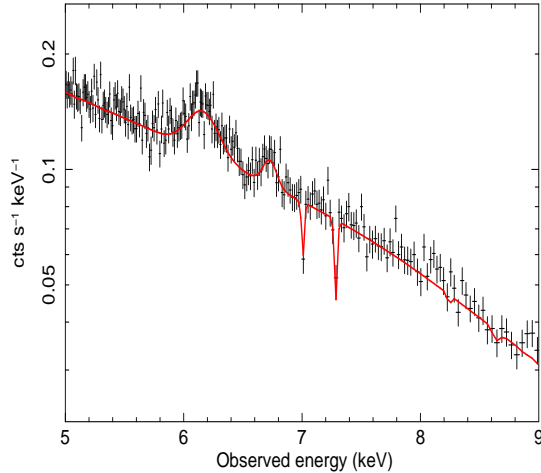


Figure 7.4: Simulated XCS spectrum of the UFO detected in the Suzaku spectrum of the BLRG 3C 120. We used the baseline models reported in Table 4.2 and the best fit parameters of the absorbers reported in Table 5.3. We used an exposure of 100 ks.

X-ray Microcalorimeter Spectrometer (XMS), the Wide Field Imager (WFI), the Hard X-ray Imager (HXI), the X-ray Grating Spectrometer (XGS), the High Timing Resolution Spectrometer (HTRS) and the X-ray Polarimeter (XPOL).

### 7.2.1 Simulations of the X-ray Microcalorimeter Spectrometer

We concentrated on the XMS, which is expected to provide a very high effective area ( $\simeq 0.65 \text{ m}^2$  at 6 keV), coupled with a high energy resolution ( $\text{FWHM} \simeq 2.5 \text{ eV}$ ) from  $\sim 0.1 \text{ keV}$  up to  $\sim 12\text{--}13 \text{ keV}$ . Its unprecedented sensitivity will give a huge improvement to high resolution X-ray spectroscopy in the Fe K band.

We derived the 2–10 keV flux limits for the  $5\sigma$  detection of narrow absorption lines in the 3–11 keV band of the XMS (the same results also apply to narrow emission lines). We assumed a typical AGN power-law continuum with  $\Gamma = 2$ . The background has been modeled with two components: the internal non-X-ray background, parametrized with an energy-independent photon flux of  $2 \times 10^{-2} \text{ ph cm}^{-2} \text{ keV}^{-1}$  and the contribution from unresolved AGN (treated as in De Luca & Molendi 2004). We used the core-glass response matrix<sup>1</sup>, with a 2.5 eV (FWHM) resolution at all energies and 0.5 eV bin channels.

The 2–10 keV flux limits for the detection of an absorption line with equivalent width of 10 eV and 50 eV are reported in the left and right panels of Fig. 7.5, respectively. We tested different exposure times, from 100 ks down to 10 ks and 5 ks, to check the lower

<sup>1</sup>A list of different XMS response matrices is provided at <http://ixo.gsfc.nasa.gov>

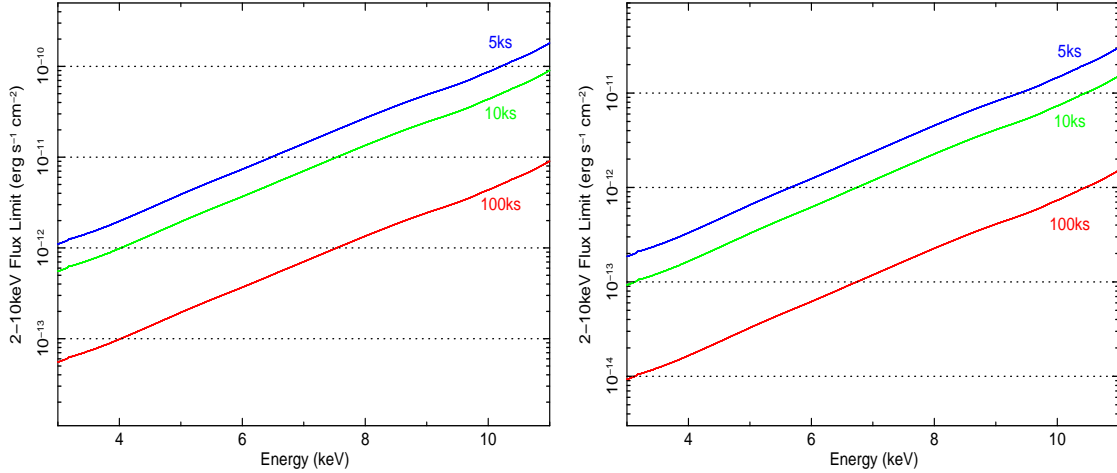


Figure 7.5: 2–10 keV flux limits for the  $5\sigma$  detection of narrow absorption lines with the XMS in the 3–11 keV band. *Left panel:* line equivalent width of 10 eV. *Right panel:* line equivalent width of 50 eV. Different exposure times are tested: 100 ks (red), 10 ks (green) and 5 ks (blue). The 2–10 keV flux levels of  $10^{-14}$ ,  $10^{-13}$ ,  $10^{-12}$ ,  $10^{-11}$  and  $10^{-10}$   $\text{erg s}^{-1} \text{cm}^{-2}$  are marked by the horizontal dotted lines.

limits for variability studies. Focusing in the region where Fe K absorption lines are more probably expected to be present ( $\sim 6\text{--}9$  keV), it will be possible to clearly detect lines with  $\text{EW} = 10$  eV (50 eV) in sources with 2–10 keV fluxes of  $\sim 10^{-12}$  ( $\sim 10^{-13}$ )  $\text{erg s}^{-1} \text{cm}^{-2}$  (for an exposure of 100 ks). Moreover, it will be possible to perform variability studies on time-scales as short as 5 (10) ks for sources with 2–10 keV fluxes of  $\sim 10^{-11}$  ( $\sim 10^{-12}$ )  $\text{erg s}^{-1} \text{cm}^{-2}$ .

We also compared the narrow lines detection flux limits for two different proposed IXO calorimeter response matrices: the core-glass and the core-pore matrices, the latter considering also the loss in effective area due to the gratings. The comparison of the effective area of the XMS using the two response matrices is shown in Fig. 7.6, left panel. Instead, the comparison of the flux limits for the detection of lines in the two cases is reported in the right panel of Fig. 7.6. The main difference in the 3–11 keV band is a lower effective area for the core-pore, which results in an increase in the flux limits for the narrow line detection of about the 60% with respect to the core-glass. We did not consider energies lower than 3 keV because of the presence of several instrumental edges in the effective areas and also because the background treatment is much more complicated. However, as it can be seen in the left panel of Fig. 7.6, the core pore matrix would provide a higher effective area at energies below  $\sim 1$  keV and above  $\sim 11$  keV.

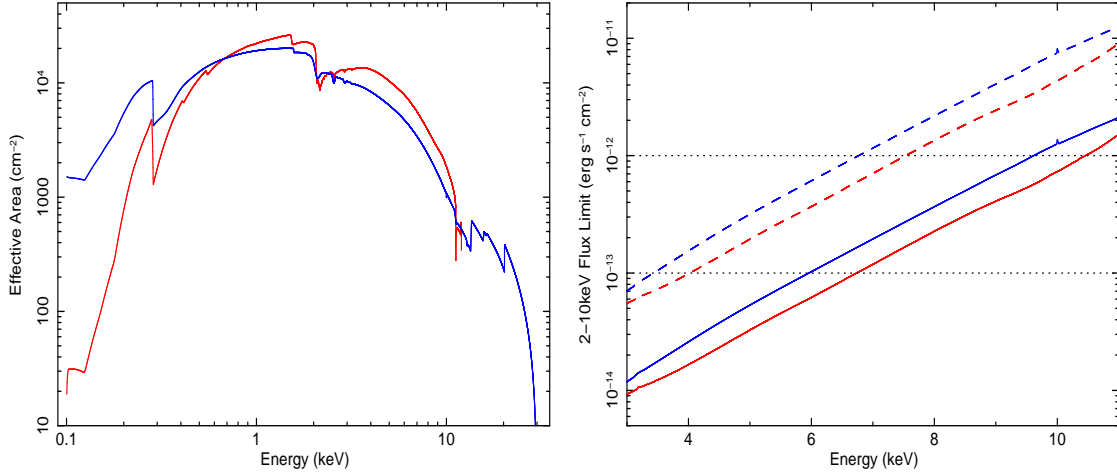


Figure 7.6: *Left panel:* Comparison of the XMS effective areas using the core glass (red) and core pore (blue) response matrices. *Right panel:* comparison of the 2–10 keV flux limits for the  $5\sigma$  detection of narrow absorption lines with the XMS in the 3–11 keV band using the core glass (red) and core pore (blue) response matrices, respectively. The equivalent widths of the lines are  $EW=10$  eV (dashed line) and  $EW=50$  eV (solid line), respectively. The exposure time is 100 ks.

We also carried out realistic spectral simulations of highly ionized absorbers observed with the IXO calorimeter. We focused in the Fe K band, between 6 keV and 9 keV. The absorbers were modeled using the photo-ionization code Xstar and we assumed the typical parameters of the UFOs discussed in this Thesis.

We assumed a simple power-law SED with photon index  $\Gamma=2$ , ranging from the IR to hard X-rays. Solar abundances were assumed. We used a high turbulent velocity value of 1000 km/s, as commonly assumed for such extreme absorbers. For the 2–10 keV flux, we assumed a typical value from the radio-quiet AGN sample of  $\sim 10^{-11}$  erg s<sup>-1</sup> cm<sup>-2</sup>. We used the core-glass response matrix and subtracted the proper background from a circular region of 5 arcsec radius. The exposure time was fixed to 100 ks.

The expected XMS spectra from an absorber with total column density  $N_H=10^{23}$  cm<sup>-2</sup> and ionization parameter  $\log\xi=3$  erg s<sup>-1</sup> cm and  $\log\xi=4$  erg s<sup>-1</sup> cm are reported in the left and right panels of Fig. 7.7, respectively. For simplicity we considered a null outflow velocity. The vertical lines in the figure indicate the rest-frame energies of the most intense expected Fe XXV (He $\alpha$  at 6.697 keV and He $\beta$  at 7.880 keV) and Fe XXVI (Ly $\alpha$  at 6.966 keV and Ly $\beta$  at 8.25 keV) resonant absorption lines. These narrow highly ionized Fe absorption lines are clearly visible in the spectrum with high significance.

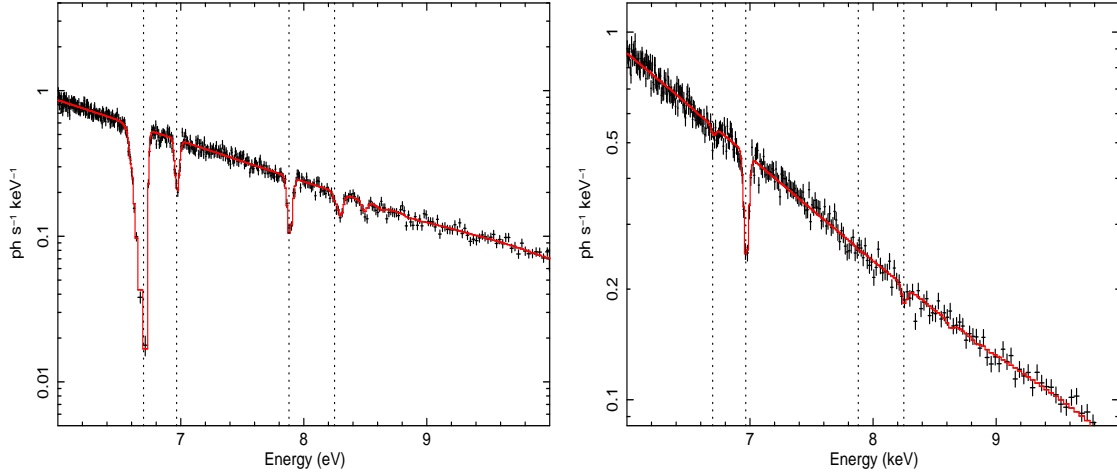


Figure 7.7: Simulated realistic XMS spectra of highly ionized absorbers in the 6–9 keV band. The column density was assumed to be  $N_H=10^{23}$  cm $^{-2}$  and the ionization parameter  $\log\xi=3$  erg s $^{-1}$  cm (*left panel*) and  $\log\xi=4$  erg s $^{-1}$  cm (*right panel*), respectively. The redshift was assumed to be null and the turbulent velocity was fixed to 1000 km/s.

The unprecedented high energy resolution and high throughput of the XMS will allow to measure their centroid energy with unprecedented accuracy and will help to unambiguously set their identification and measure any velocity shifts. It will be possible also to study the line profile with much details and to measure velocity broadening of the lines as low as  $\sim 50$ – $100$  km/s at 6 keV. The fine structure components of the lines will be discerned and also the most intense lines from a wide range of iron ions would be measurable.

In conclusion, the high effective area and high energy resolution of the calorimeter on board IXO will allow not only to detect weak absorption (emission) lines in the 3–11 keV band but also to investigate their short time-scale variability ( $\sim 5$ – $10$  ks), for sources with 2–10 keV fluxes as low as  $\sim 10^{-12}$  erg s $^{-1}$  cm $^{-2}$ . It will be possible also to discriminate the lines from different Fe ionic species and measure with high accuracy their broadening and centroid energy. This will allow to better constrain the parameters of the highly ionized absorbers, such as column density, ionization level, turbulent velocity, outflow velocity, location and to even study their dynamics. These characteristics are all of fundamental importance to bring real improvements in our understanding of high energetic phenomena, such as those related with the studies of accretion and ejection in the central regions of AGN.

# Conclusions

We have performed a uniform and systematic search for blue-shifted Fe K absorption lines in the X-ray spectra of a sample of radio-quiet (44 sources for a total of 104 observations, see Table A.1. in Appendix A) and radio-loud (5 sources for 6 combined observations, see Table 4.1) AGN observed with XMM-Newton and Suzaku. We have detected several absorption lines in the  $\sim 7\text{--}10$  keV band ascribable to Fe XXV and/or Fe XXVI K-shell resonances in their spectra. The significance of the lines has been assessed through the standard F-test and also extensive Monte Carlo simulations. Their global probability to be generated by random fluctuations is very low,  $< 3 \times 10^{-8}$  for the sample of radio-quiet AGN (see §3.3.4) and in the range  $\simeq 10^{-8}\text{--}10^{-3}$  for the sources in the radio-loud sample (see §4.3). Furthermore, the detection of several lines in the spectra of the radio-quiet AGN sample have been independently confirmed by the MOS cameras on board XMM-Newton (see §3.3.5). These results allows us to overcome the publication bias that has been claimed for the blue-shifted Fe K lines and to clearly assess their global veracity (see §6.1 and §6.2).

We rule out any contamination by absorption from local ( $z \simeq 0$ ) or intermediate red-shift material. Therefore, these lines can genuinely be attributed to blue-shifted Fe K absorption intrinsic to the sources (see §6.1 and §6.2). The lines are systematically blue-shifted and the corresponding velocities can reach up to mildly relativistic values of  $\sim 0.2\text{--}0.3c$ .

This is consistent with the presence of Ultra-fast Outflows (UFOs) in several of these sources. In fact, in §1.3.2 we defined UFOs those highly ionized absorbers detected essentially through Fe XXV and Fe XXVI K-shell absorption lines and with outflow velocities  $v_{out} \geq 10^4$  km/s ( $\simeq 0.033c$ ), i.e. much greater than the maximum value for typical X-ray warm absorbers in AGN (e.g. Blustin et al. 2005; McKernan et al. 2007).

In §6.3 we reported a detailed description of the physical parameters of UFOs detected in the radio-quiet and radio-loud AGN samples. UFOs have been detected in  $\sim 35\%$  of

the sources of the radio-quiet AGN sample. This fraction is essentially equivalent between type 1 and type 2 objects. However, if we consider also possible velocity underestimates due to the unknown inclination angle of the flow and the fraction of XMM-Newton spectra with low S/N, this fraction could be more likely in the range  $\sim 40\text{--}60\%$ . For the five BLRGs that constitute our small radio-loud AGN sample we found evidence for UFOs in 3 out of 5 sources, which corresponds to a fraction of  $\sim 60\%$ . However, we warn that this small sample is far from being complete and therefore could not be fully representative of the whole radio-loud population.

From these fractions we can estimate the global covering fraction of UFOs to be  $C \sim 0.4\text{--}0.6$ . This provides an important geometric constraint, indicating that the distribution of the absorbing material cannot be very collimated and large opening angles are favored. The velocity distribution of UFOs can be well represented by that derived from the large radio-quiet sample and showed in Fig. 3.6, with values in the range  $\sim 10^4\text{--}10^5$  km/s ( $\sim 0.03\text{--}0.3c$ ) and a peak and mean value at  $\simeq 0.1c$ .

When modeled with the photo-ionization code Xstar, the blue-shifted Fe K absorption lines indicate that the absorbers associated with UFOs are highly ionized, with ionization parameters in the range  $\log \xi \sim 3\text{--}6$  erg s $^{-1}$  cm, and have large column densities, in the range  $N_H \sim 10^{22}\text{--}10^{24}$  cm $^{-2}$ . Moreover, their location has been estimated to be close to the central SMBH, at distances of less than 0.01–0.1 pc ( $< 10^2\text{--}10^5 r_s$ ).

These physical characteristics of UFOs strongly direct towards an association with winds/outflows from the inner regions of the putative accretion disks in AGN. In fact, simulations of accretion disks in AGN ubiquitously predict the generation of mass outflows. For instance, the location, geometry, column densities, ionization and velocities of our detected UFOs are in good agreement with the AGN accretion disk wind model of Proga & Kallman (2004) (see §6.4 and Fig. 6.8).

However, whether it is possible to produce such ultra-fast outflows with velocities up to  $\sim 0.3c$  only through line-driving is unclear. Moreover, the material needs to be shielded from the high X-ray ionizing flux in the inner regions of AGN, otherwise it would become over-ionized and the efficiency of this process would be drastically reduced. As already discussed in §6.4, other mechanisms as well can accelerate winds from accretion disks, in particular radiation pressure through Thomson scattering and magnetic forces.

Indeed, Ohsuga et al. (2009) performed radiation-MHD simulations of inflow/outflow

from accretion disks in AGN and demonstrated that fast winds/outflows are naturally generated through radiation or magnetic-pressure and can easily reach mildly relativistic velocities (see Fig. 1.7).

Moreover, King & Pounds (2003) and King (2009) showed that black holes accreting with modest Eddington rates are likely to produce fast Compton-thick winds. They considered only radiation-pressure and therefore fast winds can be effectively generated by low magnetized accretion disks as well. In particular, King (2009) derived that Eddington winds from AGN are likely to have velocities of  $\sim 0.1c$  and to be highly ionized, showing the presence of helium- or hydrogen-like iron. These properties strongly point toward an association of our detected UFOs from the innermost regions of AGN with Eddington winds/outflows from the putative accretion disk. Moreover, the strong similarities with the model of King (2009) suggest that the main acceleration process for UFOs is radiation-pressure, possibly through Compton scattering (see §6.4).

Therefore, accretion disk wind models predict that high accretion rate AGN (with  $L_{bol}$  comparable to  $L_{Edd}$ ) are likely to be strongly affected by obscuration, in contrast to the clean picture generally assumed, based on the observed relation between the opening angle of the obscuring torus and AGN luminosity (e.g. Polletta et al. 2008, and references therein). Therefore, these outflows should have a very strong impact on the observed X-ray spectrum of many AGN, particularly given their significant covering factors.

In fact, in §6.4 we showed that, depending on the covering fraction, the mass outflow rate of the UFOs can be comparable to the accretion rate and their kinetic power can correspond to a significant fraction of the bolometric luminosity and is comparable to the jet power. Therefore, UFOs may have the possibility of bringing significant amount of mass and energy outward, potentially contributing to the expected feedback from the AGN. In particular, King (2009) demonstrated that fast outflows driven by black holes in AGN can explain important connections between the SMBH and the host galaxy, such as the observed  $M_{BH}-\sigma$  relation (e.g. Ferrarese & Merritt 2000) (see §6.4 and Fig. 6.11).

The detection of UFOs in both radio-quiet and radio-loud galaxies suggests a similarity of their central engines and demonstrates that the presence of strong relativistic jets does not exclude the existence of winds/outflows from the putative accretion disk. We could actually be witnessing the same physical phenomenon in the two classes of objects and this can help us improve the understanding of the relation between the disk and the formation

of winds/jets in black hole accretion systems.

However, several questions remain open. The estimate of the covering factor  $C \sim 0.4$ – $0.6$  in § 6.3 might actually be only a lower limit. Fast outflows,  $v \sim 0.2$ – $0.4c$ , are expected to come from regions close to the central black hole and to be highly ionized. Thus, a slight increase in the ionization level of the absorbers would cause iron to be completely ionized, and the gas to become invisible in the energy range up to 9 keV (e.g. Schurch et al. 2009). In this case, a possible new diagnostic tool could be provided by absorption features of highly ionized Nickel. This could be within the reach of the calorimeter on the upcoming Astro-H mission, and on a longer timescale, on the most sensitive International X-ray Observatory (see §7.1.1 and §7.2.1).

It is also quite possible that most, *if not all*, radio-quiet and radio-loud AGN contain UFOs at present not visible simply because highly ionized. Future Astro-H and IXO calorimeter observations in the energy range 7–10 keV have the potential to test this hypothesis, which would imply a covering factor  $C \sim 1$  and thus an even more important role of the outflows in AGN-environment feedback models. In the future it would be very interesting to extend this analysis also to luminous quasars and study the similarities with the fast winds routinely observed in BAL-QSOs (e.g. Ganguly & Brotherton 2008 and references therein). Moreover, we plan to study with more detail the correlations among the different physical parameters of UFOs and to check possible relations with the X-ray warm absorbers (see §6.3).

Finally, we note that present X-ray telescopes (such as XMM-Newton, Chandra and Suzaku) are able to detect blue-shifted Fe K absorption lines in the spectra of AGN with just a sufficient level of accuracy. A substantial improvement is expected from the higher effective area and supreme energy resolution (down to  $\sim 2$ – $5$  eV) in the Fe K band offered by the calorimeters on board the future Astro-H and IXO missions. In particular, the lines will be resolved and also their profiles could be measured. The parameters of UFOs will be determined with unprecedented accuracy and possibly also their dynamics could be studied through time-resolved spectroscopy on short time-scales ( $< 100$  ks) (see §7.1.1 and §7.2.1).

# Acknowledgements

I am deeply thankful to my Supervisor Prof. Giorgio G.C. Palumbo and my Co-Supervisor Dr. Massimo Cappi for the beautiful and exciting research experience of the PhD in Astronomy with them. I think I have been very lucky to have had the possibility to work next to them and to be guided by them through my first steps into the career of Astronomer. Besides being two outstanding scientists, they are also two excellent persons and always have the time for a smile and to give precious advices. This work could not have been possible without the sharp intuition and perseverance of Dr. Massimo Cappi. I am also thankful to him, or I might say to Cappi-san, for the wonderful weekend we spent together visiting Tokyo and for the help in bringing me back to the airport safely...

I thank all the colleagues that I had the honor to work with on this topic in these years, especially Dr. J. N. Reeves, Dr. R. Sambruna, Dr. T. Yaqoob and Dr. V. Braitto. I thank Prof. L. Maraschi, Prof. R. Mushotzky and Prof. K. Pounds for useful suggestions.

I thank all the colleagues and friends at the INAF-IASF of Bologna, especially Dr. M. Dadina, Dr. P. Grandi, Dr. G. Malaguti, Dr. B. de Marco, Dr. V. Bianchin, E. Torresi, D. Paoletti, M. Giustini, V. Fioretti... and also the others that unfortunately had to go abroad, L. Raimondi, Dr. G. Ponti, L. Mascetti, A. De Cia, G. Migliori... thank you for having made more pleasant the days spent in the office.

I thank my family for always being close to me in every moment. A special thank goes also to S. Dalena and to my friends, in particular R. D. Baldi, F. Giallauria, A. Dioguardi, E. Liuzzo, R. Colacicco... Finally, I thank all the wonderful people that I had the chance to meet in these years and I apologize if their names have not been listed here due to the limited space available.

# Appendices

# Appendix A

## The radio-quiet sample data

Table A.1: List of type 1 and type 2 radio-quiet AGN sources with relative XMM-Newton observations. (1) Source name. (2) Cosmological red-shift. (3) XMM-Newton observation ID. (4) Observation starting date. (5) EPIC pn 4–10 keV total counts. (6) EPIC pn net exposure, after the subtraction of high background intervals and the CCD dead time fraction. (7) Observed flux in the 4–10 keV band.

| Source         | $z$     | OBSID      | Date       | Counts<br>( $10^3$ cts) | Expo<br>(ks) | Flux<br>( $10^{-12}$ erg cm $^{-2}$ s $^{-1}$ ) |
|----------------|---------|------------|------------|-------------------------|--------------|---|
| (1)            | (2)     | (3)        | (4)        | (5)                     | (6)          | (7)   |
| Type 1 Sources |         |            |            |                         |              |   |
| NGC 4151       | 0.00332 | 0112310101 | 2000-12-21 | 51.1                    | 21.0         | 37.9  |
|                |         | 0112830501 | 2000-12-22 | 43.4                    | 17.6         | 38.5  |
|                |         | 0112830201 | 2000-12-22 | 124.0                   | 50.9         | 38.7  |
|                |         | 0143500201 | 2003-05-26 | 139.0                   | 12.7         | 170.0   |
|                |         | 0143500301 | 2003-05-27 | 176.0                   | 13.0         | 209.0   |
|                |         | 0402660201 | 2006-11-29 | 87.5                    | 19.6         | 70.7  |
| IC4329A        | 0.01605 | 0147440101 | 2003-08-06 | 301.0                   | 71.3         | 61.9  |
| NGC 3783       | 0.00973 | 0112210101 | 2000-12-28 | 63.9                    | 26.0         | 35.8  |
|                |         | 0112210201 | 2001-12-17 | 156.0                   | 80.0         | 28.9  |
|                |         | 0112210501 | 2001-12-19 | 216.0                   | 84.0         | 38.1  |
| MCG+8-11-11    | 0.02048 | 0201930201 | 2004-04-10 | 54.2                    | 26.5         | 29.7  |
| NGC 5548       | 0.01717 | 0109960101 | 2000-12-24 | 23.1                    | 16.0         | 20.8  |
|                |         | 0089960301 | 2001-07-09 | 97.9                    | 56.0         | 25.6  |
|                |         | 0089960401 | 2001-07-12 | 37.8                    | 17.5         | 31.4  |
| NGC 3516       | 0.00883 | 0107460701 | 2001-11-09 | 66.0                    | 84.0         | 11.8  |
|                |         | 0401210401 | 2006-10-06 | 82.6                    | 35.0         | 33.2  |
|                |         | 0401210501 | 2006-10-08 | 88.0                    | 42.0         | 29.6  |
|                |         | 0401210601 | 2006-10-10 | 72.0                    | 42.0         | 24.6  |
|                |         | 0401211001 | 2006-10-12 | 56.6                    | 28.0         | 28.3  |
| NGC 4593       | 0.00900 | 0059830101 | 2002-06-23 | 93.2                    | 52.1         | 26.2  |
| Mrk 509        | 0.03440 | 0130720101 | 2000-10-25 | 28.5                    | 20.7         | 20.8  |

Table A.1: Continued.

| Source         | $z$     | OBSID      | Date       | Counts<br>( $10^3$ cts) | Expo<br>(ks) | Flux<br>( $10^{-12}$ erg cm $^{-2}$ s $^{-1}$ ) |
|----------------|---------|------------|------------|-------------------------|--------------|---|
| (1)            | (2)     | (3)        | (4)        | (5)                     | (6)          | (7)   |
|                |         | 0130720201 | 2001-04-20 | 41.7                    | 23.1         | 25.1  |
|                |         | 0306090201 | 2005-10-18 | 92.4                    | 59.8         | 22.6  |
|                |         | 0306090301 | 2005-10-20 | 50.9                    | 32.4         | 22.7  |
|                |         | 0306090401 | 2006-04-25 | 89.9                    | 48.6         | 26.8  |
| MCG-6-30-15    | 0.00775 | 0111570101 | 2000-07-11 | 34.6                    | 28.8         | 16.7  |
|                |         | 0111570201 | 2000-07-11 | 57.6                    | 35.1         | 22.8  |
|                |         | 0029740101 | 2001-07-31 | 85.4                    | 47.6         | 25.2  |
|                |         | 0029740701 | 2001-08-02 | 166.0                   | 83.6         | 27.8  |
|                |         | 0029740801 | 2001-08-04 | 149.0                   | 83.9         | 24.9  |
| Ark 120        | 0.03271 | 0147190101 | 2003-08-24 | 93.3                    | 58.4         | 22.7  |
| Mrk 110        | 0.03529 | 0201130501 | 2004-11-15 | 41.8                    | 32.8         | 18.0  |
| NGC 7469       | 0.01632 | 0112170101 | 2000-12-26 | 13.8                    | 12.3         | 15.9  |
|                |         | 0112170301 | 2000-12-26 | 19.0                    | 16.2         | 16.7  |
|                |         | 0207090101 | 2004-11-30 | 72.4                    | 59.2         | 17.5  |
|                |         | 0207090201 | 2004-12-03 | 70.5                    | 55.0         | 18.4  |
| IRAS 5078+1626 | 0.01788 | 0502090501 | 2007-08-21 | 42.7                    | 38.5         | 16.2  |
| Mrk 279        | 0.03045 | 0302480401 | 2005-11-15 | 51.3                    | 41.5         | 16.8  |
|                |         | 0302480501 | 2005-11-17 | 49.5                    | 41.4         | 15.8  |
|                |         | 0302480601 | 2005-11-19 | 23.0                    | 21.0         | 15.4  |
| NGC 526A       | 0.01910 | 0150940101 | 2003-06-21 | 36.9                    | 35.5         | 15.5  |
| NGC 3227       | 0.00386 | 0101040301 | 2000-11-28 | 14.3                    | 30.4         | 7.1   |
|                |         | 0400270101 | 2006-12-03 | 142.0                   | 92.4         | 23.2  |
| NGC 7213       | 0.00584 | 0111810101 | 2001-05-28 | 28.2                    | 29.6         | 13.6  |
| ESO 511-G30    | 0.02239 | 0502090201 | 2007-08-05 | 65.0                    | 76.2         | 12.2  |
| Mrk 79         | 0.02219 | 0400070201 | 2006-09-30 | 15.3                    | 14.4         | 14.5  |
|                |         | 0400070301 | 2006-11-01 | 12.6                    | 14.0         | 13.0  |
|                |         | 0400070401 | 2007-03-19 | 11.5                    | 14.0         | 11.9  |
| NGC 4051       | 0.00233 | 0109141401 | 2001-05-16 | 71.0                    | 67.9         | 14.2  |
|                |         | 0157560101 | 2002-11-22 | 12.3                    | 41.3         | 4.3   |
| Mrk 766        | 0.01293 | 0096020101 | 2000-05-20 | 16.2                    | 24.8         | 8.9   |
|                |         | 0109141301 | 2001-05-20 | 75.6                    | 76.8         | 13.5  |
|                |         | 0304030101 | 2005-05-23 | 19.3                    | 54.5         | 5.1   |
|                |         | 0304030301 | 2005-05-25 | 34.9                    | 68.9         | 6.9   |
|                |         | 0304030401 | 2005-05-27 | 39.3                    | 65.6         | 8.2   |
|                |         | 0304030501 | 2005-05-29 | 45.8                    | 63.5         | 10.1  |
|                |         | 0304030601 | 2005-05-31 | 37.4                    | 59.1         | 8.6   |
|                |         | 0304030701 | 2005-06-03 | 8.3                     | 15.5         | 7.3   |
| Mrk 841        | 0.03642 | 0205340201 | 2005-01-16 | 14.7                    | 29.9         | 7.1   |
|                |         | 0205340401 | 2005-07-17 | 8.5                     | 15.8         | 7.6   |
| Mrk 704        | 0.02923 | 0300240101 | 2005-10-21 | 8.1                     | 14.9         | 7.4   |
| Fairall 9      | 0.04702 | 0101040201 | 2000-07-05 | 13.3                    | 25.8         | 7.4   |
| ESO 323-G77    | 0.01501 | 0300240501 | 2006-02-07 | 11.6                    | 22.5         | 7.3   |
| 1H419-577      | 0.10400 | 0148000201 | 2002-09-25 | 4.2                     | 11.0         | 5.7   |
|                |         | 0148000401 | 2003-03-30 | 5.3                     | 10.8         | 7.2   |
|                |         | 0148000601 | 2003-09-16 | 5.0                     | 11.4         | 6.5   |

Table A.1: Continued.

| Source         | $z$     | OBSID      | Date       | Counts<br>( $10^3$ cts) | Expo<br>(ks) | Flux<br>( $10^{-12}$ erg cm $^{-2}$ s $^{-1}$ ) |
|----------------|---------|------------|------------|-------------------------|--------------|---|
| (1)            | (2)     | (3)        | (4)        | (5)                     | (6)          | (7)   |
| Mrk 335        | 0.02578 | 0101040101 | 2000-12-25 | 14.8                    | 27.2         | 7.5   |
|                |         | 0306870101 | 2006-01-03 | 56.9                    | 76.9         | 10.3  |
|                |         | 0510010701 | 2007-07-10 | 2.8                     | 15.5         | 2.5   |
| ESO 198-G024   | 0.04550 | 0305370101 | 2006-02-04 | 37.3                    | 80.5         | 6.6   |
| Mrk 290        | 0.02958 | 0400360201 | 2006-04-30 | 6.3                     | 13.9         | 6.3   |
|                |         | 0400360301 | 2006-05-02 | 4.8                     | 10.5         | 5.8   |
|                |         | 0400360601 | 2006-05-04 | 3.9                     | 10.5         | 5.3   |
|                |         | 0400360801 | 2006-05-06 | 4.7                     | 13.4         | 5.1   |
| Mrk 205        | 0.07084 | 0124110101 | 2000-05-07 | 7.7                     | 31.3         | 3.4   |
|                |         | 0401240201 | 2006-10-18 | 10.3                    | 28.2         | 5.1   |
|                |         | 0401240501 | 2006-10-22 | 17.1                    | 34.6         | 6.9   |
| Mrk 590        | 0.02638 | 0201020201 | 2004-07-04 | 23.7                    | 70.7         | 4.5   |
| H 557-385      | 0.03387 | 0404260101 | 2006-08-11 | 5.1                     | 24.5         | 3.3   |
|                |         | 0404260301 | 2006-11-03 | 9.3                     | 52.5         | 2.8   |
| TON S180       | 0.06198 | 0110890401 | 2000-12-14 | 3.9                     | 20.6         | 2.6   |
|                |         | 0110890701 | 2002-06-30 | 2.2                     | 12.6         | 2.3   |
| PG 1211+143    | 0.08090 | 0112610101 | 2001-06-15 | 7.0                     | 49.5         | 2.0   |
|                |         | 0208020101 | 2004-06-21 | 4.7                     | 32.3         | 1.9   |
|                |         | 0502050101 | 2007-12-21 | 7.2                     | 42.6         | 2.2   |
|                |         | 0502050201 | 2007-12-23 | 4.8                     | 25.4         | 2.5   |
| Type 2 Sources |         |            |            |                         |              |   |
| MCG-5-23-16    | 0.00848 | 0112830401 | 2001-12-01 | 65.5                    | 19.5         | 50.5  |
|                |         | 0302850201 | 2005-12-08 | 362.7                   | 96.2         | 57.7  |
| NGC 5506       | 0.00618 | 0013140101 | 2001-02-02 | 39.3                    | 13.8         | 42.3  |
|                |         | 0201830201 | 2004-07-11 | 48.3                    | 14.8         | 48.1  |
|                |         | 0201830301 | 2004-07-14 | 44.3                    | 14.0         | 46.2  |
|                |         | 0201830401 | 2004-07-22 | 40.2                    | 13.9         | 41.9  |
|                |         | 0201830501 | 2004-08-07 | 64.9                    | 14.0         | 67.4  |
| NGC 7172       | 0.00868 | 0147920601 | 2002-11-18 | 13.1                    | 10.8         | 18.5  |
|                |         | 0414580101 | 2007-04-24 | 63.4                    | 27.7         | 35.7  |
| NGC 7314       | 0.00476 | 0111790101 | 2001-05-02 | 52.4                    | 30.1         | 24.6  |
| NGC 2110       | 0.00779 | 0145670101 | 2003-03-05 | 37.2                    | 29.7         | 19.0  |
| NGC 4507       | 0.01180 | 0006220201 | 2001-01-04 | 22.3                    | 32.3         | 12.1  |
| Ark 564        | 0.02468 | 0206400101 | 2005-01-05 | 42.1                    | 69.0         | 8.0   |
| Mrk 3          | 0.01351 | 0111220201 | 2000-10-19 | 11.3                    | 35.3         | 5.5   |
| NGC 1068       | 0.00379 | 0111200101 | 2000-07-29 | 8.7                     | 33.6         | 3.8   |
|                |         | 0111200201 | 2000-07-30 | 7.6                     | 29.1         | 3.9   |
| NGC 7582       | 0.00525 | 0112310201 | 2001-05-25 | 3.8                     | 17.5         | 3.7   |
|                |         | 0204610101 | 2005-04-29 | 7.8                     | 62.0         | 2.1   |

Table A.2: List of type 1 and type 2 radio-quiet AGN sources with best-fit parameters to their XMM-Newton EPIC pn spectra in the 3.5–10.5 keV band. The baseline models are composed by a simple absorbed power-law continuum with narrow Gaussian emission lines. The narrow absorption lines refer to those that have been detected in the E=6.4–7.1 keV band with F-test confidence levels greater than 99% and to those detected at energies greater than 7.1 keV with additional Monte Carlo probability  $\geq 95\%$ . The errors are at the  $1\sigma$  level. (1) Source name. (2) XMM-Newton observation ID. (3) Power-law continuum photon index. (4) Neutral absorber equivalent Hydrogen column density. (5) Gaussian emission line rest frame energy. (6) Emission line width. (7) Emission line equivalent width. (8) Absorption line rest frame energy. (9) Absorption line width. (10) Absorption line equivalent width. (11) Absorption line blue-shift velocity. (12)  $\Delta\chi^2$  relative to the addition of the absorption line. (13) Detection confidence level from the F-test. (14) Detection confidence level from extensive Monte Carlo simulations. (15) Absorption line identification as Fe XXV 1s<sup>2</sup>–1s2p (He $\alpha$ ), Fe XXV 1s<sup>2</sup>–1s3p (He $\beta$ ), Fe XXVI 1s–2p (Ly $\alpha$ ) or Fe XXVI 1s–3p (Ly $\beta$ ).

| Source         | OBSID      | Baseline model |   |   |                  |                                   | Absorption line |                  |            |                  |                |          |         |             |
|----------------|------------|----------------|---|---|------------------|-----------------------------------|-----------------|------------------|------------|------------------|----------------|----------|---------|-------------|
|                |            | $\Gamma$       | $N_H$<br>(10 <sup>22</sup> cm <sup>-2</sup> ) | E<br>(keV)                                | $\sigma$<br>(eV) | EW<br>(eV)                        | E<br>(keV)      | $\sigma$<br>(eV) | EW<br>(eV) | $v_{out}$<br>(c) | $\Delta\chi^2$ | F-test   | M.C.    | ID          |
| (1)            | (2)        | (3)            | (4)   | (5)                                       | (6)              | (7)                               | (8)             | (9)              | (10)       | (11)             | (12)           | (13)     | (14)    | (15)        |
| Type 1 Sources |            |                |   |   |                  |                                   |                 |                  |            |                  |                |          |         |             |
| NGC 4151       | 0112310101 | 1.46 ± 0.04    | 8.2 ± 0.5                                     | 6.398 ± 0.004                             | 100              | 290 ± 18                          |                 |                  |            |                  |                |          |         |             |
|                | 0112830501 | 1.43 ± 0.04    | 7.9 ± 0.5                                     | 6.397 ± 0.005                             | 100              | 290 ± 19                          |                 |                  |            |                  |                |          |         |             |
|                | 0112830201 | 1.37 ± 0.02    | 7.4 ± 0.1                                     | 6.391 ± 0.002                             | 62 ± 4           | 240 ± 67                          |                 |                  |            |                  |                |          |         |             |
|                |            |                |   | 6.94 ± 0.02                               | 100 ± 24         | 50 ± 12                           |                 |                  |            |                  |                |          |         |             |
|                | 0143500201 | 1.64 ± 0.02    | 7.2 ± 0.2                                     | 6.40 ± 0.01                               | 79 ± 10          | 90 <sup>+12</sup> <sub>-9</sub>   |                 |                  |            |                  |                |          |         |             |
|                | 0143500301 | 1.66 ± 0.02    | 6.4 ± 0.2                                     | 6.40 ± 0.01                               | 80 ± 9           | 80 ± 10                           |                 |                  |            |                  |                |          |         |             |
|                | 0402660201 | 1.58 ± 0.03    | 11.0 ± 0.4                                    | 6.399 <sup>+0.005</sup> <sub>-0.002</sub> | 79 ± 8           | 160 ± 12                          | 7.74 ± 0.05     | 100              | 32 ± 7     | +0.105 ± 0.005   | 18             | 99.99%   | 99.7%   | Ly $\alpha$ |
| IC4329A        | 0147440101 | 1.65 ± 0.01    |   | 6.40 ± 0.01                               | 100              | 92 ± 7                            | 7.69 ± 0.03     | 10               | 10 ± 3     | +0.098 ± 0.003   | 11             | 99.5%    | 96%     | Ly $\alpha$ |
|                |            |                |   | 6.95 ± 0.02                               | 100              | 30 ± 7                            |                 |                  |            |                  |                |          |         |             |
| NGC 3783       | 0112210101 | 1.77 ± 0.04    | 2.0 ± 0.4                                     | 6.36 ± 0.01                               | 100              | 135 <sup>+18</sup> <sub>-15</sub> | 6.61 ± 0.02     | 10               | 16 ± 5     | -0.013 ± 0.004   | 15.4           | 99.94%   |         | He $\alpha$ |
|                |            |                |   | 7.01 ± 0.02                               | 100              | 39 ± 13                           | 7.74 ± 0.03     | 10               | 25 ± 7     | -0.018 ± 0.004   | 12             | 99.7%    | 98.2%   | He $\beta$  |
|                | 0112210201 | 1.66 ± 0.02    | 1.9 ± 0.2                                     | 6.39 ± 0.01                               | 100              | 150 <sup>+10</sup> <sub>-11</sub> | 6.63 ± 0.03     | 10               | 10 ± 3     | -0.010 ± 0.005   | 13             | 99.87%   |         | He $\alpha$ |
|                |            |                |   | 7.01 ± 0.01                               | 100              | 57 ± 11                           |                 |                  |            |                  |                |          |         |             |
|                | 0112210501 | 1.74 ± 0.02    | 2.2 ± 0.2                                     | 6.39 ± 0.01                               | 100              | 120 ± 9                           | 6.67 ± 0.02     | 10               | 17 ± 2     | -0.004 ± 0.002   | 51             | > 99.99% |         | He $\alpha$ |
|                |            |                |   | 7.05 ± 0.02                               | 100              | 37 ± 9                            |                 |                  |            |                  |                |          |         |             |
| MCG+8-11-11    | 0201930201 | 1.57 ± 0.01    |   | 6.42 ± 0.01                               | 100              | 130 ± 18                          |                 |                  |            |                  |                |          |         |             |
| NGC 5548       | 0109960101 | 1.59 ± 0.02    |   | 6.41 ± 0.01                               | 10               | 72 ± 18                           |                 |                  |            |                  |                |          |         |             |
|                | 0089960301 | 1.60 ± 0.01    |   | 6.41 ± 0.01                               | 10               | 60 ± 12                           |                 |                  |            |                  |                |          |         |             |
|                | 0089960401 | 1.69 ± 0.01    |   | 6.37 ± 0.02                               | 100              | 77 ± 18                           |                 |                  |            |                  |                |          |         |             |
| NGC 3516       | 0107460701 | 1.76 ± 0.03    | 8.1 ± 0.4                                     | 6.41 ± 0.01                               | 10               | 297 ± 18                          |                 |                  |            |                  |                |          |         |             |
|                | 0401210401 | 2.07 ± 0.03    | 3.6 ± 0.4                                     | 6.39 ± 0.01                               | 100              | 93 ± 14                           | 6.73 ± 0.02     | 10               | 22 ± 5     | +0.005 ± 0.002   | 27.4           | > 99.99% |         | He $\alpha$ |
|                |            |                |   |   |                  |                                   | 7.02 ± 0.02     | 10               | 24 ± 5     | +0.008 ± 0.002   | 21.6           | 99.99%   |         | Ly $\alpha$ |
|                | 0401210501 | 2.06 ± 0.03    | 3.8 ± 0.4                                     | 6.39 ± 0.01                               | 100              | 125 ± 15                          | 6.69 ± 0.02     | 10               | 15 ± 5     | -0.001 ± 0.004   | 14             | 99.6%    |         | He $\alpha$ |
|                |            |                |   |   |                  |                                   | 7.04 ± 0.02     | 10               | 21 ± 5     | +0.010 ± 0.002   | 20.2           | 99.99%   |         | Ly $\alpha$ |
|                | 0401210601 | 2.01 ± 0.03    | 4.9 ± 0.4                                     | 6.38 ± 0.01                               | 100              | 133 <sup>+16</sup> <sub>-13</sub> | 6.77 ± 0.02     | 10               | 25 ± 6     | +0.011 ± 0.002   | 26.2           | > 99.99% |         | He $\alpha$ |
|                |            |                |   |   |                  |                                   | 7.08 ± 0.02     | 10               | 27 ± 6     | +0.016 ± 0.002   | 17             | 99.96%   |         | Ly $\alpha$ |
|                |            |                |   |   |                  |                                   | 7.95 ± 0.02     | 10               | 33 ± 9     | +0.009 ± 0.002   | 24.2           | > 99.99% | > 99.9% | He $\beta$  |
|                |            |                |   |   |                  |                                   | 8.28 ± 0.03     | 10               | 34 ± 9     | +0.004 ± 0.004   | 14.6           | 99.9%    | 99.5%   | Ly $\beta$  |
|                | 0401211001 | 2.05 ± 0.04    | 3.5 ± 0.4                                     | 6.42 ± 0.01                               | 100              | 131 ± 20                          | 6.71 ± 0.04     | 10               | 18 ± 5     | +0.002 ± 0.006   | 10.4           | 99.3%    |         | He $\alpha$ |
|                |            |                |   |   |                  |                                   | 7.09 ± 0.03     | 10               | 21 ± 7     | +0.017 ± 0.004   | 12.7           | 99.8%    |         | Ly $\alpha$ |
| NGC 4593       | 0059830101 | 1.68 ± 0.01    |   | 6.40 ± 0.01                               | 100              | 130 ± 15                          |                 |                  |            |                  |                |          |         |             |
| Mrk 509        | 0130720101 | 1.54 ± 0.02    |   | 6.38 ± 0.02                               | 100              | 84 ± 23                           | 8.29 ± 0.03     | 10               | 32 ± 12    | +0.172 ± 0.003   | 9.6            | 99.3%    | 95%     | Ly $\alpha$ |
|                | 0130720201 | 1.60 ± 0.02    |   | 6.43 ± 0.02                               | 100              | 60 ± 19                           |                 |                  |            |                  |                |          |         |             |
|                | 0306090201 | 1.70 ± 0.01    |   | 6.43 ± 0.01                               | 100              | 67 ± 11                           | 8.03 ± 0.02     | 10               | 19 ± 6     | +0.141 ± 0.002   | 15             | 99.9%    | 99.4%   | Ly $\alpha$ |
|                |            |                |   | 7.02 ± 0.04                               | 100              | 24 ± 13                           |                 |                  |            |                  |                |          |         |             |
|                | 0306090301 | 1.72 ± 0.02    |   | 6.43 ± 0.02                               | 100              | 62 ± 16                           |                 |                  |            |                  |                |          |         |             |
|                | 0306090401 | 1.68 ± 0.01    |   | 6.44 ± 0.02                               | 100              | 58 ± 12                           | 8.51 ± 0.04     | 10               | 19 ± 7     | +0.196 ± 0.003   | 10             | 99.5%    | 95.3%   | Ly $\alpha$ |
|                |            |                |   | 6.85 ± 0.08                               | 100              | 22 ± 12                           |                 |                  |            |                  |                |          |         |             |
| MCG-6-30-15    | 0111570101 | 2.09 ± 0.04    | 3.4 ± 0.5                                     | 6.35 ± 0.03                               | 100              | 78 <sup>+24</sup> <sub>-21</sub>  |                 |                  |            |                  |                |          |         |             |
|                | 0111570201 | 2.25 ± 0.04    | 4.1 ± 0.4                                     | 6.39 ± 0.02                               | 100              | 67 ± 15                           |                 |                  |            |                  |                |          |         |             |
|                | 0029740101 | 2.26 ± 0.03    | 4.4 ± 0.3                                     | 6.43 ± 0.01                               | 100              | 78 ± 13                           |                 |                  |            |                  |                |          |         |             |
|                | 0029740701 | 2.16 ± 0.02    | 2.8 ± 0.2                                     | 6.42 ± 0.01                               | 100              | 65 ± 10                           |                 |                  |            |                  |                |          |         |             |
|                | 0029740801 | 2.28 ± 0.02    | 3.8 ± 0.2                                     | 6.43 ± 0.01                               | 100              | 79 <sup>+16</sup> <sub>-10</sub>  |                 |                  |            |                  |                |          |         |             |
| Ark 120        | 0147190101 | 1.86 ± 0.01    |   | 6.39 ± 0.01                               | 100              | 90 ± 15                           | 9.18 ± 0.03     | 10               | 25 ± 9     | +0.269 ± 0.002   | 11             | 99.6%    | 97.1%   | Ly $\alpha$ |
|                |            |                |   | 6.71 ± 0.03                               | 100              | 43 ± 13                           |                 |                  |            |                  |                |          |         |             |
|                |            |                |   | 7.02 ± 0.02                               | 10               | 24 ± 12                           |                 |                  |            |                  |                |          |         |             |
| Mrk 110        | 0201130501 | 1.68 ± 0.02    |   | 6.45 ± 0.02                               | 100              | 56 ± 17                           |                 |                  |            |                  |                |          |         |             |
| NGC 7469       | 0112170101 | 1.69 ± 0.03    |   | 6.40 ± 0.01                               | 10               | 110 ± 30                          |                 |                  |            |                  |                |          |         |             |

Table A.2: Continued

| Source                    | OBSID      | Baseline model |  |             |                  |                                   | Absorption line |                  |                                  |                  |                |          |       |             |  |
|---------------------------|------------|----------------|--|-------------|------------------|-----------------------------------|-----------------|------------------|----------------------------------|------------------|----------------|----------|-------|-------------|--|
|                           |            | $\Gamma$       | $N_H$<br>( $10^{22} \text{ cm}^{-2}$ ) | E<br>(keV)  | $\sigma$<br>(eV) | EW<br>(eV)                        | E<br>(keV)      | $\sigma$<br>(eV) | EW<br>(eV)                       | $v_{out}$<br>(e) | $\Delta\chi^2$ | F-test   | M.C.  | ID          |  |
| (1)                       | (2)        | (3)            | (4)                                    | (5)         | (6)              | (7)                               | (8)             | (9)              | (10)                             | (11)             | (12)           | (13)     | (14)  | (15)        |  |
| IRAS 5078+1626<br>Mrk 279 | 0112170301 | 1.75 ± 0.02    |  | 6.43 ± 0.02 | 100              | 96 ± 29                           |                 |                  |                                  |                  |                |          |       |             |  |
|                           | 0207090101 | 1.75 ± 0.01    |  | 6.41 ± 0.01 | 100              | 110 ± 12                          |                 |                  |                                  |                  |                |          |       |             |  |
|                           | 0207090201 | 1.76 ± 0.01    |  | 6.42 ± 0.01 | 100              | 110 ± 13                          |                 |                  |                                  |                  |                |          |       |             |  |
|                           | 0502090501 | 1.55 ± 0.02    |  | 6.39 ± 0.01 | 100              | 120 ± 18                          |                 |                  |                                  |                  |                |          |       |             |  |
|                           | 0302480401 | 1.74 ± 0.02    |  | 6.43 ± 0.01 | 100              | 100 ± 18                          |                 |                  |                                  |                  |                |          |       |             |  |
|                           | 0302480501 | 1.71 ± 0.02    |  | 6.43 ± 0.01 | 100              | 115 ± 23                          | 6.69 ± 0.02     | 10               | 19 ± 9                           | -0.001 ± 0.004   | 10.5           | 99.6%    |       | He $\alpha$ |  |
|                           |            |                |  |             | 7.00 ± 0.06      | 10                                | 29 ± 16         |                  |                                  |                  |                |          |       |             |  |
|                           | 0302480601 | 1.70 ± 0.02    |  | 6.42 ± 0.01 | 100              | 130 ± 30                          |                 |                  |                                  |                  |                |          |       |             |  |
|                           | 0150940101 | 1.43 ± 0.02    |  | 6.40 ± 0.02 | 100              | 90 ± 19                           |                 |                  |                                  |                  |                |          |       |             |  |
|                           | NGC 526A   |                |  |             |                  |                                   |                 |                  |                                  |                  |                |          |       |             |  |
| NGC 3227                  | 0101040301 | 1.50 ± 0.06    | 7.3 <sup>+1.0</sup> <sub>-0.7</sub>    | 6.38 ± 0.01 | 100              | 220 <sup>+61</sup> <sub>-36</sub> |                 |                  |                                  |                  |                |          |       |             |  |
|                           | 0400270101 | 1.55 ± 0.01    |  | 6.39 ± 0.01 | 100              | 112 ± 11                          |                 |                  |                                  |                  |                |          |       |             |  |
| NGC 7213                  | 0111810101 | 1.71 ± 0.02    |  | 6.42 ± 0.02 | 100              | 110 ± 24                          |                 |                  |                                  |                  |                |          |       |             |  |
| ESO 511-G30               | 0502090201 | 1.71 ± 0.01    |  | 6.39 ± 0.01 | 100              | 100 ± 15                          |                 |                  |                                  |                  |                |          |       |             |  |
| Mrk 79                    | 0400070201 | 1.74 ± 0.03    |  | 6.43 ± 0.02 | 10               | 54 ± 24                           | 7.63 ± 0.03     | 10               | 43 ± 14                          | +0.091 ± 0.004   | 12             | 99.5%    | 97.7% | Ly $\alpha$ |  |
|                           | 0400070301 | 1.64 ± 0.03    |  | 6.42 ± 0.01 | 10               | 80 ± 27                           |                 |                  |                                  |                  |                |          |       |             |  |
|                           | 0400070401 | 1.60 ± 0.03    |  | 6.37 ± 0.02 | 100              | 115 ± 36                          |                 |                  |                                  |                  |                |          |       |             |  |
| NGC 4051                  | 0109141401 | 2.04 ± 0.03    | 1.7 ± 0.4                              | 6.39 ± 0.01 | 100              | 120 ± 18                          | 7.10 ± 0.03     | 10               | 19 ± 6                           | +0.018 ± 0.004   | 11.2           | 99.6%    | 97.5% | Ly $\alpha$ |  |
|                           | 0157560101 | 1.77 ± 0.04    | 6.5 ± 0.9                              | 6.42 ± 0.01 | 100              | 275 ± 40                          | 8.10 ± 0.05     | 100              | 96 ± 24                          | +0.150 ± 0.005   | 17             | 99.94%   | 99.7% | Ly $\alpha$ |  |
|                           |            |                |  | 7.08 ± 0.02 | 10               | 48 ± 25                           |                 |                  |                                  |                  |                |          |       |             |  |
| Mrk 766                   | 0096020101 | 1.96 ± 0.03    |  | 6.41 ± 0.02 | 10               | 65 ± 27                           |                 |                  |                                  |                  |                |          |       |             |  |
|                           |            |                |  | 6.73 ± 0.04 | 100              | 74 ± 34                           |                 |                  |                                  |                  |                |          |       |             |  |
|                           | 0109141301 | 2.02 ± 0.02    |  | 6.39 ± 0.02 | 10               | 44 ± 11                           |                 |                  |                                  |                  |                |          |       |             |  |
|                           |            |                |  | 6.73 ± 0.04 | 100              | 60 ± 15                           |                 |                  |                                  |                  |                |          |       |             |  |
|                           | 0304030101 | 1.90 ± 0.06    | 6.6 ± 0.8                              | 6.43 ± 0.02 | 10               | 57 ± 30                           |                 |                  |                                  |                  |                |          |       |             |  |
|                           |            |                |  | 6.66 ± 0.05 | 10               | 57 ± 29                           |                 |                  |                                  |                  |                |          |       |             |  |
|                           | 0304030301 | 1.88 ± 0.02    |  | 6.39 ± 0.01 | 10               | 60 ± 21                           | 7.28 ± 0.05     | 100              | 39 <sup>+13</sup> <sub>-11</sub> | +0.044 ± 0.007   | 12             | 99.6%    | 98.6% | Ly $\alpha$ |  |
|                           |            |                |  | 6.62 ± 0.04 | 100              | 63 ± 24                           |                 |                  |                                  |                  |                |          |       |             |  |
|                           | 0304030401 | 1.88 ± 0.02    |  | 6.43 ± 0.01 | 10               | 43 ± 16                           |                 |                  |                                  |                  |                |          |       |             |  |
|                           |            |                |  | 6.79 ± 0.04 | 100              | 65 ± 21                           |                 |                  |                                  |                  |                |          |       |             |  |
|                           | 0304030501 | 1.99 ± 0.02    |  | 6.41 ± 0.01 | 10               | 50 ± 15                           | 7.63 ± 0.03     | 10               | 27 ± 10                          | +0.091 ± 0.004   | 12.2           | 99.7%    | 98.7% | Ly $\alpha$ |  |
|                           |            |                |  | 6.78 ± 0.03 | 100              | 77 ± 21                           |                 |                  |                                  |                  |                |          |       |             |  |
|                           | 0304030601 | 1.89 ± 0.02    |  | 6.35 ± 0.04 | 10               | 27 ± 16                           |                 |                  |                                  |                  |                |          |       |             |  |
|                           |            |                |  | 6.67 ± 0.04 | 100              | 52 ± 23                           |                 |                  |                                  |                  |                |          |       |             |  |
|                           | 0304030701 | 1.70 ± 0.06    |  | 6.49 ± 0.04 | 10               | 54 ± 22                           |                 |                  |                                  |                  |                |          |       |             |  |
| Mrk 841                   | 0205340201 | 1.80 ± 0.06    | 5.1 <sup>+0.8</sup> <sub>-1.0</sub>    | 6.46 ± 0.02 | 100              | 100 <sup>+43</sup> <sub>-39</sub> |                 |                  |                                  |                  |                |          |       |             |  |
|                           | 0205340401 | 1.61 ± 0.04    |  | 6.49 ± 0.03 | 100              | 100 <sup>+43</sup> <sub>-36</sub> | 7.19 ± 0.02     | 10               | 46 ± 16                          | +0.034 ± 0.003   | 12             | 99.8%    | 98.4% | Ly $\alpha$ |  |
| Mrk 704                   | 0300240101 | 1.70 ± 0.10    | 5.0 ± 1.2                              | 6.36 ± 0.03 | 100              | 136 ± 46                          |                 |                  |                                  |                  |                |          |       |             |  |
| Fairall 9                 | 0101040201 | 1.64 ± 0.03    |  | 6.39 ± 0.02 | 100              | 150 ± 36                          |                 |                  |                                  |                  |                |          |       |             |  |
| ESO 323-G77               | 0300240501 | 2.36 ± 0.09    | 12 ± 1                                 | 6.40 ± 0.03 | 100              | 115 <sup>+49</sup> <sub>-36</sub> | 6.73 ± 0.01     | 10               | 78 ± 13                          | +0.005 ± 0.002   | 46.2           | > 99.99% |       | He $\alpha$ |  |
|                           |            |                |  |             |                  |                                   | 7.05 ± 0.02     | 10               | 77 ± 15                          | +0.012 ± 0.003   | 30             | > 99.99% |       | Ly $\alpha$ |  |
| 1H419-577                 | 0148000201 | 1.21 ± 0.05    |  | 6.33 ± 0.05 | 100              | 90 <sup>+56</sup> <sub>-47</sub>  | 7.23 ± 0.04     | 10               | 55 <sup>+21</sup> <sub>-18</sub> | +0.037 ± 0.005   | 10.3           | 99%      | 95.8% | Ly $\alpha$ |  |
|                           | 0148000401 | 1.55 ± 0.05    |  |             |                  |                                   |                 |                  |                                  |                  |                |          |       |             |  |
|                           | 0148000601 | 1.49 ± 0.05    |  |             |                  |                                   |                 |                  |                                  |                  |                |          |       |             |  |
| Mrk 335                   | 0101040101 | 2.00 ± 0.03    |  | 6.46 ± 0.08 | 100              | 60 ± 30                           |                 |                  |                                  |                  |                |          |       |             |  |
|                           | 0306870101 | 1.97 ± 0.01    |  | 6.41 ± 0.02 | 100              | 90 ± 18                           |                 |                  |                                  |                  |                |          |       |             |  |
|                           |            |                |  | 6.96 ± 0.02 | 100              | 64 ± 18                           |                 |                  |                                  |                  |                |          |       |             |  |
|                           | 0510010701 | 2.5 ± 0.2      | 13 ± 2                                 | 6.39 ± 0.03 | 100              | 182 <sup>+80</sup> <sub>-75</sub> |                 |                  |                                  |                  |                |          |       |             |  |
| ESO 198-G024              | 0305370101 | 1.62 ± 0.02    |  | 6.43 ± 0.02 | 100              | 90 ± 18                           |                 |                  |                                  |                  |                |          |       |             |  |
| Mrk 290                   | 0400360201 | 1.54 ± 0.05    |  |             |                  |                                   |                 |                  |                                  |                  |                |          |       |             |  |
|                           | 0400360301 | 1.50 ± 0.6     |  |             |                  |                                   |                 |                  |                                  |                  |                |          |       |             |  |
|                           | 0400360601 | 1.61 ± 0.05    |  |             |                  |                                   | 8.03 ± 0.03     | 10               | 85 <sup>+33</sup> <sub>-27</sub> | +0.141 ± 0.003   | 13.4           | 99.96%   | 99%   | Ly $\alpha$ |  |
|                           | 0400360801 | 1.54 ± 0.05    |  | 6.42 ± 0.03 | 100              | 151 <sup>+63</sup> <sub>-69</sub> |                 |                  |                                  |                  |                |          |       |             |  |
| Mrk 205                   | 0124110101 | 1.71 ± 0.04    |  | 6.37 ± 0.04 | 100              | 100 ± 43                          | 7.70 ± 0.03     | 10               | 50 ± 18                          | +0.100 ± 0.004   | 11             | 99.7%    | 96.9% | Ly $\alpha$ |  |
|                           |            |                |  | 6.86 ± 0.05 | 100              | 90 ± 49                           |                 |                  |                                  |                  |                |          |       |             |  |
|                           | 0401240201 | 1.79 ± 0.04    |  | 6.34 ± 0.02 | 10               | 70 ± 27                           |                 |                  |                                  |                  |                |          |       |             |  |
|                           | 0401240501 | 1.85 ± 0.02    |  | 6.55 ± 0.04 | 100              | 65 ± 29                           |                 |                  |                                  |                  |                |          |       |             |  |
| Mrk 590                   | 0201020201 | 1.52 ± 0.03    |  | 6.42 ± 0.01 | 10               | 110 ± 21                          |                 |                  |                                  |                  |                |          |       |             |  |

Table A.2: Continued

| Source         | OBSID      | Baseline model  |  |                 |                  |                     | Absorption line |                  |                   |                    |                |             |            |             |
|----------------|------------|-----------------|--|-----------------|------------------|---------------------|-----------------|------------------|-------------------|--------------------|----------------|-------------|------------|-------------|
|                |            | $\Gamma$        | $N_H$<br>( $10^{22} \text{ cm}^{-2}$ ) | E<br>(keV)      | $\sigma$<br>(eV) | EW<br>(eV)          | E<br>(keV)      | $\sigma$<br>(eV) | EW<br>(eV)        | $v_{out}$<br>(c)   | $\Delta\chi^2$ | F-test      | M.C.       | ID          |
| (1)            | (2)        | (3)             | (4)                                    | (5)             | (6)              | (7)                 | (8)             | (9)              | (10)              | (11)               | (12)           | (13)        | (14)       | (15)        |
| H 557-385      | 0404260101 | $1.20 \pm 0.06$ | $21 \pm 2$                             | $6.42 \pm 0.01$ | 100              | $370 \pm 67$        |                 |                  |                   |                    |                |             |            |             |
|                | 0404260301 | $1.14 \pm 0.05$ | $21 \pm 2$                             | $6.44 \pm 0.01$ | 100              | $460 \pm 55$        |                 |                  |                   |                    |                |             |            |             |
| TON S180       | 0110890401 | $2.05 \pm 0.05$ |  |                 |                  | $189^{+47}_{-41}$   |                 |                  |                   |                    |                |             |            |             |
|                | 0110890701 | $1.96 \pm 0.08$ |  |                 |                  |                     |                 |                  |                   |                    |                |             |            |             |
| PG 1211+143    | 0112610101 | $2.80 \pm 0.12$ | $11.7 \pm 1.5$                         | $6.52 \pm 0.05$ | 100              | $100 \pm 43$        | $7.62 \pm 0.02$ | 100              | $130^{+24}_{-18}$ | $+0.128 \pm 0.003$ | 56             | $> 99.99\%$ | $> 99.9\%$ | He $\alpha$ |
|                | 0208020101 | $1.71 \pm 0.05$ |  | $6.52 \pm 0.03$ | 100              | $135^{+60}_{-51}$   |                 |                  |                   |                    |                |             |            |             |
|                | 0502050101 | $2.07 \pm 0.04$ |  | $6.36 \pm 0.03$ | 100              | $141 \pm 46$        |                 |                  |                   |                    |                |             |            |             |
|                | 0502050201 | $2.06 \pm 0.05$ |  | $6.36 \pm 0.06$ | 100              | $90^{+53}_{-50}$    |                 |                  |                   |                    |                |             |            |             |
| Type 2 Sources |            |                 |  |                 |                  |                     |                 |                  |                   |                    |                |             |            |             |
| MCG-5-23-16    | 0112830401 | $1.61 \pm 0.03$ | $2.5 \pm 0.4$                          | $6.37 \pm 0.01$ | 100              | $90 \pm 15$         |                 |                  |                   |                    |                |             |            |             |
|                | 0302850201 | $1.53 \pm 0.01$ | $1.2 \pm 0.2$                          | $6.41 \pm 0.01$ | 100              | $90 \pm 6$          | $7.84 \pm 0.04$ | 100              | $18 \pm 4$        | $+0.118 \pm 0.005$ | 22.6           | 99.996%     | $> 99.9\%$ | Ly $\alpha$ |
| NGC 5506       | 0013140101 | $1.68 \pm 0.04$ | $2.8 \pm 0.5$                          | $6.44 \pm 0.01$ | 100              | $125^{+21}_{-18}$   |                 |                  |                   |                    |                |             |            |             |
|                | 0201830201 | $1.79 \pm 0.04$ | $3.4 \pm 0.4$                          | $6.39 \pm 0.01$ | 100              | $110 \pm 18$        |                 |                  |                   |                    |                |             |            |             |
|                | 0201830301 | $1.88 \pm 0.03$ | $4.7 \pm 0.5$                          | $6.39 \pm 0.01$ | 100              | $120 \pm 18$        |                 |                  |                   |                    |                |             |            |             |
|                | 0201830401 | $1.93 \pm 0.04$ | $4.8 \pm 0.5$                          | $6.41 \pm 0.01$ | 100              | $130 \pm 18$        |                 |                  |                   |                    |                |             |            |             |
|                | 0201830501 | $1.93 \pm 0.03$ | $4.2 \pm 0.4$                          | $6.41 \pm 0.02$ | 100              | $85 \pm 15$         |                 |                  |                   |                    |                |             |            |             |
| NGC 7172       | 0147920601 | $1.70 \pm 0.06$ | $9.9 \pm 0.9$                          | $6.40 \pm 0.02$ | 100              | $110^{+36}_{-30}$   |                 |                  |                   |                    |                |             |            |             |
|                | 0414580101 | $1.72 \pm 0.03$ | $9.0 \pm 0.4$                          | $6.39 \pm 0.01$ | 100              | $80 \pm 12$         |                 |                  |                   |                    |                |             |            |             |
| NGC 7314       | 0111790101 | $1.97 \pm 0.04$ | $1.8 \pm 0.4$                          | $6.42 \pm 0.02$ | 100              | $70 \pm 18$         |                 |                  |                   |                    |                |             |            |             |
| NGC 2110       | 0145670101 | $1.59 \pm 0.04$ | $4.7 \pm 0.5$                          | $6.43 \pm 0.01$ | 100              | $150^{+18}_{-24}$   |                 |                  |                   |                    |                |             |            |             |
| NGC 4507       | 0006220201 | $1.50 \pm 0.06$ | $38.0 \pm 0.5$                         | $6.37 \pm 0.01$ | $76^{+10}_{-12}$ | $227 \pm 26$        | $8.32 \pm 0.02$ | 10               | $35 \pm 12$       | $+0.177 \pm 0.002$ | 12.5           | 99.9%       | 98.7%      | Ly $\alpha$ |
|                |            |                 |  | $6.90 \pm 0.04$ | 100              | $36 \pm 20$         |                 |                  |                   |                    |                |             |            |             |
| Ark 564        | 0206400101 | $2.45 \pm 0.02$ |  | $6.34 \pm 0.04$ | 100              | $35 \pm 18$         |                 |                  |                   |                    |                |             |            |             |
|                |            |                 |  | $6.71 \pm 0.03$ | 100              | $50 \pm 18$         |                 |                  |                   |                    |                |             |            |             |
| Mrk 3          | 0111220201 | $0.50 \pm 0.03$ | $16.6^{+1.0}_{-1.9}$                   | $6.41 \pm 0.01$ | 100              | $700 \pm 61$        |                 |                  |                   |                    |                |             |            |             |
| NGC 1068       | 0111200101 | $1.21 \pm 0.05$ |  | $6.42 \pm 0.01$ | 100              | $750^{+122}_{-110}$ |                 |                  |                   |                    |                |             |            |             |
|                |            |                 |  | $6.72 \pm 0.01$ | 100              | $310 \pm 67$        |                 |                  |                   |                    |                |             |            |             |
|                | 0111200201 | $1.17 \pm 0.05$ |  | $7.03 \pm 0.01$ | 100              | $240 \pm 61$        |                 |                  |                   |                    |                |             |            |             |
|                |            |                 |  | $6.43 \pm 0.01$ | 100              | $820 \pm 122$       |                 |                  |                   |                    |                |             |            |             |
|                |            |                 |  | $6.73 \pm 0.01$ | 100              | $290^{+67}_{-49}$   |                 |                  |                   |                    |                |             |            |             |
|                |            |                 |  | $7.05 \pm 0.01$ | 100              | $250^{+73}_{-71}$   |                 |                  |                   |                    |                |             |            |             |
| NGC 7582       | 0112310201 | $0.80 \pm 0.06$ | $19.0 \pm 2.4$                         | $6.39 \pm 0.01$ | 100              | $425^{+113}_{-74}$  | $8.99 \pm 0.04$ | 10               | $91^{+41}_{-29}$  | $+0.255 \pm 0.003$ | 12             | 99.5%       | 98.2%      | He $\alpha$ |
|                |            |                 |  | $7.02 \pm 0.05$ | 100              | $143^{+68}_{-74}$   |                 |                  |                   |                    |                |             |            |             |
|                | 0204610101 | $0.50 \pm 0.06$ | $9.6^{+1.2}_{-2.1}$                    | $6.41 \pm 0.05$ | 100              | $940^{+122}_{-85}$  |                 |                  |                   |                    |                |             |            |             |
|                |            |                 |  | $6.91 \pm 0.02$ | 100              | $290 \pm 61$        |                 |                  |                   |                    |                |             |            |             |

Table A.3: Blue-shifted Fe K absorption line parameters from the MOS1 and MOS2 detectors. The baseline models are the same of the EPIC pn (a simple absorbed power-law continuum plus Gaussian emission lines, see Table A.2). In the cases that a narrow absorption line was not detected in the MOS, we put the 90% equivalent width upper limits with the line energy fixed at the EPIC pn value. In the majority of the cases we made a fit to the combined MOS1 and MOS2 data. The observations with data from only one camera have been indicated. The width of the absorption lines are  $\sim 10$  eV. The errors are at the  $1\sigma$  level. (1) Source name. (2) XMM-Newton observation ID. (3) Absorption line rest frame energy. (4) Absorption line width. (5) Absorption line equivalent width. (6)  $\Delta\chi^2$  improvement with the addition of two more parameters.

| Source      | OBSID                   | E<br>(keV)      | EW<br>(eV)        | $\Delta\chi^2$ |
|-------------|-------------------------|-----------------|-------------------|----------------|
| (1)         | (2)                     | (3)             | (4)               | (5)            |
| NGC 4151    | 0402660201              | $\equiv 7.74^c$ | $< 67$            |                |
| IC4329A     | 0147440101              | $7.71 \pm 0.04$ | $14 \pm 6$        | 8              |
| NGC 3783    | 0112210101              | $6.64 \pm 0.04$ | $18 \pm 15$       | 7              |
|             |                         | $\equiv 7.74^c$ | $< 42$            |                |
|             | 0112210201 <sup>b</sup> | $6.65 \pm 0.03$ | $22 \pm 13$       | 15.4           |
|             | 0112210501 <sup>b</sup> | $6.67 \pm 0.02$ | $25 \pm 12$       | 22.3           |
| NGC 3516    | 0401210401              | $6.72 \pm 0.02$ | $29 \pm 7$        | 25             |
|             |                         | $7.03 \pm 0.02$ | $39 \pm 8$        | 33             |
|             | 0401210501              | $6.71 \pm 0.02$ | $32 \pm 7$        | 32             |
|             |                         | $7.04 \pm 0.02$ | $35 \pm 8$        | 29             |
|             | 0401210601              | $6.72 \pm 0.02$ | $31 \pm 8$        | 24.2           |
|             |                         | $7.05 \pm 0.02$ | $33 \pm 8$        | 17.5           |
|             |                         | $7.98 \pm 0.07$ | $24 \pm 13$       | 5              |
|             |                         | $\equiv 8.28^c$ | $< 65$            |                |
|             | 0401211001              | $6.72 \pm 0.02$ | $33 \pm 8$        | 26.5           |
|             |                         | $7.06 \pm 0.02$ | $30 \pm 9$        | 16.8           |
| Mrk 509     | 0130720101              | $8.14 \pm 0.04$ | $67 \pm 21$       | 13             |
|             | 0306090201              | $8.02 \pm 0.05$ | $23 \pm 14$       | 5              |
|             | 0306090401              | $8.38 \pm 0.08$ | $18 \pm 12$       | 3              |
| Ark 120     | 0147190101 <sup>b</sup> | $\equiv 9.18^c$ | $< 50$            |                |
| Mrk 279     | 0302480501 <sup>a</sup> | $\equiv 6.69^c$ | $< 44$            |                |
| Mrk 79      | 0400070201              | $\equiv 7.63^c$ | $< 70$            |                |
| NGC 4051    | 0109141401 <sup>b</sup> | $7.11 \pm 0.04$ | $35 \pm 18$       | 6              |
|             | 0157560101              | $8.08 \pm 0.13$ | $82 \pm 42$       | 5              |
| Mrk 766     | 0304030301              | $7.30 \pm 0.03$ | $50 \pm 15$       | 17.8           |
|             | 0304030501              | $\equiv 7.63^c$ | $< 46$            |                |
| Mrk 841     | 0205340401 <sup>a</sup> | $\equiv 7.19^c$ | $< 135$           |                |
| ESO 323-G77 | 0300240501              | $6.74 \pm 0.03$ | $54 \pm 25$       | 10             |
|             |                         | $7.07 \pm 0.03$ | $82 \pm 28$       | 17.6           |
| 1H419-577   | 0148000201              | $7.43 \pm 0.08$ | $84 \pm 35$       | 8              |
| Mrk 290     | 0400360601              | $8.15 \pm 0.08$ | $142^{+70}_{-60}$ | 7              |
| Mrk 205     | 0124110101              | $\equiv 7.70^c$ | $< 100$           |                |
| PG 1211+143 | 0112610101              | $7.59 \pm 0.07$ | $174^{+86}_{-61}$ | 24             |
| MCG-5-23-16 | 0302850201              | $8.10 \pm 0.03$ | $16 \pm 6$        | 8.5            |
| NGC 4507    | 0006220201              | $\equiv 8.33^c$ | $< 80$            |                |
| NGC 7582    | 0112310201              | $\equiv 8.99^c$ | $< 600$           |                |

(a) Only MOS1 data available. (b) Only MOS2 data available.  
(c) The line energy has been fixed to the EPIC pn best fit value.

Table A.4: Mean Fe K absorption line parameters from the XMM-Newton observations for the sample sources in which they have been detected. The errors are at the  $1\sigma$  level. (1) Source name. (2)-(3) Mean EW and blue-shift velocity for Fe XXV He $\alpha$ . (4)-(5) Mean EW and blue-shift velocity for Fe XXV He $\beta$ . (6)-(7) Mean EW and blue-shift velocity for Fe XXVI Ly $\alpha$ . (8)-(9) Mean EW and blue-shift velocity for Fe XXVI Ly $\beta$ . (10) Mean blue-shift velocity from all the Fe K absorption lines.

| Source      | Fe XXV He $\alpha$ | $v_{out}$ | Fe XXV He $\beta$ | $v_{out}$ | Fe XXVI Ly $\alpha$ | $v_{out}$ | Fe XXVI Ly $\beta$ | $v_{out}$ | $\langle v_{out} \rangle$ |
|-------------|--------------------|-----------|-------------------|-----------|---------------------|-----------|--------------------|-----------|---------------------------|
| (1)         | (eV)               | (c)       | (eV)              | (c)       | (eV)                | (c)       | (eV)               | (c)       | (c)                       |
| (1)         | (2)                | (3)       | (4)               | (5)       | (6)                 | (7)       | (8)                | (9)       | (10)                      |
| NGC 4151    |                    |           |                   |           | 32                  | +0.105    |                    |           | +0.105                    |
| IC4329A     |                    |           |                   |           | 11                  | +0.098    |                    |           | +0.098                    |
| NGC 3783    | 14                 | -0.009    | 25                | -0.018    |                     |           |                    |           | -0.013                    |
| NGC 3516    | 20                 | +0.004    | 33                | +0.009    | 23                  | +0.013    | 34                 | +0.004    | +0.008                    |
| Mrk 509     |                    |           |                   |           | 24                  | +0.170    |                    |           | +0.170                    |
| Ark 120     |                    |           |                   |           | 27                  | +0.269    |                    |           | +0.269                    |
| Mrk 279     | 18                 | -0.001    |                   |           |                     |           |                    |           | -0.001                    |
| Mrk 79      |                    |           |                   |           | 43                  | +0.091    |                    |           | +0.091                    |
| NGC 4051    |                    |           |                   |           | 58                  | +0.084    |                    |           | +0.084                    |
| Mrk 766     |                    |           |                   |           | 33                  | +0.067    |                    |           | +0.067                    |
| Mrk 841     |                    |           |                   |           | 46                  | +0.032    |                    |           | +0.032                    |
| ESO 323+G77 | 78                 | +0.005    |                   |           | 77                  | +0.012    |                    |           | +0.008                    |
| 1H419-577   |                    |           |                   |           | 55                  | +0.037    |                    |           | +0.037                    |
| Mrk 290     |                    |           |                   |           | 85                  | +0.141    |                    |           | +0.141                    |
| Mrk 205     |                    |           |                   |           | 50                  | +0.100    |                    |           | +0.100                    |
| PG 1211+143 | 130                | +0.128    |                   |           |                     |           |                    |           | +0.128                    |
| MCG-5-23-16 |                    |           |                   |           | 18                  | +0.118    |                    |           | +0.118                    |
| NGC 4507    |                    |           |                   |           | 36                  | +0.177    |                    |           | +0.177                    |
| NGC 7582    |                    |           |                   |           | 91                  | +0.255    |                    |           | +0.255                    |

Table A.5: List of physical parameters of the sources of the radio-quiet AGN sample and their relative XMM-Newton observations. (1) Source name. (2) Cosmological red-shift. (3) Black hole mass estimate. (4) Eddington luminosity. (5) XMM-Newton observation ID. (6) Estimate of the bolometric luminosity of the AGN for each observation.

| Source         | $z$     | $M_{\text{BH}}$<br>( $10^6 M_{\odot}$ ) | $L_{\text{Edd}}$<br>( $10^{44} \text{ erg s}^{-1}$ ) | OBSID      | $L_{\text{bol}}$<br>( $10^{44} \text{ erg s}^{-1}$ ) |        |    |            |      |
|----------------|---------|---|--|------------|--|--------|----|------------|------|
| (1)            | (2)     | (3)                                     | (4)  | (5)        | (6)  |        |    |            |      |
| Type 1 objects |         |   |  |            |  |        |    |            |      |
| NGC 4151       | 0.00332 | $13^1$                                  | 17   | 0112310101 | 0.3  |        |    |            |      |
|                |         |   |  | 0112830501 | 0.3  |        |    |            |      |
|                |         |   |  | 0112830201 | 0.3  |        |    |            |      |
|                |         |   |  | 0143500201 | 1.8  |        |    |            |      |
|                |         |   |  | 0143500301 | 2.2  |        |    |            |      |
| IC4329A        | 0.01605 | $10^1$                                  | 13   | 0402660201 | 0.8  |        |    |            |      |
|                |         |   |  | 0147440101 | 13   |        |    |            |      |
|                |         |   |  | NGC 3783   | 0.00973  | $30^1$ | 39 | 0112210101 | 3.6  |
|                |         |   |  | 0112210201 | 2.3  |        |    |            |      |
|                |         |   |  | 0112210501 | 3.4  |        |    |            |      |
| MCG+8-11-11    | 0.02048 | $63^2$                                  | 82   | 0201930201 | 9.2  |        |    |            |      |
|                |         |   |  | NGC 5548   | 0.01717  | $70^1$ | 91 | 0109960101 | 4.6  |
| NGC 3516       | 0.00883 | $40^1$                                  | 52   | 0089960301 | 5.8  |        |    |            |      |
|                |         |   |  | 0089960401 | 8.1  |        |    |            |      |
|                |         |   |  | 0107460701 | 1.1  |        |    |            |      |
|                |         |   |  | 0401210401 | 5.7  |        |    |            |      |
|                |         |   |  | 0401210501 | 4.9  |        |    |            |      |
| NGC 4593       | 0.00900 | $5^1$                                   | 6.5  | 0401210601 | 4.4  |        |    |            |      |
|                |         |   |  | 0401211001 | 5.6  |        |    |            |      |
| Mrk 509        | 0.03440 | $140^1$                                 | 180  | 0059830101 | 1.8  |        |    |            |      |
|                |         |   |  | 0130720101 | 17.0   |        |    |            |      |
|                |         |   |  | 0130720201 | 23.3   |        |    |            |      |
|                |         |   |  | 0306090201 | 24.3   |        |    |            |      |
|                |         |   |  | 0306090301 | 25.1   |        |    |            |      |
| MCG-6-30-15    | 0.00775 | $0.7^4$                                 | 0.9  | 0306090401 | 28.1   |        |    |            |      |
|                |         |   |  | 0111570101 | 2.1  |        |    |            |      |
|                |         |   |  | 0111570201 | 5.2  |        |    |            |      |
|                |         |   |  | 0029740101 | 6.4  |        |    |            |      |
|                |         |   |  | 0029740701 | 4.8  |        |    |            |      |
| Ark 120        | 0.03271 | $150^1$                                 | 200  | 0029740801 | 6.8  |        |    |            |      |
|                |         |   |  | 0147190101 | 29.1   |        |    |            |      |
|                |         |   |  | Mrk 110    | 0.03529  | $25^1$ | 33 | 0201130501 | 19.8 |
|                |         |   |  | NGC 7469   | 0.01632  | $12^1$ | 16 | 0112170101 | 3.7  |
|                |         |   |  | 0112170301 | 4.2  |        |    |            |      |
| IRAS 5078+1626 | 0.01788 | $11^2$                                  | 14   | 0207090101 | 4.5  |        |    |            |      |
|                |         |   |  | 0207090201 | 4.7  |        |    |            |      |
|                |         |   |  | 0207090501 | 3.7  |        |    |            |      |
|                |         |   |  | Mrk 279    | 0.03045  | $35^1$ | 46 | 0302480401 | 15.0 |

Table A.5: Continued.

| Source       | $z$     | $M_{\text{BH}}$<br>( $10^6 M_{\odot}$ ) | $L_{\text{Edd}}$<br>( $10^{44} \text{ erg s}^{-1}$ ) | OBSID      | $L_{\text{bol}}$<br>( $10^{44} \text{ erg s}^{-1}$ ) |
|--------------|---------|---|--|------------|--|
| (1)          | (2)     | (3)                                     | (4)  | (5)        | (6)  |
|              |         |   |  | 0302480501 | 13.4   |
|              |         |   |  | 0302480601 | 12.7   |
| NGC 526A     | 0.01910 | 9 <sup>2</sup>                          | 12   | 0150940101 | 3.6  |
| NGC 3227     | 0.00386 | 42 <sup>1</sup>                         | 55   | 0101040301 | 0.8  |
|              |         |   |  | 0400270101 | 2.4  |
| NGC 7213     | 0.00584 | 110 <sup>2</sup>                        | 140  | 0111810101 | 4.1  |
| ESO 511-G30  | 0.02239 | 460 <sup>5</sup>                        | 600  | 0502090201 | 5.5  |
| Mrk 79       | 0.02219 | 52 <sup>1</sup>                         | 68   | 0400070201 | 7.1  |
|              |         |   |  | 0400070301 | 5.2  |
|              |         |   |  | 0400070401 | 4.5  |
| NGC 4051     | 0.00233 | 2 <sup>1</sup>                          | 2.5  | 0109141401 | 0.2  |
|              |         |   |  | 0157560101 | 0.1  |
| Mrk 766      | 0.01293 | 0.8 <sup>4</sup>                        | 1  | 0096020101 | 2.2  |
|              |         |   |  | 0109141301 | 4.5  |
|              |         |   |  | 0304030101 | 1.4  |
|              |         |   |  | 0304030301 | 1.5  |
|              |         |   |  | 0304030401 | 1.9  |
|              |         |   |  | 0304030501 | 2.8  |
|              |         |   |  | 0304030601 | 2.2  |
|              |         |   |  | 0304030701 | 1.3  |
| Mrk 841      | 0.03642 | 60 <sup>2</sup>                         | 78   | 0205340201 | 11.1   |
|              |         |   |  | 0205340401 | 8.2  |
| Mrk 704      | 0.02923 | 35 <sup>2</sup>                         | 46   | 0300240101 | 6.4  |
| Fairall 9    | 0.04702 | 250 <sup>1</sup>                        | 330  | 0101040201 | 13.6   |
| ESO 323-G77  | 0.01501 | 24 <sup>2</sup>                         | 31   | 0300240501 | 11.6   |
| 1H419-577    | 0.10400 | 130 <sup>1</sup>                        | 170  | 0148000201 | 36.2   |
|              |         |   |  | 0148000401 | 62.7   |
|              |         |   |  | 0148000601 | 51.7   |
| Mrk 335      | 0.02578 | 14 <sup>1</sup>                         | 18   | 0101040101 | 8.7  |
|              |         |   |  | 0306870101 | 10.7   |
|              |         |   |  | 0510010701 | 20.3   |
| ESO 198-G024 | 0.04550 | 240 <sup>2</sup>                        | 310  | 0305370101 | 11.2   |
| Mrk 290      | 0.02958 | 45 <sup>2</sup>                         | 59   | 0400360201 | 4.0  |
|              |         |   |  | 0400360301 | 3.4  |
|              |         |   |  | 0400360601 | 3.8  |
|              |         |   |  | 0400360801 | 3.1  |
| Mrk 205      | 0.07084 | 440 <sup>3</sup>                        | 570  | 0124110101 | 16.9   |
|              |         |   |  | 0401240201 | 28.6   |
|              |         |   |  | 0401240501 | 44.3   |
| Mrk 590      | 0.02638 | 47 <sup>1</sup>                         | 61   | 0201020201 | 2.2  |
| H 557-385    | 0.03387 | 20 <sup>7</sup>                         | 26   | 0404260101 | 3.0  |
|              |         |   |  | 0404260301 | 2.0  |
| TON S180     | 0.06198 | 12 <sup>8</sup>                         | 16   | 0110890401 | 20.8   |
|              |         |   |  | 0110890701 | 10.2   |
| PG 1211+143  | 0.08090 | 150 <sup>1</sup>                        | 200  | 0112610101 | 18.9   |

Table A.5: Continued.

| Source         | $z$     | $M_{\text{BH}}$<br>( $10^6 M_{\odot}$ ) | $L_{\text{Edd}}$<br>( $10^{44} \text{ erg s}^{-1}$ ) | OBSID      | $L_{\text{bol}}$<br>( $10^{44} \text{ erg s}^{-1}$ ) |
|----------------|---------|---|--|------------|--|
| (1)            | (2)     | (3)                                     | (4)  | (5)        | (6)  |
|                |         |   |  | 0208020101 | 12.9   |
|                |         |   |  | 0502050101 | 32.8   |
|                |         |   |  | 0502050201 | 35.8   |
| Type 2 objects |         |   |  |            |  |
| MCG-5-23-16    | 0.00848 | $40^3$                                  | 52   | 0112830401 | 2.9  |
|                |         |   |  | 0302850201 | 3.0  |
| NGC 5506       | 0.00618 | $40^3$                                  | 52   | 0013140101 | 1.4  |
|                |         |   |  | 0201830201 | 2.0  |
|                |         |   |  | 0201830301 | 2.4  |
|                |         |   |  | 0201830401 | 2.4  |
|                |         |   |  | 0201830501 | 3.9  |
| NGC 7172       | 0.00868 | $10^9$                                  | 13   | 0147920601 | 1.5  |
|                |         |   |  | 0414580101 | 3.0  |
| NGC 7314       | 0.00476 | $5^{10}$                                | 6.5  | 0111790101 | 0.9  |
| NGC 2110       | 0.00779 | $84^3$                                  | 100  | 0145670101 | 1.0  |
| NGC 4507       | 0.01180 | $3^2$                                   | 3.4  | 0006220201 | 2.3  |
| Ark 564        | 0.02468 | $3^8$                                   | 3.9  | 0206400101 | 40.6   |
| Mrk 3          | 0.01351 | $320^2$                                 | 420  | 0111220201 | 0.6  |
| NGC 1068       | 0.00379 | $400^2$                                 | 520  | 0111200101 | 0.1  |
|                |         |   |  | 0111200201 | 0.1  |
| NGC 7582       | 0.00525 | $24^3$                                  | 31   | 0112310201 | 0.1  |
|                |         |   |  | 0204610101 | 0.1  |

References: (1) Peterson et al. 2004; (2) Wang & Zhang 2007; (3) Wandel & Mushotzky 1986; (4) Bian & Zhao 2003; (5) Winter et al. 2008; (6) Pounds et al. 2004; (7) Rokaki & Boisson 1999; (8) Wang & Lu 2001; (9) Guainazzi et al. 1998; (10) Padovani & Rafanelli 1988.

## Appendix B

# Ratios and contour plots of the radio-quiet sample

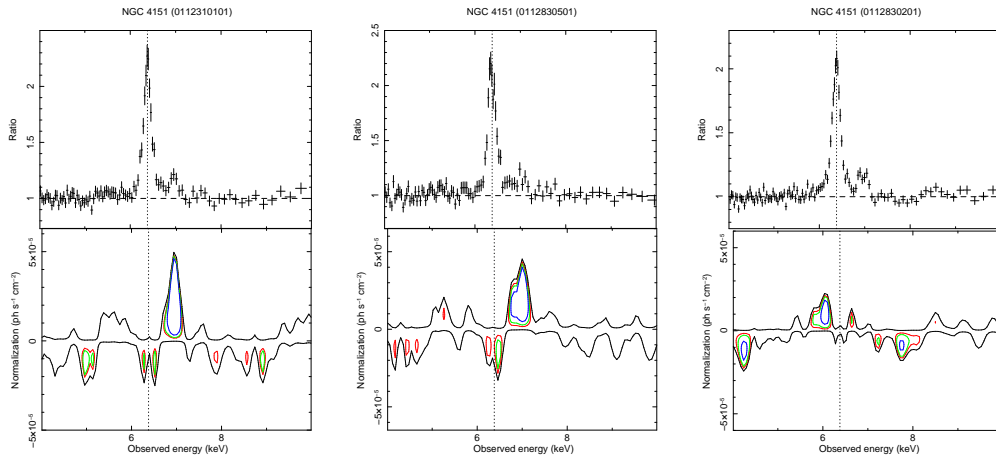


Figure B.1: Ratio against an absorbed power-law continuum (upper panel) and contour plots with respect to the best-fit baseline model listed in Table A.2 (lower panel) for the EPIC pn observations of the type 1 sources. The blue-shifted Fe K absorption lines are pointed by arrows. The location of the neutral Fe K $\alpha$  emission line (rest-frame energy  $E=6.4$  keV) is marked by a vertical line for reference.

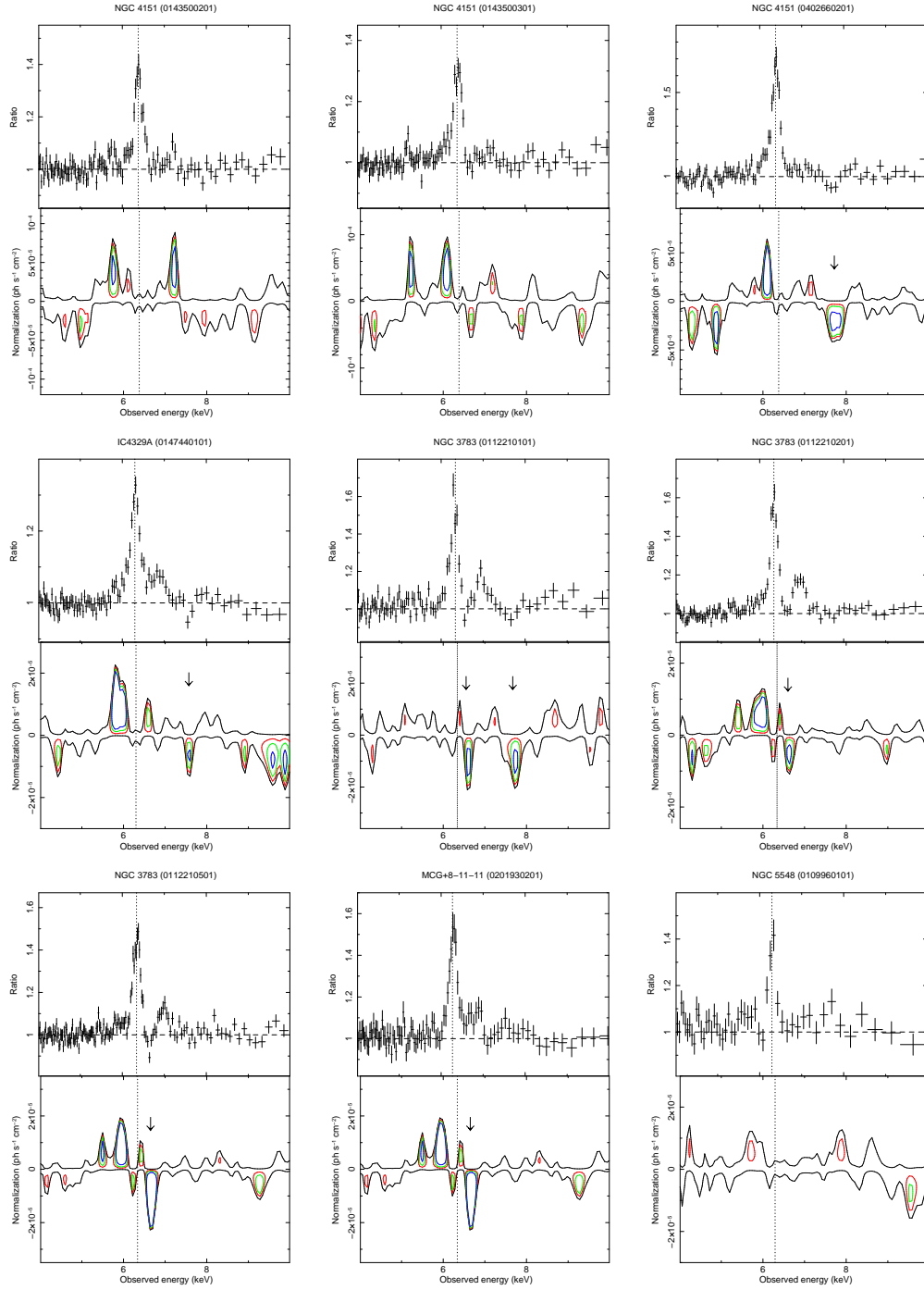


Figure B.2: Ratio against an absorbed power-law continuum (upper panel) and contour plots with respect to the best-fit baseline model listed in Table A.2 (lower panel) for the EPIC pn observations of the type 1 sources. The blue-shifted Fe K absorption lines are pointed by arrows. The location of the neutral Fe K $\alpha$  emission line (rest-frame energy  $E=6.4$  keV) is marked by a vertical line for reference.

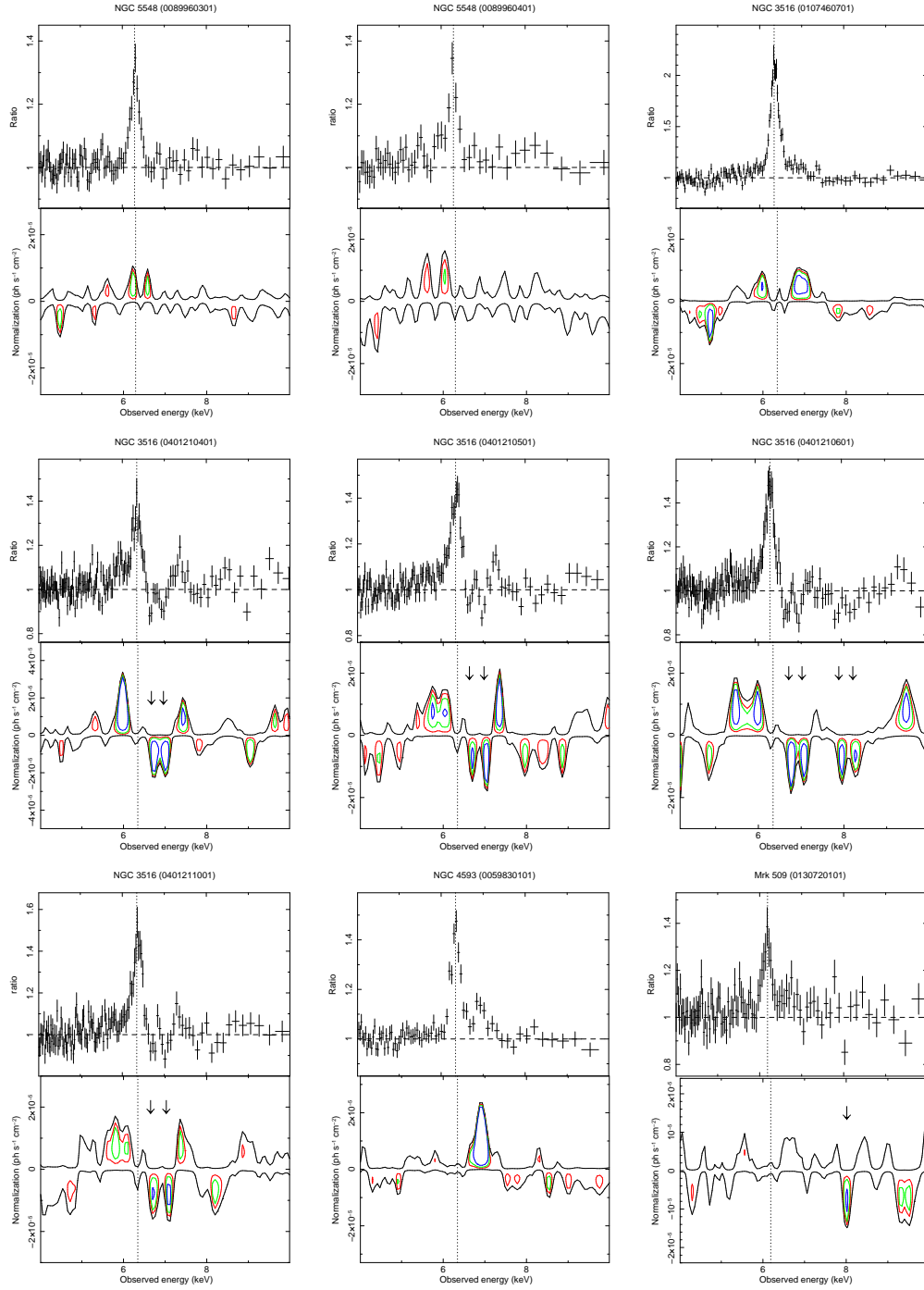


Figure B.3: Ratio against an absorbed power-law continuum (upper panel) and contour plots with respect to the best-fit baseline model listed in Table A.2 (lower panel) for the EPIC pn observations of the type 1 sources. The blue-shifted Fe K absorption lines are pointed by arrows. The location of the neutral Fe K $\alpha$  emission line (rest-frame energy  $E=6.4$  keV) is marked by a vertical line for reference.

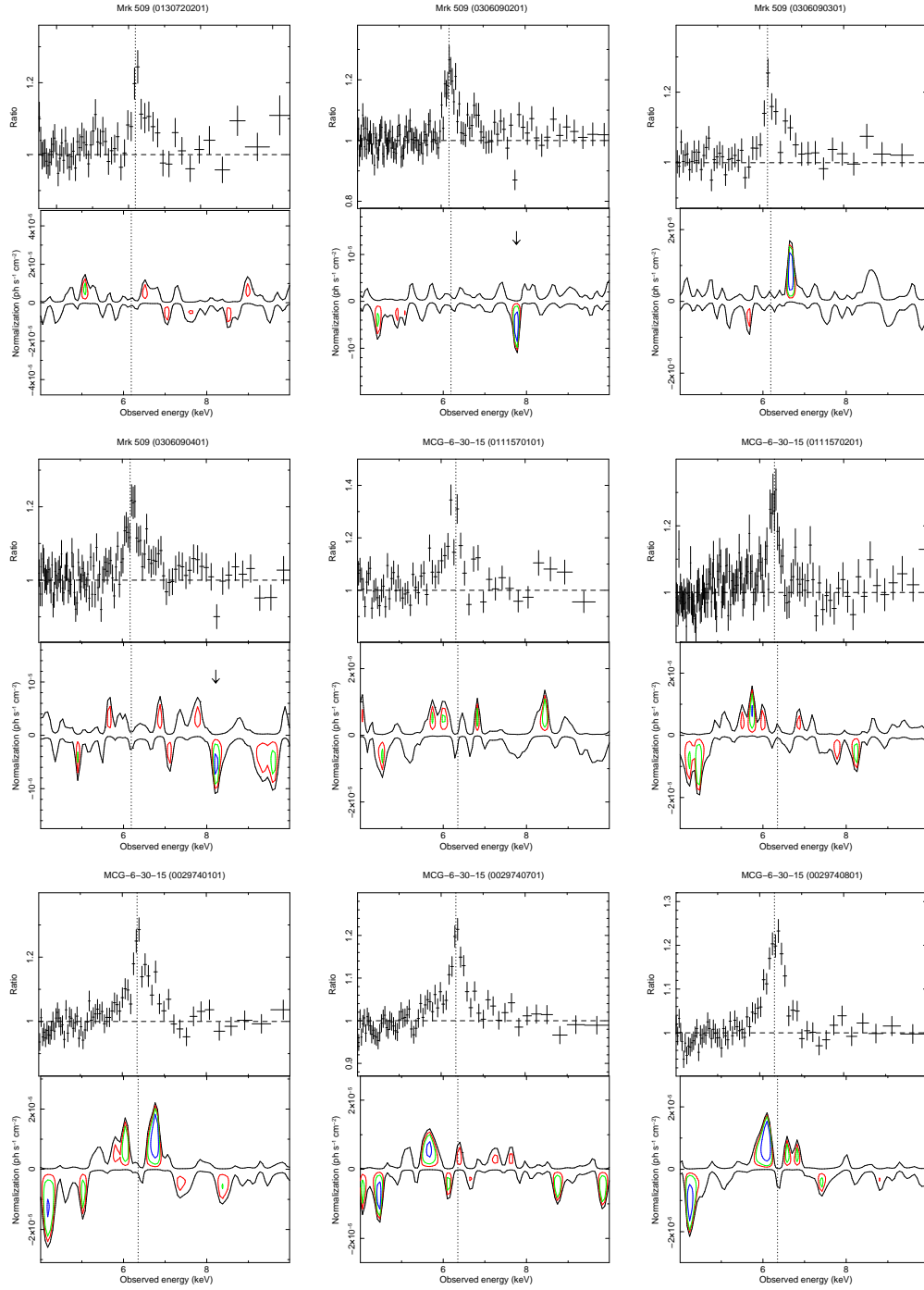


Figure B.4: Ratio against an absorbed power-law continuum (upper panel) and contour plots with respect to the best-fit baseline model listed in Table A.2 (lower panel) for the EPIC pn observations of the type 1 sources. The blue-shifted Fe K absorption lines are pointed by arrows. The location of the neutral Fe K $\alpha$  emission line (rest-frame energy  $E=6.4$  keV) is marked by a vertical line for reference.

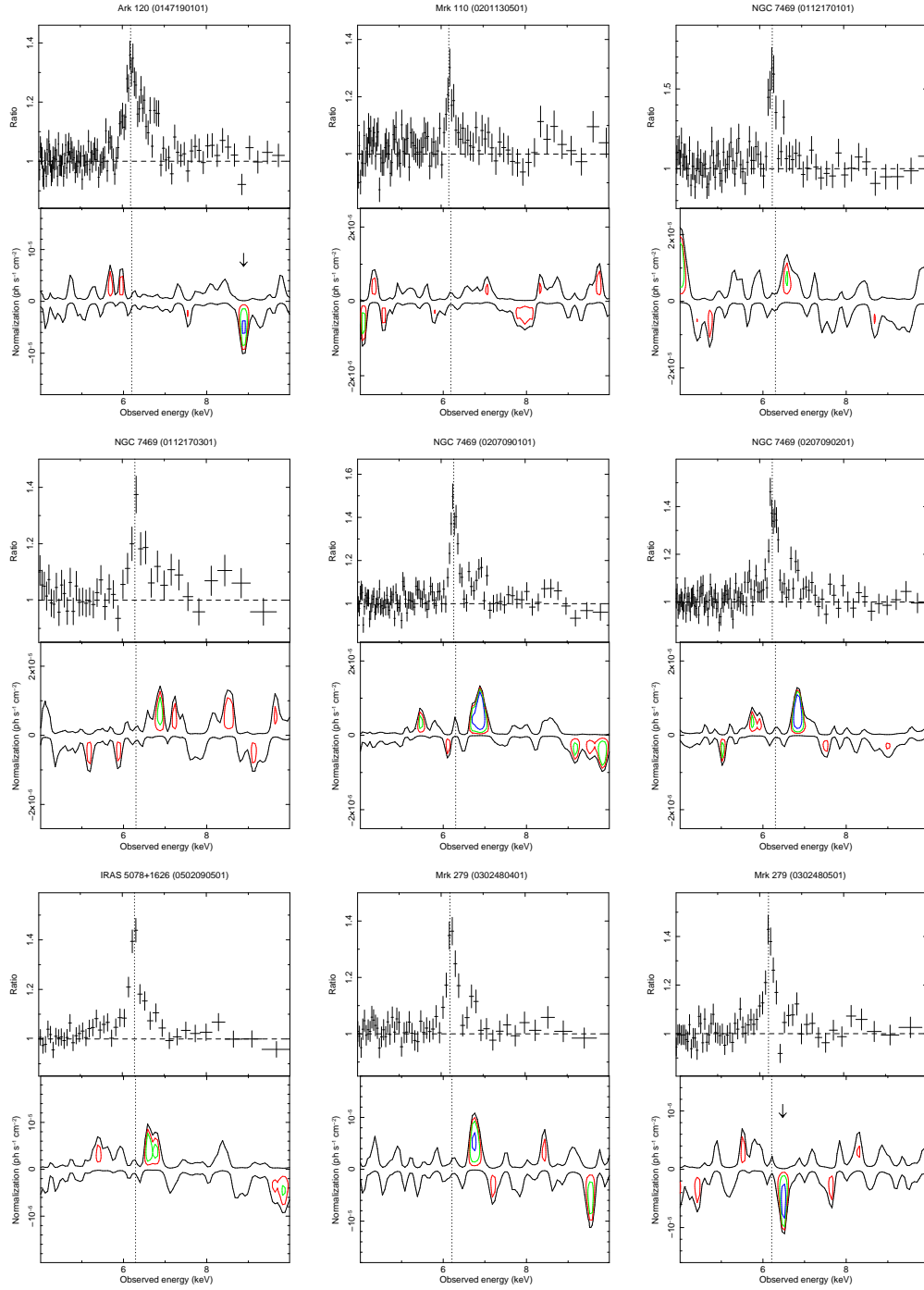


Figure B.5: Ratio against an absorbed power-law continuum (upper panel) and contour plots with respect to the best-fit baseline model listed in Table A.2 (lower panel) for the EPIC pn observations of the type 1 sources. The blue-shifted Fe K absorption lines are pointed by arrows. The location of the neutral Fe  $K\alpha$  emission line (rest-frame energy  $E=6.4$  keV) is marked by a vertical line for reference.

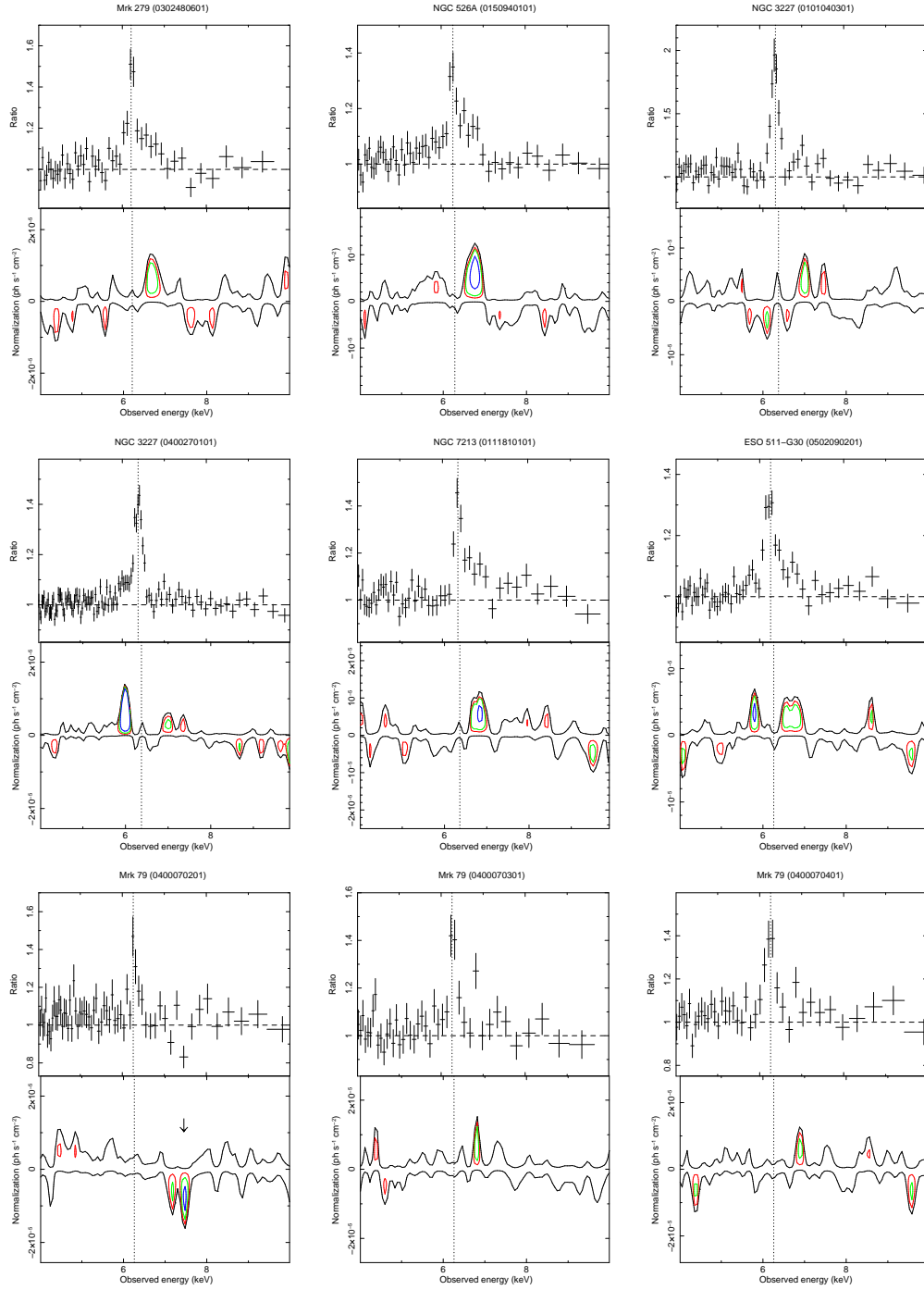


Figure B.6: Ratio against an absorbed power-law continuum (upper panel) and contour plots with respect to the best-fit baseline model listed in Table A.2 (lower panel) for the EPIC pn observations of the type 1 sources. The blue-shifted Fe K absorption lines are pointed by arrows. The location of the neutral Fe K $\alpha$  emission line (rest-frame energy E=6.4 keV) is marked by a vertical line for reference.

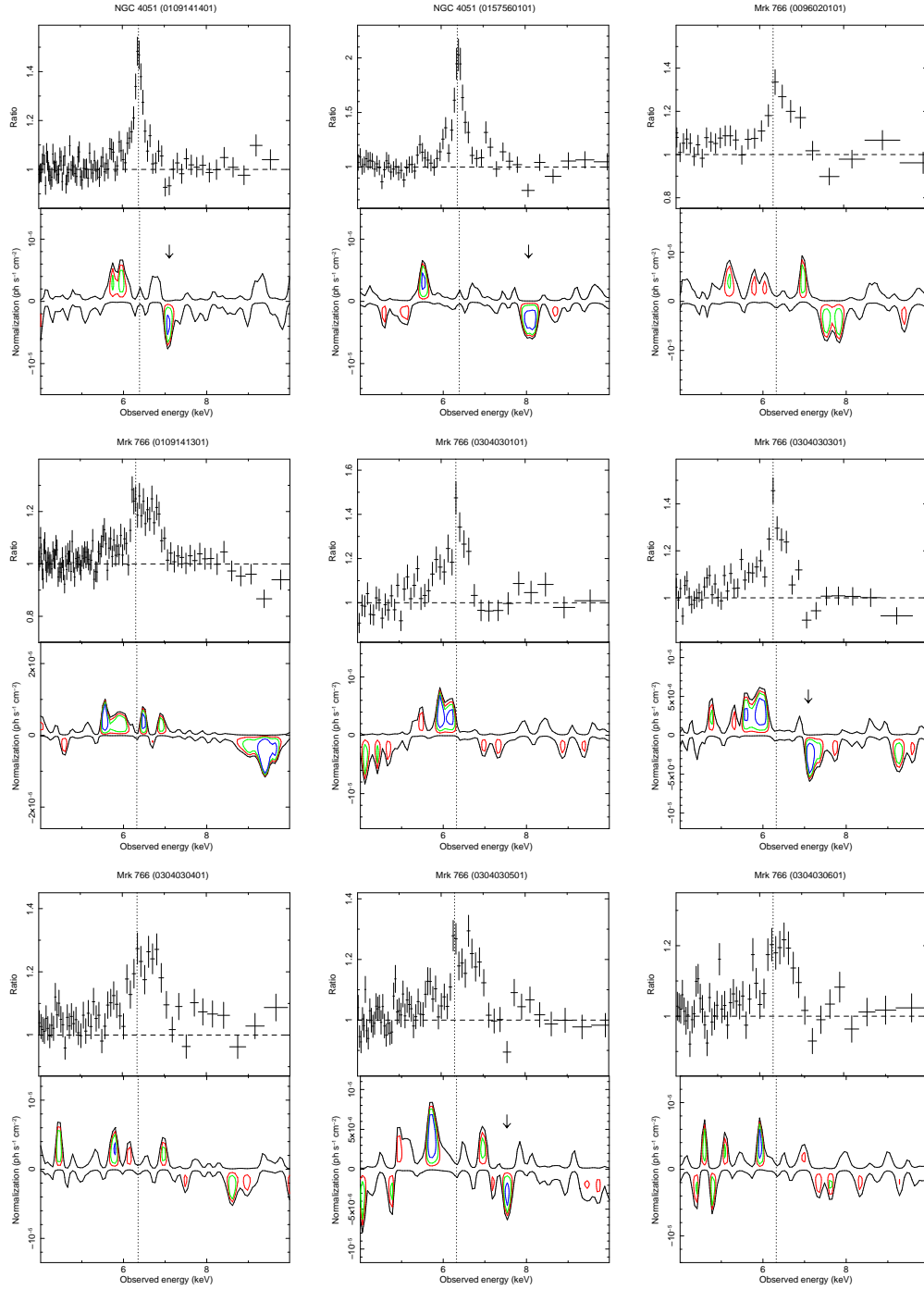


Figure B.7: Ratio against an absorbed power-law continuum (upper panel) and contour plots with respect to the best-fit baseline model listed in Table A.2 (lower panel) for the EPIC pn observations of the type 1 sources. The blue-shifted Fe K absorption lines are pointed by arrows. The location of the neutral Fe K $\alpha$  emission line (rest-frame energy  $E=6.4$  keV) is marked by a vertical line for reference.

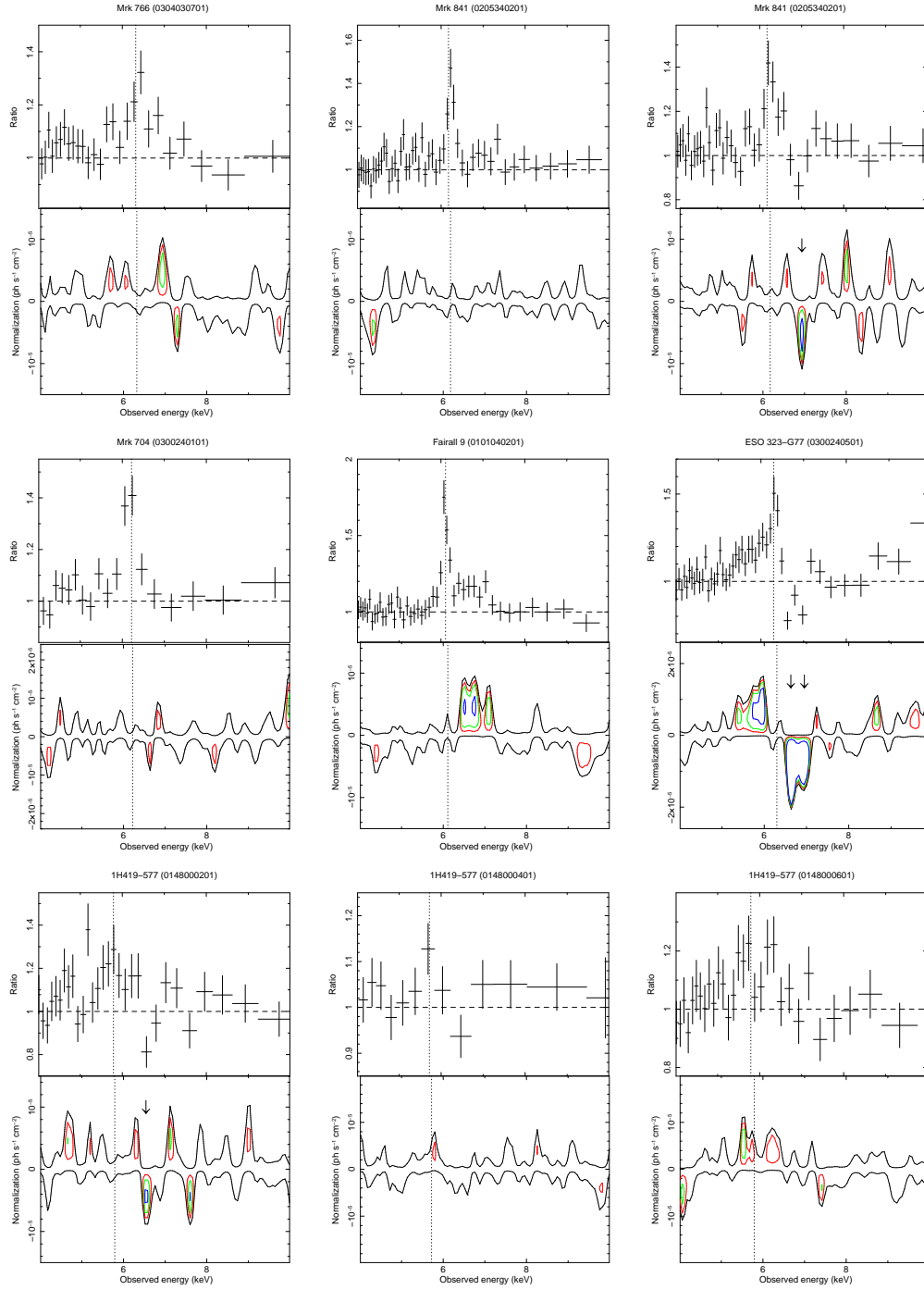


Figure B.8: Ratio against an absorbed power-law continuum (upper panel) and contour plots with respect to the best-fit baseline model listed in Table A.2 (lower panel) for the EPIC pn observations of the type 1 sources. The blue-shifted Fe K absorption lines are pointed by arrows. The location of the neutral Fe K $\alpha$  emission line (rest-frame energy  $E=6.4$  keV) is marked by a vertical line for reference.

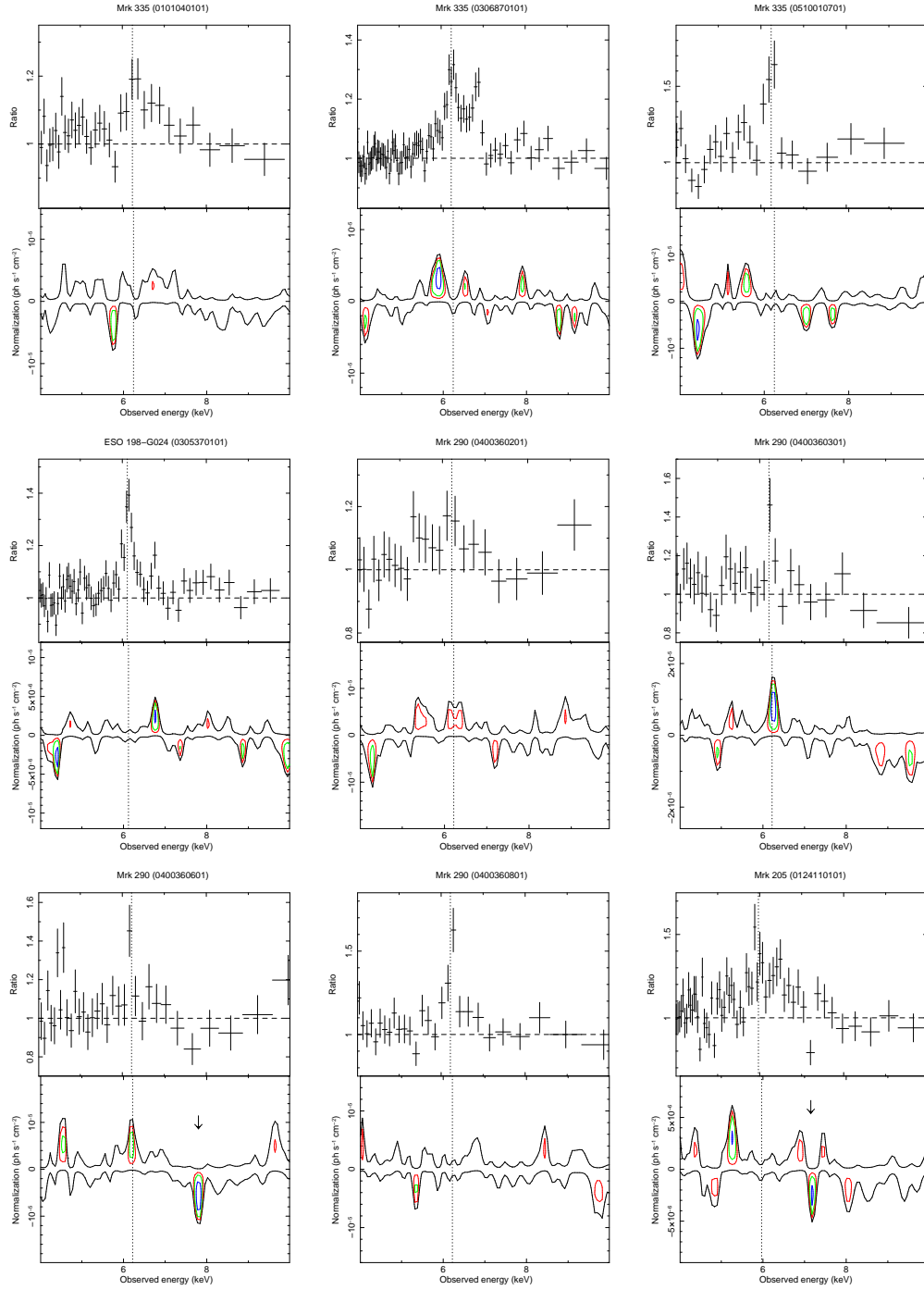


Figure B.9: Ratio against an absorbed power-law continuum (upper panel) and contour plots with respect to the best-fit baseline model listed in Table A.2 (lower panel) for the EPIC pn observations of the type 1 sources. The blue-shifted Fe K absorption lines are pointed by arrows. The location of the neutral Fe K $\alpha$  emission line (rest-frame energy  $E=6.4$  keV) is marked by a vertical line for reference.

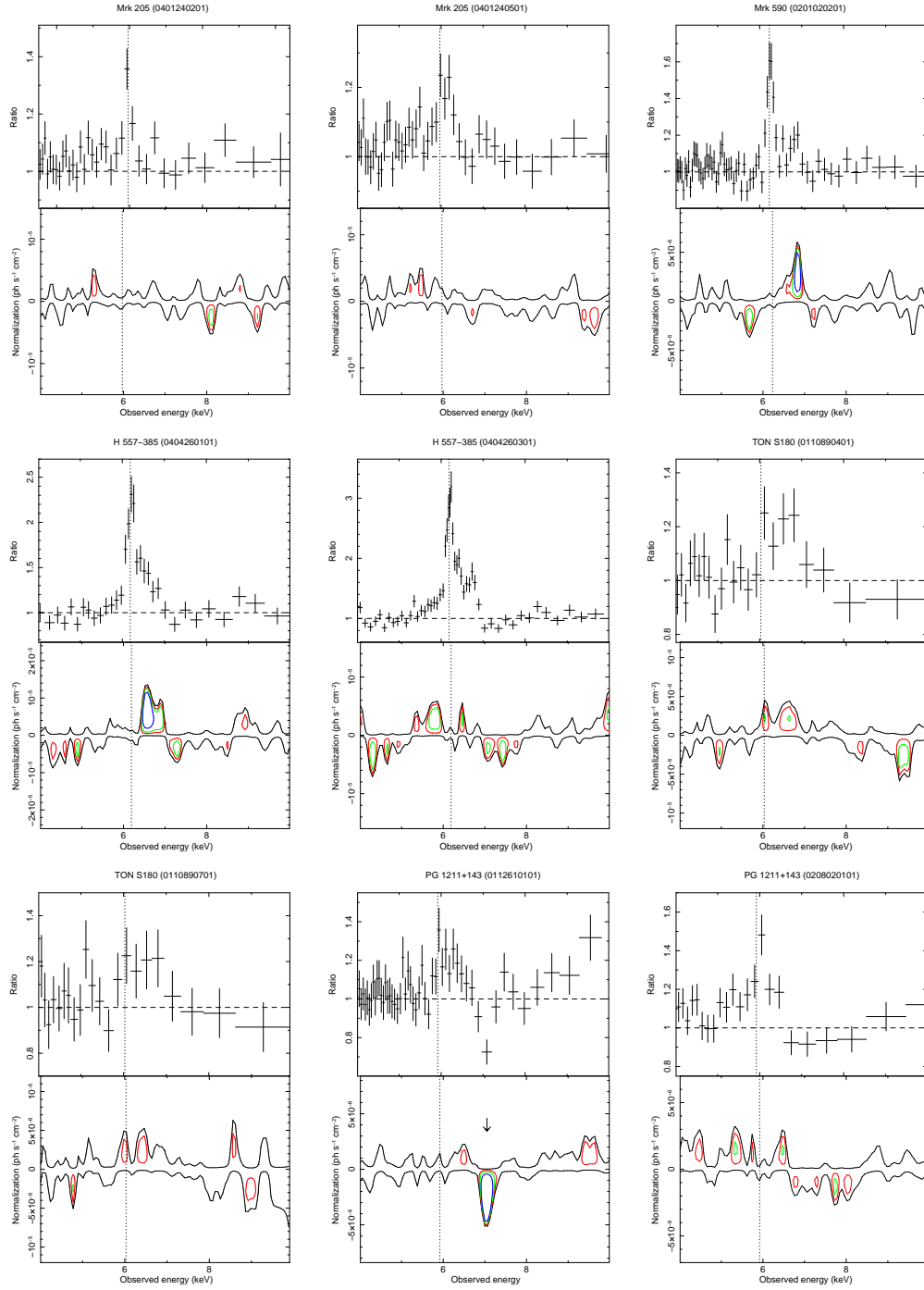


Figure B.10: Ratio against an absorbed power-law continuum (upper panel) and contour plots with respect to the best-fit baseline model listed in Table A.2 (lower panel) for the EPIC pn observations of the type 1 sources. The blue-shifted Fe K absorption lines are pointed by arrows. The location of the neutral Fe K $\alpha$  emission line (rest-frame energy  $E=6.4$  keV) is marked by a vertical line for reference.

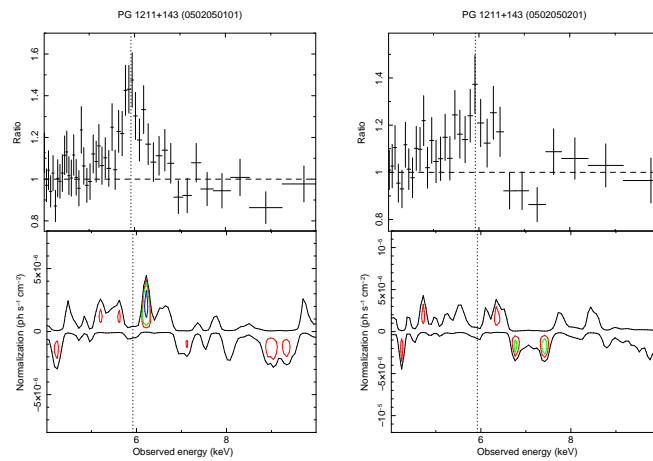


Figure B.11: Ratio against an absorbed power-law continuum (upper panel) and contour plots with respect to the best-fit baseline model listed in Table A.2 (lower panel) for the EPIC pn observations of the type 1 sources. The blue-shifted Fe K absorption lines are pointed by arrows. The location of the neutral Fe K $\alpha$  emission line (rest-frame energy  $E=6.4$  keV) is marked by a vertical line for reference.

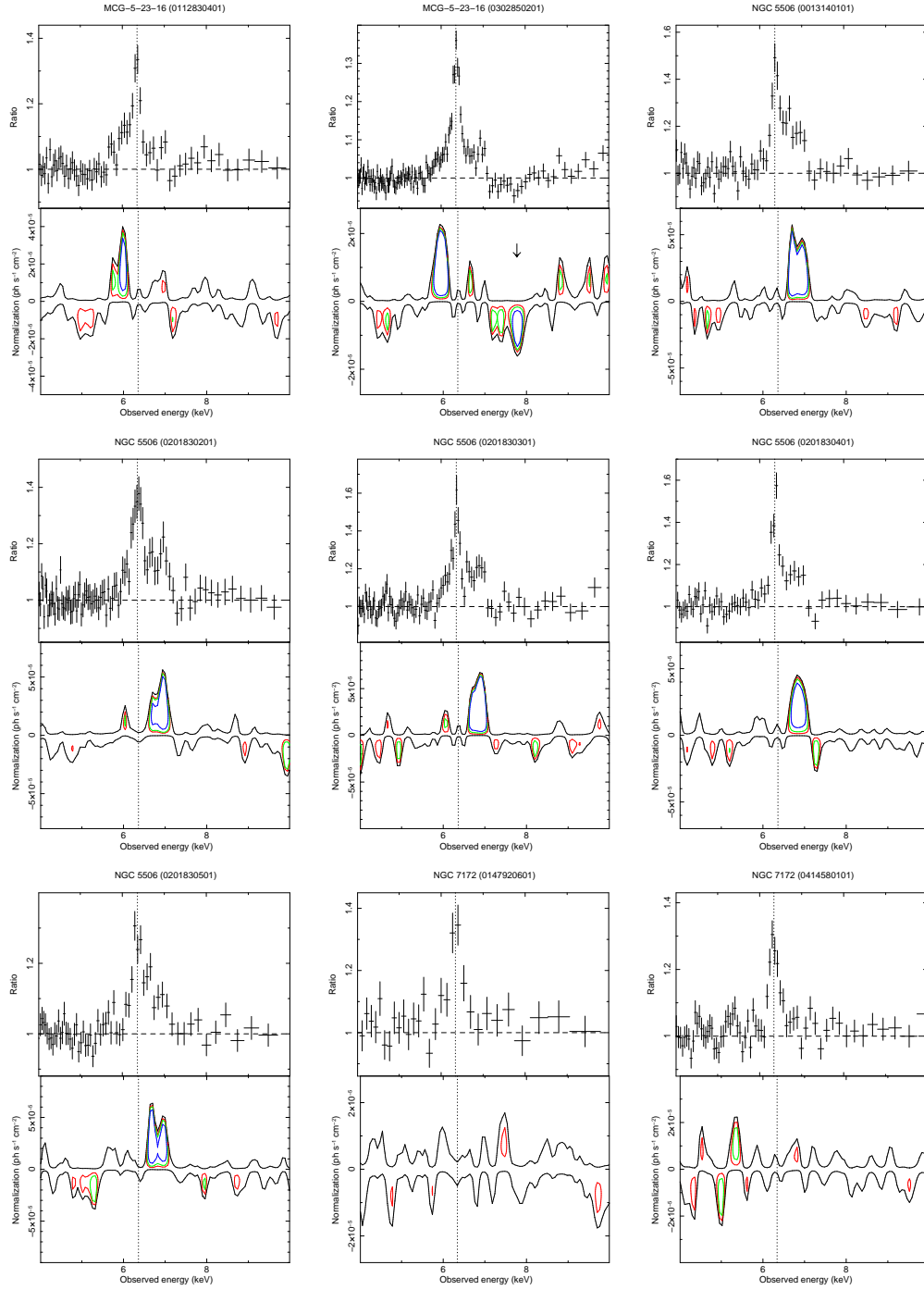


Figure B.12: Ratio against an absorbed power-law continuum (upper panel) and contour plots with respect to the best-fit baseline model listed in Table A.2 (lower panel) for the EPIC pn observations of the type 2 sources. The blue-shifted Fe K absorption lines are pointed by arrows. The location of the neutral Fe K $\alpha$  emission line (rest-frame energy  $E=6.4$  keV) is marked by a vertical line for reference.

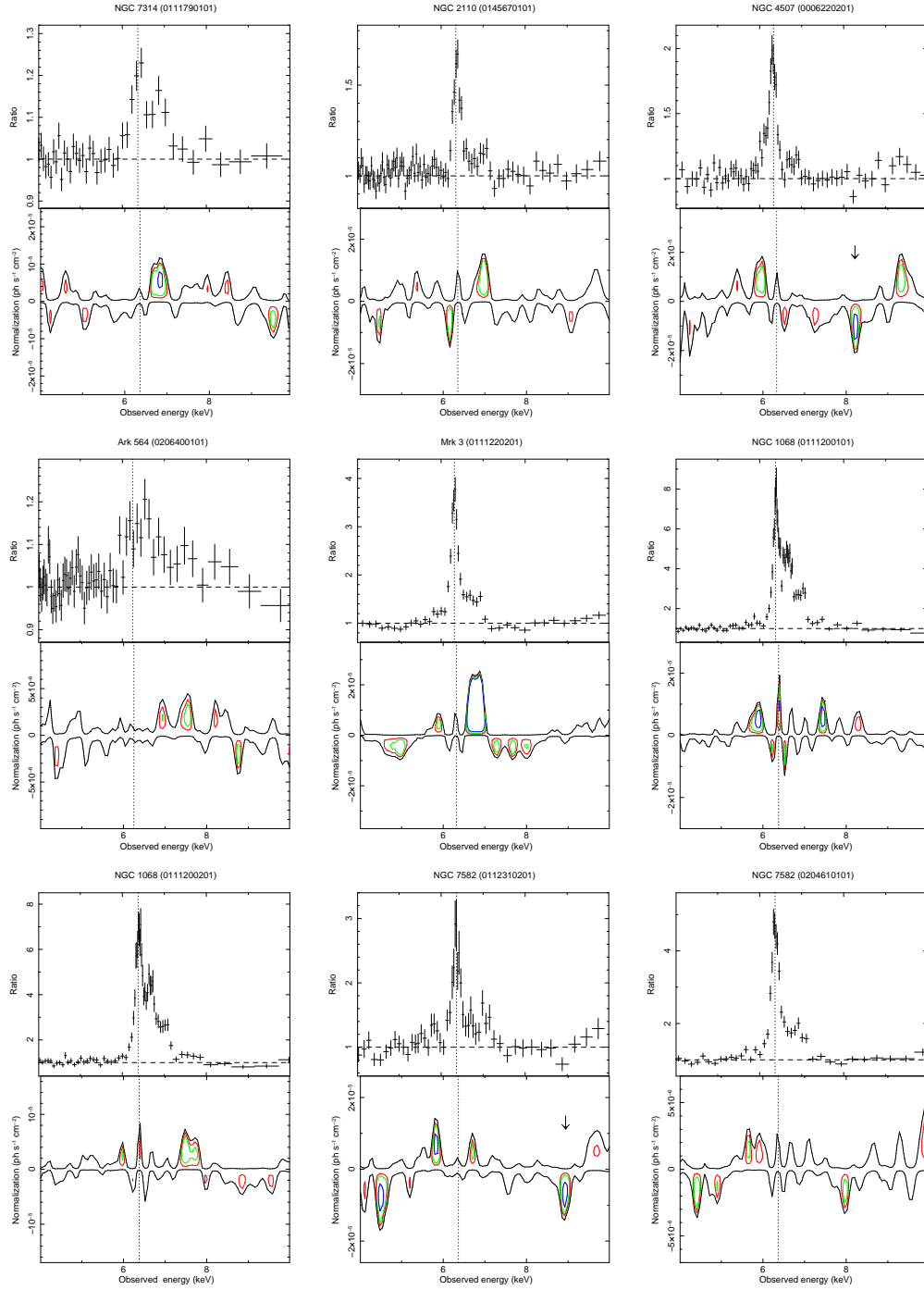


Figure B.13: Ratio against an absorbed power-law continuum (upper panel) and contour plots with respect to the best-fit baseline model listed in Table A.2 (lower panel) for the EPIC pn observations of the type 2 sources. The blue-shifted Fe K absorption lines are pointed by arrows. The location of the neutral Fe K $\alpha$  emission line (rest-frame energy  $E=6.4$  keV) is marked by a vertical line for reference.

## Appendix C

# Notes on single sources of the radio-quiet sample

In this section we discuss and compare our work with the results already published in the literature. We payed particular attention to the works reporting a spectral analysis of the Fe K band of each radio-quiet sample source, especially if performed with the XMM-Newton EPIC pn instrument.

*NGC 4151*: Piro et al. (2005) reported the detection of an absorption feature around  $E \simeq 8.5\text{--}9$  keV with a statistical significance of 99.96% in one out of five Beppo-SAX observations of this source. Due to the low energy resolution of that instrument, the feature could be fitted either with an absorption edge due to highly ionized iron at rest or with an absorption line due to Fe XXV/XXVI with blue-shift velocity of  $\sim 0.1\text{--}0.2c$ . The presence of a complex and possibly multi-phase ionized absorber in NGC 4151 has also been reported by other authors, such as Schurch et al. (2003) using XMM-Newton data and Kraemer et al. (2005) using simultaneous HST and Chandra observations. These results are in agreement with our findings of two narrow blue-shifted absorption lines identified as Fe XXVI Ly $\alpha$  at  $E \simeq 7.7\text{--}7.8$  keV in two XMM-Newton observations of the source (obs. 0112830201 and 0402660201). Moreover, in these observations we found also the presence of narrow absorption lines at the energies of  $E \simeq 4.3$  keV and  $E \simeq 4.8$  keV (see contour plots in Appendix B) with confidence levels  $\simeq 99\%$ . If identified as blue-shifted absorption lines from Ca XIX He $\alpha$  ( $E \simeq 3.9$  keV) and Ca XX Ly $\alpha$  ( $E \simeq 4.11$  keV), their velocity is completely consistent with that inferred from the Fe K lines of  $\simeq 0.1c$ . However, it should be noted that the blue-shifted Fe K absorption line in the first observation has not been included in Table A.2 and in the successive discussion because its Monte Carlo confidence level was

lower than the threshold value of 95%.

*IC4329A*: the detection of a narrow blue-shifted absorption feature at  $E \simeq 7.7$  keV ascribable to Fe XXVI Ly $\alpha$  in the XMM-Newton spectrum of IC4329A has already been reported by Markowitz et al. (2006). We confirm their result. Moreover, from the contour plot in Appendix B, a broad absorption trough can be observed at an energy greater than  $\simeq 9$  keV. We tried to model it with an ionized Fe K edge. However, we obtained a better fit modeling it as a blend of three further unresolved Fe XXVI Lyman series lines (Ly $\beta$ , Ly $\gamma$  and Ly $\delta$ ) with a blue-shift consistent with that of the Fe XXVI Ly $\alpha$ . In fact, we performed a fit adding to the baseline model (see Table A.2) four additional narrow absorption lines with energies fixed to the expected values for the Fe XXVI Lyman series and leaving their common energy shift as a free parameter. These lines provide a very good modeling of all the absorption features, with a global  $\Delta\chi^2 = 30$  for five additional parameters. The probability of having these four absorption lines at these exact energies simply from random fluctuations is very low, about  $10^{-4}$ . Interestingly enough, their common blue-shift velocity is  $+0.097 \pm 0.005c$ , completely consistent with that estimated for the single Fe XXVI Ly $\alpha$  line. The resultant EWs of the four Fe XXVI lines are: EW=  $11 \pm 6$  eV for the Ly $\alpha$ , EW=  $11 \pm 8$  eV for the Ly $\beta$ , EW=  $10 \pm 6$  for the Ly $\gamma$  and EW=  $15 \pm 7$  eV for the Ly $\delta$ . Their ratios are close to unity, which suggest possible saturation effects.

*NGC 3783*: a strong absorption line at the rest frame energy of  $E \simeq 6.7$  keV has been detected by Reeves et al. (2004) in the XMM-Newton spectrum of this source. The authors pointed out that the line energy is consistent with rest-frame resonant absorption from a blend of different highly ionized iron ions, such as Fe XXIII ( $E \simeq 6.62$  keV), Fe XXIV ( $E \simeq 6.66$  keV) and Fe XXV ( $E \simeq 6.70$  keV). We confirm their detection and the line parameters we derived are in agreement.

*MCG+8-11-11*: a detailed analysis of the XMM-Newton spectrum of this source has already been published by Matt et al. (2006). We confirm their overall results. We did not detect any narrow Fe K absorption line.

*NGC 5548*: a detailed analysis of the XMM-Newton spectrum of this source has already been published by Pounds et al. (2003b). Our analysis confirms their overall results. We did not detect any narrow Fe K absorption line.

*NGC 3516*: the detection of narrow highly ionized absorption features in the Chandra HETG and XMM-Newton EPIC pn spectra of this source have already been reported by

Turner et al. (2005) and Turner et al. (2008). In particular, the authors reported the presence of H/He-like resonant absorption lines from Mg, Si, S and Fe. These features are indicative of the existence of different layers of complex absorption, with outflow velocities of few 1000 km/s. Our analysis gave results in complete agreement with these conclusions.

*NGC 4593*: a detailed analysis of the XMM-Newton spectrum of this source has already been published by Reynolds et al. (2004). Our analysis confirms their overall results. We did not detect any narrow Fe K absorption line.

*Mrk 509*: the detection of narrow blue-shifted absorption lines ascribable to the Fe XXVI Ly $\alpha$  resonant transition in the XMM-Newton spectra of this source has already been reported by Dadina et al. (2005) and Cappi et al. (2009). Our results are in complete agreement with theirs.

*MCG-6-30-15*: the Fe K band of this source is known to be complex, with the overlapping of several spectral components, such as a broad relativistic emission line, narrow emission/absorption features and warm absorption. Therefore, even if the EPIC pn has a high effective area in this energy band, its moderate energy resolution can be not sufficient to unambiguously disentangle all the spectral features. For instance, Fabian et al. (2002) and Vaughan & Fabian (2004) have found hints for a narrow absorption feature at  $\sim 6.7$  keV probably due to Fe XXV He $\alpha$  in the EPIC pn spectrum of this source. However, they stated that it is difficult to clearly discriminate between narrow absorption and emission features due to the spectral complexity.

Instead, from a deep spectral analysis of this source performed with the higher energy resolution Chandra HETG spectrometer, Young et al. (2005) have been able to clearly detect two narrow (unresolved) absorption lines ascribable to Fe XXV He $\alpha$  and Fe XXVI Ly $\alpha$ . The lines have blue-shift velocities of  $\sim 0.007c$  and equivalent widths of the order of 20 eV.

In our analysis we have not been able to unambiguously detect these blue-shifted narrow Fe K absorption features. This demonstrates the need to perform such systematic studies with other observatories as well, in order to exploit the different capabilities offered by each instrument.

*Ark 120*: a detailed analysis of the XMM-Newton spectrum of this source has already been published by Vaughan et al. (2004). The authors argued that from a broad-band X-ray analysis of the combined RGS and EPIC pn data there is no evidence for an intrinsic

warm absorber and placed upper limits on the ionic column densities that are substantially lower than those of more typical, absorbed Seyfert 1s. This led them to claim that Ark 120 could actually represent a “bare” Seyfert 1 nucleus.

However, the reason for the lack of an X-ray warm absorber is quite unclear. It is plausible that a substantial column of ionized gas exists but it is either too highly ionized to show significant spectral features below a few keV or lies out of the line of sight (requiring a covering factor less than unity). These arguments are in agreement with our finding of a substantially blue-shifted Fe XXVI Ly $\alpha$  absorption line at the rest frame energy of  $\sim 9.18$  keV.

*Mrk 110*: a deep analysis of the XMM-Newton spectrum of this source has been reported by Boller et al. (2007). We did not detect any narrow blue-shifted Fe K absorption feature.

*NGC 7469*: a detailed analysis of the XMM-Newton spectrum of this source has already been published by Blustin et al. (2003). Our analysis confirms their overall results. We did not detect any significant Fe K absorption feature.

*IRAS 05078+1626*: the analysis of the XMM-Newton EPIC pn spectrum of the source has never been published. We found that a simple power-law continuum plus a neutral Fe K $\alpha$  emission line at  $\sim 6.4$  keV provides a good fit to the spectral data in the 4–10 keV band. We did not find evidence for narrow Fe K absorption features.

*Mrk 279*: we did not find any published work on the XMM-Newton EPIC pn spectrum of the source. However, Fields et al. (2007) found evidence for the presence of different layers of highly ionized absorbing material from the spectral analysis of the soft X-ray Chandra LETG data. The associated column densities are low (of the order of  $\sim 10^{20}$  cm $^{-2}$ ) and the outflow velocities are of few  $\sim 1000$  km/s. The authors also stated that the existence of a more ionized outflow component with iron ions from Fe XXIV to Fe XXVI cannot be ruled out. This is consistent with our detection of a narrow absorption line ascribable to Fe XXV He $\alpha$  in the EPIC pn spectrum of the source, at a rest frame energy of  $\simeq 6.69$  keV.

*NGC 526A*: the analysis of the XMM-Newton EPIC pn spectrum of the source has never been published. We found that a simple power-law continuum plus a neutral Fe K $\alpha$  emission line at  $\sim 6.4$  keV provides a good fit to the spectral data in the 4–10 keV band. We did not find evidence for narrow Fe K absorption features.

*NGC 3227*: a deep analysis of the EPIC pn spectrum of the source has been reported by Gondoin et al. (2003) and Markowitz et al. (2009). The 4–10 keV spectrum of the source is well modeled by a simple power-law continuum plus a neutral Fe K $\alpha$  emission line at  $\sim 6.4$  keV. However, in the first XMM-Newton observation there is the need for a substantial neutral absorption component with column density of  $\sim 10^{23}$  cm $^{-2}$ . This has been reported to be consistent with an eclipsing event by a broad line region cloud (Lamer et al. 2003). Our overall results are consistent with these conclusions and we did not find evidence for narrow Fe K absorption features.

*NGC 7213*: a deep analysis of the XMM-Newton EPIC pn spectrum of the source in the Fe K band has been performed by Bianchi et al. (2003a). We refer the reader to that paper for detailed information. However, our overall results are consistent with theirs and we did not find evidence for highly ionized Fe absorption features.

*ESO 511-G030*: the analysis of the XMM-Newton EPIC pn spectrum of the source has never been published. We found that a simple power-law continuum plus a neutral Fe K $\alpha$  emission line at  $\sim 6.4$  keV provide a good fit to the spectral data in the 4–10 keV band. We did not find evidence for narrow Fe K absorption features.

*Mrk 79*: (or UGC3973) the spectral analysis of two snapshot XMM-Newton observations of the source has been reported by Gallo et al. (2005). We did not consider those observations because of their too short exposures ( $< 10$  ks). Instead, here we report for the first time the spectral analysis of three new longer XMM-Newton EPIC pn observations of the source. In all the cases the baseline model is constituted by a simple power-law continuum plus a neutral Fe K $\alpha$  emission line at  $\sim 6.4$  keV, with parameters consistent with those of Gallo et al. (2005). However, in one observation we have detected a narrow absorption feature ascribable to Fe XXVI Ly $\alpha$  at  $E \simeq 7.63$  keV, consistent with a blue-shift velocity of  $\sim 0.1c$ .

*NGC 4051*: a detailed analysis of the two XMM-Newton observations of this source has been published by Pounds et al. (2004a). The overall spectral fit is consistent with ours. We confirm their detection of a narrow blue-shifted absorption line ascribable to Fe XXVI Ly $\alpha$  at the energy of  $\sim 7.1$  keV in the first observation. We detected a further absorption line at  $\simeq 8.1$  keV in the spectrum of the second observation. We interpreted this feature as a blue-shifted Fe XXVI Ly $\alpha$  absorption line.

*Mrk 766*: a detailed analysis of the XMM-Newton EPIC pn spectra of the source has

already been reported by Pounds et al. (2003c), Miller et al. (2007) and Turner et al. (2007). The spectral analysis of the Fe K band show the presence of both broad absorption troughs and narrow absorption line-like features at energies  $\geq 7$  keV. This complexity could indicate absorption from various layers of gas in different physical states. In fact, in two spectra we detected absorption features at energies greater than 7 keV that could only be modeled by narrow (unresolved) absorption lines. We interpreted such features as blue-shifted Fe XXVI Ly $\alpha$  absorption lines. The presence of the first one at a rest-frame energy of  $\sim 7.3$  keV has already been suggested by Miller et al. (2007) and Turner et al. (2007). The detection of the second one at  $\sim 7.6$  keV has instead never been reported. However, in another observation of the source (0109141301) a significant broad absorption trough between  $E \simeq 8-9$  keV can be observed (see contour plot in Appendix B). As already reported by Pounds et al. (2003c), this feature is well modeled by a photoelectric edge, whose energy is consistent with the rest-frame Fe XXV K edge ( $E \simeq 8.8$  keV). We did not include this feature in Table A.2.

*Mrk 841*: a detailed analysis of the XMM-Newton EPIC pn spectra of this source has already been published by Longinotti et al. (2004) and Petrucci et al. (2007). The authors tested different complex models in order to explain the broad-band X-ray spectral shape. However, our simple spectral parametrization is in agreement with their results in the 4–10 keV band. Moreover, we detected a narrow absorption feature ascribable to a blue-shifted Fe XXVI Ly $\alpha$  resonance absorption line at the rest frame energy of  $\sim 7.2$  keV.

*Mrk 704*: the XMM-Newton EPIC pn spectral analysis of this source has never been published in the literature. We have found the 4–10 keV spectrum to be well modeled by an absorbed power-law continuum plus a narrow neutral Fe K $\alpha$  emission line. We did not find evidence for additional narrow Fe K absorption features.

*Fairall 9*: the XMM-Newton EPIC pn spectral analysis of this source has already been published by Gondoin et al. (2001). We confirm their overall results. We did not detect any narrow Fe K absorption line.

*ESO 323-G77*: the detailed XMM-Newton EPIC pn spectral analysis of this source has been published by Jiménez-Bailón et al. (2008). We confirm their detection of a couple of narrow absorption features at the rest frame energy of  $\sim 6.7$  keV and  $\sim 7$  keV ascribable to Fe XXV He $\alpha$  and Fe XXVI Ly $\alpha$  resonant absorption.

*1H419-577*: the detailed broad-band spectral analysis of the XMM-Newton EPIC

pn observations of this source has been published by Pounds et al. (2004b) and Fabian et al. (2005). From their study, the authors argued that a good fit to the data can be provided either by an absorption dominated or by a reflection dominated model. However, these two models cannot be distinguished in the narrow energy band we considered (4–10 keV) and the continuum can be well approximated by a simple power-law. We detected a blue-shifted narrow absorption line ascribable to Fe XXVI Ly $\alpha$  at the rest frame energy of  $\sim 7.2$  keV.

*Mrk 335*: the detection of an absorption feature at the rest frame energy of  $\sim 5.9$  keV in the XMM-Newton EPIC pn spectrum of this source has been reported by Longinotti et al. (2007a). If identified with Fe XXVI Ly $\alpha$  resonant absorption, this would indicate a red-shift velocity for the line of  $\sim 0.16$  c. We did not detect any narrow blue-shifted Fe K absorption lines.

*ESO 198-G024*: the analysis of the XMM-Newton EPIC pn spectrum of this source has been reported by Guainazzi (2003) and Porquet et al. (2004). We agree with their overall results in the 4–10 keV band and we did not find evidence for highly ionized Fe K absorption lines.

*Mrk 290*: we did not find any published analysis of the XMM-Newton EPIC pn spectrum of the source. We have detected a narrow absorption line ascribable to Fe XXVI Ly $\alpha$  in one out of four observations. The line rest frame energy is  $E \simeq 8$  keV, which would suggest a blue-shift velocity of  $\sim 0.14$ c.

*Mrk 205*: the Fe K band analysis of the XMM-Newton EPIC pn spectrum of the source has already been published by Reeves et al. (2001) and Page et al. (2003). We found that the spectrum in this band can be well modeled by a simple power-law continuum plus narrow Gaussian emission lines. However, we detected an additional narrow absorption feature at the rest frame energy of  $\sim 7.7$  keV in one observation. If identified with Fe XXVI Ly $\alpha$  resonant absorption this would suggest an outflow velocity of  $\sim 0.1$ c.

*Mrk 590*: the detailed analysis of the XMM-Newton EPIC pn spectrum of the source has already been published by Longinotti et al. (2007b). We confirm their overall results. We did not detect any narrow Fe K absorption lines.

*H 577-385*: the detailed spectral analysis of the XMM-Newton EPIC pn observations of the source has already been reported by Longinotti et al. (2009). We agree with their overall results. We did not find evidence for Fe K absorption features.

*TON S180*: we did not find any published analysis of the XMM-Newton EPIC pn spectrum of the source. The 4–10 keV band is well modeled by a simple power-law continuum without additional spectral features.

*PG 1211+143*: a detailed analysis of the XMM-Newton EPIC pn spectra of the source has already been reported by Pounds et al. (2003a), Pounds & Page (2006) and Pounds & Reeves (2009). In particular, Pounds et al (2003) clearly detected a narrow blue-shifted Fe K absorption line at the rest frame energy of  $\sim 7.6$  keV in the pn spectrum of the first XMM observation. The identification of this line with Fe XXVI Ly $\alpha$  suggests a relativistic outflow velocity of  $\sim 0.08c$ . Moreover, the presence of a highly ionized absorber in this source was confirmed also by the detection of several other blue-shifted narrow absorption lines due to lighter elements in the RGS as well. In a subsequent re-analysis of this observation using also the MOS data Pounds & Page (2006) have been able to confirm the presence of additional absorption lines, yielding a revised outflow velocity of  $\sim 0.13$ – $0.15c$ . Furthermore, the authors stated that they removed the ambiguity in the identification of the  $\sim 7.6$  keV absorption feature, with a preference for Fe XXV He $\alpha$ . This would imply a consequently higher outflow velocity of  $\sim 0.13c$ . We adopted this latter line identification.

*MCG-5-23-16*: a detailed spectral analysis of the XMM-Newton EPIC pn observations of this source has already been published by Dewangan et al. (2003) and Braitto et al. (2007). We agree with their overall results in the 4–10 keV band. Moreover, we confirm the detection made by Braitto et al. (2007) of a narrow absorption feature at the rest frame energy of  $\sim 7.8$  keV in the last observation. If identified with Fe XXVI Ly $\alpha$  resonant absorption, the feature indicates a substantial blue-shift velocity of  $\sim 0.12c$ .

*NGC 5506*: the analysis of the XMM-Newton spectra of the source have been reported by Matt et al. (2001) and Bianchi et al. (2003b). We agree with their overall results and we did not find evidence for narrow ionized Fe K absorption lines.

*NGC 7172*: the 4–10 keV spectra of the XMM-Newton EPIC pn observations of the source have never been published. We found them to be well modeled by a simple absorbed power-law continuum plus a neutral Fe K $\alpha$  emission line. We did not detect additional Fe K absorption features.

*NGC 7314*: we did not find any reported analysis of the XMM-Newton EPIC pn spectrum of the source. We found the 4–10 keV band to be well modeled by a simple absorbed power-law continuum plus a narrow neutral Fe K $\alpha$  emission line. We did not

find evidence for narrow Fe K absorption lines.

*NGC 2110*: a detailed analysis of the broad-band X-ray spectrum of the source observed by XMM-Newton has been reported by Evans et al. (2007). We agree with their results in the 4–10 keV band. We did not detect any Fe K absorption line.

*NGC 4507*: a detailed broad-band analysis of the XMM-Newton EPIC pn spectrum of the source has been reported by Matt et al. (2004a). We agree with their results in the 4–10 keV band. Furthermore, we have detected a narrow absorption feature at the rest frame energy of  $\sim 8.3$  keV. If associated with Fe XXVI Ly $\alpha$  resonant absorption, the corresponding blue-shift velocity is substantial, of the order of 0.18c.

*Ark 564*: we did not find any published analysis of the XMM-Newton EPIC pn spectrum of the source. We found the 4–10 keV spectrum to be well modeled by a simple power-law continuum and Gaussian emission lines. We did not detect additional Fe K absorption features.

*Mrk 3*: the analysis of the broad-band X-ray spectrum of the source observed with the XMM-Newton EPIC pn camera has already been reported by Bianchi et al. (2005b) and Pounds & Page (2005). We did not detect any Fe K absorption line.

*NGC 1068*: the detailed analysis of the XMM-Newton EPIC pn spectra of the source has been reported by Matt et al. (2004b) and Pounds & Vaughan (2006). We agree with their overall results in the 4–10 keV band and we did not find evidence for Fe K absorption lines.

*NGC 7582*: a broad-band spectral analysis of the XMM-Newton observations of this source has been reported by Piconcelli et al. (2007). However, we reported for the first time the detection a narrow absorption feature at the rest frame energy of  $E \simeq 9$  keV in the first observation (obs. 0112310201). The description of this line has been included in Table A.2. Moreover, in the contour plots in Appendix B, there is evidence for a narrow absorption line at the energy of  $\sim 4.5$  keV with F-test confidence contours  $\geq 99\%$ . From a detailed spectral analysis, we derived the rest-frame line energy of  $E = 4.52 \pm 0.03$  keV and equivalent width  $EW = 76^{+21}_{-18}$  eV. We also found the presence of two further absorption lines with F-test confidence levels  $\simeq 95$ – $98\%$  at  $E = 4.12 \pm 0.03$  keV, with  $EW = 63^{+25}_{-18}$  eV, and  $E = 5.22 \pm 0.03$  keV, with  $EW = 41^{+22}_{-19}$  eV. If the absorption line at  $E \simeq 9$  keV is identified with the Fe XXV He $\alpha$  transition ( $E \simeq 6.7$  keV), these lower energy lines turn out to be consistent with being absorption from Ar XVII He $\alpha$  ( $E \simeq 3.14$  keV), Ar XVIII Ly $\alpha$  ( $E \simeq 3.3$  keV)

and Ca XIX He $\alpha$  ( $E \simeq 3.9$  keV), blue-shifted by the same common velocity of  $\simeq 0.255c$ . Moreover, we performed a test fitting the spectrum with the baseline model and adding four absorption lines with energies fixed to the theoretical values for these elements, letting the common blue-shift free to vary. We obtained a very good fit with a  $\chi^2$  improvement of 35 for five additional parameters and the derived blue-shift velocity is  $+0.255 \pm 0.003c$ , completely consistent with the value determined only from the Fe XXV He $\alpha$  line. The probability for random fluctuations to give rise to this series of lines with the exact energy spacing and common blue-shift is very low,  $\simeq 2 \times 10^{-6}$ .

## Appendix D

# The XMM-Newton and Suzaku X-ray observatories

### D.1 XMM-Newton

#### D.1.1 General characteristics

The XMM-Newton X-ray observatory (X-ray Multi Mirror Mission) is an ESA (European Space Agency) cornerstone mission launched in December 1999 (Jansen et al. 2001). It hosts two types of telescopes: three “Wolter type-1”, composed by 58 nested mirrors, for the focusing of X-rays and an Optical/UV telescope of 30 cm diameter. On the focal planes of these instruments are positioned the following cameras:

- **European Photon Imaging Camera (EPIC)**: composed by three CCDs, two MOS and one pn, each with its relative X-ray mirror module. They simultaneously allow to perform X-ray imaging, timing and moderate resolution spectroscopy.
- **Reflection Grating Spectrometer (RGS)**: they are two identical reflection grating spectrometers, which allow high resolution X-ray spectroscopy in the 0.3–2 keV band. Their incident flux derives from a partial deviation ( $\sim 40\%$ ) of that focused by the X-ray mirrors related with the MOS cameras.
- **Optical Monitor (OM)**: this is the CCD associated with the Optical/UV telescope. It allows the production of images and spectra as well.

In Table D.1 we report a detailed description of the characteristics of each instrument. The contemporaneous presence of this different instrumentation allows XMM-Newton to

Table D.1: General characteristics of the different instruments on board XMM-Newton.

|                          | pn                        | MOS                       | RGS                                      | OM               |
|--------------------------|---------------------------|---------------------------|--|------------------|
| Energy band              | 0.15–15 keV               | 0.15–12 keV               | 0.35–2.5 keV                             | 180–600 nm       |
| Sensibility <sup>a</sup> | $\sim 10^{-14}$           | $\sim 10^{-14}$           | $\sim 8 \times 10^{-5}$                  | 20.7 mag         |
| Field of view            | 30'                       | 30'                       | $\sim 5'$                                | 17'              |
| PSF <sup>b</sup>         | 6"/15"                    | 5"/14"                    | –  | 1.4" – 1.9"      |
| Pixel                    | 150 $\mu\text{m}$ (4.1")  | 40 $\mu\text{m}$ (1.1")   | 81 $\mu\text{m}$ ( $9 \times 10^{-3}$ Å) | $\sim 0.48''$    |
| Time res. <sup>c</sup>   | 0.03 ms                   | 1.5 ms                    | 16 ms                                    | 0.5 s            |
| Spectral res.            | $\sim 80$ eV <sup>d</sup> | $\sim 70$ eV <sup>d</sup> | 0.04/0.025 Å <sup>e</sup>                | 350 <sup>f</sup> |

(a) In the 0.15–15 keV energy band, in units of  $\text{erg s}^{-1} \text{cm}^{-2}$ .

(b) FWHM/HEW, where the half energy width (HEW) represents the integration radius of the PSF at which corresponds an encircled energy of 50%.

(c) Refers to the fastest data acquisition mode for each instrument.

(d) At 1 keV; at the energy of  $E \simeq 6.4$  keV it is  $\simeq 150$  eV for both EPIC cameras.

(e) At 1 keV it corresponds to a resolution of 3.2 eV.

(f) Resolving power expressed in  $\lambda/\Delta\lambda$ .

be very versatile and makes it one of the best tools available for study of observational X-ray astronomy. Its main properties are:

**Simultaneity** of operation of all the six scientific instruments. The different cameras work independently and can be set in different data acquisition modes. This allows a better adjustment to the different characteristics of the objects that are observed and to obtain higher performances.

**High sensitivity**, thanks to the large area of the X-ray telescopes. In fact, the geometric area at  $\sim 1.5$  keV is  $\sim 1550 \text{ cm}^2$  ( $\sim 4650 \text{ cm}^2$  in total) and the EPIC pn instrument provides the highest effective area among current X-ray satellites in the Fe K band ( $\sim 700\text{--}800 \text{ cm}^2$  at 6.4 keV).

**Good angular resolution**, provided by the elevate capacity of the telescope to focus the X-ray photons. The *Point Spread Function* (PSF), which describes how the radiation from a point source gets distributed on the focal plane, is  $\simeq 6''$  (at FWHM).

**Moderate spectral resolution** of the EPIC cameras, with a resolving power of  $E/\Delta E \sim 20\text{--}50$ . In particular, the energy resolution at  $E \simeq 6.4$  keV is  $\text{FWHM} \simeq 150$  eV.

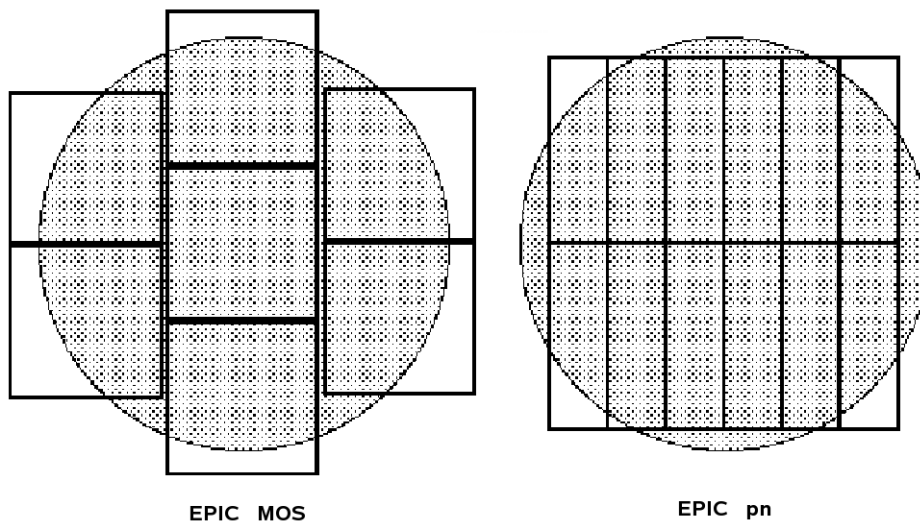


Figure D.1: Field of view (shaded circle) and arrangement of the CCDs on the focal plane of the two different EPIC cameras. *Left*: the MOS detector. *Right*: the pn detector.

Instead, the RGS spectrometers provide a higher energy resolution with  $E/\Delta E \sim 200$ – $800$ , but limited at the soft X-ray band.

**Simultaneous Optical/UV** observations with those in X-rays. This allows the monitoring and identification of the Optical/UV counterpart of the X-ray object observed.

**Long and continuous visibility** of the targets. In fact, the high eccentricity of the elliptical orbit of XMM-Newton allows continuous pointings of sources for  $\sim 50$  hr ( $\sim 145$  ks), which makes it very efficient also for variability studies.

### D.1.2 The EPIC cameras

The European Photon Imaging Camera (EPIC) on board the XMM-Newton satellite is composed by three detectors, placed on the focal planes of the three distinct X-ray telescopes. We will focus our description only on these instruments because their data have been analyzed in this thesis. Two CCD cameras are front illuminated and of type MOS (Metal Oxide Semiconductor). The other is back illuminated and of type pn. These CCDs operate in photon counting mode, with a read-out frequency of the charges that depends on the observation mode. The collected data are organized in event files, in which it is stored the position, energy and time of arrival for each detected photon. Besides the

PN encircled energy (from PSF integration)

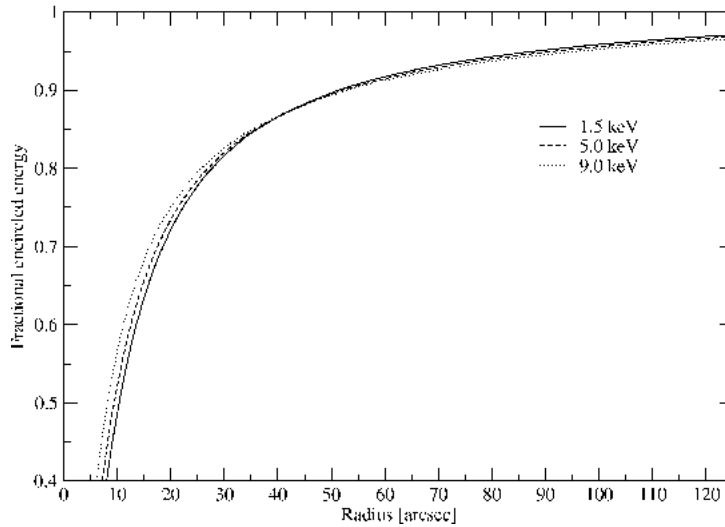


Figure D.2: *Fractional encircled energy* derived integrating the PSF of the X-ray telescope associated to the EPIC pn detector, as a function of the extraction radius (in arcsec). It can be seen that the curve is energy dependent, with a slight change going from 1.5 keV up to 5 keV and 9 keV.

distinct composing material, the two types of CCD cameras that constitute the EPIC have also several other differences, such as:

- **CCD geometry:** as it is shown in Fig. D.1, both cameras have a field of view (FOV) of  $\simeq 30'$  (diameter) but the structure and placement of their chips is different. The MOS are composed by 7 squared CCD of  $10.9'$  per side, not arranged on the same plane. Instead, the pn chips are 12 with dimensions  $13.6' \times 4.4'$ , arranged all on the same plane.
- **Read-out velocity:** once the CCD has been exposed to the X-ray radiation, the charged induced on each pixel must be read and the events recorded. The frequency of this process depends on the observing mode of the detector. However, the read-out velocity is higher for the pn compared to the MOS because each column of pixel of that CCD has its own reading node.
- **Quantum efficiency:** the number of incident photons is different from the number of events that are actually detected by the CCD and it is a function of their energy. The ratio between these two quantities is higher in the pn with respect to the MOS.

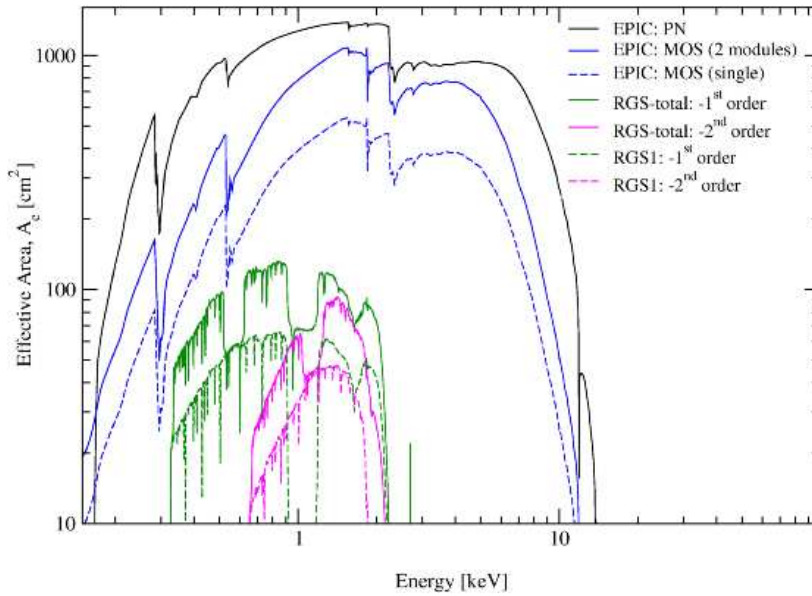


Figure D.3: Effective areas of the different instruments on board XMM-Newton: EPIC pn (black), EPIC MOS (blue) e RGS (purple and green).

This is due to the fact that the CCDs of the pn are back illuminated and thicker than those of the MOS.

The actual instrumental characteristics of an observatory like XMM-Newton depend on the convolution of the properties of the reflecting structures, i.e. the X-ray telescopes, with those of the detectors. A fundamental parameter is the *Point Spread Function* (PSF), which describes the distribution of the photons from a point source on the focal plane. This quantity depends on the capability of the telescopes to focus the X-ray photons. As already stated, the peak of the PSF of the EPIC cameras is sharp ( $\text{FWHM} \simeq 6''$ ) and almost completely energy independent. Integrating the PSF as a function of the distance from the center, we obtain an estimate of the fraction of energy that is contained in that radius (see Fig. D.2). This quantity is called *fractional encircled energy* and it is very important to take into account when selecting the source extraction region from the image produced by the detector.

From the convolution of the quantum efficiency of the detector with the effective area of the telescope, we obtain the resulting effective area of the detector–telescope system. In Fig. D.3 we show the effective area for all the X-ray instruments on board XMM-Newton. It is important to note that this is highest in the 0.1–10 keV band and drops for

Table D.2: Field of view and time resolution for different observing modes of the EPIC pn and EPIC MOS cameras.

| EPIC pn<br>(1 pixel=4.1'') | Field of view<br>(pixel) | Time resolution<br>(ms) |
|----------------------------|--------------------------|-------------------------|
| Full frame                 | 376 × 384                | 73.4                    |
| Extended full frame        | 376 × 384                | 200                     |
| Large window               | 198 × 384                | 48                      |
| Small window               | 63 × 64                  | 6                       |
| Timing <sup>a</sup>        | 64 × 200                 | 0.03                    |
| Burst <sup>a</sup>         | 64 × 20                  | 0.007                   |

| EPIC MOS<br>(1 pixel=1.1'') | Field of view<br>(pixel) | Time resolution<br>(s) |
|-----------------------------|--------------------------|------------------------|
| Full frame                  | 600 × 600                | 2.6                    |
| Large window                | 300 × 300                | 0.9                    |
| Small window                | 100 × 100                | 0.3                    |
| Timing <sup>a</sup>         | 100 × 600                | 1.5 × 10 <sup>-3</sup> |

(a) In this mode the length of the read-out cycle of the chips is reduced significantly due to the fact that the events detected on different pixels are integrated along only one spatial co-ordinate.

higher energies. The absorbing structures are due to different materials that compose the instrumentation. The pn provides the highest instrumental response, with a maximum of  $\sim 1270 \text{ cm}^2$  at  $E \sim 1.5 \text{ keV}$  and an effective area of  $\sim 700\text{--}800 \text{ cm}^2$  at the energies of the Fe K $\alpha$  line ( $E \simeq 6\text{--}7 \text{ keV}$ ). Instead, the effective area of the MOS cameras cannot reach this level, even if combined together. This is due to the fact that only part of the X-ray radiation focused by the mirrors ( $\sim 44\%$ ) actually reach the MOS CCDs. The other part ( $\sim 40\%$ ) is dispersed by the reflection gratings toward the RGS spectrometers.

The capabilities of the instrumentation can degrade over time and therefore continuous calibrations and corrections are required. The actual instrumental response in each performed observation is reported in two different files, called response matrices: the RMF (Redistribution Matrix File), which provides the actual response of the detector as a function of the energy channels; the ARF (Auxiliary Response File), instead, contains the information relative to the effective area, quantum efficiency, filter applied and other

effects due to the CCD geometry and the structure of the mirrors.

The EPIC cameras are able to simultaneously provide the image, light curve and spectrum of the X-ray source that is observed. For this reason, it is fundamental to avoid the superimposition of different events with a precise determination of their location and time of arrival on the CCD. In particular, if the observed source is very bright, the read-out and integration time of the charges can be reduced by decreasing the active area of the detectors. Therefore, as reported in Table D.2, the EPIC cameras can operate in different data acquisition modes. Given the particular arrangement of the CCDs of the MOS cameras on the focal plane, the six external chips always work on the standard mode and only the central one is changed. Instead, for the pn, it is allowed to select regions of the detector that include different chips. However, for the mode with the minimum active area, only the chip directly illuminated by the central part of the PSF is selected.

## D.2 Suzaku

### D.2.1 General characteristics

Suzaku is the last in the series of Japanese X-ray satellites and it was launched into orbit on the 10th of July 2005 (Mitsuda et al. 2007). It is a joint Japanese-US mission, developed mainly by the Institute of Space and Aeronautical Science (part of the Japan Aerospace Exploration Agency, ISAS/JAXA) in collaboration with the NASA's Goddard Space Flight Center.

Suzaku is placed in a near-circular orbit with an apogee of 568 km, an inclination of  $32.9^\circ$  and an orbital period of about 96 minutes. The normal mode of operations has the spacecraft pointing in a single direction for at least 1/4 day ( $\simeq 10$  ks of net exposure time). With this constrain, most targets will be occulted by the Earth for about one third of each orbit, but some objects near the orbital poles can be observed nearly continuously. Therefore, the observing efficiency of the satellite is about 45%.

Unfortunately, despite the initial success of the launch, on the 8th of August 2005 a thermal short between the helium and neon tanks resulted in the liquid helium coolant venting into space, leaving the X-Ray Spectrometer (XRS) inoperable. This instrument (a microcalorimeter) was devoted to high resolution ( $\text{FWHM} \leq 10$  eV) spectroscopy in the  $E \sim 0.5\text{--}10$  keV band.

However, the other instruments, the X-ray Imaging Spectrometer (XIS) and Hard X-

ray Detector (HXD) are all working well. As a result, Suzaku retains its excellent X-ray sensitivity, with high throughput over a broad-band energy range of 0.2 to 500 keV. The broad bandpass, low background and good CCD resolution make Suzaku one of the best tools available for observational studies in X-ray astronomy.

Broadly speaking, Suzaku excels for observations such as:

- Studies of diffuse soft X-ray sources with low surface brightness. This is due to the low background, high soft X-ray sensitivity and near-Gaussian response provided by the XIS BI CCDs.
- Observations requiring high sensitivity both above and below 10 keV, especially measuring the Fe K complex simultaneously with the hard ( $E > 10$  keV) continuum.
- Rapid variability studies on 10 ms time scales.

On the other hand, Suzaku is less appropriate for:

- Studies requiring primarily high spatial resolution. The PSF of the Chandra X-ray satellite is  $\sim 100$  times smaller than that of Suzaku, while the XMM-Newton PSF is  $\sim 10$  times smaller. However, this makes Suzaku less subjected by photon pile-up problems.
- Studies requiring primarily high spectral resolution. The gratings on Chandra and XMM-Newton have significantly higher resolution than the XIS.

### D.2.2 XIS

The four X-ray sensitive imaging CCD cameras (X-ray Imaging Spectrometers, XIS) are composed by three identical front-illuminated CCDs (XIS-FI; energy range  $E=0.4$ – $12$  keV), i.e. XIS 0, XIS 2 (unfortunately this is no longer operative) and XIS 3, and one back-illuminated (XIS BI; energy range  $E=0.2$ – $12$  keV), i.e. the XIS 1. The CCDs are capable of performing imaging, timing and moderate energy resolution spectroscopy. A comparison of the effective areas of the XIS-FI and XIS-BI is showed in Fig. D.4. It can be seen that there are several features due to the elemental composition of the XIS and XRT. K-shell absorption edges from oxygen ( $E \simeq 0.54$  keV) and aluminium ( $E \simeq 1.56$  keV) in the blocking filters are present, as well as a number of weak M-shell features between

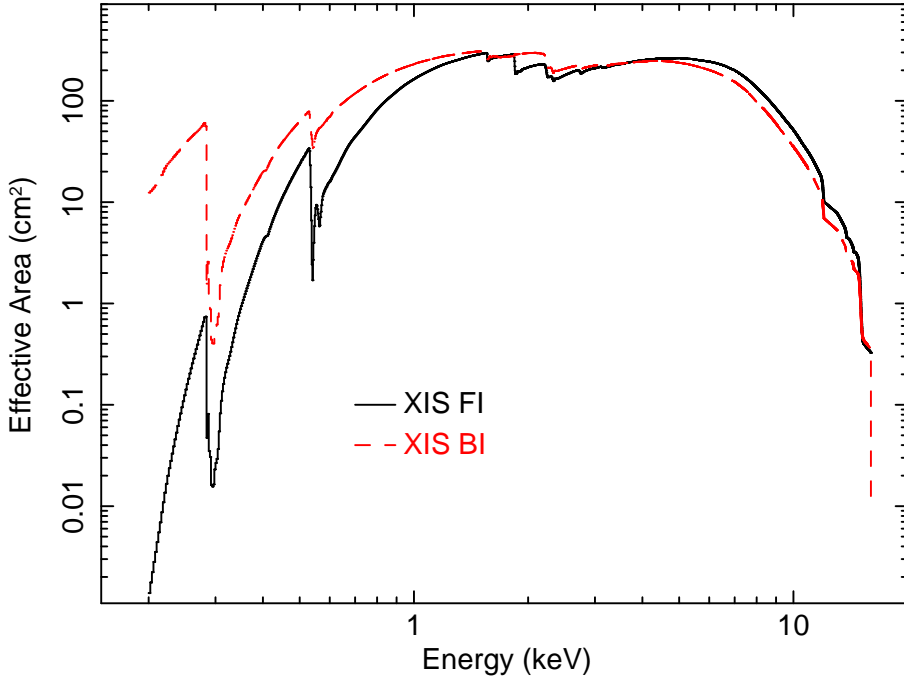


Figure D.4: XIS cameras effective area. The XIS-FI (black solid line) refers to one of the front illuminated detectors XIS 0, XIS 2 and XIS 3. The XIS-BI (red dashed line) refers to the back illuminated XIS 1 detector.

$E=2-3$  keV arising from the gold in the XRT. The effective area of each XIS-FI camera in the Fe K band is  $\sim 200$  cm<sup>2</sup>. These instruments all operate simultaneously and each of them is located in the focal plane of a dedicated X-ray telescope (XRT), with an angular resolution of  $\sim 2'$ . In Table D.3 we report the general characteristics of the XRT and XIS cameras.

Finally, it is important to note that the total effective area of the three combined XIS-FI cameras in the Fe K band is comparable to that of the EPIC pn of XMM-Newton (see §D.1.2) and therefore for slightly longer exposures the XIS-FI can even reach higher S/N ratios.

### D.2.3 HXD

The second instrument is the non-imaging, collimated Hard X-ray Detector (HXD), which extends the bandpass of the observatory to much higher energies, in the range  $E \simeq 10-500$  keV. It has an effective area of  $\simeq 260$  cm<sup>2</sup> and a low background level.

It consists of two type of sensors: 2 mm thick silicon PIN diodes, sensitive over the  $E \simeq 10-70$  keV band, and GSO crystal scintillators placed behind the PIN diodes, covering the  $E \simeq 40-600$  keV interval. The total effective area of the HXD instrument, composed by the PIN at lower and the GSO at higher energies, is shown in Fig. D.5.

The HXD field of view is actively collimated to  $4.5^\circ \times 4.5^\circ$  by well-shaped scintillators,

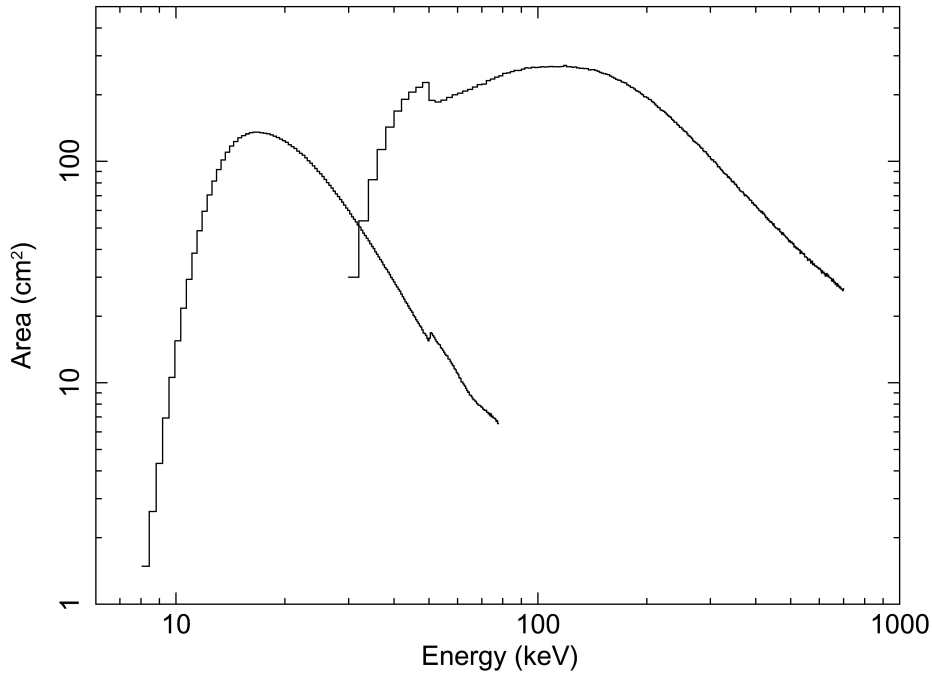


Figure D.5: Total effective area of the HXD detectors, PIN (left curve) and GSO (right curve), as a function of energy.

which, in combination with the GSO scintillators, are arranged in the so-called phoswich configuration. At energies below  $\sim 100$  keV, an additional passive collimation further reduces the field of view to  $34' \times 34'$ . The energy resolution is  $\sim 4$  keV (FWHM) for the PIN and  $7.6/\sqrt{E}$  % (FWHM) for the scintillators (where  $E$  is the energy in MeV). The HXD time resolution for both PIN and GSO sensors is  $61 \mu\text{s}$ . Moreover, while the HXD is intended mainly to explore the faintest hard X-ray sources, it can also tolerate very bright sources up to  $\sim 10$  Crab. The list of the main characteristics of the HXD instrument is reported in Table D.3.

Finally, due to the fact that HXD bore-sight axis, with the highest effective area, is about 3.5 arcmin shifted from that of the XISs, Suzaku supports two aim-points, XIS and HXD oriented. For the XIS, choosing the XIS aim-point provides  $\sim 10\%$  larger XIS effective area than the HXD aim-point. Conversely for the HXD, the HXD aimpoint provides a  $\sim 10\%$  larger effective area than the XIS aimpoint.

Table D.3: General characteristics of the Suzaku instruments.

| Instrument | Parameter         | Value  |
|------------|-------------------|--|
| XRT        | Focal length      | 4.75 m   |
|            | Field of view     | 17' at 1.5 keV<br>13' at 8 keV   |
|            | Eff. area         | 440 cm <sup>2</sup> at 1.5 keV<br>250 cm <sup>2</sup> at 8 keV   |
|            | Angular res.      | 2'   |
|            |                   |  |
| XIS        | Field of view     | 17.8' × 17.8'  |
|            | Bandpass          | 0.2-12 keV   |
|            | Energy res.       | ≈130 eV at 6 keV   |
|            | Eff. area         | 340 cm <sup>2</sup> at 1.5 keV (FI)<br>150 cm <sup>2</sup> at 8 keV (FI)<br>390 cm <sup>2</sup> at 1.5 keV (BI)<br>100 cm <sup>2</sup> at 8 keV (BI) |
|            | Time res.         | 8 s (Normal mode)<br>7.8 ms (P-Sum mode)   |
|            |                   |  |
| HXD        | Field of view     | 4.5° × 4.5° (>100 keV)<br>34' × 34' (≤100 keV)   |
|            | Bandpass          | 10-600 keV   |
|            | -(PIN)            | 10-70 keV  |
|            | -(GSO)            | 40-600 keV   |
|            | Energy res. (PIN) | ≈4 keV   |
|            | Energy res. (GSO) | ≈7.6√ <i>E</i> <sub>MeV</sub> %  |
|            | Eff. area         | ≈160 cm <sup>2</sup> at 20 keV<br>≈260 cm <sup>2</sup> at 100 keV  |
|            | Time res.         | 61 μs  |

# Bibliography

- [1] Antonucci, R. R. J., & Miller, J. S. 1985, *ApJ*, 297, 621
- [2] Antonucci, R. 1993, *ARA&A*, 31, 473
- [3] Bian, W., & Zhao, Y. 2003, *MNRAS*, 343, 164
- [4] Bianchi, S., Matt, G., Balestra, I., & Perola, G. C. 2003, *A&A*, 407, L21 (Bianchi et al. 2003a)
- [5] Bianchi, S., Balestra, I., Matt, G., Guainazzi, M., & Perola, G. C. 2003, *A&A*, 402, 141 (Bianchi et al. 2003b)
- [6] Bianchi, S., Matt, G., Nicastro, F., Porquet, D., & Dubau, J. 2005, *MNRAS*, 357, 599 (Bianchi et al. 2005a)
- [7] Bianchi, S., Miniutti, G., Fabian, A. C., & Iwasawa, K. 2005, *MNRAS*, 360, 380 (Bianchi et al. 2005b)
- [8] Blandford, R. D., & Payne, D. G. 1982, *MNRAS*, 199, 883
- [9] Blustin, A. J., et al. 2003, *A&A*, 403, 481
- [10] Blustin, A. J., Page, M. J., Fuerst, S. V., Branduardi-Raymont, G., & Ashton, C. E. 2005, *A&A*, 431, 111
- [11] Boller, T., Balestra, I., & Kollatschny, W. 2007, *A&A*, 465, 87
- [12] Braitto, V., et al. 2007, *ApJ*, 670, 978
- [13] Burm, H., 1986, *A&A*, 165, 120
- [14] Cappi, M. 2006, *Astronomische Nachrichten*, 327, 1012

- [15] Cappi, M., et al. 2009, *A&A*, 504, 401
- [16] Crenshaw, D. M., Kraemer, S. B., & George, I. M. 2003, *ARA&A*, 41, 117
- [17] Crenshaw, D. M., Kraemer, S. B., Boggess, A., Maran, S. P., Mushotzky, R. F., & Wu, C.-C. 1999, *ApJ*, 516, 750
- [18] Dadina, M., Cappi, M., Malaguti, G., Ponti, G., & de Rosa, A. 2005, *A&A*, 442, 461
- [19] Dadina, M. 2008, *A&A*, 485, 417
- [20] De Luca, A., & Molendi, S. 2004, *A&A*, 419, 837
- [21] de Marco, B., Iwasawa, K., Cappi, M., Dadina, M., Tombesi, F., Ponti, G., Celotti, A., & Miniutti, G. 2009, *A&A*, 507, 159
- [22] Dewangan, G. C., Griffiths, R. E., & Schurch, N. J. 2003, *ApJ*, 592, 52
- [23] Dickey, J. M., & Lockman, F. J. 1990, *ARA&A*, 28, 215
- [24] Elvis, M., et al. 1994, *ApJS*, 95, 1
- [25] Elvis, M. 2000, *ApJ*, 545, 63
- [26] Elvis, M. 2006, *Memorie della Societa Astronomica Italiana*, 77, 573
- [27] Eracleous, M., & Halpern, J. P. 1998, *ApJ*, 505, 577
- [28] Evans, D. A., Lee, J. C., Turner, T. J., Weaver, K. A., & Marshall, H. L. 2007, *ApJ*, 671, 1345
- [29] Fabian, A. C., Iwasawa, K., Reynolds, C. S., Young, A. J., 2000, *PASP*, 112, 1145
- [30] Fabian, A. C. 2009, [arXiv:0912.0880](https://arxiv.org/abs/0912.0880)
- [31] Fabian, A. C., et al. 2009, *Nature*, 459, 540
- [32] Ferrarese, L., & Merritt, D. 2000, *ApJ*, 539, L9
- [33] Fields, D. L., Mathur, S., Krongold, Y., Williams, R., & Nicastro, F. 2007, *ApJ*, 666, 828

- [34] Frank, J., King, A., Raine, D., 1992, *Accretion power in astrophysics*, Cambridge University Press
- [35] Gallo, L. C., Fabian, A. C., Boller, T., & Pietsch, W. 2005, MNRAS, 363, 64
- [36] Ganguly, R., & Brotherton, M. S. 2008, ApJ, 672, 102
- [37] George, I. M., Fabian, A. C., 1991, MNRAS, 249, 352
- [38] George, I. M., Turner, T. J., Netzer, H., Nandra, K., Mushotzky, R. F., & Yaqoob, T. 1998, ApJS, 114, 73
- [39] Ghisellini, G., Haardt, F., & Matt, G. 2004, A&A, 413, 535
- [40] Gondoin, P., Lumb, D., Siddiqui, H., Guainazzi, M., & Scharrel, N. 2001, A&A, 373, 805
- [41] Gondoin, P., Orr, A., Lumb, D., & Siddiqui, H. 2003, A&A, 397, 883
- [42] Grevesse, N., Noels, A., & Sauval, A. J. 1996, *Cosmic Abundances*, 99, 117
- [43] Guainazzi, M., Matt, G., Antonelli, L. A., Fiore, F., Piro, L., & Ueno, S. 1998, MNRAS, 298, 824
- [44] Guainazzi, M. 2003, A&A, 401, 903
- [45] Guilbert, P. W.; Rees, M. J., 1988, MNRAS, 233, 475G
- [46] Güdel, M., et al. 2007, A&A, 468, 353
- [47] Haardt, F., Maraschi, L., 1991, ApJ, 380, L51
- [48] Häring, N., & Rix, H.-W. 2004, ApJ, 604, L89
- [49] Jansen, F., et al. 2001, A&A, 365, L1
- [50] Jiménez-Bailón, E., Krongold, Y., Bianchi, S., Matt, G., Santos-Lleó, M., Piconcelli, E., & Scharrel, N. 2008, MNRAS, 391, 1359
- [51] Kalberla, P. M. W., Burton, W. B., Hartmann, D., Arnal, E. M., Bajaja, E., Morras, R., Pöppel, W. G. L. 2005, A&A, 440, 775

- [52] Kallman, T., & Bautista, M. 2001, *ApJS*, 133, 221
- [53] Kallman, T. R., Palmeri, P., Bautista, M. A., Mendoza, C., & Krolik, J. H. 2004, *ApJS*, 155, 675
- [54] Kataoka, J., et al. 2007, *PASJ*, 59, 279
- [55] Katayama, H., Takahashi, I., Ikebe, Y., Matsushita, K., & Freyberg, M. J. 2004, *A&A*, 414, 767
- [56] Kinkhabwala, A., et al. 2002, *ApJ*, 575, 732
- [57] King, A. R., & Pounds, K. A. 2003, *MNRAS*, 345, 657
- [58] King, A. R. 2009, *MNRAS*, 1914
- [59] Koyama, K., et al., 2007, *PASJ*, 59, 23
- [60] Kraemer, S. B., et al. 2005, *ApJ*, 633, 693
- [61] Krolik, J. H., McKee, C. F., & Tarter, C. B. 1981, *ApJ*, 249, 422
- [62] Krolik, J. H., & Kriss, G. A. 1995, *ApJ*, 447, 512
- [63] Krolik, J. H., & Kriss, G. A. 2001, *ApJ*, 561, 684
- [64] Lapi, A., Cavaliere, A., & Menci, N. 2005, *ApJ*, 619, 60
- [65] Lightman, Alan P.; White, Timothy R., 1988, *ApJ* 335 57L
- [66] Longinotti, A. L., Nandra, K., Petrucci, P. O., & O'Neill, P. M. 2004, *MNRAS*, 355, 929
- [67] Longinotti, A. L., Sim, S. A., Nandra, K., & Cappi, M. 2007, *MNRAS*, 374, 237 (Longinotti et al. 2007a)
- [68] Longinotti, A. L., Bianchi, S., Santos-Lleo, M., Rodríguez-Pascual, P., Guainazzi, M., Cardaci, M., & Pollock, A. M. T. 2007, *A&A*, 470, 73 (Longinotti et al. 2007b)
- [69] Longinotti, A. L., Bianchi, S., Ballo, L., de La Calle, I., & Guainazzi, M. 2009, *MNRAS*, 394, L1

- [70] Low, B. C. 1996, *Sol. Phys.*, 167, 217
- [71] Marchesini, D., Celotti, A., & Ferrarese, L. 2004, *MNRAS*, 351, 733
- [72] Markowitz, A., Reeves, J. N., & Braitto, V. 2006, *ApJ*, 646, 783
- [73] Markowitz, A., Reeves, J. N., George, I. M., Braitto, V., Smith, R., Vaughan, S., Arévalo, P., & Tombesi, F. 2009, *ApJ*, 691, 922
- [74] Marscher, A. P., Jorstad, S. G., Gómez, J.-L., Aller, M. F., Teräsranta, H., Lister, M. L., & Stirling, A. M. 2002, *Nature*, 417, 625
- [75] Mathews, W. G., & Ferland, G. J. 1987, *ApJ*, 323, 456
- [76] Matt, G., Guainazzi, M., Perola, G. C., Fiore, F., Nicastro, F., Cappi, M., & Piro, L. 2001, *A&A*, 377, L31
- [77] Matt, G., Bianchi, S., D'Ammando, F., & Martocchia, A. 2004, *A&A*, 421, 473 (Matt et al. 2004a)
- [78] Matt, G., Bianchi, S., Guainazzi, M., & Molendi, S. 2004, *A&A*, 414, 155 (Matt et al. 2004b)
- [79] Matt, G., Bianchi, S., de Rosa, A., Grandi, P., & Perola, G. C. 2006, *A&A*, 445, 451
- [80] McKernan, B., Yaqoob, T., George, I. M., & Turner, T. J. 2003, *ApJ*, 593, 142 (McKernan et al. 2003a)
- [81] McKernan, B., Yaqoob, T., Mushotzky, R., George, I. M., & Turner, T. J. 2003, *ApJ*, 598, L83 (McKernan et al. 2003b)
- [82] McKernan, B., Yaqoob, T., & Reynolds, C. S. 2004, *ApJ*, 617, 232
- [83] McKernan, B., Yaqoob, T., & Reynolds, C. S. 2005, *MNRAS*, 361, 1337
- [84] McKernan, B., Yaqoob, T., & Reynolds, C. S. 2007, *MNRAS*, 379, 1359
- [85] Miller, L., Turner, T. J., Reeves, J. N., George, I. M., Kraemer, S. B., & Wingert, B. 2007, *A&A*, 463, 131
- [86] Miller, L., Turner, T. J., & Reeves, J. N. 2009, *MNRAS*, 399, L69

- [87] Miniutti, G., & Fabian, A. C. 2004, MNRAS, 349, 1435
- [88] Miniutti, G., & Fabian, A. C. 2006, MNRAS, 366, 115
- [89] Miniutti, G., Ponti, G., Dadina, M., Cappi, M., & Malaguti, G. 2007, MNRAS, 375, 227
- [90] Mitsuda, K., et al., 2007, PASJ, 59, 1
- [91] Mushotzky, R. F., Done, C., Pounds, K. A., 1993, ARA&A, 31, 717
- [92] Nandra, K., George, I. M., Mushotzky, R. F., Turner, T. J., & Yaqoob, T. 1999, ApJ, 523, L17
- [93] Nandra, K., O'Neill, P. M., George, I. M., & Reeves, J. N. 2007, MNRAS, 382, 194
- [94] Neilsen, J., & Lee, J. C. 2009, Nature, 458, 481
- [95] Nicastro, F., Fiore, F., & Matt, G. 1999, ApJ, 517, 108
- [96] Ohsuga, K., Mineshige, S., Mori, M., & Kato, Y. 2009, PASJ, 61, L7
- [97] Padovani, P., & Rafanelli, P. 1988, A&A, 205, 53
- [98] Palmeri, P., Mendoza, C., Kallman, T. R., & Bautista, M. A. 2002, ApJ, 577, L119
- [99] Page, M. J., Davis, S. W., & Salvi, N. J. 2003, MNRAS, 343, 1241
- [100] Parmar, A. 2009, High Resolution X-ray Spectroscopy: Towards IXO
- [101] Peterson, B. M., 1997, *An introduction to Active Galactic Nuclei*, Cambridge University Press
- [102] Peterson, B. M., et al. 2004, ApJ, 613, 682
- [103] Petrucci, P. O., et al. 2007, A&A, 470, 889
- [104] Piconcelli, E., Bianchi, S., Guainazzi, M., Fiore, F., & Chiaberge, M. 2007, A&A, 466, 855
- [105] Piro, L., de Rosa, A., Matt, G., & Perola, G. C. 2005, A&A, 441, L13

- [106] Polletta, M., Weedman, D., Hönig, S., Lonsdale, C. J., Smith, H. E., & Houck, J. 2008, *ApJ*, 675, 960
- [107] Porquet, D., Reeves, J. N., Uttley, P., & Turner, T. J. 2004, *A&A*, 427, 101
- [108] Pounds, K. A., Reeves, J. N., King, A. R., Page, K. L., O'Brien, P. T., & Turner, M. J. L. 2003, *MNRAS*, 345, 705 (Pounds et al. 2003a)
- [109] Pounds, K. A., Reeves, J. N., Page, K. L., Edelson, R., Matt, G., & Perola, G. C. 2003, *MNRAS*, 341, 953 (Pounds et al. 2003b)
- [110] Pounds, K. A., Reeves, J. N., Page, K. L., Wynn, G. A., & O'Brien, P. T. 2003, *MNRAS*, 342, 1147 (Pounds et al. 2003c)
- [111] Pounds, K. A., Reeves, J. N., King, A. R., & Page, K. L. 2004, *MNRAS*, 350, 10 (Pounds et al. 2004a)
- [112] Pounds, K. A., Reeves, J. N., Page, K. L., & O'Brien, P. T. 2004, *ApJ*, 616, 696 (Pounds et al. 2004b)
- [113] Pounds, K. A., & Page, K. L. 2005, *MNRAS*, 360, 1123
- [114] Pounds, K. A., & Page, K. L. 2006, *MNRAS*, 372, 1275
- [115] Pounds, K., & Vaughan, S. 2006, *MNRAS*, 368, 707
- [116] Pounds, K. A., & Reeves, J. N. 2009, *MNRAS*, 397, 249
- [117] Proga, D., Stone, J. M., & Kallman, T. R. 2000, *ApJ*, 543, 686
- [118] Proga, D., & Kallman, T. R. 2004, *ApJ*, 616, 688
- [119] Proga, D. 2007, *The Central Engine of Active Galactic Nuclei*, 373, 267
- [120] Protassov, R., van Dyk, D. A., Connors, A., Kashyap, V. L., & Siemiginowska, A. 2002, *ApJ*, 571, 545
- [121] Rawlings, S., & Saunders, R. 1991, *Nature*, 349, 138
- [122] Reeves, J. N., Turner, M. J. L., Pounds, K. A., O'Brien, P. T., Boller, T., Ferrando, P., Kendziorra, E., & Vercellone, S. 2001, *A&A*, 365, L134

- [123] Reeves, J. N., Nandra, K., George, I. M., Pounds, K. A., Turner, T. J., & Yaqoob, T. 2004, *ApJ*, 602, 648
- [124] Reeves, J. N., Pounds, K., Uttley, P., Kraemer, S., Mushotzky, R., Yaqoob, T., George, I. M., & Turner, T. J. 2005, *ApJ*, 633, L81
- [125] Reeves, J., Done, C., Pounds, K., Terashima, Y., Hayashida, K., Anabuki, N., Uchino, M., & Turner, M. 2008, *MNRAS*, 385, L108
- [126] Reeves, J. N., Sambruna, R. M., Braitto, V., & Eracleous, M. 2009, *ApJ*, 702, L187
- [127] Revnivtsev, M., Sazonov, S., Jahoda, K., & Gilfanov, M. 2004, *A&A*, 418, 927
- [128] Reynolds, C. S., & Fabian, A. C. 1995, *MNRAS*, 273,
- [129] Reynolds, C. S., Brenneman, L. W., Wilms, J., & Kaiser, M. E. 2004, *MNRAS*, 352, 2051167
- [130] Risaliti, G., Bianchi, S., Matt, G., Baldi, A., Elvis, M., Fabbiano, G., & Zezas, A. 2005, *ApJ*, 630, L129
- [131] Rokaki, E., & Boisson, C. 1999, *MNRAS*, 307, 41
- [132] Rybicki, G. B., & Lightman, A. P. 1979, New York, Wiley-Interscience, 1979. 393 p.
- [133] Salpeter, E. E. 1964, *ApJ*, 140, 796
- [134] Sambruna, R. M., Eracleous, M., & Mushotzky, R. F. 1999, *ApJ*, 526, 60
- [135] Sambruna, R. M., Reeves, J. N., & Braitto, V. 2007, *ApJ*, 665, 1030
- [136] Sambruna, R. M., et al. 2009, *ApJ*, 700, 1473
- [137] Schurch, N. J., Warwick, R. S., Griffiths, R. E., & Sembay, S. 2003, *MNRAS*, 345, 423
- [138] Schurch, N. J., Done, C., & Proga, D. 2009, *ApJ*, 694, 1
- [139] Takahashi, T., et al. 2008, *Proc. SPIE*, 7011,
- [140] Tanaka, Y., et al. 1995, *Nature*, 375, 659

- [141] Tarter, C. B., Tucker, W. H., & Salpeter, E. E. 1969, *ApJ*, 156, 943
- [142] Tombesi, F., Cappi, M., Yaqoob, T., Reeves, J., & Palumbo, G. G. C. 2009, arXiv:0910.0654
- [143] Torresi, E., Grandi, P., Longinotti, A. L., Guainazzi, M., Palumbo, G. G. C., Tombesi, F., & Nucita, A. 2009, *MNRAS*, L348
- [144] Turner, T. J., Kraemer, S. B., George, I. M., Reeves, J. N., & Bottorff, M. C. 2005, *ApJ*, 618, 155
- [145] Turner, T. J., Miller, L., Reeves, J. N., & Kraemer, S. B. 2007, *A&A*, 475, 121
- [146] Turner, T. J., Reeves, J. N., Kraemer, S. B., & Miller, L. 2008, *A&A*, 483, 161
- [147] Ungerer, V., Nguyen-Quang-Rieu, Maunon, N., & Brillet, J. 1985, *A&A*, 146, 123
- [148] Urry, C. M., & Padovani, P. 1995, *PASP*, 107, 803
- [149] Vaughan, S., & Fabian, A. C. 2004, *MNRAS*, 348, 1415
- [150] Vaughan, S., Fabian, A. C., Ballantyne, D. R., De Rosa, A., Piro, L., & Matt, G. 2004, *MNRAS*, 351, 193
- [151] Vaughan, S., & Uttley, P. 2008, *MNRAS*, 390, 421
- [152] Verner, D. A., Verner, E. M., & Ferland, G. J. 1996, *Atomic Data and Nuclear Data Tables*, 64, 1
- [153] Wandel, A., & Mushotzky, R. F. 1986, *ApJ*, 306, L61
- [154] Wang, T., & Lu, Y. 2001, *A&A*, 377, 52
- [155] Wang, J.-M., & Zhang, E.-P. 2007, *ApJ*, 660, 1072
- [156] Winter, L. M., Mushotzky, R. F., Tueller, J., & Markwardt, C. 2008, *ApJ*, 674, 686
- [157] Yamaguchi, H., et al. 2006, *Proc. SPIE*, 6266
- [158] Yaqoob, T., McKernan, B., Kraemer, S. B., Crenshaw, D. M., Gabel, J. R., George, I. M., & Turner, T. J. 2003, *ApJ*, 582, 105

[159] Yaqoob, T., & Serlemitsos, P. 2005, *ApJ*, 623, 112

[160] Young, A. J., Lee, J. C., Fabian, A. C., Reynolds, C. S., Gibson, R. R., & Canizares, C. R. 2005, *ApJ*, 631, 733